

**High-energy phenomena in
laboratory and thunderstorm
discharges**

High-energy phenomena in laboratory and thunderstorm discharges

PROEFSCHRIFT

ter verkrijging van de graad van doctor aan de Technische Universiteit
Eindhoven, op gezag van de rector magnificus prof.dr.ir. C.J. van Duijn,
voor een commissie aangewezen door het College voor Promoties, in het
openbaar te verdedigen op dinsdag 28 oktober 2014 om 14:00 uur

door

Christoph Köhn

geboren te Oldenburg in Holstein, Duitsland

Dit proefschrift is goedgekeurd door de promotoren en de samenstelling van de promotiecommissie is als volgt:

voorzitter: prof.dr. H.J.H. Clercx
promotor: prof.dr. U.M. Ebert
copromotor: dr. A.P.J. van Deursen
leden: prof.dr. N.J. Lopes Cardozo
Prof.Dr.rer.net. H. Kersten (Christian-Albrechts-
Universität zu Kiel)
Prof.Dr. L. Schäfer (Universität Duisburg-Essen)
prof.dr. N. Østgaard (University of Bergen)
adviseur: dr. T. Neubert (Technical University of Denmark)

Dit onderzoek werd gesteund door project 10757 van Technologiestichting STW dat deel uitmaakt van de Nederland Organisatie voor Wetenschappelijk Onderzoek (NWO). STW heeft bijgedragen in de drukkosten van het proefschrift.



Centrum Wiskunde & Informatica



Nieuwe technologie
mogelijk maken



Nederlandse Organisatie voor Wetenschappelijk Onderzoek

ISBN: 978-94-6203-669-7

Copyright © 2014 by C. Köhn

Cover design: Ramona Uthmann

Printed in The Netherlands by: Wöhrmann Print Service Zutphen

Pro familiā meā et amicis meis

Summary

Above thunderstorms and in laboratory discharges X- and gamma-rays with energies up to tens of MeV are detected. Additionally electron beams, electron-positron beams and neutron beams are emitted from a thundercloud. We model the generation and propagation of these species using a three dimensional relativistic Monte Carlo code tracing individual particles.

In the first part of the thesis, we investigate how gamma-rays, positrons and hadrons are produced in a thundercloud from an upwards directed negative leader as a part of intracloud lightning. To relate the photon energy and direction, we integrate the Bethe - Heitler cross section for electron-nucleus Bremsstrahlung. We compare our results with cross sections used by other scientists and show that other cross sections lead to unphysically high photon energies. We model the acceleration of electrons in the leader field from some sub-eV to tens of MeV where we also include electron-electron Bremsstrahlung. We calculate the photon distribution and see that electron-electron Bremsstrahlung leads to an enrichment of electrons with energies above 100 keV and consequently to a larger number of high-energy photons. We calculate the energy distribution of positrons and hadrons. We show that a significant number of positrons with energies of up to several MeV is produced and can be detected several kilometers above their source.

The second part is motivated by work of P. Kochkin who studies the emission of X-rays from a discharge of 1 m length and 1 MV voltage. We model the motion of pre-accelerated, monoenergetic electron beams with energies from 100 keV up to 1 MeV in air at standard temperature and pressure (300 K and 1 bar) and calculate the spatial and energy distribution of photons. This gives an insight into how the electron energy is transformed into photon energies.

In the third part we aim towards the understanding how high-energy cosmic rays up to 10^{20} eV influence lightning inception and how lightning influences measurements of cosmic rays. For such a problem, a model to trace particles from 10^{20} eV to sub-eV is

needed. However, the range of validity of the high-energy models stops at 1 MeV when pair production does not occur anymore. Therefore we model the motion of electrons with energies from 1 keV up to 1 GeV in air at 10, 100 and 1000 mbar with and without a constant ambient electric field. We calculate the number of electrons and ions as a function of time and present the energy and spatial distribution of electrons after different time steps. We calculate that the average ionization energy per ion pair is 33 eV for 250 MeV and above. For smaller incident electron energies, however, this energy tends to 20 eV.

In the end this thesis contributes to the understanding of the generation and propagation of different high-energy species at different pressures. We give a new analysis of the production mechanisms and of the observation of beams of electrons, photons, positrons and hadrons in the atmosphere.

Samenvatting

Boven onweer en in ontladingen in het laboratorium worden röntgen- en gammastralen gemeten met energieën tot tientallen MeV. Daarnaast worden vanuit een onweerswolk elektronen-, elektronen-positronen- en neutronbundels uitgezonden. Wij modelleren de productie en beweging van deze deeltjes met een driedimensionale, relativistische Monte Carlo code waarmee individuele deeltjes worden gevolgd.

In het eerste deel van dit proefschrift onderzoeken wij hoe gammastraling, positronen en hadronen in een onweerswolk worden geproduceerd vanuit een naar boven gerichte negatieve *leader* als deel van een *intracloud* bliksem (bliksem binnen een wolk). Om de energie en de richting van fotonen met elkaar te verbinden, wordt de Bethe - Heitler werkzame doorsnede voor elektron-nucleus remstraling geïntegreerd. Wij vergelijken onze resultaten met doorsnedes die door andere onderzoekers worden gebruikt, en laten zien dat andere doorsnedes tot onfysisch hoge energieën leiden. Wij modelleren de versnelling van elektronen in het veld van een *leader* van enkele sub-eV tot enkele MeV waarbij ook elektron-elektron remstraling toegevoegd is. Wij berekenen de fotonenverdeling en zien dat elektron-elektron remstraling tot een verrijking van elektronen met energieën boven 100 keV en daardoor tot een hoger aantal hoogenergetische fotonen leidt. Ook de energieverdeling van positronen en hadronen worden berekend. Wij laten zien dat een aanzienlijk aantal positronen met energieën van enkele MeV wordt geproduceerd en enkele kilometers boven hun bron kan worden gemeten.

Het tweede deel wordt gemotiveerd door werk van P. Kochkin die het uitzenden van röntgenstralen van een ontlading met een lengte van 1 m en een spanning van 1 MV bestudeert. Wij modelleren de beweging van voorversnelde, mono-energetische elektronbundels met energieën van 100 keV t/m 1 MeV in lucht bij 300 K en 1 bar en berekenen de ruimtelijke en energieverdeling van fotonen. Dit geeft nieuw inzicht in hoe de elektronenenergie in fotonenenergie wordt getransformeerd.

Het derde deel is gemotiveerd door de vraag hoe hoogenergetische kosmische straling

t/m 10^{20} eV de inwerkingtreding van bliksems beïnvloedt en hoe bliksems het meten van kosmische deeltjes beïnvloeden. Voor een dergelijk probleem is een model dat deeltjes van 10^{20} tot en met sub-eV volgt, nodig. Echter eindigt het geldigheidsbereik van hoogenergetische modellen bij 1 MeV waar paarproductie niet meer optreedt. Daarom wordt de beweging van elektronen van 1 keV t/m 1 GeV in lucht bij 10, 100 en 1000 mbar met en zonder een constant achtergrond elektrisch veld gemodelleerd. Het aantal elektronen en ionen als functie van tijd wordt berekend en de energie en ruimtelijke verdeling van elektronen na verschillende tijdstappen gepresenteerd. De gemiddelde ionisatieënergie per ion is 33 eV voor 250 MeV en daarboven. Echter neigt deze energie naar 20 eV voor kleinere beginenergieën.

Uiteindelijk draagt dit proefschrift bij aan het begrip van de productie en propagatie van verschillende hoogenergetische deeltjes bij verschillende luchtdrukken. Wij geven een nieuwe analyse van de productiemechanismen en van de observatie van elektronen, fotonen, positronen en hadronen in de atmosfeer.

Zusammenfassung

Oberhalb von Gewittern und in Laborentladungen werden Röntgen- und Gammastrahlen mit Energien von einigen MeV gemessen. Des Weiteren werden von einer Gewitterwolke auch Elektronen-, Elektronen-Positronen- und Neutronenbündel ausgesandt. Wir modellieren die Produktion und Bewegung dieser Teilchen mit Hilfe eines dreidimensionalen, relativistischen Monte Carlo Codes, mit dem wir individuellen Teilchen folgen.

Im ersten Teil dieser Arbeit untersuchen wir, wie Gammastrahlen, Positronen und Hadronen in einer Gewitterwolke von einem nach oben gerichteten negativen *Leader* als Teil eines *intracloud* Blitzes (eines Blitzes innerhalb einer Wolke) produziert werden. Um die Energie und die Richtung eines Photons miteinander zu verbinden, haben wir den Bethe - Heitler Wirkungsquerschnitt für Elektron-Kern Bremsstrahlung integriert. Wir vergleichen unsere Ergebnisse mit Querschnitten, die von anderen Wissenschaftlern benutzt werden, und zeigen, dass andere Querschnitte zu unphysikalisch hohen Energien führen. Wir modellieren die Beschleunigung von Elektronen im Feld eines *Leaders* von einigen sub-eV bis zu einigen MeV, wobei wir auch Elektron-Elektron Bremsstrahlung benutzen. Wir berechnen die Photonverteilung und sehen, dass Elektron-Elektron Bremsstrahlung zu einer Anreicherung von Elektronen mit Energien über 100 keV und dadurch zu einer größeren Anzahl hochenergetischer Photonen führt. Zudem berechnen wir auch die Energieverteilung von Positronen und Hadronen. Wir zeigen, dass eine erhebliche Anzahl von Positronen mit Energien von einigen MeV produziert wird, die einige Kilometer oberhalb ihrer Quelle gemessen werden kann.

Der zweite Teil ist durch die Arbeit von P. Kochkin motiviert, der die Emission von Röntgenstrahlen von einer Entladung einer Länge von 1 m und einer Spannung von 1 MV studiert. Wir modellieren die Bewegung von vorbeschleunigten, monoenergetischen Elektronenschwärmen mit Energien von 100 keV bis 1 MeV in Luft bei 300 K und 1 Bar und berechnen die räumliche und Energieverteilung der Photonen. Dies liefert einen neuen Einblick, in wie genau die Elektronenenergie in Photonenenergie umgewandelt wird.

Der dritte Teil ist durch die Frage motiviert, inwiefern hochenergetische Strahlung bis 10^{20} eV das Entstehen von Blitzen beeinflusst und inwiefern Blitze die Messung kosmischer Teilchen beeinflussen. Für ein solches Problem braucht man ein Model, das Teilchen von 10^{20} eV bis zu einigen sub-eV folgt. Jedoch endet der Gültigkeitsbereich hochenergetischer Modelle bei 1 MeV, worunter Paarerzeugung nicht mehr auftritt. Deshalb modellieren wir die Bewegung von Elektronen mit Energien von 1 keV bis 1 GeV in Luft bei 10, 100 und 1000 mbar mit und ohne konstantes elektrisches Hintergrundfeld. Wir berechnen die Anzahl der Elektronen und Ionen als Funktion der Zeit sowie präsentieren die Energie und räumliche Verteilung der Elektronen nach verschiedenen Zeitschritten. Die durchschnittliche Ionisationsenergie pro Ion is 33 eV für 250 MeV und höher. Jedoch tendiert diese Energie gegen 20 eV für kleinere Anfangsenergien.

Schließlich trägt diese Arbeit zum Verständnis der Produktion und Propagation verschiedener hochenergetischer Teilchen bei verschiedenen Luftdrücken bei. Wir geben eine neue Analyse der Produktionsmechanismen und der Observationen von Elektronen, Photonen, Positronen und Hadronen in der Atmosphäre.

Résumé

Au-dessus des nuages orageux et dans les décharges électriques en laboratoire on peut mesurer des rayonnements X et gammas avec des énergies de quelques MeV. De plus les nuages orageux émettent des faisceaux d'électrons, d'électrons-positrons et de neutrons. Nous modelisons la production et le mouvement de ces particules avec un programme de Monte Carlo tridimensionnel et relativiste avec laquelle nous suivons des particules individuelles.

Dans la première partie de ce travail nous étudions comme les rayonnements gammas, les positrons et les hadrons sont produits dans un nuage orageux par un *leader* négatif orienté vers le haut qui fait parti d'un éclair *intracloud* (éclair dans un nuage orageux). Pour coupler l'énergie et la direction d'un photon, nous intégrons la section efficace de Bethe-Heitler pour rayonnement de freinage électron-noyau. Nous comparons nos résultats avec des sections efficaces utilisées par d'autres scientifiques, et nous montrons que d'autres sections efficaces conduisent à des énergies non-physiquement hautes. Nous modelisons l'accélération des électrons dans le champ d'un *leader* de moins d'un eV à quelques MeV, où nous utilisons aussi un rayonnement de freinage électron-électron. Nous calculons la distribution des photons et nous observons que le rayonnement de freinage électron-électron conduit à l'enrichissement des électrons avec des énergies supérieures à 100 keV et, comme cela, à un plus grand nombre de photons de haute énergie. Nous calculons la distribution énergétique des positrons et des hadrons. Nous démontrons qu'il est possible de mesurer un nombre considérable de positrons avec des énergies de quelques MeV quelques km au-dessus de leur source.

La deuxième partie de cette thèse est motivée par le travail de P. Kochkin qui étudie l'émission des rayonnements X d'une décharge d'une longueur de 1 m et d'un voltage de 1 MV. Nous modelisons le mouvement des électrons pré-accélérés et mono-énergétiques avec des énergies de 100 keV à 1 MeV dans des conditions atmosphériques standard (300 K et 1 bar) et nous calculons la distribution spatiale et énergétique des photons. Cela

fournit une nouvelle vue sur le façon dont l'énergie des électrons est transformée dans l'énergie des photons.

La troisième partie de cette thèse étudie comment le rayonnement très énergétique (jusque 10^{20} eV) influence la formation des éclairs, et comment les éclairs influencent les mesures des particules cosmiques. Pour un tel problème, nous avons besoin d'un modèle pour suivre des particules dont l'énergie décroît de 10^{20} eV jusqu'à moins d'un eV. Toutefois le domaine de validité des modèles appropriés aux hautes énergies se limite à 1 MeV, où il n'y a plus de production de paires électron-positron. Ainsi, nous modélisons le mouvement des électrons avec des énergies de 1 keV à 1 GeV dans l'air, à une pression de 10, 100 et 1000 mbar avec et sans champ électrique constant. Nous calculons le nombre d'électrons et d'ions en fonction du temps, et présentons l'énergie et la distribution spatiale des électrons à différents moments. L'énergie d'ionisation moyenne par ion est de 33 eV pour un faisceau de 250 MeV et au delà. Pourtant cette énergie tend vers 20 eV pour des faisceaux de plus petite énergie.

Finalement ce travail contribue à la compréhension de la production et de la propagation de différentes particules très énergétiques pour différentes pressions atmosphériques. Nous donnons une nouvelle analyse des mécanismes de production et d'observation des électrons, photons, positrons et hadrons dans l'atmosphère.

Summarium

Supra tempestatem et in emisso officina radii Roentgeniani et radiationes gammae cum energiis de nonnullis MeV metirentur. Ultra de nube tempestatis et fascies electrones, electrones-positrones neutronesque emittentur. Productionem et motum harum particularum cum auxilio tres dimensionis relativitatisque Monte Carlo codinis fingimus quo singularem particulam sequimus.

Prima parte huius laboris examinamus quomodo radiationes gammae, positrones hadronesque in nube tempestatis surso directo neganto *leader* ac parte *intracloud* fulminis (fulminis intra nubem) creantur. Ut energia directioque inter se iungerentur, Bethe-Heitler sectionem transversam efficacitatis pro electrone-nucleo radiatione frenata integravimus. Nostras resultates cum sectione transversa, quas alii scientifici utuntur, comparamus et demonstramus quia ceterae sectiones transversae ad inphysicas altas energias ducent. Accelerationem electronum in campo de *leader* de nonnullis eV ad nonnullos MeV electronem-electronem radiationem frenatam utientem fingimus. Distributionem photonum computamus et videmus quia electron-electron radiatio frenata ad accumulationem electronum cum energiis plus C keV et hac re ad maiorem numerum photonum energeticorum ducit. Praeterea distributionem energeticam positronum hadronumque computamus. Demonstramus quia magnus numerus positronum cum energiis de nonnullis MeV creatur, qui nonnullis km supra suam fontem metirentur.

Pars secunda a labore de P. Kochkin incitatur qui emissionem radiorum Roentgenianorum de emisso longitudine I m et tenione electrica I MV studet. Motum praeacceleratorum, monoenergeticorum fascium electronum cum energiis de C keV ad I MeV CCC K et I Bar fingimus et distributionem spatii energiaeque photonum. Perspicium novum confert quomodo energia electronum in energiam photonum commutatur.

Pars tertia a quaestione incitatur quomodo alta energetica radiatio ad X^{XX} eV ortum fulminum movet et quomodo fulmines mensionem cosmicarum particularum movent. Pro tale quaestione exemplo opus est quod particulae a X^{XX} ad nonnullos eV sequitur. Sed

ratio validatis aliorum energeticorum exemplorum I MeV quibus socius productio non iam existit, finem habet. Itaque motum electronum cum energiis ab I keV ad I GeV in aëre X, C et M mbar cum et sine constanta electrico campo recesso fingimus. Numerum electronum et ionum functione temporis computamus atque energiam distributionemque spatii electronum post tempora varia demonstramus. Media energia ionizationis pro ionte XXXIII eV pro CCL MeV altioreque est. Sed ea energia ad XX eV pro parviore energia principia tendit.

Denique hic labor ad intelligentiam productionis et propagationis variarum energeticarum particularum in varia pressione aëre confert. Analysem novam machinationum productionis et observationis electronum, photonum, positronum hadronumque in aëre donamus.

Contents

Summary	i
Samenvatting	ii
Zusammenfassung	iv
Résumé	vi
Summarium	viii
1 Introduction	1
1.1 Extreme particle acceleration in thunderstorms and in laboratory discharges	1
1.1.1 Gamma- and X-rays from thunderstorms and laboratory discharges	1
1.1.2 Beams of high-energy electrons, positrons and hadrons	2
1.2 Relativistic run-away electron avalanches and the streamer-leader process .	3
1.3 The simulation of the creation and motion of highly energetic particles in the atmosphere	4
1.3.1 The particle model	4
1.3.2 The need for appropriate cross sections	4
1.4 Structure of the thesis	5
2 Angular distribution of Bremsstrahlung photons and of positrons for calculations of terrestrial gamma-ray flashes and positron beams	7
2.1 Introduction	8
2.1.1 Flashes of gamma-rays, electrons and positrons above thunderclouds	8
2.1.2 The need for doubly differential cross-sections	8
2.1.3 Available cross-sections for Bremsstrahlung	10

2.1.4	Bremsstrahlung data used by other TGF researchers	13
2.1.5	Organization of the chapter	13
2.2	Bremsstrahlung	14
2.2.1	Definition of the process	14
2.2.2	Validity of the cross sections of Bethe and Heitler	15
2.2.3	Integration over Φ	16
2.2.4	Integration over Θ_f	19
2.2.5	Special limits: $\Theta_i = 0, \pi$ and $\hbar\omega \rightarrow E_{kin,i}$	23
2.3	Pair production	26
2.4	Discussion	29
2.4.1	Bremsstrahlung	29
2.4.2	Pair production	37
2.5	Conclusion	41
2.A	The residual theorem to calculate integrals with trigonometric functions	42
2.A.1	The residual theorem	43
2.A.2	Integral with trigonometric functions	43
2.B	The doubly differential cross section for $\Theta_i = 0$ and $\Theta_i = \pi$	44
2.C	The doubly differential cross section for $\hbar\omega \rightarrow E_{kin,i}$	46
2.D	Discussion of Geant 4	48
2.E	Comparison with Lehtinen	52
2.F	Contribution of the atomic form factor	52
2.G	Contribution of the integrals	54
2.H	Conservation of energy and momentum	54
2.I	Approximation for Θ_i	58
2.J	C++ code	59
3	The importance of electron-electron Bremsstrahlung for terrestrial gamma-ray flashes, electron beams and electron-positron beams	65
3.1	Introduction	66
3.1.1	Energetic radiation from thunderstorms and laboratory discharges	66
3.1.2	Energetic electrons from discharges and the previously used Bremsstrahlung cross sections	66
3.2	Electron-nucleus versus electron-electron Bremsstrahlung	67
3.2.1	Overview of mechanisms	67
3.2.2	Comparison of processes	69
3.3	Electron and photon spectra for a stepped lightning leader	70
3.3.1	Set-up of model and its validation	70
3.3.2	Results and discussion	71
3.4	Conclusion	72

4	Calculation of beams of positrons, neutrons and protons associated with terrestrial gamma-ray flashes	75
4.1	Introduction	76
4.1.1	High-energy emissions from thunderstorms	76
4.1.2	Organization of the chapter	77
4.2	Gamma-ray production by a negative stepped lightning leader	78
4.2.1	Set-up of the model	78
4.2.2	Simulation results	82
4.3	Production and motion of positrons, neutrons and protons in a TGF . . .	85
4.3.1	Modeling	85
4.3.2	The energy and the temporal evolution of positrons and the energy of hadrons	90
4.4	Conclusion and outlook	93
4.A	The electric field of a negative leader	94
4.A.1	Calculation of the electric field of a negative leader	94
4.A.2	Field enhancement close to the tip	95
5	The production of X-rays in air by monoenergetic electron beams with energies of 1 MeV or less	97
5.1	Introduction	98
5.1.1	Organization of the chapter	98
5.2	Set-up of the model	98
5.3	Results	99
5.3.1	Number and energy of electrons	99
5.3.2	The number, energy and spatial distribution of photons	100
5.4	Conclusion	103
6	The structure of ionization showers in air generated by electrons with 1 MeV energy or less	105
6.1	Introduction	106
6.1.1	Energetic particles and discharges	106
6.1.2	Simulating showers created by electrons with energies ≤ 1 MeV . .	106
6.1.3	Content and organization of the chapter	107
6.2	Cross sections and air temperature model	107
6.2.1	Elastic scattering	108
6.2.2	Ionization cross section	108
6.2.3	Electron attachment	109
6.2.4	Air temperature	109
6.3	Results	110
6.3.1	Evolution of electron and ion number in the shower	110
6.3.2	Growth and decay rates	113

6.3.3	Spatial structure of the shower	116
6.3.4	Swarm induced electric field	118
6.3.5	Energy of electrons and O^- ions	119
6.4	Influence of an ambient electric field	121
6.5	Conclusion and outlook	123
6.A	The relativistic binary-encounter Bethe (RBEB) approach	125
6.B	Speed of oxygen ions	127
6.C	Dependence on the cross sections	127
7	Conclusion and outlook	129
7.1	Bremsstrahlung cross sections for free electrons in air	129
7.2	Generation of photons, positrons and hadrons above a thundercloud	130
7.3	Generation of photons from monoenergetic electron beams	131
7.4	Electron showers for energies below 1 MeV	131
A	The relativistic leap-frog scheme	133
A.1	Test in a uniform, constant electric field	135
A.2	Test in a constant, uniform magnetic field	136
	Bibliography	139
	Acknowledgements	153
	Curriculum vitae	157
	Publications	159
	Presentations	161

1.1 Extreme particle acceleration in thunderstorms and in laboratory discharges

1.1.1 Gamma- and X-rays from thunderstorms and laboratory discharges

Lightning strokes and other transient discharges in thunderstorms belong to the most extreme phenomena in earth's atmosphere. Transient luminous events (TLEs), such as blue jets, sprites and elves, occur above thunderclouds up to 100 km altitude. While in later stages the lightning return stroke can heat up to ten thousands of kelvin, it is the earlier stage of the growing lightning leader that can emit flashes of gamma-rays with energies of several tens of MeV. These terrestrial gamma-ray flashes (TGFs) were first measured in 1994 [54] by the BATSE satellite. The measurements were confirmed by the RHESSI satellite [35, 149, 65, 150], by the Fermi satellite [17] and by the GROWTH experiment [162]; measurements by AGILE [112, 155] have shown that the flashes might have quantum energies of up to 100 MeV. High-energy photons were also measured from lightning leaders approaching the earth's surface [115, 40]. Shortly after their discovery it was understood that the acceleration of electrons together with the Bremsstrahlung process is the mechanism to create high energy photons in the atmosphere [54, 158]: energetic electrons collide with air molecules and emit a Bremsstrahlung photon [12, 75, 90]. However, the exact mechanisms how electrons get accelerated into the range of tens of MeV and how they transfer their energy into gamma-rays is still under investigation.

In the laboratory long discharges can emit hard radiation, in this case hard X-rays, during their growth stage as well, similarly to lightning leaders. In a number of laboratory investigations of long sparks, X-rays were measured [152, 40, 93, 43, 121, 134, 136, 122, 111, 143]. Recently, Kochkin et al. [88, 89] have complemented highly time resolved X-ray measurements with discharge images of similarly high resolution. They have shown that

X-rays are created when positive and negative streamers approach each other, enhance the electric field between them further due to their proximity, accelerate electrons to high energies and create hard X-rays by Bremsstrahlung. However, there are no quantitative models for these observations yet.

1.1.2 Beams of high-energy electrons, positrons and hadrons

Besides gamma-ray flashes also beams of electrons [44] and of electron-positron pairs [18] from thunderstorms have been measured by satellites. Electrons and positrons can be distinguished from photons by their dispersion relation and their position relative to the thundercloud. Once electrons or positrons are above a critical altitude, the air density is so small that their motion is not governed by collisions with air molecules any more, and they will follow the geomagnetic field, rather than continuing their path with constant velocity like photons.

Babich [6] has predicted that neutrons with a mean energy of approximately 10 MeV can be produced as well within a thundercloud; the production of neutrons from lightning had already been measured by Fleisher [55] in 1974. Two mechanisms were proposed for neutron production: Either fusion involving deuterium [171] or photoproduction where a photon ejects a neutron from an air molecule. Babich has argued that in thunderstorms only the photonuclear effect can form a sufficiently large source to get a signal distinguishable from the background flux. One should note as well that Agafonov et al. [1] recently have stated that they have measured neutrons with kinetic energies from sub-eV to 10 MeV in laboratory discharges with 1 MV applied to a 1 meter gap. However, it is not clear how these neutrons could gain energies of up to 10 MeV, if only an electric potential of 1 MV is available.

Electron showers are of interest in their own. If a cosmic ray with energy of up to 10^{20} eV enters the earth's atmosphere, it creates an extensive air shower consisting of photons, leptons and hadrons. Energetic secondary electrons might contribute to lightning inception; likewise secondary electrons of radioactive decays can deliver preionization to initiate a laboratory discharge. In order to describe these phenomena, it is important to cover energy ranges from 10^{20} eV down to thermal energies. However, there is little known about the motion and behaviour of electrons between the lower energy cut-off of high energy particle models like EGS5 [49] and CORSIKA [21, 33] or GEANT4 [2, 58] at 10 to 1 MeV and the upper energy cut-off of gas discharge data bases like LXCat at 1 keV [110].

1.2 Relativistic run-away electron avalanches and the streamer-leader process

Quantum particles with energies of up to tens of MeV are observed from thunderstorms. At these energies, the collisional transfer of energy and momentum of electrons to air molecules can be so low, that they are in the run-away regime within the electric fields that can exist inside a thundercloud, i.e., they gain more energy from the field than they lose in collisions [165, 67]. In such fields they can form relativistic runaway electron avalanches [68, 69, 37, 42, 114] or relativistic impact ionization fronts [109] if the electron number increases so much that space charge effects become important.

The first high energy electrons starting avalanches or fronts could either be due to cosmic rays [105, 148, 7, 19] which enter the earth's atmosphere with energies of up to 10^{20} eV and move predominantly downwards, or they could be accelerated into the run-away regime by electric discharges, in particular, in the streamer leader process [117, 100, 29, 101, 24, 26, 104].

While long lasting TGFs have been observed that might be related to a relativistic runaway electron avalanche in a rather uniform thunderstorm electric field, there are clear observations showing that hard radiation is correlated with stepping negative lightning leaders [40]. We will focus on this process in chapters 3 and 4, following the modeling approach of Xu et al. [169, 170].

Streamers and leaders are conducting channels that grow under the influence of high electric potential differences. Ultimately they create a conducting channel that can discharge the potential difference. Leaders are the visible large discharge channels growing inside and between clouds or between clouds and ground over distances of kilometer size. Their path is created by streamer coronas. Streamers consist of a long conductive channel and a propagating head. They are covered by a thin layer of space charge that largely screens their interior from the external field while the field is largely enhanced ahead of the head. As long as this enhanced field is above the breakdown value, impact ionization creates additional ionization at the head and makes the conducting channel grow. Negative streamers carry a negative net charge in their front region and move against the electric field, thus in the direction of the electron drift [107]. Therefore electrons are naturally accelerated away from the streamer tip ionizing the air further. At this location, electrons can be accelerated into the run-away regime [117, 30, 101, 26].

However, due to electron attachment, the conductivity of a streamer eventually is lost, and therefore a streamer cannot bridge distances of much more than a meter in ambient air. But sufficiently high electric currents can heat the air and maintain conductivity; these hot channels are called leaders [10, 135] which can propagate over kilometer distances. The formation of both positive and negative streamers and leaders over one meter distance has recently been observed in laboratory experiments with high temporal resolution by Kochkin et al [88, 89]. In thunderstorms, negative lightning leaders move in steps, i.e., they propagate rapidly, decelerate and stop, then do the next step. This is

well observed [168, 135, 14, 76, 166, 48], but not well understood. Similar observations have been done in laboratory experiments [57] for discharges with a maximal voltage of 2.8 MV over a gap length of 7 m.

1.3 The simulation of the creation and motion of highly energetic particles in the atmosphere

1.3.1 The particle model

To simulate the generation and motion of particles in the atmosphere, we use a particle Monte Carlo code where we refer to electrons, photons, hadrons and positrons as particles. The neutral air molecules are taken as a random background. For our simulations we have implemented a three dimensional relativistic Monte Carlo code as an extension of available discharge codes with electron energies of up to 1 keV to trace positions and momenta of electrons and other leptons as well as photons and hadrons in the atmosphere. As the energies of these particles range from sub-eV to several tens of MeV, they cannot be captured easily with a fluid approximation that only traces densities as well as mean momenta and mean energies of particles.

With a particle code the positions and momenta of the particles can be traced individually. A Monte Carlo particle code consists of two alternating steps: First, between two collisions the position \mathbf{r} and momentum \mathbf{p} of each particle are updated according to the relativistic equations of motion

$$\frac{d\mathbf{r}(t)}{dt} = \mathbf{v}(t) \quad (1.1)$$

$$\frac{d\mathbf{p}(t)}{dt} = e\mathbf{E}(\mathbf{r}, t) \quad (1.2)$$

where \mathbf{E} is the local electric field and the relativistic momentum $\mathbf{p} = m\mathbf{v}/\sqrt{1 - |\mathbf{v}|^2/c^2}$ relates the momentum of a particle to its velocity. Second, particles scatter on air molecules. For different species we have included different collision types as described in sections 3.3.1, 4.2.1, 4.3.1 and 6.2 where the probability of a given collision is proportional to the air density $n(z)$ at altitude z and to the total cross section $\sigma_i(|\mathbf{v}|)$ of process i for a particle with velocity \mathbf{v} [29]. In a Monte Carlo code, random numbers are drawn to determine whether a collision, and, if so, which collision takes place. After a certain collision type is selected, differential cross sections give information about scattering angles or secondary energies [12, 146, 118, 83, 90] that are sampled again by drawing random numbers.

1.3.2 The need for appropriate cross sections

The range of validity of Monte Carlo codes depends on the implementation of classical or relativistic equations of motion and on the range of validity of the used cross sections.

The Monte Carlo code that we use, was originally designed for the inception and motion of streamers [103] in pure nitrogen and in air, where the electrons ahead of a negative streamer reached the run-away regime slightly with energies of up to 3.5 keV [101]. On the other hand, the range of validity of CORSIKA (COsmic Ray SIMulations for KAscade) [33] simulating extensive air showers initiated by high-energy cosmic rays, extends only down to 1 MeV. The Geant 4 toolkit [2] was developed to understand the physics in particle accelerators and detectors, thus for energies above 1 MeV and for atomic numbers for heavy elements such as lead ($Z = 82$), while the atomic numbers of oxygen, nitrogen and argon are $Z = 7, 8, 18$. Part of the present work is devoted to filling the gap of cross sections for energies between 1 keV and 1 MeV as we want to understand the acceleration of electrons in the atmosphere from sub-eV to several tens of MeV as well as the deceleration of electrons from several MeV to thermal energies and the emission of photons, positrons and hadrons.

For the simulation of electrons with energies above 1 keV in the atmosphere at pressures between 1 bar and 10 mbar we have included relativistic equations of motion, three dimensional in position and velocity. Beyond that we have extended the energy range of cross sections for elastic electron-nucleus scattering [146, 118] and electron impact ionization [84], we have deduced the cross sections for electron-nucleus Bremsstrahlung in chapter 2 and we have introduced electron-electron Bremsstrahlung as an additional important mechanism into our simulation. In chapter 6 we describe how we have implemented the cross sections for elastic scattering and electron impact ionization. In Appendix A we describe how we have implemented the relativistic leap-frog scheme, and how we validate the implementation by comparing simulation results with analytical results.

1.4 Structure of the thesis

In chapter 2 and 3 we deal with different Bremsstrahlung cross sections. In chapter 2 we give an extended historical overview over Bremsstrahlung cross sections and calculate the doubly differential cross section for electron-nucleus Bremsstrahlung which relates the photon energy to its emission angle, by integrating out the geometry of the scattered electron. We give a detailed overview of the necessary calculations. We use the quantum field theoretical symmetry between Bremsstrahlung and pair production to calculate the cross section which relates the positron energy to its emission angle. We show that the Bremsstrahlung cross section we have derived, is most appropriate to simulate the production of Bremsstrahlung photons in the atmosphere. In chapter 3 we show that the electron-electron Bremsstrahlung process is important for incident electron energies above 1 MeV leading to an enrichment of high-energy electrons and subsequently of high-energy photons. Thus this process dominates the high-energy tail of terrestrial gamma-ray flashes in thunderstorm discharges.

In chapter 4 we adopt the model of Xu et al. [169, 170] and simulate the acceleration

of electrons in the field of a negative stepped lightning leader at 16 km altitude. We present the spatial and energy distribution of electrons and of Bremsstrahlung photons. In this chapter we also investigate how results alter when exchanging the cross sections from chapter 2 for cross sections by other authors [98]. We see that the energy distribution of photons depends significantly on the implemented Bremsstrahlung cross sections; since we have shown in chapter 2 that our cross sections are appropriate for the generation of Bremsstrahlung photons by free electrons interacting with air molecules, we conclude that previously used cross sections lead to an unphysical photon energy distribution in air. Given the photon distribution, we calculate the generation and motion of positrons as well as the production of hadrons and present their energy distribution. We also trace these positrons through the atmosphere deriving the temporal evolution of their spatial and energy distribution.

In chapter 5 we model the motion of monodirected, pre-accelerated electrons with energies between 100 keV and 1 MeV over several cm and the subsequent production of Bremsstrahlung photons in air at standard temperature and pressure. This gives us information on how electron energy is transformed into photon energies in laboratory discharges [88, 89]. We present the electron number as a function of time and the spatial and energy distribution of Bremsstrahlung photons. We show that the energy distributions have a significant photon number at energies between 30 keV and 250 keV for initial electron energies above 400 keV as mentioned in [38].

In chapter 6 we model the motion of electron swarms with energies below 1 MeV at pressures of 10 mbar, 100 mbar and 1000 mbar with and without ambient fields. This is a first step in coupling high-energy particle models from 10^{20} eV to 1 MeV and models from 1 MeV to thermal energies to investigate the influence of cosmic rays on lightning inception and vice versa the influence of thunderstorm fields on the measurements of cosmic rays. Electrons are liberated through impact ionization and they are lost through dissociative and three-body attachment to oxygen molecules. We present the numbers of electrons and negative oxygen ions as a function of time. We show that the average energy per ion depends on the initial electron energy. We calculate the electric field induced by space charges of residual ions and electrons and the influence of an ambient electric field on the electron swarm.

In Appendix A we explain the leap-frog scheme for relativistic equations of motion. We simulate the motion of an electron in vacuum for a constant uniform electric or magnetic field. We compare the simulation results with analytical results and conclude that we have implemented the leap-frog scheme correctly.

Angular distribution of Bremsstrahlung photons and of positrons for calculations of terrestrial gamma-ray flashes and positron beams

Within thunderstorms electrons can gain energies of up to hundred(s) of MeV. These electrons can create X-rays and gamma-rays as Bremsstrahlung when they collide with air molecules. Here we calculate the distribution of angles between incident electrons and emitted photons as a function of electron and photon energy. We derive these doubly differential cross-sections by integrating analytically over the triply differential cross-sections derived by Bethe and Heitler; this is appropriate for light atoms like nitrogen and oxygen ($Z=7,8$) if the energy of incident and emitted electron is larger than 1 keV. We compare our results with the approximations and cross section used by other authors. We also discuss some simplifying limit cases, and we derive some simple approximation for the most probable scattering angle.

We also provide cross sections for the production of electron positron pairs from energetic photons when they interact with air molecules. This process is related to the Bremsstrahlung process by some physical symmetry. Therefore the results above can be transferred to predictions on the angles between incident photon and emitted positron, again as a function of photon and positron energy. We present the distribution of angles and again a simple approximation for the most probable scattering angle.

Our results are given as analytical expressions as well as in the form of a C++ code that can be directly be implemented into Monte Carlo codes.

This chapter has been published as [C. Köhn and U. Ebert, 2014. Atmos. Res., **135-136**, 432-465]

2.1 Introduction

2.1.1 Flashes of gamma-rays, electrons and positrons above thunderclouds

Terrestrial gamma ray flashes (TGFs) were first observed above thunderclouds by the Burst and Transient Source Experiment (BATSE) [54]. It was soon understood that these energetic photons were generated by the Bremsstrahlung process when energetic electrons collide with air molecules [54, 158]; these electrons were accelerated by some mechanism within the thunderstorm. Since then, measurements of TGFs were extended and largely refined by the Reuven Ramaty High Energy Solar Spectroscopic Imager (RHESSI) [35, 149, 65, 150], by the Fermi Gamma-ray Space Telescope [17], by the Astrorivelatore Gamma a Immagini Leggero (AGILE) satellite which recently measured TGFs with quantum energies of up to 100 MeV [112, 155], and by the Gamma-Ray Observation of Winter Thunderclouds (GROWTH) experiment [162].

Hard radiation was also measured from approaching lightning leaders [115, 40]; and there are also a number of laboratory experiments where very energetic photons were generated during the streamer-leader stage of discharges in open air [152, 41, 93, 43, 121, 134, 136, 122, 111, 143].

Next to gamma-ray flashes, flashes of energetic electrons have been detected above thunderstorms [44]; they are distinguished from gamma-ray flashes by their dispersion and their location relative to the cloud - as charged particles in sufficiently thin air follow the geomagnetic field lines. In December 2009 NASA's Fermi satellite detected a substantial amount of positrons within these electron beams [18]. It is now generally assumed that these positrons come from electron positron pairs that are generated when gamma-rays collide with air molecules.

Two different mechanisms for creating large amounts of energetic electrons in thunderclouds are presently discussed in the literature. The older suggestion is a relativistic run-away process in a rather homogeneous electric field inside the cloud [165, 67, 68, 69, 37, 42, 114].

More recently research focuses on electron acceleration in the streamer-leader process with its strong local field enhancement [117, 100, 29, 101, 24, 26, 103].

2.1.2 The need for doubly differential cross-sections

Whatever the mechanism of electron acceleration in thunderstorms is, ultimately one needs to calculate the energy spectrum and angular distribution of the emitted Bremsstrahlung photons. As the electrons at the source form a rather directed beam pointing against the direction of the local field, the electron energy distribution together with the angles and energies of the emitted photons determine the photon energy spectrum measured by some remote detector. The energy resolved photon scattering angles are de-

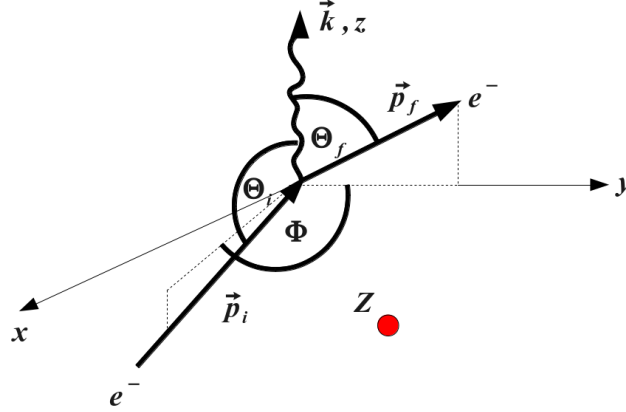


Figure 2.1: Parametrization of the Bremsstrahlung process: Momenta of incident electron \mathbf{p}_i , scattered electron \mathbf{p}_f and emitted photon $\hbar\mathbf{k}$ form the angles $\Theta_i = \sphericalangle(\mathbf{p}_i, \mathbf{k})$ and $\Theta_f = \sphericalangle(\mathbf{p}_f, \mathbf{k})$, and Φ is the angle between the planes spanned by the vector pairs $(\mathbf{p}_i, \mathbf{k})$ and $(\mathbf{p}_f, \mathbf{k})$. The scattering nucleus has atomic number Z .

terminated by so-called doubly differential cross-sections that resolve simultaneously energy $\hbar\omega$ and scattering angle Θ_i of the photons for given energy E_i of the incident electrons. The data is required for scattering on the light elements nitrogen and oxygen with atomic numbers $Z = 7$ and $Z = 8$, while much research in the past has focused on metals with large atomic numbers Z . The energy range up to 1 GeV is relevant for TGFs; we here will provide data valid for energies above 1 keV.

As illustrated by Fig. 1, the full scattering problem is characterized by three angles. The two additional angles Θ_f and Φ determine the direction of the scattered electron relative to the incident electron and the emitted photon. The full angular and energy dependence of this process is determined by so-called triply differential cross-sections. A main result of the present paper is the analytical integration over the angles Θ_f and Φ to determine the doubly differential cross-sections relevant for TGFs.

As the cross-sections for the production of electron positron pairs from photons in the field of some nucleus are related by some physical symmetry to the Bremsstrahlung process, we study these processes as well; we provide doubly differential cross-sections for scattering angle Θ_+ and energy E_+ of the emitted positrons for given incident photon energy $\hbar\omega$ and atomic number Z .

With the doubly differential cross sections for Bremsstrahlung and pair production a feedback model can be constructed tracing Bremsstrahlung photons and positrons as a possible explanation of TGFs [45].

2.1.3 Available cross-sections for Bremsstrahlung

Our present understanding of Bremsstrahlung and pair production was largely developed in the first half of the 20th century. It was first calculated by Bethe and Heitler [12]. Important older reviews are by Heitler [75], by Hough [78], and by Koch and Motz [87]. We also used some recent text books [66, 128]; together with Heitler [75] and Hough [78], they provide a good introduction into the quantum field theoretical description of Bremsstrahlung and pair production. The calculation of these two processes is related through some physical symmetry as will be explained in section 2.3.

As drawn in Fig. 1, when an electron scatters at a nucleus, a photon with frequency ω can be emitted. The geometry of this process is described by the three angles Θ_i , Θ_f and Φ . Cross sections can be total or differential. Total cross sections determine whether a collision takes place for given incident electron energy, singly differential cross sections give additional information on the photon energy or on the angle between incident electron and emitted photon, and doubly differential cross sections contain both. Triply differential cross sections additionally contain the angle at which the electron is scattered. As two angles are required to characterize the direction of the scattered electron, one could argue that this cross section should actually be called quadruply differential, but the standard terminology for the process is triply differential.

Koch and Motz [87] review many different expressions for different limiting cases, but without derivations. Moreover, some experimental results are discussed and compared with the presented theory. Bethe and Heitler [12], Heitler [75], Hough [78], Koch and Motz [87], Peskin and Schroeder [128] and Greiner and Reinhardt [66] use the Born approximation to derive and describe Bremsstrahlung and pair production cross sections.

Several years later new ansatzes were made to describe Bremsstrahlung. Elwert and Haug [51] use approximate Sommerfeld-Maue eigenfunctions to derive cross sections for Bremsstrahlung under the assumption of a pure Coulomb field. They derive a triply differential cross section and beyond that also numerically a doubly differential cross section. Furthermore they compare with results obtained by using the Born approximation. They show that there is a small discrepancy for high atomic numbers between the Bethe-Heitler theory and experimental data, and they provide a correcting factor to fit the Bethe-Heitler approximation better to experimental data for large Z . However, they only investigate properties of Bremsstrahlung for $Z = 13$ (aluminum) and $Z = 79$ (gold).

Tseng and Tseng and Pratt [161] and Fink and Pratt [53] use exact numerical calculations using Coulomb screened potentials and Furry-Sommerfeld-Maue wave functions, respectively. They investigate Bremsstrahlung and pair production for $Z = 13$ and for $Z = 79$ and show that their results with more accurate wave functions do not fit with the Bethe Heitler cross section exactly. This is not surprising as the Bethe-Heitler approximation is developed for low atomic numbers Z and for Z dependent electron energies as discussed in section 2.2.2.

Shaffer et al. [140] review the Bethe Heitler and the Elwert Haug theory. They dis-

cuss that the Bethe Heitler approach is good for small atomic numbers and give a limit of $Z > 29$ for experiments to deviate from theory. For $Z < 29$ the theory of Bethe and Heitler, however, is stated to be in good agreement with experiments for energies above the keV range. They calculate triply differential cross sections using partial-wave and multipole expansions in a screened potential numerically for $Z = 47$ (silver) and $Z = 79$ and compare their results with experimental data. Actually their results are close to the Elwert Haug theory which fits the experimental data better than their theory.

Shaffer and Pratt [141] also discuss the theory of Elwert and Haug [51] and compare it with the Bethe Heitler theory and, additionally, with the Bethe Heitler results multiplied with the Elwert factor and with the exact partial wave method. They show that all theories agree within a factor 10 in the keV energy range, and that the Elwert-Haug theory fits the exact partial wave method best. However, they only investigate Bremsstrahlung for atomic nuclei with $Z = 47, 53$ (iodine), 60 (neodymium), 68 (erbium) and 79, but not for small atomic numbers $Z = 7$ and 8 as relevant in air. In summary, Elwert and Haug [51], Tseng and Pratt [161], Fink and Pratt [53], Shaffer et al. [140] and Shaffer and Pratt [141] calculate cross sections for Bremsstrahlung and pair production for atomic numbers $Z = 13$ and $Z > 47$ numerically, but not analytically, and they do not provide any formula or data which can be used to simulate discharges in air.

The EEDL database consists mainly of experimental data which have been adjusted to nuclear model calculations. For the low energy range Geant4 takes over this data and gives a fit formula. The singly differential cross section related to ω which is used in the Geant4 toolkit is valid in an energy range from 1 keV to 10 GeV and taken from Seltzer and Berger [138]. The singly differential cross section related to Θ_i is based on the doubly differential cross section by [159, 160] and valid for very high energies, i.e., well above (1 – 10) MeV. But in the preimplemented cross sections of Geant4 the dependence on the photon energy is neglected in this case so that it is actually a singly differential cross section describing Θ_i .

Table 2.1 gives an overview of the available literature and data for total or singly, doubly or triply differential Bremsstrahlung cross sections; parameterized angles or photon energies are given, as well as the different energy ranges of the incident electron. Furthermore, the table shows the atomic number Z investigated and includes some further remarks.

For calculating the angularly resolved photon energy spectrum of TGFs, we need a doubly differential cross section resolving both energy and emission angle of the photons; we need it in the energy range between 1 keV and 1 GeV for the small atomic numbers $Z = 7$ and 8. Therefore most of the literature reviewed here is not applicable. However, the Bethe-Heitler approximation is valid for atomic numbers $Z < 29$ and for electron energies above 1 keV [140]. How the range of validity depends on the atomic number Z is discussed in section 2.2.2. We therefore will use the triply differential cross section derived by Bethe and Heitler [12] to determine the correct doubly differential cross.

Data/Paper	Information	Energy range	Atomic Number Z	Remarks
Bethe and Heitler [12, 75]	ω $\omega, \Theta_i, \Theta_f, \Phi$	1 keV - 1 GeV	7,8	energy range depends on Z
Koch and Motz [87]	Total ω ω, Θ_i, Φ $\omega, \Theta_i, \Theta_f, \Phi$	different lower bounds, no upper bounds	depends on the used formulae	
Aiginger [3]	ω, Θ_i	180, 380 keV	79, Al ₂ O ₃	experimental
Elwert and Haug [51]	ω, Θ_i $\omega, \Theta_i, \Theta_f, \Phi$	keV range	13,79	
Penczynski and Wehner [126]	ω, Θ_i	(300 ± 10) keV	82	experimental
Tseng and Pratt [161]	$\omega, \Theta_i, \Theta_f, \Phi$	keV, MeV range	13,79	
Fink and Pratt [53]	ω $\omega, \Theta_i, \Theta_f, \Phi$	keV, MeV range	6,13,79,92	also for pair production
Tsai [159, 160]	ω, Θ_i	> few 10 MeV	all	
Seltzer and Berger [138]	ω	1 keV - 10 GeV	Z=6,13,29,47,74,92	
EEDL [34]	Total	5 eV - 1 TeV	all	see [34]
Nackel [119]	ω, Θ_i	keV	6,29,47,79	only twodimensional description
Schaffer et al. [140]	ω, Θ_i, Φ	keV range	6,13,29,47,74,92	
Schaffer and Pratt [141]	$\omega, \Theta_i, \Theta_f, \Phi$ ω, Θ_i	keV range	47,53,60,68,79	
Lehtinen [98]	ω, Θ_i	1 keV - 1 GeV	7,8	Simple product ansatz for angular and frequency part
Geant 4 [2]	Total ω Θ_i	5 eV - 1 TeV 1 keV - 10 GeV > few 10 MeV	all 6,13,29,47,74,92 all	based on EEDL [34] based on Seltzer and Berger [138] based on Tsai [159, 160]

Table 2.1: Available data for Bremsstrahlung cross sections. Besides the available information on total or singly, doubly or triply differential cross-sections, the range of validity of the incident electron energy and of the atomic number is given. If not stated otherwise, these are theoretical expressions.

2.1.4 Bremsstrahlung data used by other TGF researchers

Carlson et al. [23, 24] use Geant 4, a library of software tools with a preimplemented database to simulate the production of Terrestrial Gamma-Ray Flashes. But Geant 4 does not supply an energy resolved angular distribution as it does not contain a doubly differential cross section, parameterizing both energy and emission angle of the Bremsstrahlung photons (see Table 2.1). Furthermore, it is designed for high electron energies. It also includes the Landau-Pomeranchuk-Migdal (LPM) [96] effect and dielectric suppression [156] which do not contribute in the keV and MeV range. We will briefly discuss the cross sections and effects implemented in Geant 4 in 2.D.

Lehtinen has suggested a doubly differential cross section in his PhD thesis [98] that is also used by Xu et al. [169]. Lehtinen's ansatz is a heuristic approach based on factorization into two factors. The first factor is the singly differential cross section of Bethe and Heitler [12] that resolves only electron and photon energies, but no angles. The second factor is due to Jackson (1975, p. 712 et seq.) [81], it depends on the variable $(1 - \beta^2) [(1 - \beta \cos \Theta_i)^2 + (\cos \Theta_i - \beta)^2] / (1 - \beta \cos \Theta_i)^4$, where $\beta = |v_i|/c$ measures the incident electron velocity on the relativistic scale. However, this factor derived in Jackson is calculated in the classical and not quantum mechanical case, and it is valid only if the photon energy is much smaller than the total energy of the incident electron. We will compare this ansatz with our results in 2.E.

Dwyer [42] chooses to use the triply differential cross section by Bethe and Heitler [12], but with an additional form factor parameterizing the structure of the nucleus [87]. We will show in 2.F that this form factor, however, does not contribute for energies above 1 keV. This cross section depends on all three angles as shown in Fig. 1. If one is only interested in the angle Θ_i between incident electron and emitted Bremsstrahlung photon, the angles Θ_f and Φ have to be integrated out — either numerically, or the analytical results derived in the present paper can be used.

2.1.5 Organization of the chapter

In section 2.2 we introduce the triply differential cross section derived by Bethe and Heitler. Then we integrate over the two angles Θ_f and Φ to obtain the doubly differential cross section which gives a correlation between the energy of the emitted photon and its direction relative to the incident electron. Furthermore, we investigate the limit of very small or very large angles and of high photon energies; this also serves as a consistency check for the correct integration of the full expression.

In section 2.3 we perform the same calculations for pair production, i.e., when an incident photon interacts with an atomic nucleus and creates a positron electron pair. As we explain, this process is actually related by some physical symmetry to Bremsstrahlung, therefore results can be transferred from Bremsstrahlung to pair production. We get a doubly differential cross section for energy and emission angle of the created positron

relative to direction and energy of the incident photon.

The physical interpretation and implications of our analytical results are discussed in section 2.4. Energies and emission angles of the created photons and positrons are described in the particular case of scattering on nitrogen nuclei. For electron energies below 100 keV, the emission of Bremsstrahlung photons in different directions varies typically by not more than an order of magnitude, while for higher electron energies the photons are mainly emitted in forward direction. For this case, we derive an analytical approximation for the most likely emission angle of Bremsstrahlung photons and positrons for given particle energies.

In section 2.5 we will briefly summarize the results of our calculations.

Details of our calculations can be found in sections 2.A - 2.I. Beyond that we provide a C++ code in section 2.J which can be used to create data tables of our analytical results for doubly differential cross-sections both for Bremsstrahlung photons and for pair production positrons for the use in Monte Carlo codes.

2.2 Bremsstrahlung

2.2.1 Definition of the process

If an electron with momentum \mathbf{p}_i approaches the nucleus of an atom, it can change its direction due to Coulomb interaction with the nucleus; the electron acceleration creates a Bremsstrahlung photon with momentum \mathbf{k} that can be emitted at an angle Θ_i relative to the initial direction of the electron. The new direction of the electron forms an angle Θ_f with the direction of the photon. The angle Φ is the angle between the planes spanned by the vector pairs $(\mathbf{p}_i, \mathbf{k})$ and $(\mathbf{p}_f, \mathbf{k})$. This process is shown in figure 1. A virtual photon (allowed by Heisenberg's uncertainty principle) transfers a momentum \mathbf{q} between the electron and the nucleus. Therefore both energy and momentum are conserved in the scattering process.

The corresponding triply differential cross section was derived by Bethe and Heitler [12]:

$$\begin{aligned}
 d^4\sigma &= \frac{Z^2\alpha_{fine}^3\hbar^2}{(2\pi)^2} \frac{|\mathbf{p}_f|}{|\mathbf{p}_i|} \frac{d\omega}{\omega} \frac{d\Omega_i d\Omega_f d\Phi}{|\mathbf{q}|^4} \times \\
 &\times \left[\frac{\mathbf{p}_f^2 \sin^2 \Theta_f}{(E_f - c|\mathbf{p}_f| \cos \Theta_f)^2} (4E_i^2 - c^2\mathbf{q}^2) + \frac{\mathbf{p}_i^2 \sin^2 \Theta_i}{(E_i - c|\mathbf{p}_i| \cos \Theta_i)^2} (4E_f^2 - c^2\mathbf{q}^2) \right. \\
 &+ 2\hbar^2\omega^2 \frac{\mathbf{p}_i^2 \sin^2 \Theta_i + \mathbf{p}_f^2 \sin^2 \Theta_f}{(E_f - c|\mathbf{p}_f| \cos \Theta_f)(E_i - c|\mathbf{p}_i| \cos \Theta_i)} \\
 &\left. - 2 \frac{|\mathbf{p}_i||\mathbf{p}_f| \sin \Theta_i \sin \Theta_f \cos \Phi}{(E_f - c|\mathbf{p}_f| \cos \Theta_f)(E_i - c|\mathbf{p}_i| \cos \Theta_i)} (2E_i^2 + 2E_f^2 - c^2\mathbf{q}^2) \right]. \quad (2.1)
 \end{aligned}$$

Here Z is the atomic number of the nucleus, $\alpha_{fine} \approx 1/137$ is the fine structure constant, $h \approx 6.63 \cdot 10^{-34}$ Js is Planck's constant, $\hbar = h/2\pi$ and $c \approx 3 \cdot 10^8$ m/s is the speed of light. The kinetic energy $E_{kin,i/f}$ of the electron in the initial and final state is related to its total energy and momentum as

$$E_{i/f} = E_{kin,i/f} + m_e c^2 = \sqrt{m_e^2 c^4 + \mathbf{p}_{i/f}^2 c^2} \quad (2.2)$$

where $m_e \approx 9.1 \cdot 10^{-31}$ kg is the electron mass. The conservation of energy implies

$$E_f = E_i - \hbar\omega \quad (2.3)$$

which determines E_f as a function of E_i and $\hbar\omega$. The directions of the emitted photon with energy $\hbar\omega$ and of the scattered electron are parameterized by the three angles (see Fig. 1)

$$\Theta_i = \sphericalangle(\mathbf{p}_i, \mathbf{k}), \quad (2.4)$$

$$\Theta_f = \sphericalangle(\mathbf{p}_f, \mathbf{k}), \quad (2.5)$$

$$\Phi = \text{Angle between the planes } (\mathbf{p}_i, \mathbf{k}) \text{ and } (\mathbf{p}_f, \mathbf{k}). \quad (2.6)$$

The differentials are

$$d\Omega_i = \sin \Theta_i d\Theta_i, \quad (2.7)$$

$$d\Omega_f = \sin \Theta_f d\Theta_f. \quad (2.8)$$

Furthermore one can get an expression for the absolute value of the virtual photon \mathbf{q} with the help of the momenta, the photon energy $\hbar\omega$ and the angles (2.4) - (2.6). Its value is

$$\begin{aligned} -\mathbf{q}^2 &= -|\mathbf{p}_i|^2 - |\mathbf{p}_f|^2 - \left(\frac{\hbar\omega}{c}\right)^2 + 2|\mathbf{p}_i|\frac{\hbar\omega}{c}\cos\Theta_i - 2|\mathbf{p}_f|\frac{\hbar\omega}{c}\cos\Theta_f \\ &+ 2|\mathbf{p}_i||\mathbf{p}_f|(\cos\Theta_f\cos\Theta_i + \sin\Theta_f\sin\Theta_i\cos\Phi). \end{aligned} \quad (2.9)$$

2.2.2 Validity of the cross sections of Bethe and Heitler

The cross sections of Bethe and Heitler (2.1) are valid if the Born approximation [12] holds

$$v \gg \frac{Zc}{137} \quad (2.10)$$

For nitrogen with $Z = 7$ and for oxygen with $Z = 8$, this holds for electron velocities $|\mathbf{v}_{Z=7}| \gg 15 \cdot 10^6$ m/s and $|\mathbf{v}_{Z=8}| \gg 18 \cdot 10^6$ m/s; this is equivalent to a kinetic energy of

$$E_{kin} = \frac{m_e c^2}{\sqrt{1 - \frac{v^2}{c^2}}} - m_e c^2 \gg \begin{cases} 670 \text{ eV}, & Z = 7 \\ 875 \text{ eV}, & Z = 8 \end{cases}. \quad (2.11)$$

This means that incident electron energies above 1 keV can be treated with Eq. 2.1, for lower energies, one cannot calculate with free electron waves anymore, but has to use Coulomb waves [75, 66]; in this case one cannot derive cross sections like (2.1) analytically any more. Thus the Bethe Heitler cross section and our results must not be used for energies of the electron in the initial and final state smaller than 1 keV. However, for higher energies of the electron in the initial and final state, the approximation by Bethe and Heitler becomes more accurate; thus this approximation is better if $E_{kin} \geq 10$ keV.

2.2.3 Integration over Φ

The easiest way is to integrate over the angle Φ between the scattering planes first (see Fig. 2.1) . For this purpose it is useful to redefine some quantities in the following way; therefore (2.1) can be written much more simply:

$$\alpha := 2|\mathbf{p}_i||\mathbf{p}_f| \sin \Theta_i \sin \Theta_f, \quad (2.12)$$

$$\begin{aligned} \beta &:= -\mathbf{p}_i^2 - \mathbf{p}_f^2 - \left(\frac{\hbar}{c}\omega\right)^2 - 2\frac{\hbar}{c}\omega|\mathbf{p}_f| \cos \Theta_f + 2\frac{\hbar}{c}\omega|\mathbf{p}_i| \cos \Theta_i \\ &+ 2|\mathbf{p}_i||\mathbf{p}_f| \cos \Theta_i \cos \Theta_f \end{aligned} \quad (2.13)$$

$$A := \frac{Z^2 \alpha_{fine}^3 |\mathbf{p}_f| \hbar^2}{(2\pi)^2 |\mathbf{p}_i| \omega}, \quad (2.14)$$

$$a_1 := \left(\frac{|\mathbf{p}_f|^2 c^2 \sin^2 \Theta_f}{(E_f - |\mathbf{p}_f|c \cos \Theta_f)^2} + \frac{|\mathbf{p}_i|^2 c^2 \sin^2 \Theta_i}{(E_i - |\mathbf{p}_i|c \cos \Theta_i)^2} \right) \cdot A, \quad (2.15)$$

$$a_2 := \left(-\frac{2|\mathbf{p}_i||\mathbf{p}_f|c^2 \sin \Theta_i \sin \Theta_f}{(E_i - |\mathbf{p}_i|c \cos \Theta_i)(E_f - |\mathbf{p}_f|c \cos \Theta_f)} \right) \cdot A, \quad (2.16)$$

$$\begin{aligned} a_3 &:= \left(\frac{4E_i^2 |\mathbf{p}_f|^2 \sin^2 \Theta_f}{(E_f - |\mathbf{p}_f|c \cos \Theta_f)^2} + \frac{4E_f^2 |\mathbf{p}_i|^2 \sin^2 \Theta_i}{(E_i - |\mathbf{p}_i|c \cos \Theta_i)^2} \right. \\ &\left. + \frac{2\hbar^2 \omega^2 (|\mathbf{p}_i|^2 \sin \Theta_i + |\mathbf{p}_f|^2 \sin^2 \Theta_f)}{(E_i - |\mathbf{p}_i|c \cos \Theta_i)(E_f - |\mathbf{p}_f|c \cos \Theta_f)} \right) \cdot A, \end{aligned} \quad (2.17)$$

$$a_4 := \left(-\frac{|\mathbf{p}_i||\mathbf{p}_f| \sin \Theta_i \sin \Theta_f (4E_i^2 + 4E_f^2)}{(E_i - |\mathbf{p}_i|c \cos \Theta_i)(E_f - |\mathbf{p}_f|c \cos \Theta_f)} \right) \cdot A. \quad (2.18)$$

With (2.12) - (2.18), Eq. (2.1) can be written as:

$$\begin{aligned} \frac{d^4 \sigma}{d\omega d\Omega_i d\Omega_f d\Phi} &= \frac{a_1}{\alpha \cos \Phi + \beta} + \frac{a_2 \cos \Phi}{\alpha \cos \Phi + \beta} \\ &+ \frac{a_3}{(\alpha \cos \Phi + \beta)^2} + \frac{a_4 \cos \Phi}{(\alpha \cos \Phi + \beta)^2}; \end{aligned} \quad (2.19)$$

thus the integration over Φ simply reads

$$\begin{aligned} \frac{d^3\sigma}{d\omega d\Omega_i d\Omega_f} &= \int_0^{2\pi} d\Phi \left[\frac{a_1}{\alpha \cos \Phi + \beta} + \frac{a_2 \cos \Phi}{\alpha \cos \Phi + \beta} \right. \\ &\quad \left. + \frac{a_3}{(\alpha \cos \Phi + \beta)^2} + \frac{a_4 \cos \Phi}{(\alpha \cos \Phi + \beta)^2} \right] \end{aligned} \quad (2.20)$$

where a_i , $i \in \{1, \dots, 4\}$, α and β still depend on Θ_f and Θ_i . These integrals can be calculated with the help of the residue theorem which is reviewed briefly in 2.A. If $R(x, y) : \mathbb{R}^2 \rightarrow \mathbb{R}$ is a rational function without poles on the unit circle $x^2 + y^2 = 1$, then

$$\int_0^{2\pi} R(\cos \Phi, \sin \Phi) d\Phi = 2\pi i \sum_{|z| < 1} \text{Res}(f, z) \quad (2.21)$$

where f is a complex function which is defined as

$$f(z) := \frac{1}{iz} R\left(\frac{1}{2}\left(z + \frac{1}{z}\right), \frac{1}{2i}\left(z - \frac{1}{z}\right)\right). \quad (2.22)$$

The residuum of a pole z_j of order n is defined as

$$\text{Res}(f, z_j) = \frac{1}{(n-1)!} \lim_{z \rightarrow z_j} \frac{d^{n-1}}{dz^{n-1}} \left[(z - z_j) f(z) \right]. \quad (2.23)$$

To integrate the functions in Eq. (2.20), we write

$$R_1(x, y) := \frac{a_1}{\alpha x + \beta}, \quad (2.24)$$

$$R_2(x, y) := \frac{a_2 x}{\alpha x + \beta}, \quad (2.25)$$

$$R_3(x, y) := \frac{a_3}{(\alpha x + \beta)^2}, \quad (2.26)$$

$$R_4(x, y) := \frac{a_4 x}{(\alpha x + \beta)^2}; \quad (2.27)$$

and get from (2.22)

$$f_1(z) = \frac{2a_1}{i(\alpha z^2 + 2\beta z + \alpha)}, \quad (2.28)$$

$$f_2(z) = \frac{a_2 z^2 + a_2}{zi(\alpha z^2 + 2\beta z + \alpha)}, \quad (2.29)$$

$$f_3(z) = \frac{4a_3 z}{i(\alpha z^2 + 2\beta z + \alpha)^2}, \quad (2.30)$$

$$f_4(z) = \frac{2a_4(z^2 + 1)}{i(\alpha z^2 + 2\beta z + \alpha)^2}. \quad (2.31)$$

The poles of the functions $f_i(z)$ in (2.28) - (2.31) are given by

$$z_{1,2} = -\frac{\beta}{\alpha} \pm \sqrt{\left(\frac{\beta}{\alpha}\right)^2 - 1}. \quad (2.32)$$

For $f_{1,2}$ poles are of order one and for $f_{3,4}$ of order two. In addition f_2 has a pole at

$$z_3 = 0. \quad (2.33)$$

According to (2.21) one needs poles with $|z_i| < 1$. For z_3 it is quite clear that $|z_3| = 0 < 1$.

As the angles Θ_i and Θ_f are between 0 and π , the expression $\alpha > 0$ in Eq. (2.12). Furthermore $\cos \Theta_f > -1$, $\cos \Theta_i < 1$ and $|\mathbf{p}_i| > \hbar/c \omega$. Hence

$$\beta \quad (2.34)$$

$$= -\mathbf{p}_i^2 - \mathbf{p}_f^2 - \left(\frac{\hbar}{c}\omega\right)^2 - 2\frac{\hbar}{c}\omega|\mathbf{p}_f|\cos\Theta_f + 2\frac{\hbar}{c}\omega|\mathbf{p}_i|\cos\Theta_i + 2|\mathbf{p}_i||\mathbf{p}_f|\cos\Theta_i\cos\Theta_f \quad (2.35)$$

$$= -\mathbf{p}_i^2 - \mathbf{p}_f^2 - \left(\frac{\hbar}{c}\omega\right)^2 + 2\frac{\hbar}{c}\omega|\mathbf{p}_i|\cos\Theta_i + 2|\mathbf{p}_f|\cos\Theta_f\left(-\frac{\hbar}{c}\omega + |\mathbf{p}_i|\cos\Theta_i\right) \quad (2.36)$$

$$< -\mathbf{p}_i^2 - \mathbf{p}_f^2 - \left(\frac{\hbar}{c}\omega\right)^2 + 2\frac{\hbar}{c}\omega|\mathbf{p}_i| + 2|\mathbf{p}_f|\cos\Theta_f\left(-\frac{\hbar}{c}\omega + |\mathbf{p}_i|\right) \quad (2.37)$$

$$< -\mathbf{p}_i^2 - \mathbf{p}_f^2 - \left(\frac{\hbar}{c}\omega\right)^2 + 2\frac{\hbar}{c}\omega|\mathbf{p}_i| + 2|\mathbf{p}_f|\left(-\frac{\hbar}{c}\omega + |\mathbf{p}_i|\right) \quad (2.38)$$

$$= -\mathbf{p}_i^2 - \mathbf{p}_f^2 - \left(\frac{\hbar}{c}\omega\right)^2 + 2\frac{\hbar}{c}\omega|\mathbf{p}_i| - 2|\mathbf{p}_f|\frac{\hbar}{c}\omega + 2|\mathbf{p}_f||\mathbf{p}_i| \quad (2.39)$$

$$= -\left(|\mathbf{p}_i| - |\mathbf{p}_f| - \frac{\hbar}{c}\omega\right)^2 < 0 \quad (2.40)$$

Therefore β/α in Eq. (2.32) is a negative real number. Furthermore $\sin\Theta_i < 1$ and

$\sin \Theta_f < 1$. Thus

$$-\beta - \alpha \tag{2.41}$$

$$\begin{aligned} &= \mathbf{p}_i^2 + \mathbf{p}_f^2 + \left(\frac{\hbar}{c}\omega\right)^2 + 2\frac{\hbar}{c}\omega|\mathbf{p}_f| \cos \Theta_f - 2\frac{\hbar}{c}\omega|\mathbf{p}_i| \cos \Theta_i \\ &- 2|\mathbf{p}_i||\mathbf{p}_f| \cos \Theta_i \cos \Theta_f - 2|\mathbf{p}_i||\mathbf{p}_f| \sin \Theta_i \sin \Theta_f \end{aligned} \tag{2.42}$$

$$> \mathbf{p}_i^2 + \mathbf{p}_f^2 + \left(\frac{\hbar}{c}\omega\right)^2 - 2\frac{\hbar}{c}\omega|\mathbf{p}_f| - 2\frac{\hbar}{c}\omega|\mathbf{p}_i| - 4|\mathbf{p}_i||\mathbf{p}_f| \tag{2.43}$$

$$> \mathbf{p}_i^2 + \mathbf{p}_f^2 + \left(\frac{\hbar}{c}\omega\right)^2 > 0 \tag{2.44}$$

$$\Rightarrow -\frac{\beta}{\alpha} > 1 \tag{2.45}$$

It follows immediately that $|z_1| > 1$ and $|z_2| < 1$. For all residua one obtains

$$\text{Res}(f_1, z_2) = -\frac{a_1}{i} \frac{1}{\sqrt{\beta^2 - \alpha^2}}, \tag{2.46}$$

$$\text{Res}(f_2, z_2) = \frac{a_2\beta}{\alpha i} \frac{1}{\sqrt{\beta^2 - \alpha^2}}, \tag{2.47}$$

$$\text{Res}(f_2, z_3) = \frac{a_2}{\alpha i}, \tag{2.48}$$

$$\text{Res}(f_3, z_2) = -\frac{a_3\beta}{i} \frac{1}{(\sqrt{\beta^2 - \alpha^2})^3}, \tag{2.49}$$

$$\text{Res}(f_4, z_2) = a_4\alpha \frac{1}{(\sqrt{\beta^2 - \alpha^2})^3}. \tag{2.50}$$

With the knowledge of these residua and using (2.21), the integral in (2.20) can be calculated elementarily

$$\begin{aligned} \frac{d^3\sigma}{d\omega d\Omega_i d\Omega_f} &= \frac{2\pi a_2}{\alpha} + \frac{2\pi}{\sqrt{\beta^2 - \alpha^2}} \left[-a_1 + \frac{a_2\beta}{\alpha} \right. \\ &\quad \left. - \frac{a_3\beta}{|\beta^2 - \alpha^2|} + \frac{a_4\alpha}{|\beta^2 - \alpha^2|} \right]. \end{aligned} \tag{2.51}$$

2.2.4 Integration over Θ_f

After having obtained an expression for the “triply”¹ differential cross section, there is still the integration over Θ_f left. This calculation is mainly straight forward, but rather

¹Here “triply” really means the dependence on the photon frequency and two angles.

tedious. Using expression (2.51), it is

$$\frac{d^2\sigma}{d\omega d\Omega_i} = \int_0^\pi d\Theta_f \left[\frac{2\pi a_2}{\alpha} + \frac{2\pi}{\sqrt{\beta^2 - \alpha^2}} \left(-a_1 + \frac{a_2\beta}{\alpha} - \frac{a_3\beta}{|\beta^2 - \alpha^2|} + \frac{a_4\alpha}{|\beta^2 - \alpha^2|} \right) \right] \sin \Theta_f. \quad (2.52)$$

Let's now consider the first integral of (2.52). If one inserts (2.12) and (2.16), it becomes

$$\int_0^\pi d\Theta_f \frac{2\pi a_2}{\alpha} \sin \Theta_f = -\frac{2\pi A c^2}{E_i - c p_i \cos \Theta_i} \int_0^\pi d\Theta_f \frac{\sin \Theta_f}{E_f - c p_f \cos \Theta_f} \quad (2.53)$$

$$= -\frac{2\pi A c^2}{E_i - c p_i \cos \Theta_i} \int_{-1}^{+1} dx \frac{1}{E_f - c p_f x} \quad (2.54)$$

where the substitution $x := \cos \Theta_f$ was made in the second step. (2.54) is rather simple and yields

$$\int_0^\pi d\Theta_f \frac{2\pi a_2}{\alpha} \sin \Theta_f = -\frac{2\pi A c}{(E_i - c p_i \cos \Theta_i) p_f} \ln \left(\frac{E_f + p_f c}{E_f - p_f c} \right). \quad (2.55)$$

This was a quite simple calculation. All the other integrals can be calculated similarly, but with more effort. As another example let's consider the last integral. Before inserting (2.12), (2.13) and (2.18) one can define for simplicity

$$\Delta_1 := -\mathbf{p}_i^2 - \mathbf{p}_f^2 - \left(\frac{\hbar}{c} \omega \right)^2 + 2 \frac{\hbar}{c} \omega |\mathbf{p}_i| \cos \Theta_i, \quad (2.56)$$

$$\Delta_2 := -2 \frac{\hbar}{c} \omega |\mathbf{p}_f| + 2 |\mathbf{p}_i| |\mathbf{p}_f| \cos \Theta_i. \quad (2.57)$$

The expression β from Eq. (2.13) is then

$$\beta = \Delta_1 + \Delta_2 \cos \Theta_f. \quad (2.58)$$

Thus the regularly appearing term $\beta^2 - \alpha^2$ can be written as

$$\begin{aligned} \beta^2 - \alpha^2 &= (\Delta_2^2 + 4 p_i^2 p_f^2 \sin^2 \Theta_i) \cos^2 \Theta_f + 2 \Delta_1 \Delta_2 \cos \Theta_f \\ &+ (\Delta_1^2 - 4 p_i^2 p_f^2 \sin^2 \Theta_i) \end{aligned} \quad (2.59)$$

$$= \square_1^2 \cos^2 \Theta_f + 2 \Delta_1 \Delta_2 \cos \Theta_f + \square_2^2 \quad (2.60)$$

where the definitions

$$\square_1^2 := \Delta_2^2 + 4p_i^2 p_f^2 \sin^2 \Theta_i, \quad (2.61)$$

$$\square_2^2 := \Delta_1^2 - 4p_i^2 p_f^2 \sin^2 \Theta_i \quad (2.62)$$

have been introduced.

By using (2.12), (2.18) and (2.60), the last integral of (2.51) becomes

$$\begin{aligned} & \int_0^\pi d\Theta_f \frac{2\pi a_4 \alpha}{\sqrt{(\beta^2 - \alpha^2)^3}} \sin \Theta_f = -\frac{16\pi A p_i^2 p_f^2 \sin^2 \Theta_i (E_i^2 + E_f^2)}{E_i - c p_i \cos \Theta_i} \\ & \times \int_0^\pi d\Theta_f \frac{\sin^2 \Theta_f}{\sqrt{(\square_1^2 \cos^2 \Theta_f + 2\Delta_1 \Delta_2 \cos \Theta_f + \square_2^2)^3} (E_f - c p_f \cos \Theta_f)} \sin \Theta_f \end{aligned} \quad (2.63)$$

$$\begin{aligned} & = -\frac{16\pi A p_i^2 p_f^2 \sin^2 \Theta_i (E_i^2 + E_f^2)}{E_i - c p_i \cos \Theta_i} \\ & \times \int_{-1}^{+1} dx \frac{1 - x^2}{\sqrt{(\square_1^2 x^2 + 2\Delta_1 \Delta_2 x + \square_2^2)^3} (E_f - c p_f x)} \end{aligned} \quad (2.64)$$

where $x = \cos \Theta_f$ has been substituted again.

This integration can be performed elementarily by finding the indefinite integral

$$\begin{aligned} & \frac{\square_1^2 x^2 + 2\Delta_1 \Delta_2 x + \square_2^2}{\sqrt{(\square_1^2 x^2 + 2\Delta_1 \Delta_2 x + \square_2^2)^3} (\Delta_1^2 \Delta_2^2 - \square_1^2 \square_2^2) (\square_1^2 E_f^2 + 2\Delta_1 \Delta_2 E_f p_f c + \square_2^2 p_f c)} \times \\ & \times \left(-\square_1^4 E_f x + \square_2^4 p_f c + 2\Delta_1^2 \Delta_2^2 (E_f x - p_f c) + \Delta_1 \Delta_2 \square_2^2 (E_f + p_f c x) \right. \\ & \left. - \square_1^2 (\square_2^2 (E_f x - p_f c) \Delta_1 \Delta_2 (E_f + p_f c x)) \right) \\ & + \frac{E_f^2 - p_f^2 c^2}{\sqrt{(\square_1^2 E_f^2 + 2\Delta_1 \Delta_2 E_f p_f c + \square_2^2 p_f c)^3}} \ln \left((E_f - p_f c x) (\square_1^2 E_f x + \square_2^2 p_f c \right. \\ & \left. + \Delta_1 \Delta_2 (E_f + p_f c x) + \sqrt{\square_1^2 x^2 + 2\Delta_1 \Delta_2 x + \square_2^2} \times \right. \\ & \left. \times \sqrt{\square_1^2 E_f^2 + 2\Delta_1 \Delta_2 E_f p_f c + \square_2^2 p_f c} \right), \end{aligned} \quad (2.65)$$

by inserting +1 and -1 as upper and lower limit, using (2.61) and (2.62) and simplifying.

The integral in (2.63) is then finally

$$\begin{aligned}
\int_0^\pi d\Theta_f \frac{2\pi a_4 \alpha}{\sqrt{(\beta^2 - \alpha^2)^3}} \sin \Theta_f &= \frac{16\pi A p_i^2 p_f^2 \sin^2 \Theta_i (E_i^2 + E_f^2)}{E_i - c p_i \cos \Theta_i} \times \\
&\times \left[-\frac{2(\Delta_2 p_f c + \Delta_1 E_f)}{(-\Delta_2^2 + \Delta_1^2 - 4p_i^2 p_f^2 \sin^2 \Theta_i)((\Delta_2 E_f + \Delta_1 p_f c)^2 + 4m^2 c^4 p_i^2 p_f^2 \sin^2 \Theta_i)} \right. \\
&+ \frac{m^2 c^4}{\sqrt{((\Delta_2 E_f + \Delta_1 p_f c)^2 + 4m^2 c^4 p_i^2 p_f^2 \sin^2 \Theta_i)^3}} \times \\
&\times \ln \left(\left((E_f - c p_f)(4p_i^2 p_f^2 \sin^2 \Theta_i (-E_f - p_f c) + (\Delta_1 - \Delta_2)((\Delta_2 E_f + \Delta_1 p_f c) \right. \right. \\
&- \left. \left. \sqrt{\square_1^2 E_f^2 + 2\Delta_1 \Delta_2 E_f p_f c + \square_2^2 p_f c} \right) (E_f + c p_f)(4p_i^2 p_f^2 \sin^2 \Theta_i + E_f - p_f c) \right. \\
&\left. \left. + (\Delta_1 + \Delta_2)((\Delta_2 E_f + \Delta_1 p_f c) - \sqrt{\square_1^2 E_f^2 + 2\Delta_1 \Delta_2 E_f p_f c + \square_2^2 p_f c})^{-1} \right) \right]. \tag{2.66}
\end{aligned}$$

All the other integrals can be calculated similarly where one always has to substitute $x = \cos \Theta_f$. With this technique the whole doubly differential cross section finally becomes

$$\frac{d^2 \sigma(E_i, \omega, \Theta_i)}{d\omega d\Omega_i} = \sum_{j=1}^6 I_j \tag{2.67}$$

with the following contributions:

$$\begin{aligned}
I_1 &= \frac{2\pi A}{\sqrt{\Delta_2^2 + 4p_i^2 p_f^2 \sin^2 \Theta_i}} \ln \left(\frac{\Delta_2^2 + 4p_i^2 p_f^2 \sin^2 \Theta_i - \sqrt{\Delta_2^2 + 4p_i^2 p_f^2 \sin^2 \Theta_i} (\Delta_1 + \Delta_2) + \Delta_1 \Delta_2}{-\Delta_2^2 - 4p_i^2 p_f^2 \sin^2 \Theta_i - \sqrt{\Delta_2^2 + 4p_i^2 p_f^2 \sin^2 \Theta_i} (\Delta_1 - \Delta_2) + \Delta_1 \Delta_2} \right) \\
&\times \left[1 + \frac{c \Delta_2}{p_f (E_i - c p_i \cos \Theta_i)} - \frac{p_i^2 c^2 \sin^2 \Theta_i}{(E_i - c p_i \cos \Theta_i)^2} - \frac{2h^2 \omega^2 p_f \Delta_2}{c (E_i - c p_i \cos \Theta_i) (\Delta_2^2 + 4p_i^2 p_f^2 \sin^2 \Theta_i)} \right], \tag{2.68}
\end{aligned}$$

$$I_2 = -\frac{2\pi A c}{p_f (E_i - c p_i \cos \Theta_i)} \ln \left(\frac{E_f + p_f c}{E_f - p_f c} \right), \tag{2.69}$$

$$\begin{aligned}
I_3 &= \frac{2\pi A}{\sqrt{(\Delta_2 E_f + \Delta_1 p_f c)^2 + 4m^2 c^4 p_i^2 p_f^2 \sin^2 \Theta_i}} \\
&\times \ln \left(\left((E_f + p_f c)(4p_i^2 p_f^2 \sin^2 \Theta_i (E_f - p_f c) + (\Delta_1 + \Delta_2)((\Delta_2 E_f + \Delta_1 p_f c) \right. \right. \right. \\
&- \left. \left. \sqrt{(\Delta_2 E_f + \Delta_1 p_f c)^2 + 4m^2 c^4 p_i^2 p_f^2 \sin^2 \Theta_i} \right) (E_f - p_f c)(4p_i^2 p_f^2 \sin^2 \Theta_i (-E_f - p_f c) \right. \\
&\left. \left. + (\Delta_1 - \Delta_2)((\Delta_2 E_f + \Delta_1 p_f c) - \sqrt{(\Delta_2 E_f + \Delta_1 p_f c)^2 + 4m^2 c^4 p_i^2 p_f^2 \sin^2 \Theta_i}) \right)^{-1} \right) \\
&\times \left[-\frac{(\Delta_2^2 + 4p_i^2 p_f^2 \sin^2 \Theta_i)(E_f^2 + E_f p_f c^2) + p_f c(2(\Delta_1^2 - 4p_i^2 p_f^2 \sin^2 \Theta_i)E_f p_f c + \Delta_1 \Delta_2(3E_f^2 + p_f^2 c^2))}{(\Delta_2 E_f + \Delta_1 p_f c)^2 + 4m^2 c^4 p_i^2 p_f^2 \sin^2 \Theta_i} \right. \\
&- \frac{c(\Delta_2 E_f + \Delta_1 p_f c)}{p_f (E_i - c p_i \cos \Theta_i)} \\
&- \frac{4E_i^2 p_f^2 (2(\Delta_2 E_f + \Delta_1 p_f c)^2 - 4m^2 c^4 p_i^2 p_f^2 \sin^2 \Theta_i)(\Delta_1 E_f + \Delta_2 p_f c)}{((\Delta_2 E_f + \Delta_1 p_f c)^2 + 4m^2 c^4 p_i^2 p_f^2 \sin^2 \Theta_i)^2} \\
&\left. + \frac{8p_i^2 p_f^2 m^2 c^4 \sin^2 \Theta_i (E_i^2 + E_f^2) - 2h^2 \omega^2 p_i^2 \sin^2 \Theta_i p_f c (\Delta_2 E_f + \Delta_1 p_f c) + 2h^2 \omega^2 p_f m^2 c^3 (\Delta_2 E_f + \Delta_1 p_f c)}{(E_i - c p_i \cos \Theta_i)((\Delta_2 E_f + \Delta_1 p_f c)^2 + 4m^2 c^4 p_i^2 p_f^2 \sin^2 \Theta_i)} \right], \tag{2.70}
\end{aligned}$$

$$I_4 = -\frac{4\pi A p_f c (\Delta_2 E_f + \Delta_1 p_f c)}{(\Delta_2 E_f + \Delta_1 p_f c)^2 + 4m^2 c^4 p_i^2 p_f^2 \sin^2 \Theta_i} - \frac{16\pi E_i^2 p_f^2 A (\Delta_2 E_f + \Delta_1 p_f c)^2}{((\Delta_2 E_f + \Delta_1 p_f c)^2 + 4m^2 c^4 p_i^2 p_f^2 \sin^2 \Theta_i)^2}, \tag{2.71}$$

$$I_5 = \frac{4\pi A}{(-\Delta_2^2 + \Delta_1^2 - 4p_i^2 p_f^2 \sin^2 \Theta_i)((\Delta_2 E_f + \Delta_1 p_f c)^2 + 4m^2 c^4 p_i^2 p_f^2 \sin^2 \Theta_i)}$$

$$\begin{aligned}
& \times \left[\frac{\hbar^2 \omega^2 p_f^2}{E_i - cp_i \cos \Theta_i} \right. \\
& \times \frac{E_f [2\Delta_2^2 (\Delta_2^2 - \Delta_1^2) + 8p_i^2 p_f^2 \sin^2 \Theta_i (\Delta_2^2 + \Delta_1^2)] + p_f c [2\Delta_1 \Delta_2 (\Delta_2^2 - \Delta_1^2) + 16\Delta_1 \Delta_2 p_i^2 p_f^2 \sin^2 \Theta_i]}{\Delta_2^2 + 4p_i^2 p_f^2 \sin^2 \Theta_i} \\
& + \frac{2\hbar^2 \omega^2 p_i^2 \sin^2 \Theta_i (2\Delta_1 \Delta_2 p_f c + 2\Delta_2^2 E_f + 8p_i^2 p_f^2 \sin^2 \Theta_i E_f)}{E_i - cp_i \cos \Theta_i} \\
& + \frac{2E_i^2 p_f^2 \{2(\Delta_2^2 - \Delta_1^2)(\Delta_2 E_f + \Delta_1 p_f c)^2 + 8p_i^2 p_f^2 \sin^2 \Theta_i [(\Delta_1^2 + \Delta_2^2)(E_f^2 + p_f^2 c^2) + 4\Delta_1 \Delta_2 E_f p_f c]\}}{((\Delta_2 E_f + \Delta_1 p_f c)^2 + 4m^2 c^4 p_i^2 p_f^2 \sin^2 \Theta_i)} \\
& \left. + \frac{8p_i^2 p_f^2 \sin^2 \Theta_i (E_i^2 + E_f^2)(\Delta_2 p_f c + \Delta_1 E_f)}{E_i - cp_i \cos \Theta_i} \right], \tag{2.72}
\end{aligned}$$

$$I_6 = \frac{16\pi E_f^2 p_i^2 \sin^2 \Theta_i A}{(E_i - cp_i \cos \Theta_i)^2 (-\Delta_2^2 + \Delta_1^2 - 4p_i^2 p_f^2 \sin^2 \Theta_i)}. \tag{2.73}$$

Eq. (2.67) depends explicitly on E_i, ω and Θ_i while E_f and p_f are functions of E_i and ω through (2.2) and (2.3). (2.67) is the final result of the integration of (2.1) over Φ and Θ_f with the help of the residue theorem and some basic calculations. Now this result can be used both as input for Monte Carlo code and for discussing some basic properties of the behaviour of produced Bremsstrahlung photons.

Actually (2.67) is also valid for $\Theta_i = 0$, as will be shown in the next section, but the simple way just to set $\Theta_i = 0$ in (2.67) will fail, especially for numerical purposes, because the logarithmic part in (2.68) tends to “ $\ln(0/0)$ ” for $\Theta_i \rightarrow 0$ and so fails for numerical applications. Thus we need an additional expression for $\Theta_i = 0$ which has to be consistent with (2.67).

2.2.5 Special limits: $\Theta_i = 0, \pi$ and $\hbar\omega \rightarrow E_{kin,i}$

For some special cases the integration of (2.1) over Φ and Θ_f is easier. This information can also be used to verify (2.67) by checking consistency and use them for Monte Carlo codes.

$\Theta_i = 0$ or $\Theta_i = \pi$

If one is only interested in forward and backward scattering, one can set $\Theta_i = 0$ or $\Theta_i = \pi$ before integrating; then (2.1) becomes

$$\begin{aligned}
\frac{d^4 \sigma}{d\omega d\Omega_i d\Omega_f d\Phi} &= \frac{Z^2 \alpha_{fine}^3 \hbar^2 |\mathbf{p}_f|}{(2\pi)^2 |\mathbf{p}_i|} \frac{1}{\omega} \frac{1}{|\mathbf{q}|^4} \\
&\times \left(\frac{\mathbf{p}_f^2 \sin^2 \Theta_f}{(E_f - c|\mathbf{p}_f| \cos \Theta_f)^2} (4E_i^2 - c^2 \mathbf{q}^2) \right. \\
&\left. + 2 \hbar^2 \omega^2 \frac{\mathbf{p}_f^2 \sin^2 \Theta_f}{(E_f - c|\mathbf{p}_f| \cos \Theta_f)(E_i \mp c|\mathbf{p}_i|)} \right) \tag{2.74}
\end{aligned}$$

where the momentum \mathbf{q} of the virtual photon can be written as

$$-\mathbf{q}^2 = -\mathbf{p}_i^2 - \mathbf{p}_f^2 - \left(\frac{\hbar}{c}\omega\right)^2 - 2\frac{\hbar}{c}|\mathbf{p}_f|\cos\Theta_f \pm 2\frac{\hbar}{c}\omega|\mathbf{p}_i| \pm 2|\mathbf{p}_i||\mathbf{p}_f|\cos\Theta_f. \quad (2.75)$$

Here the upper sign corresponds to $\Theta_i = 0$ and the lower one to $\Theta_i = \pi$.

As (2.74) and (2.75) do not depend on Φ at all, the Φ integration simply gives a factor of 2π , and (2.74) becomes

$$\begin{aligned} \frac{d^3\sigma}{d\omega d\Omega_i d\Omega_f} &= \frac{Z^2\alpha_{fine}^3\hbar^2}{2\pi} \frac{|\mathbf{p}_f|}{|\mathbf{p}_i|} \frac{1}{\omega} \frac{1}{|\mathbf{q}|^4} \\ &\times \left(\frac{\mathbf{p}_f^2 \sin^2\Theta_f}{(E_f - c|\mathbf{p}_f|\cos\Theta_f)^2} (4E_i^2 - c^2\mathbf{q}^2) \right. \\ &\left. + 2\hbar^2\omega^2 \frac{\mathbf{p}_f^2 \sin^2\Theta_f}{(E_f - c|\mathbf{p}_f|\cos\Theta_f)(E_i \mp c|\mathbf{p}_i|)} \right). \end{aligned} \quad (2.76)$$

Finally this expression has to be integrated over Θ_f in order to obtain the doubly differential cross section. Similarly to the total integration of (2.52) it is convenient to define

$$\tilde{\Delta}_1 := -\left(p_i \mp \frac{\hbar}{c}\omega\right)^2 - p_f^2, \quad (2.77)$$

$$\tilde{\Delta}_2 := -2\frac{\hbar}{c}\omega p_f \pm 2p_i p_f \quad (2.78)$$

where $\tilde{\Delta}_{1,2} = \Delta_{1,2}(\Theta_i = 0, \pi), j \in \{1, 2\}$, with definitions (2.56) and (2.57). Eq. (2.75) can then be rewritten as

$$-\mathbf{q}^2 = \tilde{\Delta}_1 + \tilde{\Delta}_2 \cos\Theta_f \quad (2.79)$$

and

$$\begin{aligned} \frac{d^2\sigma}{d\omega d\Omega_i} &= \frac{Z^2\alpha_{fine}^3\hbar^2}{2\pi} \frac{|\mathbf{p}_f|}{|\mathbf{p}_i|} \frac{1}{\omega} \int_0^\pi d\Theta_f \left[\frac{|\mathbf{p}_f|^2 c^2 \sin^2\Theta_f}{(E_f - |\mathbf{p}_f|c \cos\Theta_f)^2 (\tilde{\Delta}_1 + \tilde{\Delta}_2 \cos\Theta_f)} \right. \\ &+ \frac{4E_i^2 |\mathbf{p}_f|^2 \sin^2\Theta_f}{(E_f - |\mathbf{p}_f|c \cos\Theta_f)^2 (\tilde{\Delta}_1 + \tilde{\Delta}_2 \cos\Theta_f)^2} \\ &\left. + \frac{2\hbar^2\omega^2 |\mathbf{p}_f|^2 \sin^2\Theta_f}{(E_i \mp c|\mathbf{p}_i|)(E_f - |\mathbf{p}_f|c \cos\Theta_f)(\tilde{\Delta}_1 + \tilde{\Delta}_2 \cos\Theta_f)^2} \right] \sin\Theta_f \end{aligned} \quad (2.80)$$

where the integration is rather elementary and can be performed by substituting $x = \cos \Theta_f$ again. Thus (2.80) yields

$$\begin{aligned}
\frac{d^2\sigma}{d\omega d\Omega_i}(E_i, \omega, \Theta_i = 0, \pi) &= \frac{Z^2 \alpha^3 \hbar^2 |\mathbf{p}_f|}{2\pi |\mathbf{p}_i| \omega} \frac{1}{\omega} \left[-\frac{2|\mathbf{p}_f|c}{\tilde{\Delta}_2 E_f + \tilde{\Delta}_1 |\mathbf{p}_f|c} \right. \\
&+ \frac{|\mathbf{p}_f|^2 c^2 (-\tilde{\Delta}_1^2 + \tilde{\Delta}_2^2)}{\tilde{\Delta}_2 (\tilde{\Delta}_2 E_f + \tilde{\Delta}_1 |\mathbf{p}_f|c)^2} \ln \left(\frac{\tilde{\Delta}_1 + \tilde{\Delta}_2}{\tilde{\Delta}_1 - \tilde{\Delta}_2} \right) \\
&+ \frac{2\tilde{\Delta}_1 E_f |\mathbf{p}_f|c + \tilde{\Delta}_2 (E_f^2 + |\mathbf{p}_f|^2 c^2)}{(\tilde{\Delta}_2 E_f + \tilde{\Delta}_1 |\mathbf{p}_f|c)^2} \ln \left(\frac{E_f + |\mathbf{p}_f|c}{E_f - |\mathbf{p}_f|c} \right) \\
&- \frac{16E_i^2 |\mathbf{p}_f|^2}{(\tilde{\Delta}_2 E_f + \tilde{\Delta}_1 |\mathbf{p}_f|c)^2} - \frac{4\hbar^2 |\mathbf{p}_f|^2 \omega^2}{(\tilde{\Delta}_2 E_f + \tilde{\Delta}_1 |\mathbf{p}_f|c)(E_i \mp c|\mathbf{p}_i|)\tilde{\Delta}_2} \\
&- \frac{8E_i^2 |\mathbf{p}_f|^2 (\tilde{\Delta}_1 E_f + \tilde{\Delta}_2 |\mathbf{p}_f|c)}{(\tilde{\Delta}_2 E_f + \tilde{\Delta}_1 |\mathbf{p}_f|c)^3} \ln \left(\frac{(\tilde{\Delta}_1 - \tilde{\Delta}_2)(E_f - |\mathbf{p}_f|c)}{(\tilde{\Delta}_1 + \tilde{\Delta}_2)(E_f + |\mathbf{p}_f|c)} \right) \\
&+ \frac{2\hbar^2 |\mathbf{p}_f|^2 \omega^2 (2\tilde{\Delta}_1 \tilde{\Delta}_2 E_f + \tilde{\Delta}_1^2 |\mathbf{p}_f|c + \tilde{\Delta}_2^2 |\mathbf{p}_f|c)}{(\tilde{\Delta}_2 E_f + \tilde{\Delta}_1 |\mathbf{p}_f|c)^2 (E_i \mp c|\mathbf{p}_i|)\tilde{\Delta}_2^2} \ln \left(\frac{\tilde{\Delta}_1 + \tilde{\Delta}_2}{\tilde{\Delta}_1 - \tilde{\Delta}_2} \right) \\
&+ \left. \frac{2\hbar^2 |\mathbf{p}_f| \omega^2 (E_f^2 - c^2 |\mathbf{p}_f|^2)}{(\tilde{\Delta}_2 E_f + \tilde{\Delta}_1 |\mathbf{p}_f|c)^2 (E_i \mp c|\mathbf{p}_i|)c} \ln \left(\frac{E_f - |\mathbf{p}_f|c}{E_f + |\mathbf{p}_f|c} \right) \right]. \quad (2.81)
\end{aligned}$$

This expression is much simpler than (2.67), but only valid for $\Theta_i = 0$ or $\Theta_i = \pi$. Actually this expression has also been obtained by calculating the limit $\Theta_i \rightarrow 0$ or $\Theta_i \rightarrow \pi$ in (2.67); hence the consistency check is successful. Details can be found in 2.B.

$\hbar\omega \rightarrow E_{kin,i}$

The other case which can be investigated easily is when almost all kinetic energy of the incident electron is transferred to the emitted photon, i.e.,

$$E_f = E_i - \hbar\omega = E_{kin,i} + m_e c^2 - \hbar\omega \xrightarrow{\hbar\omega \rightarrow E_{kin,i}} m_e c^2 \quad (2.82)$$

and

$$|\mathbf{p}_f| = \sqrt{\frac{E_f^2}{c^2} - m_e^2 c^2} \xrightarrow{\hbar\omega \rightarrow E_{kin,i}} \sqrt{\frac{m_e^2 c^4}{c^2} - m_e^2 c^2} \equiv 0 \quad (2.83)$$

and consequently from Eq. (2.9)

$$-\mathbf{q}^2 \xrightarrow{\hbar\omega \rightarrow E_{kin,i}} -\mathbf{p}_i^2 - \left(\frac{\hbar}{c}\omega\right)^2 + 2\frac{\hbar}{c}\omega |\mathbf{p}_i| \cos \Theta_i =: \delta \quad (2.84)$$

$$\Rightarrow \mathbf{q}^4 \xrightarrow{\hbar\omega \rightarrow E_{kin,i}} \delta^2. \quad (2.85)$$

With these limits it follows for the triply differential cross section (2.1)

$$\begin{aligned} \frac{d^4\sigma}{d\omega d\Omega_i d\Omega_f d\Phi} \xrightarrow{\hbar\omega \rightarrow E_{kin,i}} & \frac{Z^2 \alpha_{fine}^3 \hbar^2 |\mathbf{p}_f|}{(2\pi)^2 |\mathbf{p}_i| \omega \delta^2} \frac{1}{\omega} \frac{1}{\delta^2} \left[\frac{|\mathbf{p}_i|^2 \sin^2 \Theta_i}{(E_i - c|\mathbf{p}_i| \cos \Theta_i)^2} \right. \\ & \times \left. (4E_f^2 + \delta c^2) + 2 \hbar^2 \omega^2 \frac{|\mathbf{p}_i|^2 \sin^2 \Theta_i}{(E_i - c|\mathbf{p}_i| \cos \Theta_i) E_f} \right]. \end{aligned} \quad (2.86)$$

Actually (2.86) depends neither on Φ , nor on Θ_f . Therefore

$$\int_0^{2\pi} d\Phi \int_0^\pi \sin \Theta_i d\Theta_i = 4\pi \quad (2.87)$$

which leads to a very simple expression for the doubly differential cross section

$$\begin{aligned} \frac{d^2\sigma}{d\omega d\Omega_i} \xrightarrow{\hbar\omega \rightarrow E_{kin,i}} & \frac{Z^2 \alpha^3 \hbar^2 |\mathbf{p}_f|}{\pi |\mathbf{p}_i| \omega \delta^2} \frac{1}{\omega} \frac{1}{\delta^2} \left[\frac{|\mathbf{p}_i|^2 \sin^2 \Theta_i}{(E_i - c|\mathbf{p}_i| \cos \Theta_i)^2} (4E_f^2 + \delta c^2) \right. \\ & \left. + 2 \hbar^2 \omega^2 \frac{|\mathbf{p}_i|^2 \sin^2 \Theta_i}{(E_i - c|\mathbf{p}_i| \cos \Theta_i) E_f} \right]. \end{aligned} \quad (2.88)$$

Although taking the limit $\hbar\omega \rightarrow E_{kin,i}$ contradicts Eq. (2.11) as the energy of the emitted electron should be larger than 1 keV (2.11), (2.88) can be used for two purposes.

As (2.88) can be obtained, as well, by taking the limit $|\mathbf{p}_f| \rightarrow 0$ in (2.67), the complicated expression (2.67) is checked for consistency analytically. For further details the reader is referred to section 2.C. Furthermore we will see in section 2.4.1 that the most probable scattering angle does not depend on the photon energy for $E_{kin,i} \geq 1$ MeV. Therefore this cross section can be used for calculating the most probable scattering angle in this energy range.

2.3 Pair production

Pairs of electrons and positrons can be produced if a photon interacts with the nucleus of an atom. This process is related by some symmetry to the production of Bremsstrahlung photons. Bremsstrahlung occurs when an electron is affected by the nucleus of an atom, scattered and then emits a photon. So there are three real particles involved: incident electron, scattered electron and emitted photon. As the photon has no antiparticle one can change the time direction of the photon. For antimatter it is well known that antiparticles can be interpreted as the corresponding particles moving back in time. So one can substitute the incident electron by a positron moving forward in time. Thus by substituting emitted photon by incident photon and incident electron by emitted positron

(due to time reversal and changing its charge) it is possible to describe pair production from Bremsstrahlung. Thus the emitted photon in the Bremsstrahlung process has to be substituted by the incident photon from the nucleus and the incident electron by the produced positron. With these two replacements one gets the differential cross section for pair production [75, 66]

$$\begin{aligned}
d^4\sigma &= \frac{Z^2 \alpha_{fine}^3 c^2}{(2\pi)^2 \hbar} |\mathbf{p}_+| |\mathbf{p}_-| \frac{dE_+}{\omega^3} \frac{d\Omega_+ d\Omega_- d\Phi}{|\mathbf{q}|^4} \times \\
&\times \left[-\frac{\mathbf{p}_-^2 \sin^2 \Theta_-}{(E_- - c|\mathbf{p}_-| \cos \Theta_-)^2} (4E_+^2 - c^2 \mathbf{q}^2) \right. \\
&- \frac{\mathbf{p}_+^2 \sin^2 \Theta_+}{(E_+ - c|\mathbf{p}_+| \cos \Theta_+)^2} (4E_-^2 - c^2 \mathbf{q}^2) \\
&+ 2\hbar^2 \omega^2 \frac{\mathbf{p}_+^2 \sin^2 \Theta_+ + \mathbf{p}_-^2 \sin^2 \Theta_-}{(E_+ - c|\mathbf{p}_+| \cos \Theta_+)(E_- - c|\mathbf{p}_-| \cos \Theta_-)} \\
&\left. + 2 \frac{|\mathbf{p}_+| |\mathbf{p}_-| \sin \Theta_+ \sin \Theta_- \cos \Phi}{(E_+ - c|\mathbf{p}_+| \cos \Theta_+)(E_- - c|\mathbf{p}_-| \cos \Theta_-)} (2E_+^2 + 2E_-^2 - c^2 \mathbf{q}^2) \right], \tag{2.89}
\end{aligned}$$

where Z , α_{fine} , h , \hbar and c are the same parameters as in Eq. (2.1). ω is the frequency of the incident photon, E_{\pm} and p_{\pm} are the total energy and the momentum of the positron/electron with

$$E_{\pm} = \sqrt{\mathbf{p}_{\pm}^2 c^2 + m_e^2 c^4}. \tag{2.90}$$

Similarly to (2.1) there are three angles, Θ_{\pm} between the direction of the photon and the positron/electron direction, $\Theta_+ = \angle(\mathbf{p}_+, \mathbf{k})$, $\Theta_- = \angle(\mathbf{p}_-, \mathbf{k})$, and Φ is the angle between the scattering planes $(\mathbf{p}_+, \mathbf{k})$ and $(\mathbf{p}_-, \mathbf{k})$. The absolute value of the momentum of the virtual photon is

$$\begin{aligned}
-\mathbf{q}^2 &= -|\mathbf{p}_+|^2 - |\mathbf{p}_-|^2 - \left(\frac{\hbar}{c}\omega\right)^2 + 2|\mathbf{p}_+| \frac{\hbar}{c}\omega \cos \Theta_+ + 2|\mathbf{p}_-| \frac{\hbar}{c}\omega \cos \Theta_- \\
&- 2|\mathbf{p}_+| |\mathbf{p}_-| (\cos \Theta_+ \cos \Theta_- + \sin \Theta_+ \sin \Theta_- \cos \Phi). \tag{2.91}
\end{aligned}$$

Algebraically one obtains (2.89) from (2.1) by replacing

$$E_f \rightarrow E_-, \tag{2.92}$$

$$E_i \rightarrow -E_+, \tag{2.93}$$

$$\mathbf{p}_i \rightarrow -\mathbf{p}_+, \tag{2.94}$$

$$\mathbf{p}_f \rightarrow \mathbf{p}_-, \tag{2.95}$$

$$\omega \rightarrow -\omega, \tag{2.96}$$

$$\Theta_i \rightarrow \pi - \Theta_+, \quad (2.97)$$

$$\Theta_f \rightarrow \Theta_-, \quad (2.98)$$

$$\Phi \rightarrow \Phi - \pi \quad (2.99)$$

where the quantities on the left hand side are for Bremsstrahlung, and those on the right hand side for pair production. At the end one has to multiply with an additional factor to get the correct prefactor. With all the mentioned substitutions it is

$$d^4\sigma_{brem} \leftarrow \frac{\hbar^3\omega^2}{|\mathbf{p}_+|^2 c^2} \frac{d\omega}{dE_+} d^4\sigma_{pair}, \quad (2.100)$$

Because of this symmetry the results for pair production follow easily from those for Bremsstrahlung.

The direction of the positron relative to the incident photon is given by integrating (2.89) over Φ and Θ_- . But this is the same exercise as to integrate (2.1) over Φ and Θ_f . Because of the symmetry between Bremsstrahlung and pair production one can take (2.67) and substitute (2.92) - (2.99) to obtain a doubly differential cross section

$$\frac{d^2\sigma(E_+, \omega, \Theta_+)}{dE_+ d\Omega_+} = \sum_{j=1}^6 I_j \quad (2.101)$$

with the following contributions

$$\begin{aligned} I_1 &= \frac{2\pi A}{\sqrt{(\Delta_2^{(p)})^2 + 4p_+^2 p_-^2 \sin^2 \Theta_+}} \\ &\times \ln \left(\frac{(\Delta_2^{(p)})^2 + 4p_+^2 p_-^2 \sin^2 \Theta_+ - \sqrt{(\Delta_2^{(p)})^2 + 4p_+^2 p_-^2 \sin^2 \Theta_+} (\Delta_1^{(p)} + \Delta_2^{(p)}) + \Delta_1^{(p)} \Delta_2^{(p)}}{-(\Delta_2^{(p)})^2 - 4p_+^2 p_-^2 \sin^2 \Theta_+ - \sqrt{(\Delta_2^{(p)})^2 + 4p_+^2 p_-^2 \sin^2 \Theta_+} (\Delta_1^{(p)} - \Delta_2^{(p)}) + \Delta_1^{(p)} \Delta_2^{(p)}} \right) \\ &\times \left[-1 - \frac{c\Delta_2^{(p)}}{p_-(E_+ - cp_+ \cos \Theta_+)} + \frac{p_+^2 c^2 \sin^2 \Theta_+}{(E_+ - cp_+ \cos \Theta_+)^2} - \frac{2\hbar^2 \omega^2 p_- \Delta_2^{(p)}}{c(E_+ - cp_+ \cos \Theta_+) ((\Delta_2^{(p)})^2 + 4p_+^2 p_-^2 \sin^2 \Theta_+)} \right], \end{aligned} \quad (2.102)$$

$$I_2 = \frac{2\pi A c}{p_-(E_+ - cp_+ \cos \Theta_+)} \ln \left(\frac{E_- + p_- c}{E_- - p_- c} \right), \quad (2.103)$$

$$\begin{aligned} I_3 &= \frac{2\pi A}{\sqrt{(\Delta_2^{(p)} E_- + \Delta_1^{(p)} p_- c)^2 + 4m^2 c^4 p_+^2 p_-^2 \sin^2 \Theta_+}} \\ &\times \ln \left(\frac{((E_- + p_- c)(4p_+^2 p_-^2 \sin^2 \Theta_+ (E_- - p_- c) + (\Delta_1^{(p)} + \Delta_2^{(p)})((\Delta_2^{(p)} E_- + \Delta_1^{(p)} p_- c) \right. \\ &\quad \left. - \sqrt{(\Delta_2^{(p)} E_- + \Delta_1^{(p)} p_- c)^2 + 4m^2 c^4 p_+^2 p_-^2 \sin^2 \Theta_+})) ((E_- - p_- c)(4p_+^2 p_-^2 \sin^2 \Theta_+ (-E_- - p_- c) \right. \\ &\quad \left. + (\Delta_1^{(p)} - \Delta_2^{(p)})((\Delta_2^{(p)} E_- + \Delta_1^{(p)} p_- c) - \sqrt{(\Delta_2^{(p)} E_- + \Delta_1^{(p)} p_- c)^2 + 4m^2 c^4 p_+^2 p_-^2 \sin^2 \Theta_+}))^{-1}}{c(\Delta_2^{(p)} E_- + \Delta_1^{(p)} p_- c)} \right. \\ &\quad \left. + \frac{c(\Delta_2^{(p)} E_- + \Delta_1^{(p)} p_- c)}{p_-(E_+ - cp_+ \cos \Theta_+)} \right. \\ &\quad \left. + [((\Delta_2^{(p)})^2 + 4p_+^2 p_-^2 \sin^2 \Theta_+)(E_-^3 + E_- p_- c) + p_- c(2((\Delta_1^{(p)})^2 - 4p_+^2 p_-^2 \sin^2 \Theta_+) E_- p_- c \right. \\ &\quad \left. + \Delta_1^{(p)} \Delta_2^{(p)} (3E_-^2 + p_-^2 c^2))] [(\Delta_2^{(p)} E_- + \Delta_1^{(p)} p_- c)^2 + 4m^2 c^4 p_+^2 p_-^2 \sin^2 \Theta_+]^{-1} \right. \\ &\quad \left. + [-8p_+^2 p_-^2 m^2 c^4 \sin^2 \Theta_+ (E_+^2 + E_-^2) - 2\hbar^2 \omega^2 p_+^2 \sin^2 \Theta_+ p_- c (\Delta_2^{(p)} E_- + \Delta_1^{(p)} p_- c) \right] \end{aligned}$$

$$\begin{aligned}
& + 2\hbar^2\omega^2 p_- m^2 c^3 (\Delta_2^{(p)} E_- + \Delta_1^{(p)} p_{-c}) \left[(E_+ - cp_+ \cos \Theta_+) ((\Delta_2^{(p)} E_- + \Delta_1^{(p)} p_{-c})^2 + 4m^2 c^4 p_+^2 p_-^2 \sin^2 \Theta_+) \right]^{-1} \\
& + \frac{4E_+^2 p_-^2 (2(\Delta_2^{(p)} E_- + \Delta_1^{(p)} p_{-c})^2 - 4m^2 c^4 p_+^2 p_-^2 \sin^2 \Theta_+) (\Delta_1^{(p)} E_- + \Delta_2^{(p)} p_{-c})}{((\Delta_2^{(p)} E_- + \Delta_1^{(p)} p_{-c})^2 + 4m^2 c^4 p_+^2 p_-^2 \sin^2 \Theta_+)^2}, \tag{2.104}
\end{aligned}$$

$$I_4 = \frac{4\pi A p_{-c} (\Delta_2^{(p)} E_- + \Delta_1^{(p)} p_{-c})}{(\Delta_2^{(p)} E_- + \Delta_1^{(p)} p_{-c})^2 + 4m^2 c^4 p_+^2 p_-^2 \sin^2 \Theta_+} + \frac{16\pi E_+^2 p_-^2 A (\Delta_2^{(p)} E_- + \Delta_1^{(p)} p_{-c})^2}{((\Delta_2^{(p)} E_- + \Delta_1^{(p)} p_{-c})^2 + 4m^2 c^4 p_+^2 p_-^2 \sin^2 \Theta_+)^2}, \tag{2.105}$$

$$\begin{aligned}
I_5 & = \frac{4\pi A}{(-(\Delta_2^{(p)})^2 + (\Delta_1^{(p)})^2 - 4p_+^2 p_-^2 \sin^2 \Theta_+) ((\Delta_2^{(p)} E_- + \Delta_1^{(p)} p_{-c})^2 + 4m^2 c^4 p_+^2 p_-^2 \sin^2 \Theta_+)} \\
& \times \left[\frac{\hbar^2 \omega^2 p_-^2}{E_+ cp_+ \cos \Theta_+} \left[E_- [2(\Delta_2^{(p)})^2 ((\Delta_2^{(p)})^2 - (\Delta_1^{(p)})^2) + 8p_+^2 p_-^2 \sin^2 \Theta_+ ((\Delta_2^{(p)})^2 + (\Delta_1^{(p)})^2)] \right. \right. \\
& + p_{-c} [2\Delta_1^{(p)} \Delta_2^{(p)} ((\Delta_2^{(p)})^2 - (\Delta_1^{(p)})^2) + 16\Delta_1^{(p)} \Delta_2^{(p)} p_+^2 p_-^2 \sin^2 \Theta_+] \left. \left. [(\Delta_2^{(p)})^2 + 4p_+^2 p_-^2 \sin^2 \Theta_+]^{-1} \right. \right. \\
& + \frac{2\hbar^2 \omega^2 p_+^2 \sin^2 \Theta_+ (2\Delta_1^{(p)} \Delta_2^{(p)} p_{-c} + 2(\Delta_2^{(p)})^2 E_- + 8p_+^2 p_-^2 \sin^2 \Theta_+ E_-)}{E_+ - cp_+ \cos \Theta_+} \\
& - \left. \left. [2E_+^2 p_-^2 \{2((\Delta_2^{(p)})^2 - (\Delta_1^{(p)})^2) (\Delta_2^{(p)} E_- + \Delta_1^{(p)} p_{-c})^2 + 8p_+^2 p_-^2 \sin^2 \Theta_+ [((\Delta_1^{(p)})^2 + (\Delta_2^{(p)})^2) (E_-^2 + p_-^2 c^2) \right. \right. \right. \\
& + \left. \left. 4\Delta_1^{(p)} \Delta_2^{(p)} E_- p_{-c}]\right] [(\Delta_2^{(p)} E_- + \Delta_1^{(p)} p_{-c})^2 + 4m^2 c^4 p_+^2 p_-^2 \sin^2 \Theta_+]^{-1} \right. \\
& - \left. \left. \frac{8p_+^2 p_-^2 \sin^2 \Theta_+ (E_+^2 + E_-^2) (\Delta_2^{(p)} p_{-c} + \Delta_1^{(p)} E_-)}{E_+ - cp_+ \cos \Theta_+} \right], \tag{2.106}
\end{aligned}$$

$$I_6 = -\frac{16\pi E_-^2 p_+^2 \sin^2 \Theta_+ A}{(E_+ - cp_+ \cos \Theta_+)^2 (-(\Delta_2^{(p)})^2 + (\Delta_1^{(p)})^2 - 4p_+^2 p_-^2 \sin^2 \Theta_+)} \tag{2.107}$$

with

$$A = \frac{Z^2 \alpha_{fine}^3 c^2}{(2\pi)^2 \hbar} \frac{|\mathbf{p}_+| |\mathbf{p}_-|}{\omega^3}, \tag{2.108}$$

and with $\Delta_1^{(p)}$, $\Delta_2^{(p)}$ defined as

$$\Delta_1^{(p)} := -|\mathbf{p}_+|^2 - |\mathbf{p}_-|^2 - \left(\frac{\hbar}{c} \omega \right) + 2 \frac{\hbar}{c} \omega |\mathbf{p}_+| \cos \Theta_+, \tag{2.109}$$

$$\Delta_2^{(p)} := 2 \frac{\hbar}{c} \omega |\mathbf{p}_i| - 2 |\mathbf{p}_+| |\mathbf{p}_-| \cos \Theta_+. \tag{2.110}$$

2.4 Discussion

2.4.1 Bremsstrahlung

Comparison with experiments

If electrons are scattered at nuclei, they can produce hard Bremsstrahlung photons with frequency ω and direction Θ_i relative to the direction of the electrons.

Figure 2.2 compares our equation (2.67) with experimental results for gold ($Z = 79$) for different electron and photon energies [3]. For $Z = 79$ the minimal electron energy (2.11) for the Born approximation to be valid, is $E_{kin, \{i, f\}} = 115$ keV. Figure 2.2 shows that the cross sections agree overall in size for $E_{kin, i} = 180$ keV, $\hbar\omega = 50$ keV and for $E_{kin, i} = 380$ keV, $\hbar\omega = 100$ keV. However, for the first case, the energy of the electron in the final state is $E_{kin, f} = 130$ keV ≈ 115 keV, thus close to the velocity limit. Therefore

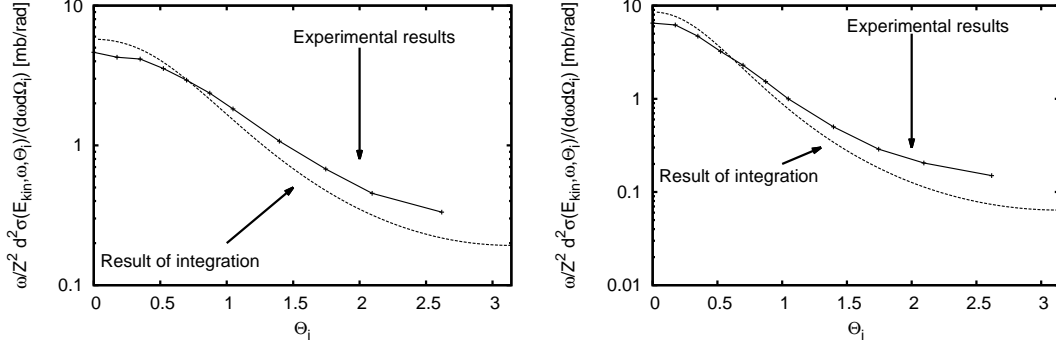
a) $E_{kin,i} = 180$ keV, $\hbar\omega = 50$ keVb) $E_{kin,i} = 380$ keV, $\hbar\omega = 100$ keV

Figure 2.2: $\omega/Z^2 \cdot d^2\sigma/(d\omega d\Omega_i)(E_{kin,i}, \omega, \Theta_i)$ for Bremsstrahlung as a function of the scattering angle Θ_i between emitted photon and incident electron for gold $Z = 79$ where $1 \text{ mb} = 10^{-31} \text{ m}^2$. The energies are a) $E_{kin,i} = 180$ keV, $\hbar\omega = 50$ keV and b) $E_{kin,i} = 380$ keV, $\hbar\omega = 100$ keV. The dotted lines show our result (2.67); the solid lines show experimental values [3].

there is a larger deviation, especially for small angles, than for the second case where a very good agreement can be observed.

Angular distribution of Bremsstrahlung

Figure 2.3 shows the doubly differential cross section (2.67) for Bremsstrahlung for several electron and photon energies. At first, the probability for generating photons decreases with increasing photon energy for fixed electron energy. This can be understood easily by applying (2.88). As can be seen there, the doubly differential cross section grows linearly in the momentum of the electron in the final state which is equivalent to

$$\frac{d^2\sigma}{d\omega d\Omega_i} \sim |\mathbf{p}_f| \quad (2.111)$$

for high photon energies. So, if all kinetic energy is transferred from the electron onto the photon, the final momentum $|\mathbf{p}_f|$ vanishes, and thus

$$\frac{d^2\sigma}{d\omega d\Omega_i} \rightarrow 0. \quad (2.112)$$

For nonrelativistic electron and photon energies the scattering angle tends to be mainly equally distributed, i.e. the photons do not have a preference for a particular direction. When the photon energy increases, photons are mainly emitted in forward direction, but the ratio between forward and backward scattering is at least three orders of magnitude

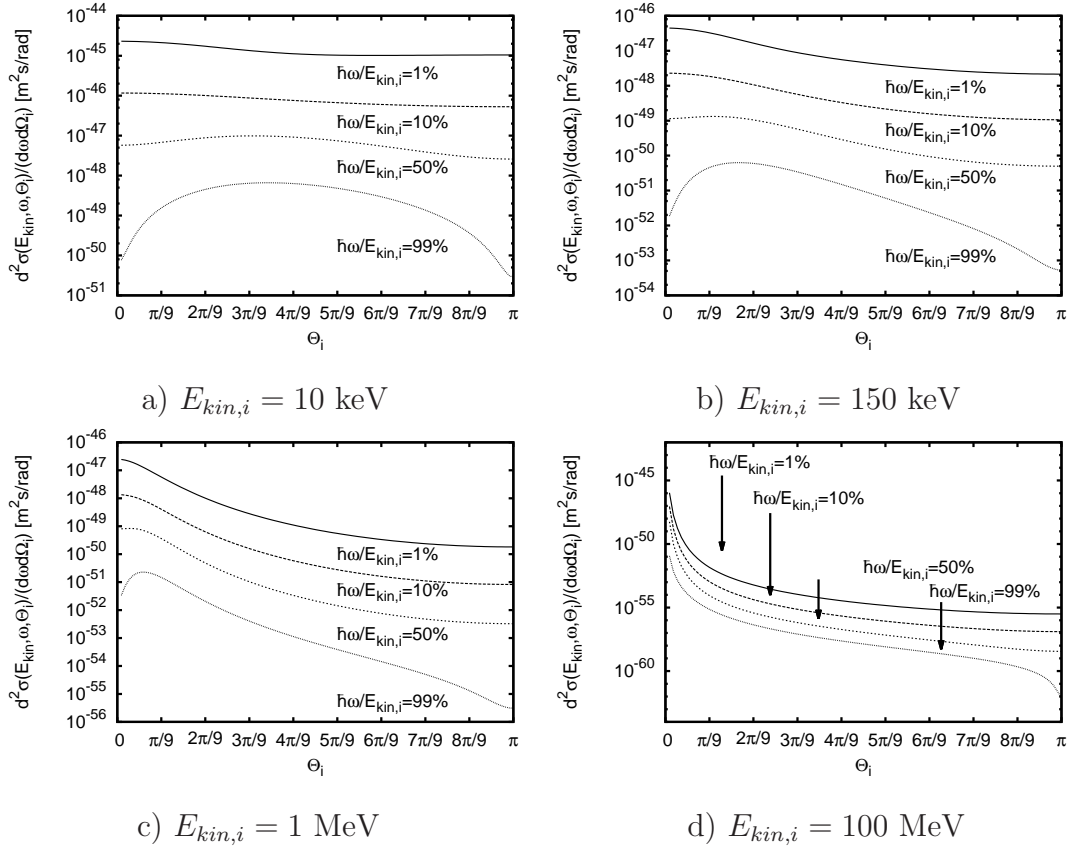


Figure 2.3: The doubly differential cross section $d^2\sigma/(d\omega d\Omega_i)(E_{kin,i}, \omega, \Theta_i)$ for Bremsstrahlung ($Z = 7$) versus the scattering angle Θ_i between emitted photon and incident electron. The electron energies are a) $E_{kin,i} = 10 \text{ keV}$, b) $E_{kin,i} = 150 \text{ keV}$, c) $E_{kin,i} = 1 \text{ MeV}$ and d) $E_{kin,i} = 100 \text{ MeV}$. In each plot the the photon energy $\hbar\omega$ amounts to 1%, 10%, 50% and 99% of the kinetic energy of the incident electron.

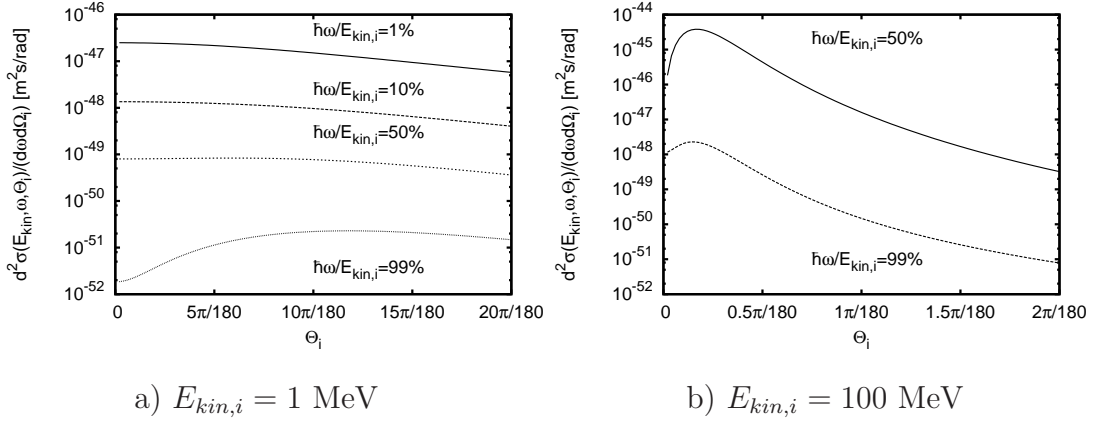


Figure 2.4: The doubly differential cross section $d^2\sigma/(d\omega d\Omega_i)$ for Bremsstrahlung as in Figure 2.3 for a smaller angular range

lower than for a relativistic electron. This case belongs to the classical case where the velocity is small compared to the speed of light. Namely, it is $v/c|_{E_{kin,i}=10\text{keV}} \approx 0.20$ and non-relativistic equations will be enough to describe these phenomena. In the relativistic case ($v/c|_{E_{kin,i}=1\text{MeV}} \approx 0.94$ and $v/c|_{E_{kin,i}=100\text{MeV}} \approx 0.99999$) the differential cross section becomes more and more anisotropic. Forward scattering is preferred to backward scattering although the maximal cross section does not lie precisely at $\Theta_i = 0$ as can be seen in Figure 2.3 c). But the more the electron energy increases the more the maximum wanders to smaller angles, for example, it seems in Figure 2.3 d) that the maximal emission is indeed for $\Theta_i=0$. As mentioned in sections 2.2.4 and 2.B, Eq. (2.68) cannot be evaluated directly at $\Theta_i = 0$. However, for this purpose, we derived (2.81) which is valid for $\Theta_i = 0$ and $\Theta_i = \pi$. Figure 2.4 shows again (2.67) for two relativistic electron and different photon energies but for a smaller range of angles. It shows in more detail that the angle of maximal scattering is small, but not 0.

Figure 2.5 shows the ratio between the cross section for backward scattering and forward scattering. It can be clearly seen that the tendency for backward scattering decreases for increasing electron energy. The lower the electron energy becomes, the more forward and backward scattering become similar and in general, the scattering tends to be isotropic. Only for ratios between photon energies and electron energies close to 1, forward scattering is preferred for the whole range of energies, but still decreases with increasing electron energies.

In energetic electron avalanches electrons scatter frequently which leads to a large velocity dispersion. It depends on the direction of the applied electric field whether electrons move forward or whether their directions are distributed arbitrarily. If so, however, this implies that photons will not necessarily move in a preferred direction, but in the direction of the incident electron. Their motion and thus change of direction depend on

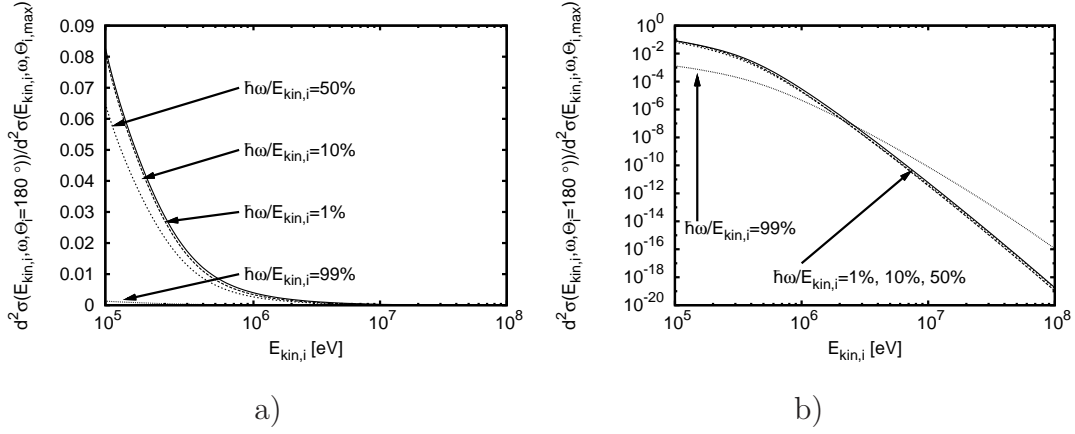


Figure 2.5: The ratio between the doubly differential cross section for backward scattering ($\Theta_i = 180^\circ$) $d^2\sigma(E_{kin,i}, \omega, \Theta_i = 180^\circ)/(d\omega d\Omega_i)$ and the maximum of this cross section $\max(d^2\sigma(E_{kin,i}, \omega, \Theta_i)/(d\omega d\Omega_i))$ vs. the kinetic energy of the incident electron for different ratios between photon and electron energies in a) linear and b) logarithmic scale for $Z = 7$.

photon processes, such as Compton scattering.

Relativistic transformation

The tendency of forward scattering in the case of relativistic incident electrons can be understood by applying the laws of relativistic transformations. Imagine a non-quantum field theoretical description of Bremsstrahlung [81]. If one regards an inertial system in which the incident particle is at rest (Fig. 2.6 a)), radiation is emitted isotropically with a small-angle deflection. If the physical laws for this process are relativistically transformed into the laboratory system where the nucleus is at rest and the electron moving, most of the radiation is emitted in forward direction relative to the electron direction (Fig. 2.6 b)). Because this transformation is valid for a non-quantum field theoretical, relativistic electron, it must also be true for a relativistic quantum theoretical description, therefore we see that the forward scattering of photons can simply be explained as a result of the relativistic transformation.

The forward scattering can moreover be understood by using the conservation laws of energy and momentum. They predict that photons have to be scattered in forward direction if electron and photon energy are high. The interested reader is referred to 2.H.

Although Figure 2.3 shows that the maxima of the doubly differential cross section form with increasing electron energy, it is difficult to determine in these plots when these maxima really start to be generated clearly. Figure 2.7 shows the doubly differential cross section in dependence of the incident electron energy for $E_{kin,i} = 400$ keV and $E_{kin,i} \approx 511$ keV when the kinetic energy is equal to the rest energy. For 400 keV and

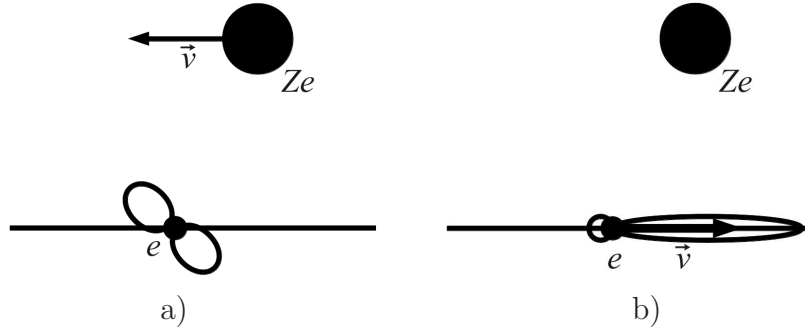


Figure 2.6: a) In the rest frame of the electron where the nucleus is moving instead radiation is emitted isotropically with a small-angle deflection. b) If, however, one transforms the situation into the rest frame of the nucleus where the electron is moving, most of the radiation is emitted in forward direction relative to the direction of the electron.

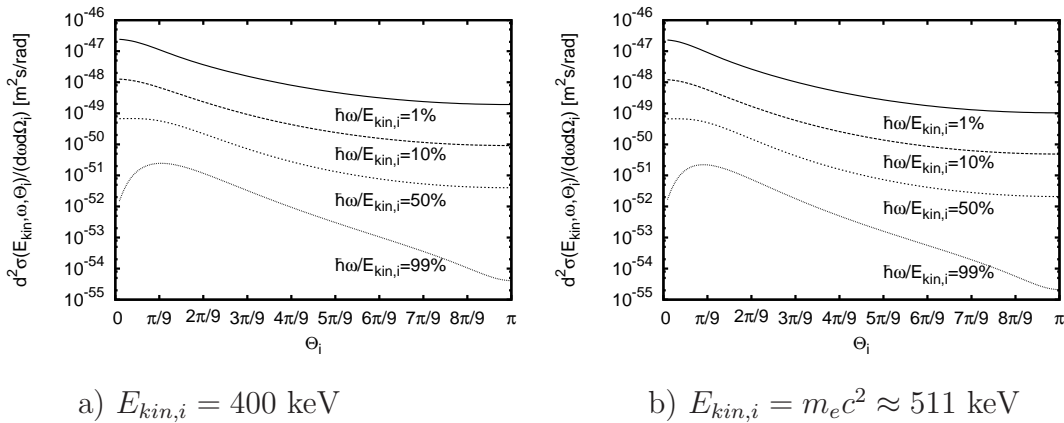


Figure 2.7: The doubly differential cross section $d^2\sigma/(d\omega d\Omega_i)(E_{kin,i}, \omega, \Theta_i)$ for Bremsstrahlung ($Z = 7$) versus the scattering angle Θ_i between emitted photon and incident electron. The electron energies are a) $E_{kin,i} = 400 \text{ keV}$, b) $E_{kin,i} \approx 511 \text{ keV}$. In each plot the the photon energy $\hbar\omega$ amounts to 1%, 10%, 50% and 99% of the kinetic energy of the incident electron.

for $\hbar\omega/E_{kin,i} = 0.01$ the cross section for forward scattering is already two orders of magnitude larger than for backward scattering, but a clear maximum cannot be seen. However, for the same kinetic energy, but for $\hbar\omega/E_{kin,i} = 0.95$ there is already a clear maximum formed. But if the kinetic energy grows up to 511 keV which is equal to the rest energy of the electron, there is even a maximum for $\hbar\omega = 0.01E_{kin,i}$. This can be expected due to the relativistic transformation. If $E_{kin,i} \ll m_e c^2$, then the photon emission is relatively isotropic. But if the kinetic energy is approximately equal to the rest energy of the electron, relativistic laws are valid. Especially for $E_{kin,i} = m_e c^2$

$$\frac{v}{c} = \frac{\sqrt{3}}{2} \approx 87\%, \quad (2.113)$$

therefore the electron has to be treated relativistically and clear maxima close to $\Theta_i = 0$ form for every possible photon energy.

Dependence on the energy of the emitted photon

Figure 2.3 shows that for both slow and relativistic electrons the doubly differential cross section also varies with the photon energy for fixed electron energies. For fixed electron energy, lower photon energies are more likely. Moreover, photons are more likely for certain angles. They are more likely for lowly energetic electrons in the limit $\Theta_i \rightarrow 180^\circ$ and for highly energetic electrons in the limit $\Theta_i \rightarrow 0^\circ$. Figure 2.8 shows the doubly differential cross section in another way. Now the photon energy is fixed and the electron energy differs within one plot. For all cases it is more likely that low energetic electrons create photons than relativistic electrons do, in the limit $\Theta_i \rightarrow 180^\circ$. But for small angles, i.e. for forward emission of photons, the probability rapidly increases for relativistic electrons and exceeds the probability at small electron energies.

The most probable scattering angle

Figure 2.3 also shows that the angle for which maximal scattering takes place, is rather independent of the photon energy. Hence, one can use (2.88) to determine a formula for that scattering angle. Actually this derivation leads to a quartic equation which can, however, be approximated for small angles, i.e. $\Theta_i \lesssim 20^\circ$, through a quadratic equation. The reader is referred to section 2.I for the detailed calculation. The solution of the quadratic equation reads

$$\Theta_i = \sqrt{\frac{-\frac{\delta_0}{\hbar\omega}(4E_f^2 + \delta_0 c^2) - \frac{2\delta_0 \hbar\omega}{E_f}(E_i - c|\mathbf{p}_i|)}{2\frac{|\mathbf{p}_i|}{c} \left[4E_f^2 + \delta_0 c^2 + \frac{2\hbar^2 \omega^2}{E_f}(E_i - c|\mathbf{p}_i|) \right] - |\mathbf{p}_i| \delta_0 c - \frac{\hbar\omega}{E_f} c |\mathbf{p}_i| \delta_0}} \quad (2.114)$$

with

$$\delta_0 := -|\mathbf{p}_i|^2 - \left(\frac{\hbar}{c}\omega\right)^2 + 2\frac{\hbar}{c}\omega|\mathbf{p}_i|, \quad (2.115)$$

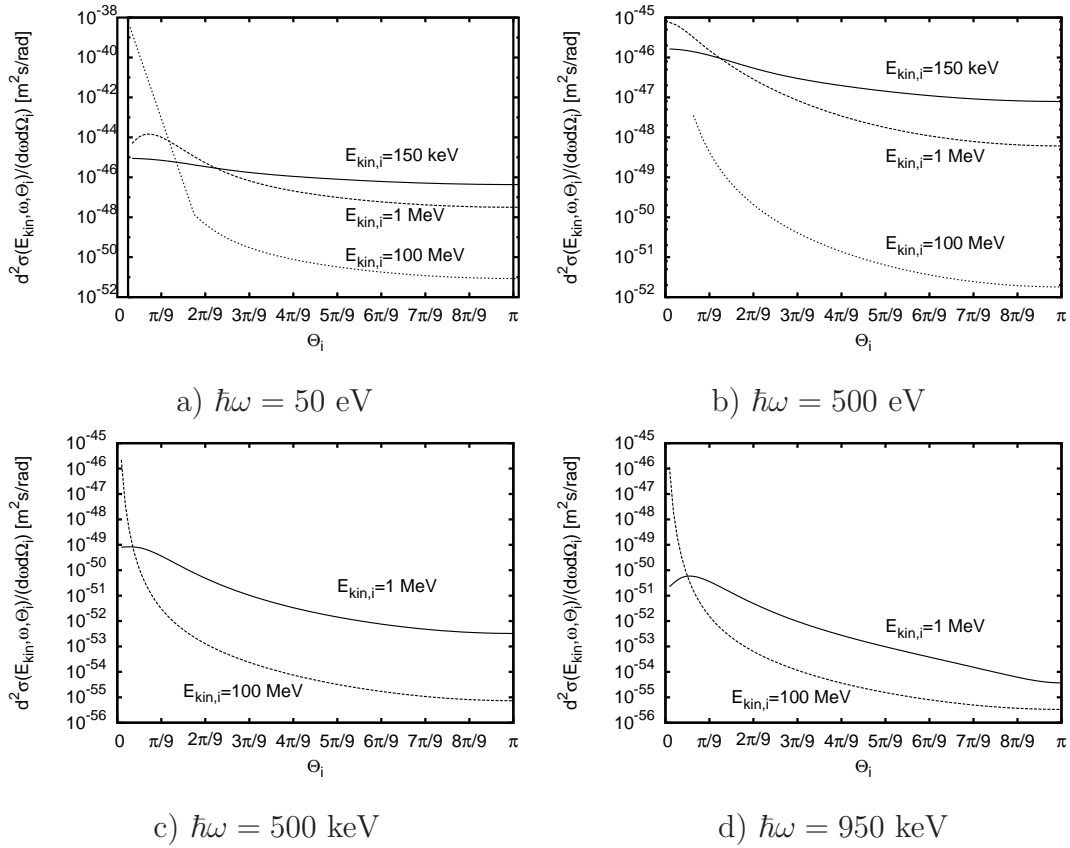


Figure 2.8: The doubly differential cross section $d^2\sigma/(d\omega d\Omega_i)(E_{kin,i}, \omega, \Theta_i)$ for Bremsstrahlung ($Z = 7$) vs. the scattering angle Θ_i for several electron and photon energies. In each panel the photon energy $\hbar\omega$ is fixed and the cross section is plotted for various kinetic energies of the incident electron.

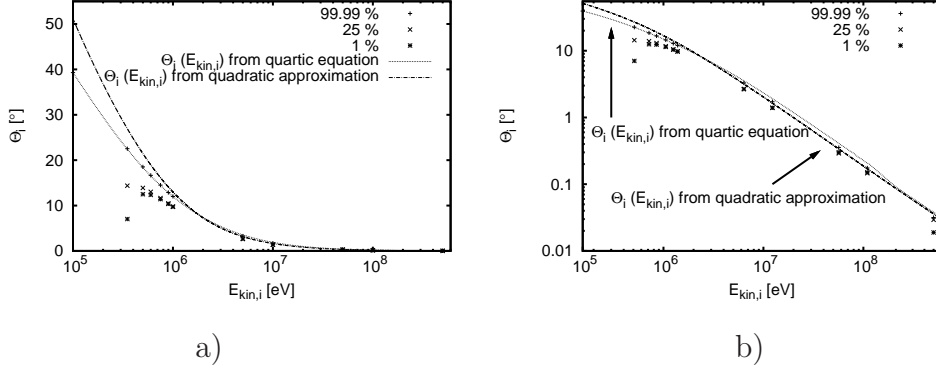


Figure 2.9: Θ_i for maximal scattering vs. incident electron energy in a) semilog and b) loglog plot for $Z = 7$. Besides (2.114) for $\hbar\omega = 0.9999E_{kin,i}$, the exact solution of the quartic equation and various data for different $\hbar\omega/E_{kin,i}$ are shown.

$\hbar\omega \rightarrow E_{kin,i}$, e.g. $\hbar\omega = 0.9999E_{kin,i}$ and

$$p_i = \sqrt{E_{kin,i} \left(\frac{E_{kin,i}}{c^2} + 2m_e \right)}. \quad (2.116)$$

Figure 2.9 shows (2.114) and manually extracted values for Θ_i for different photon energies. It shows much better than Figure 2.3 that Θ_i is rather independent of the photon energy for relativistic electron energies. Besides (2.114), the solution of the quartic equation, is shown. Moreover, it shows that (2.114) gives a good approximation for those angles Θ_i for which scattering is maximal. Actually, we see that the exact solution describes the angle for maximal scattering better, especially for low energies, but for high energies both curves fit very well.

By inserting $E_{kin,i} = \hbar\omega/0.9999$ into (2.114) one obtains a formula which relates the photon energy to the most probable scattering angle.

2.4.2 Pair production

Basic properties of pair production

We now proceed from Bremsstrahlung to pair production. One photon with energy $\hbar\omega$ creates two particles, namely an electron and a positron, both with rest energy $m_e c^2$. Therefore

$$E_{kin,-} + E_{kin,+} = \hbar\omega - 2m_e c^2 \quad (2.117)$$

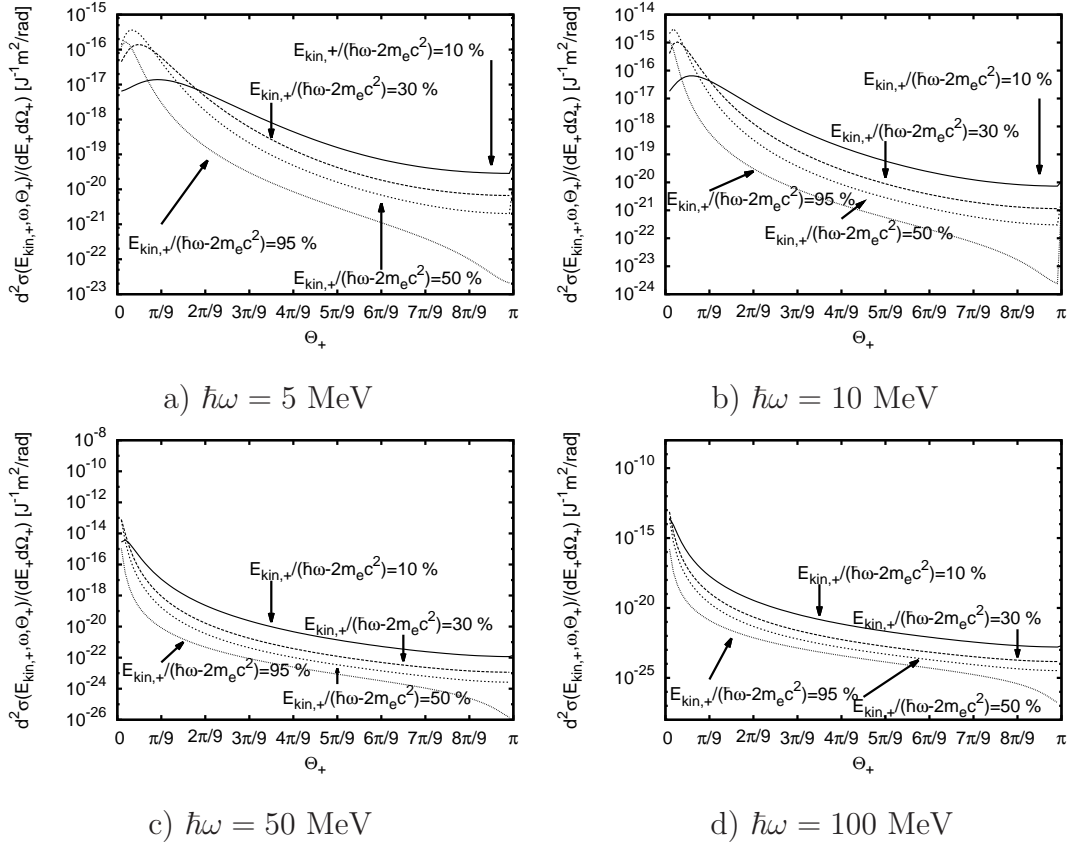


Figure 2.10: Doubly differential cross section $d^2\sigma(E_+, \omega, \Theta_+)/ (dE_+ d\Omega_+)$ for pair production as a function of the angle Θ_+ between incident photon and created positron for $Z = 7$: The cross section is shown for fixed photon energies a) $\hbar\omega = 5$ MeV, b) $\hbar\omega = 10$ MeV, c) $\hbar\omega = 50$ MeV and d) $\hbar\omega = 100$ MeV. In each panel different positron energies E_+ relative to the available photon energy $\hbar\omega - 2m_e c^2$ are plotted.

follows for the kinetic energies of these two particles. Thus the photon energy has to be $\hbar\omega \geq 2m_e c^2 \approx 1.022$ MeV for pair production and the kinetic energy of the particles is bounded as $E_{kin,\pm} \leq \hbar\omega - 2m_e c^2$. Figure 2.10 shows the doubly differential cross section (2.101) for different photon and positron energies. Forward scattering is dominant, there is almost no case now of more isotropic scattering. This results from the fact that almost all positron energies in Figure 2.10 are relativistic. For very highly energetic photons, e.g. 50 MeV and 100 MeV, and thus relativistic positron energies in Fig. 2.10 there are clear maxima for forward scattering. For energies $\hbar\omega < 50$ MeV, however, the maxima are $> 5^\circ$, but forward scattering is still preferred. Pair production is symmetric in positron

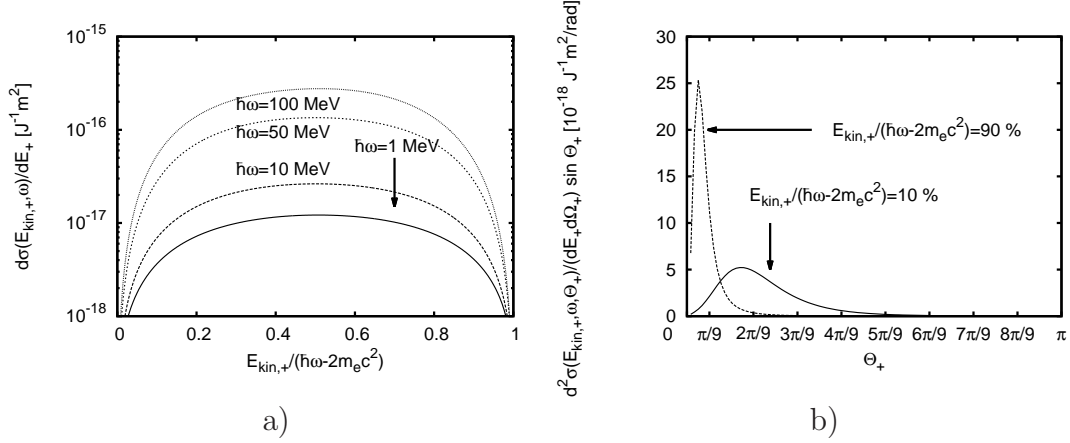


Figure 2.11: a) The singly differential cross section $d\sigma/dE_+$ for pair production ($Z = 7$) as a function of the ratio between the kinetic energy of the positron and the incident photon for different photon energies. b) $d^2\sigma/(dE_+d\Omega_+) \cdot \sin(\Theta_+)$ as a function of the scattering angle Θ_+ between photon and positron for $\hbar\omega = 5$ MeV. The ratio between the kinetic energy of the created positron and the energy of the incident photon amounts to 10 % and 90 %.

and electron energy. Thus for the singly differential cross section

$$\frac{d\sigma}{dE_+}(E_+, \omega) = \int_0^\pi \frac{d^2\sigma(E_+, \omega, \Theta_+)}{dE_+ d\Omega_+} \sin \Theta_+ d\Theta_+ \quad (2.118)$$

the probability of the creation of a positron with a given energy is as large as the probability to create an electron with this energy:

$$\left. \frac{d\sigma}{dE_+} \right|_{\frac{E_{kin,+}}{\hbar\omega - 2m_e c^2}} = \left. \frac{d\sigma}{dE_+} \right|_{1 - \frac{E_{kin,+}}{\hbar\omega - 2m_e c^2}} \quad (2.119)$$

as can be seen in Figure 2.11 a) where we performed the integration in (2.118) numerically. Figure 2.11 b) shows the integrand of (2.118) for $\hbar\omega = 5$ MeV. The ratio of the kinetic energy of the created positron and the energy of the incident photon amounts to 10 % and 90 %. Both functions are not equal, but the integrand for a high ratio has a higher maximum and is more narrow while the integrand for small ratios shows a smaller maximum and a wider full half width. Thus the areas under both functions are equal and (2.119) is fulfilled.

Figure 2.12 shows the doubly differential cross section (2.101) for fixed positron and different photon energies. Again positrons which are generated with high velocities predominantly scatter forward while this tendency vanishes if the positron energy is very

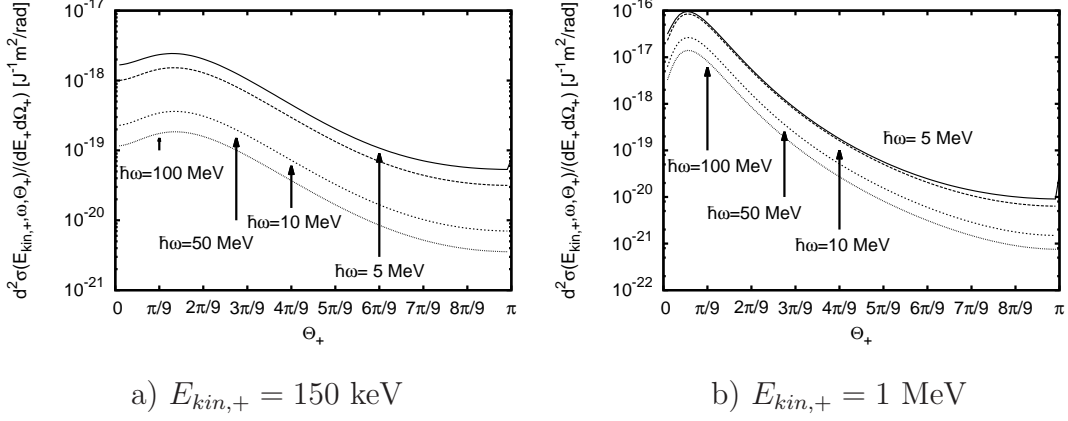


Figure 2.12: Doubly differential cross section $d^2\sigma(E_+, \omega, \Theta_+)/dE_+d\Omega_+$ for pair production as a function of the angle Θ_+ between incident photon and created positron for $Z = 7$: The cross section is shown for fixed positron energies a) $E_{kin,+} = 150 \text{ keV}$ and b) $E_{kin,+} = 1 \text{ MeV}$. In each panel curves for the photon energies $\hbar\omega = 5 \text{ MeV}$, 10 MeV , 50 MeV and 100 MeV are included.

low. This can be traced back to the relativistic behaviour again. If a positron is very energetic, it has to be treated relativistically and the relativistic transformation leads to forward scattering (this is the same explanation as for Bremsstrahlung). We also see that the creation of positrons is more likely for highly energetic photons.

The most probable scattering angle

As for Bremsstrahlung one can get a simple formula for the preferred direction. Performing the same calculation as for Bremsstrahlung one obtains

$$\begin{aligned}
 \Theta_+ &= \left[\left(-\frac{\delta_0^{(p)}}{\hbar\omega} (-4E_-^2 - \delta_0^{(p)} c^2) - \frac{2\delta_0^{(p)} \hbar\omega}{E_-} (E_+ - c|\mathbf{p}_+|) \right) \right. \\
 &\times \left(2\frac{|\mathbf{p}_+|}{c} \left[-4E_-^2 - \delta_0^{(p)} c^2 + \frac{2\hbar^2\omega^2}{E_-} (E_+ - c|\mathbf{p}_+|) \right] - |\mathbf{p}_+| \delta_0^{(p)} c \right. \\
 &\left. \left. - \frac{\hbar\omega}{E_-} c|\mathbf{p}_+| \delta_0^{(p)} \right)^{-1} \right]^{\frac{1}{2}} \quad (2.120)
 \end{aligned}$$

with

$$\delta^{(p)} := -|\mathbf{p}_+|^2 - \left(\frac{\hbar}{c} \omega \right)^2 + 2|\mathbf{p}_+| \frac{\hbar}{c} \omega \quad (2.121)$$

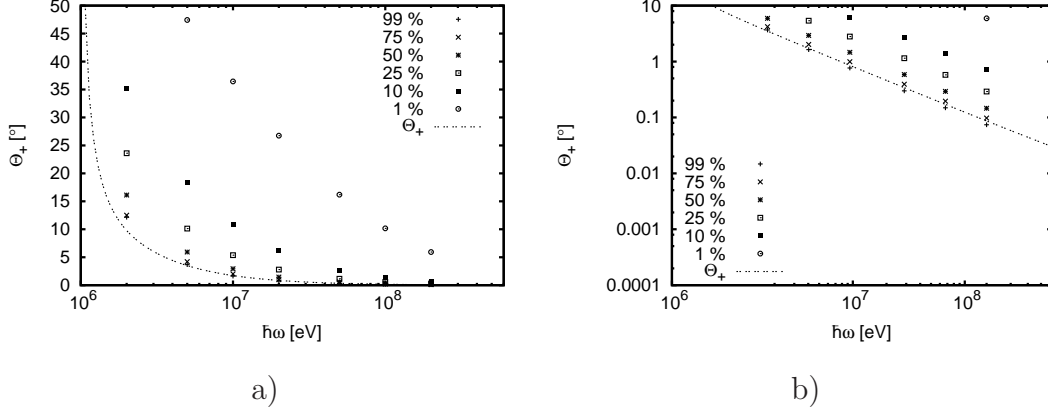


Figure 2.13: Θ_+ for maximal scattering vs. incident photon energy in a) semilog and b) loglog plot for $Z = 7$. Besides (2.120) for $E_{kin,+}/(\hbar\omega - 2m_e c^2) = 0.9999$ various data for different $E_{kin,+}/(\hbar\omega - 2m_e c^2)$ are shown.

and

$$\frac{E_+ - m_e c^2}{\hbar\omega - 2m_e c^2} \approx 1. \quad (2.122)$$

Figure 2.13 shows that (2.120) is a good approximation for Θ_+ for high photon energies and high ratios between photon and positron energy. The smaller the ratio between photon and positron energy, however, is, the worse (2.120) becomes for low photon energies. If the photon energy is larger than 50 MeV, relativistic positrons are created; therefore forward scattering takes place and Θ_+ can be calculated with (2.120).

2.5 Conclusion

We have reviewed literature relevant for Bremsstrahlung in Terrestrial gamma-ray flashes (TGFs) [12, 75, 51, 138, 140, 2]. Focusing on atomic numbers $Z = 7$ (nitrogen) and $Z = 8$ (oxygen) and an energy range of 1 keV to 1 GeV, no good parametrization of an energy resolved angular distribution in the form of doubly differential cross section is available. The theory of Bethe and Heitler covers this energy range for $Z = 7, 8$, but it parameterizes the direction of the scattered electron as well; therefore we integrated their triply differential cross section to obtain the correct energy resolved angular distribution for Bremsstrahlung and pair production. Other authors [98, 42, 23, 24] used different approaches, as discussed in the introduction. They use singly or triply differential cross sections which do not give a direct relation between the photon energy and the direction of the photon relative to the motion of the electron. As positrons are created within a thundercloud as well [17], we used a symmetry between the production of Bremsstrahlung

and the creation of an electron-positron pair both in the field of a nucleus to obtain a cross section which relates the energy of the created positron with its direction.

We have seen that emitted Bremsstrahlung photons are mainly released in forward direction if the electron which interacts with the nucleus has such a high energy that it has to be treated relativistically. For lower energies scattering tends to be more isotropic. For the case that almost all kinetic energy of the incident electron is transformed into photon energy, we derived an approximation for the most probable photon emission angle as a function of the incident electron energy and of the photon energy. The expression is valid for all ratios of photon over electron energy if the electron motion is relativistic. So, when photons have been created within a thundercloud or discharge, they are mainly scattered in forward direction as long as the electrons move relativistically, i.e. if their kinetic energy is at least as large as their rest energy.

Similar results hold for pair production. Next to the doubly differential cross section we derived a simple approximation for the most probable positron emission angle for the case that the photon energy is larger than 10 MeV (for ratios between the kinetic energy of the positron and available photon energy down to 25%) or than 100 MeV (for ratios lower than 25%). We have seen that for very highly energetic photons that almost all positrons are scattered in forward direction. If, however, the photon energy decreases, the probability of forward scattering decreases as well. Instead the maximal cross section can be found at $\Theta_+ \approx 90^\circ$ for low ratios between E_+ and $\hbar\omega - 2m_e c^2$ and is, beyond that, symmetric to this angle.

Our analytical results for the doubly differential cross-sections for Bremsstrahlung and pair production are also supplied in the form of two functions written in C++. In this form the functions can be implemented into Monte Carlo codes simulating energetic processes like the production of gamma-rays or electron positron pairs in thunderstorms.

2.A The residual theorem to calculate integrals with trigonometric functions

In this appendix the method how to calculate integrals of the form

$$\int_0^{2\pi} R(\cos \Phi, \sin \Phi) d\Phi \quad (2.123)$$

shall be discussed where $R(x, y) : \mathbb{R}^2 \setminus \{x, y \in \mathbb{R} | y = \pm\sqrt{1-x^2}\} \rightarrow \mathbb{R}$ is a rational function without poles on the unit circle $x^2 + y^2 = 1$. But before explaining this method let's briefly review some general facts about residua.

2.A.1 The residual theorem

Let $f : \mathbb{C} \supset I \rightarrow \mathbb{C}$, $z \mapsto f(z)$, be a holomorphic function and $\Gamma : [a, b] \rightarrow \mathbb{C}$, $t \mapsto \Gamma(t)$, a closed curve in the complex plane. Then one can calculate complex curve integrals via

$$\int_{\Gamma} f(z)dz = 2\pi i \sum_j \operatorname{Res}(f, z_j) \quad (2.124)$$

where the sum has to be taken over all poles z_j of f and complex curve integrals are defined as

$$\int_{\Gamma} f(z)dz := \int_a^b f(\Gamma(t)) \cdot \frac{d\Gamma}{dt}(t)dt. \quad (2.125)$$

The residuum of a pole z_j can be calculated via

$$\operatorname{Res}(f, z_j) = \frac{1}{(n-1)!} \lim_{z \rightarrow z_j} \frac{d^{n-1}}{dz^{n-1}} \left[(z - z_j)f(z) \right] \quad (2.126)$$

where n denotes the order of the pole.

2.A.2 Integral with trigonometric functions

With the help of the (2.124) one can simply perform the integration of (2.123). For that purpose define

$$f(z) := \frac{1}{iz} R \left(\frac{1}{2} \left(z + \frac{1}{z} \right), \frac{1}{2i} \left(z - \frac{1}{z} \right) \right) \quad (2.127)$$

and choose the unit circle

$$\Gamma(t) = e^{it}, t \in [0, 2\pi] \quad (2.128)$$

as closed curve; hence (2.125) becomes

$$\int_{\Gamma} f(z)dz = \int_0^{2\pi} \frac{1}{ie^{it}} R \left(\frac{1}{2} (e^{it} + e^{-it}), \frac{1}{2i} (e^{it} - e^{-it}) \right) ie^{it} dt \quad (2.129)$$

$$= \int_0^{2\pi} R \left(\frac{1}{2} (e^{it} + e^{-it}), \frac{1}{2i} (e^{it} - e^{-it}) \right) dt \quad (2.130)$$

$$= \int_0^{2\pi} R(\cos t, \sin t) dt \quad (2.131)$$

where the identities $\cos t = 1/2(e^{it} + e^{-it})$ and $\sin t = 1/(2i)(e^{it} - e^{-it})$ were used in the last step.

Finally with (2.124) and (2.131) one gets a simple formula to calculate (2.123):

$$\int_0^{2\pi} R(\cos \Phi, \sin \Phi) d\Phi = 2\pi i \sum_{|z|<1} \text{Res}(f, z) \quad (2.132)$$

with f being defined in (2.127).

2.B The doubly differential cross section for $\Theta_i = 0$ and $\Theta_i = \pi$

In order to get (2.81) from (2.67) it is rather straight forward to set $\Theta_i = 0$ or $\Theta_i = \pi$. Especially it is

$$\Delta_1(\Theta_i = 0, \pi) = \tilde{\Delta}_1, \quad (2.133)$$

$$\Delta_2(\Theta_i = 0, \pi) = \tilde{\Delta}_2. \quad (2.134)$$

But there is one case which should be considered a bit more thoroughly.

This regards the logarithm in (2.68). For $\Theta_i = \pi$ it is $\Delta_2(\Theta = \pi) = \tilde{\Delta}_2 = -2p_f(\hbar/c\omega + p_i) < 0$; thus $|\tilde{\Delta}_2| = -\tilde{\Delta}_2$ and

$$\left. \frac{\ln \left(\frac{\Delta_2^2 + 4p_i^2 p_f^2 \sin^2 \Theta_i - \sqrt{\Delta_2^2 + 4p_i^2 p_f^2 \sin^2 \Theta_i} (\Delta_1 + \Delta_2) + \Delta_1 \Delta_2}{-\Delta_2^2 - 4p_i^2 p_f^2 \sin^2 \Theta_i - \sqrt{\Delta_2^2 + 4p_i^2 p_f^2 \sin^2 \Theta_i} (\Delta_1 - \Delta_2) + \Delta_1 \Delta_2} \right)}{\sqrt{\Delta_2^2 + 4p_i^2 p_f^2 \sin^2 \Theta_i}} \right|_{\Theta_i=\pi} \quad (2.135)$$

$$= \frac{1}{|\tilde{\Delta}_2|} \ln \left(\frac{\tilde{\Delta}_2^2 - |\tilde{\Delta}_2|(\tilde{\Delta}_1 + \tilde{\Delta}_2) + \tilde{\Delta}_1 \tilde{\Delta}_2}{-\tilde{\Delta}_2^2 - |\tilde{\Delta}_2|(\tilde{\Delta}_1 - \tilde{\Delta}_2) + \tilde{\Delta}_1 \tilde{\Delta}_2} \right) \quad (2.136)$$

$$= -\frac{1}{\tilde{\Delta}_2} \ln \left(\frac{\tilde{\Delta}_1 + \tilde{\Delta}_2}{\tilde{\Delta}_1 - \tilde{\Delta}_2} \right) \quad (2.137)$$

which is a very simple calculation. However, for $\Theta_i = 0$ it is $\Delta_2(\Theta_i = 0) = \tilde{\Delta}_2 = -2p_f(\hbar/c\omega - p_i)$ which can be both negative or positive depending on values of p_i and $\hbar/c\omega$. If $\tilde{\Delta}_2 < 0$ then equations (2.135) - (2.137) are valid again. If $\tilde{\Delta}_2 > 0$, however, it follows for the argument of the logarithm

$$\left. \frac{\Delta_2^2 + 4p_i^2 p_f^2 \sin^2 \Theta_i - \sqrt{\Delta_2^2 + 4p_i^2 p_f^2 \sin^2 \Theta_i} (\Delta_1 + \Delta_2) + \Delta_1 \Delta_2}{-\Delta_2^2 - 4p_i^2 p_f^2 \sin^2 \Theta_i - \sqrt{\Delta_2^2 + 4p_i^2 p_f^2 \sin^2 \Theta_i} (\Delta_1 - \Delta_2) + \Delta_1 \Delta_2} \right|_{\Theta_i=0} \quad (2.138)$$

$$= \frac{\tilde{\Delta}_2^2 - \tilde{\Delta}_2(\tilde{\Delta}_1 + \tilde{\Delta}_2) + \tilde{\Delta}_1 \tilde{\Delta}_2}{-\tilde{\Delta}_2^2 - \tilde{\Delta}_2(\tilde{\Delta}_1 - \tilde{\Delta}_2) + \tilde{\Delta}_1 \tilde{\Delta}_2} = \frac{0}{0}. \quad (2.139)$$

Hence it is necessary to use the rule of L'Hôpital:

$$\lim_{\Theta_i \rightarrow 0} \frac{\Delta_2^2 + 4p_i^2 p_f^2 \sin^2 \Theta_i - \sqrt{\Delta_2^2 + 4p_i^2 p_f^2 \sin^2 \Theta_i} (\Delta_1 + \Delta_2) + \Delta_1 \Delta_2}{-\Delta_2^2 - 4p_i^2 p_f^2 \sin^2 \Theta_i - \sqrt{\Delta_2^2 + 4p_i^2 p_f^2 \sin^2 \Theta_i} (\Delta_1 - \Delta_2) + \Delta_1 \Delta_2} \quad (2.140)$$

$$= \lim_{\Theta_i \rightarrow 0} \frac{8p_i^2 p_f^2 \sin \Theta_i \cos \Theta_i - \frac{\Delta_1 + \Delta_2}{2\sqrt{\Delta_2^2 + 4p_i^2 p_f^2 \sin^2 \Theta_i}} \cdot 8p_i^2 p_f^2 \sin \Theta_i \cos \Theta_i}{-8p_i^2 p_f^2 \sin \Theta_i \cos \Theta_i - \frac{\Delta_1 - \Delta_2}{2\sqrt{\Delta_2^2 + 4p_i^2 p_f^2 \sin^2 \Theta_i}} \cdot 8p_i^2 p_f^2 \sin \Theta_i \cos \Theta_i} \quad (2.141)$$

$$= \ln \left(\frac{\tilde{\Delta}_1 - \tilde{\Delta}_2}{\tilde{\Delta}_1 + \tilde{\Delta}_2} \right). \quad (2.142)$$

With (2.142) the whole limit yields

$$\ln \left(\frac{\Delta_2^2 + 4p_i^2 p_f^2 \sin^2 \Theta_i - \sqrt{\Delta_2^2 + 4p_i^2 p_f^2 \sin^2 \Theta_i} (\Delta_1 + \Delta_2) + \Delta_1 \Delta_2}{-\Delta_2^2 - 4p_i^2 p_f^2 \sin^2 \Theta_i - \sqrt{\Delta_2^2 + 4p_i^2 p_f^2 \sin^2 \Theta_i} (\Delta_1 - \Delta_2) + \Delta_1 \Delta_2} \right) \Bigg|_{\Theta_i=0} \quad (2.143)$$

$$= \frac{1}{\tilde{\Delta}_2} \ln \left(\frac{\tilde{\Delta}_1 - \tilde{\Delta}_2}{\tilde{\Delta}_1 + \tilde{\Delta}_2} \right) = -\frac{1}{\tilde{\Delta}_2} \ln \left(\frac{\tilde{\Delta}_1 + \tilde{\Delta}_2}{\tilde{\Delta}_1 - \tilde{\Delta}_2} \right) \quad (2.144)$$

which is and has to be identical with (2.137). So in both cases, $\tilde{\Delta}_2 > 0$ and $\tilde{\Delta}_2 < 0$, (2.137,2.144) are generated by setting $\Theta_i = 0, \pi$; therefore one does not have to distinguish between these cases in (2.81).

But it is of importance to mention that due to (2.139) one can get numerical problems if one only implements (2.67) and wants to calculate the doubly differential cross section for $\Theta_i = 0$. Thus it is useful to distinguish for $\Theta_i \neq 0$ and $\Theta_i = 0$ and to use (2.81) instead for the latter case.

For the rest of limiting forward and/or backward scattering it is, however, straight forward to insert $\Theta_i = 0, \pi$ and thus can deduce (2.81) from (2.67) with the additional help of (2.142).

2.C The doubly differential cross section for $\hbar\omega \rightarrow E_{kin,i}$

There are three contributions from (2.67) which lead to (2.88) in the limit $\hbar\omega \rightarrow E_{kin,i} \Leftrightarrow |\mathbf{p}_f| \rightarrow 0$:

$$\iota_1 = \frac{16\pi E_f^2 p_i^2 \sin^2 \Theta_i A}{(E_i - cp_i \cos \Theta_i)^2 (\Delta_1^2 - \Delta_2^2 - 4p_i^2 p_f^2 \sin^2 \Theta_i)}, \quad (2.145)$$

$$\begin{aligned} \iota_2 &= -\frac{2\pi A p_i^2 c^2 \sin^2 \Theta_i}{(E_i - cp_i \cos \Theta_i)^2} \frac{1}{\sqrt{\Delta_2^2 + 4p_i^2 p_f^2 \sin^2 \Theta_i}} \\ &\times \ln \left(\frac{\Delta_2^2 + 4p_i^2 p_f^2 \sin^2 \Theta_i - \sqrt{\Delta_2^2 + 4p_i^2 p_f^2 \sin^2 \Theta_i} (\Delta_1 + \Delta_2) + \Delta_1 \Delta_2}{-\Delta_2^2 - 4p_i^2 p_f^2 \sin^2 \Theta_i - \sqrt{\Delta_2^2 + 4p_i^2 p_f^2 \sin^2 \Theta_i} (\Delta_1 - \Delta_2) + \Delta_1 \Delta_2} \right), \end{aligned} \quad (2.146)$$

$$\begin{aligned} \iota_3 &= -\frac{4\pi \hbar^2 \omega^2 p_i^2 \sin^2 \Theta_i A}{E_i - cp_i \cos \Theta_i} \left[\frac{2\Delta_1 \Delta_2 p_f c + 2\Delta_2^2 E_f + 8p_i^2 p_f^2 \sin^2 \Theta_i E_f}{(-\Delta_2^2 + \Delta_1^2 - 4p_i^2 p_f^2 \sin^2 \Theta_i)((\Delta_2 E_f + \Delta_1 p_f c)^2 + 4m^2 c^4 p_i^2 p_f^2 \sin^2 \Theta_i)} \right. \\ &+ \frac{p_f c (\Delta_2 E_f + \Delta_1 p_f c)}{\sqrt{((\Delta_2 E_f + \Delta_1 p_f c)^2 + 4m^2 c^4 p_i^2 p_f^2 \sin^2 \Theta_i)^3}} \\ &\times \ln \left(\frac{(E_f + p_f c)(4p_i^2 p_f^2 \sin^2 \Theta_i (E_f - p_f c) + (\Delta_1 + \Delta_2)((\Delta_2 E_f + \Delta_1 p_f c) \right. \\ &- \sqrt{(\Delta_2 E_f + \Delta_1 p_f c)^2 + 4m^2 c^4 p_i^2 p_f^2 \sin^2 \Theta_i}))}{(E_f - p_f c)(4p_i^2 p_f^2 \sin^2 \Theta_i (-E_f - p_f c) \right. \\ &\left. \left. + (\Delta_1 - \Delta_2)((\Delta_2 E_f + \Delta_1 p_f c) - \sqrt{(\Delta_2 E_f + \Delta_1 p_f c)^2 + 4m^2 c^4 p_i^2 p_f^2 \sin^2 \Theta_i}))^{-1}} \right) \right] \end{aligned} \quad (2.147)$$

while all other integrals which appear in (2.67) cancel each other (which will be shown in an example later). It can be verified easily that

$$\lim_{p_f \rightarrow 0} \Delta_1 = \delta, \quad (2.148)$$

$$\lim_{p_f \rightarrow 0} \Delta_2 = 0 \quad \text{with } \Delta_2 \sim |\mathbf{p}_f| \quad (2.149)$$

according to definitions (2.56), (2.57) and (2.84). With these limits the behavior of ι_1 for small p_f can be calculated in a straight forward way:

$$\lim_{p_f \rightarrow 0} \iota_1 = \frac{16\pi A E_f^2 p_i^2 \sin^2 \Theta_i}{(E_i - cp_i \cos \Theta_i)^2 \delta^2}. \quad (2.150)$$

For (2.146) and (2.147), however, there is more effort to be invested. As $\sqrt{\Delta_2^2 + 4p_i^2 p_f^2 \sin^2 \Theta_i} \rightarrow 0$ and $\ln \left(\frac{(\Delta_2^2 + 4p_i^2 p_f^2 \sin^2 \Theta_i - \sqrt{\Delta_2^2 + 4p_i^2 p_f^2 \sin^2 \Theta_i} (\Delta_1 + \Delta_2) + \Delta_1 \Delta_2)}{(-\Delta_2^2 - 4p_i^2 p_f^2 \sin^2 \Theta_i - \sqrt{\Delta_2^2 + 4p_i^2 p_f^2 \sin^2 \Theta_i} (\Delta_1 - \Delta_2) + \Delta_1 \Delta_2)} \right) \rightarrow 0$ for $p_f \rightarrow 0$, one has to use the rule of L'Hôpital. If one rewrites

$$\Delta_2 = \Psi p_f \quad (2.151)$$

with

$$\Psi := -2\frac{\hbar}{c}\omega + 2p_i \cos \Theta_i \quad (2.152)$$

this rule leads to

$$\begin{aligned} & \lim_{p_f \rightarrow 0} \left[\frac{1}{\sqrt{\Delta_2^2 + 4p_i^2 p_f^2 \sin^2 \Theta_i}} \times \right. \\ & \times \left. \ln \left(\frac{\Delta_2^2 + 4p_i^2 p_f^2 \sin^2 \Theta_i - \sqrt{\Delta_2^2 + 4p_i^2 p_f^2 \sin^2 \Theta_i}(\Delta_1 + \Delta_2) + \Delta_1 \Delta_2}{-\Delta_2^2 - 4p_i^2 p_f^2 \sin^2 \Theta_i - \sqrt{\Delta_2^2 + 4p_i^2 p_f^2 \sin^2 \Theta_i}(\Delta_1 - \Delta_2) + \Delta_1 \Delta_2} \right) \right] \\ & = -\frac{2}{\delta}; \end{aligned} \quad (2.153)$$

thus

$$\lim_{p_f \rightarrow 0} \iota_2 = \frac{4\pi A p_i^2 c^2 \sin^2 \Theta_i}{(E_i - c p_i \cos \Theta_i)^2 \delta}. \quad (2.154)$$

The limit of (2.147) can also be calculated by using (2.151). It is

$$\begin{aligned} \iota_3 &= -\frac{4\pi \hbar^2 \omega^2 p_i^2 \sin^2 \Theta_i A}{E_i - c p_i \cos \Theta_i} \left[-\frac{p_f^2 (2\Delta_1 \Psi c + 2\Psi^2 E_f + 8p_i^2 \sin^2 \Theta_i E_f)}{p_f^2 (-\Delta_2^2 + \Delta_1^2 - 4p_i^2 \sin^2 \Theta_i) ((\Psi E_f + \Delta_1 c)^2 + 4m^2 c^4 p_i^2 \sin^2 \Theta_i)} \right. \\ & \times \frac{p_f^2 c (\Psi E_f + \Delta_1 c)}{p_f^2 ((\Psi E_f + \Delta_1 c)^2 + 4m^2 c^4 p_i^2 \sin^2 \Theta_i)} \\ & \times \frac{1}{p_f \sqrt{(\Psi E_f + \Delta_1 c)^2 + 4m^2 c^4 p_i^2 \sin^2 \Theta_i}} \\ & \times \ln \left(\left((E_f + p_f c) (4p_i^2 p_f^2 \sin^2 \Theta_i (E_f - p_f c) + (\Delta_1 + \Psi p_f) (p_f (\Psi E_f + \Delta_1 c) \right. \right. \\ & \left. \left. - p_f \sqrt{(\Psi E_f + \Delta_1 c)^2 + 4m^2 c^4 p_i^2 \sin^2 \Theta_i}) \right) \left((E_f - p_f c) (4p_i^2 p_f^2 \sin^2 \Theta_i (-E_f - p_f c) \right. \right. \\ & \left. \left. + (\Delta_1 - \Psi p_f) (p_f (\Psi E_f + \Delta_1 c) - p_f \sqrt{(\Psi E_f + \Delta_1 c)^2 + 4m^2 c^4 p_i^2 \sin^2 \Theta_i}) \right)^{-1} \right) \right] \end{aligned} \quad (2.155)$$

While p_f can simply be reduced in the fractions, one has to use the rule of L'Hôpital again for the logarithmic part because it is $p_f \sqrt{(\Psi E_f + \Delta_1 c)^2 + 4m^2 c^4 p_i^2 \sin^2 \Theta_i} \rightarrow 0$ and the logarithm $\rightarrow 0$ for $p_f \rightarrow 0$. Its limit is

$$\begin{aligned} & \lim_{p_f \rightarrow 0} \frac{1}{p_f \sqrt{(\Psi E_f + \Delta_1 c)^2 + 4m^2 c^4 p_i^2 \sin^2 \Theta_i}} \\ & \times \ln \left(\left((E_f + p_f c) (4p_i^2 p_f^2 \sin^2 \Theta_i (E_f - p_f c) + (\Delta_1 + \Psi p_f) (p_f (\Psi E_f + \Delta_1 c) \right. \right. \\ & \left. \left. - p_f \sqrt{(\Psi E_f + \Delta_1 c)^2 + 4m^2 c^4 p_i^2 \sin^2 \Theta_i}) \right) \left((E_f - p_f c) (4p_i^2 p_f^2 \sin^2 \Theta_i (-E_f - p_f c) \right. \right. \\ & \left. \left. + (\Delta_1 - \Psi p_f) (p_f (\Psi E_f + \Delta_1 c) - p_f \sqrt{(\Psi E_f + \Delta_1 c)^2 + 4m^2 c^4 p_i^2 \sin^2 \Theta_i}) \right)^{-1} \right) \right] \\ & = -\frac{2}{E_f \Delta_1} \Big|_{p_f \rightarrow 0} = -\frac{2}{E_f \delta}; \end{aligned} \quad (2.156)$$

thus the whole limit yields after some further calculations

$$\lim_{p_f \rightarrow 0} \iota_3 = \frac{8\pi\hbar^2\omega^2 p_i^2 \sin^2 \Theta_i A}{(E_i - cp_i \cos \Theta_i)\delta^2 E_f}. \quad (2.157)$$

Finally, if one inserts (2.14), the sum of (2.150), (2.154) and (2.157) leads to (2.88).

All other terms which appear in (2.67) vanish. For this purpose one should regroup all terms according to their origin. As an example let's consider the three contributions

which have arisen from $\int_{\Theta_f=0}^{\pi} \int_{\Phi=0}^{2\pi} \frac{a_2 \cos \Phi}{\alpha \cos \Phi + \beta} d\Phi d\Omega_f$. For this integral it follows

$$\begin{aligned} & \int_{\Theta_f=0}^{\pi} \int_{\Phi=0}^{2\pi} \frac{a_2 \cos \Phi}{\alpha \cos \Phi + \beta} d\Phi d\Omega_f \\ = & -\frac{2\pi A c}{(E_i - cp_i \cos \Theta_i)p_f} \ln \left(\frac{E_f + p_f c}{E_f - p_f c} \right) \\ - & \frac{2\pi A c^2}{E_i - cp_i \cos \Theta_i} \left[-\frac{\Delta_2}{\sqrt{\Delta_2^2 + 4p_i^2 p_f^2 \sin^2 \Theta_i p_f c}} \right. \\ \times & \ln \left(\frac{\Delta_2^2 + 4p_i^2 p_f^2 \sin^2 \Theta_i - \sqrt{\Delta_2^2 + 4p_i^2 p_f^2 \sin^2 \Theta_i}(\Delta_1 + \Delta_2) + \Delta_1 \Delta_2}{-\Delta_2^2 - 4p_i^2 p_f^2 \sin^2 \Theta_i - \sqrt{\Delta_2^2 + 4p_i^2 p_f^2 \sin^2 \Theta_i}(\Delta_1 - \Delta_2) + \Delta_1 \Delta_2} \right) \\ - & \frac{\Delta_2 E_f + \Delta_1 p_f c}{p_f c \sqrt{(\Delta_2 E_f + \Delta_1 p_f c)^2 + 4m^2 c^4 p_i^2 p_f^2 \sin^2 \Theta_i}} \\ \times & \ln \left(\left((E_f + p_f c)(4p_i^2 p_f^2 \sin^2 \Theta_i (E_f - p_f c) + (\Delta_1 + \Delta_2)((\Delta_2 E_f + \Delta_1 p_f c) \right. \right. \\ - & \left. \left. \sqrt{(\Delta_2 E_f + \Delta_1 p_f c)^2 + 4m^2 c^4 p_i^2 p_f^2 \sin^2 \Theta_i}) \right) \left((E_f - p_f c)(4p_i^2 p_f^2 \sin^2 \Theta_i (-E_f - p_f c) \right. \right. \\ + & \left. \left. (\Delta_1 - \Delta_2)((\Delta_2 E_f + \Delta_1 p_f c) - \sqrt{(\Delta_2 E_f + \Delta_1 p_f c)^2 + 4m^2 c^4 p_i^2 p_f^2 \sin^2 \Theta_i}) \right)^{-1} \right) \right] \\ \xrightarrow{\hbar\omega \rightarrow E_{kin,i}} & \frac{2\pi A c}{E_i - cp_i \cos \Theta_i} \left[-\frac{2c}{E_f} + \Psi \left(-\frac{2}{\delta} \right) + (\Psi E_f + \delta c) \frac{2}{E_f \delta} \right] \\ = & 0 \end{aligned} \quad (2.158)$$

where we have used (2.153), (2.156) and

$$\lim_{p_f \rightarrow 0} \frac{1}{p_f} \ln \left(\frac{E_f + p_f c}{E_f - p_f c} \right) = \frac{2c}{E_f} \quad (2.159)$$

in the limiting step. Of course, this term has to vanish because $a_2 \sim p_f$, but the concrete calculation after having integrated over Φ and Θ_f is much more complicated. Therefore we have just given an example here. Similarly, all other terms cancel so that only the limits of ι_i , $i \in \{1, 2, 3\}$, stay.

2.D Discussion of Geant 4

As mentioned in the introduction, preimplemented cross sections for Bremsstrahlung can be found in the Geant 4 software library [2]. Geant 4 contains data for the total cross section σ , the singly differential cross section $d\sigma/d\omega$ and a singly differential cross section

$d\sigma/d\Omega_i$ depending on Θ_i , but not on ω .

The singly differential cross section $d\sigma/d\omega$ by Bethe and Heitler is appropriate for small Z ; it is [12, 75]

$$\frac{d\sigma}{d\omega}(E_i, \omega) = \chi_0 \frac{1}{\omega} \frac{p_f}{p_i} (\chi_1 + L\chi_2) \quad (2.160)$$

with

$$\chi_0 = \frac{Z^2 r_0^2}{137}, \quad (2.161)$$

$$L = \ln \left(\frac{p_i^2 + p_i p_f - \frac{E_i \hbar \omega}{c^2}}{p_i^2 - p_i p_f - \frac{E_i \hbar \omega}{c^2}} \right), \quad (2.162)$$

$$\epsilon_0 = 2 \ln \left(\frac{E_i + c p_i}{m_e c^2} \right), \quad (2.163)$$

$$\epsilon = 2 \ln \left(\frac{E_f + c p_f}{m_e c^2} \right), \quad (2.164)$$

$$\chi_1 = \frac{4}{3} - 2 \frac{E_i E_f p_f^2 + p_i^2}{c^2 p_i^2 p_f^2} + m_e^2 c^2 \left(\frac{\epsilon_0 E_f}{c p_i^3} + \frac{\epsilon E_i}{c p_f^3} - \frac{\epsilon_0 \epsilon}{p_i p_f} \right), \quad (2.165)$$

$$\begin{aligned} \chi_2 = & \frac{8}{3} \frac{E_i E_f}{c^2 p_i p_f} + \left(\frac{\hbar \omega}{c} \right)^2 \frac{1}{p_i^3 p_f^3} \left(\frac{E_i^2 E_f^2}{c^4} + p_i^2 p_f^2 \right) \\ & + \frac{m_e^2 c \hbar \omega}{2 p_i p_f} \left(\frac{E_i E_f}{c^2} + p_i^2 \epsilon_0 - \frac{E_i E_f + p_f^2}{p_f^3} \epsilon + 2 \frac{\hbar \omega E_i E_f}{c^3 p_f^2 p_i^2} \right) \end{aligned} \quad (2.166)$$

with the quantities as described in section 2.2.1.

Geant 4 uses a fit formula which is appropriate for large Z ; it is [2]

$$\frac{d\sigma}{d\omega}(E_i, \omega) = \frac{S \left(\frac{\hbar \omega}{E_{kin,i}}, \omega \right)}{C \omega} \quad (2.167)$$

where C is a constant which is not specified in the Geant 4 documentation, nor in the source code. S is defined as

$$S \left(\frac{\hbar \omega}{E_{kin,i}}, \omega \right) = \begin{cases} 1 + a_l \frac{\hbar \omega}{E_{kin,i}} + b_l \left(\frac{\hbar \omega}{E_{kin,i}} \right)^2, & E_{kin,i} < 1 \text{ MeV} \\ 1 - a_h \frac{\hbar \omega}{E_i} F_1 + b_h \left(\frac{\hbar \omega}{E_i} \right)^2 F_2, & E_{kin,i} \geq 1 \text{ MeV} \end{cases} \quad (2.168)$$

where $E_{kin,i} = E_i - m_e c^2$ is the kinetic energy of the incident electron. F_1 and F_2 are defined as

$$F_1 = \begin{cases} F_0(42.392 - 7.796\delta + 1.961\delta^2 - F), & \delta \leq 1 \\ F_0(42.24 - 8.368 \ln(\delta + 0.952) - F), & \delta > 1 \end{cases}, \quad (2.169)$$

$$F_2 = \begin{cases} F_0(41.734 - 6.484\delta + 1.250\delta^2 - F), & \delta \leq 1 \\ F_0(42.24 - 8.368 \ln(\delta + 0.952) - F), & \delta > 1 \end{cases} \quad (2.170)$$

with $F = 4 \ln(Z) - 0.55(\ln(Z))^2$, $F_0 = 1/(42.392 - F)$ and $\delta = 136m_e c^2 \epsilon / (Z^{1/3} E_i (1 - \epsilon))$ where $\epsilon = \hbar\omega/E_i$ is the ratio between the photon energy and the total energy of the incident electron.

a_h, b_h, a_l and b_l in (2.168) are defined as

$$a_h = 1 + \frac{a_{h1}}{u} + \frac{a_{h2}}{u^2} + \frac{a_{h3}}{u^3}, \quad (2.171)$$

$$b_h = 0.75 + \frac{b_{h1}}{u} + \frac{b_{h2}}{u^2} + \frac{b_{h3}}{u^3}, \quad (2.172)$$

$$a_l = a_{l0} + a_{l1}u + a_{l2}u^2, \quad (2.173)$$

$$b_l = b_{l0} + b_{l1}u + b_{l2}u^2, \quad (2.174)$$

with $u = \ln(E_{kin,i}/(m_e c^2))$. The $a_{hi}, b_{hi}, a_{li}, b_{li}$ are directly defined in the Geant 4 source code as

$$a_{hj} = a_{hj,0}[Z(Z+1)]^{\frac{1}{3}} \left(a_{hj,1} + [Z(Z+1)]^{\frac{1}{3}} a_{hj,2} \right), \quad j \in \{1, 2, 3\}, \quad (2.175)$$

$$b_{hj} = b_{hj,0}[Z(Z+1)]^{\frac{1}{3}} \left(b_{hj,1} + [Z(Z+1)]^{\frac{1}{3}} b_{hj,2} \right), \quad j \in \{1, 2, 3\}, \quad (2.176)$$

$$a_{lj} = a_{lj,0}[Z(Z+1)]^{\frac{1}{3}} \left(a_{lj,1} + [Z(Z+1)]^{\frac{1}{3}} a_{lj,2} \right), \quad j \in \{1, 2, 3\}, \quad (2.177)$$

$$b_{lj} = b_{lj,0}[Z(Z+1)]^{\frac{1}{3}} \left(b_{lj,1} + [Z(Z+1)]^{\frac{1}{3}} b_{lj,2} \right), \quad j \in \{1, 2, 3\}, \quad (2.178)$$

where all the coefficients are also defined in the source code:

$$(a_h)_{i,j} = \begin{pmatrix} 4.67733 & -0.619012 & -0.020225 \\ -7.34101 & 1.00462 & -0.0320985 \\ 2.93119 & -0.403761 & 0.0125153 \end{pmatrix}, \quad (2.179)$$

$$(b_h)_{i,j} = \begin{pmatrix} 4.23071 & -6.10995 & -0.0195531 \\ -7.12527 & 0.969160 & -0.0274255 \\ 2.69925 & -0.363283 & -0.00955316 \end{pmatrix}, \quad (2.180)$$

$$(a_l)_{i,j} = \begin{pmatrix} -2.05398 & 0.0238815 & 0.000525483 \\ -0.0769748 & -0.0691499 & 0.00222453 \\ 0.0406463 & -0.0101281 & 0.000340919 \end{pmatrix}, \quad (2.181)$$

$$(b_l)_{i,j} = \begin{pmatrix} 1.04133 & -0.00943291 & -0.000454758 \\ 0.119253 & 0.0407467 & -0.00130718 \\ -0.0159391 & 0.00727752 & -0.000194405 \end{pmatrix}, \quad (2.182)$$

with $i \in \{1, 2, 3\}$ and $j \in \{0, 1, 2\}$. In (2.179) - (2.182) the first index denotes columns, the second one denotes rows.

Figure 2.14 compares the Bethe Heitler cross section (2.160) with that of Geant 4 (2.167) where we have chosen $C = 10^{28}$ for all energies in such a way that the orders

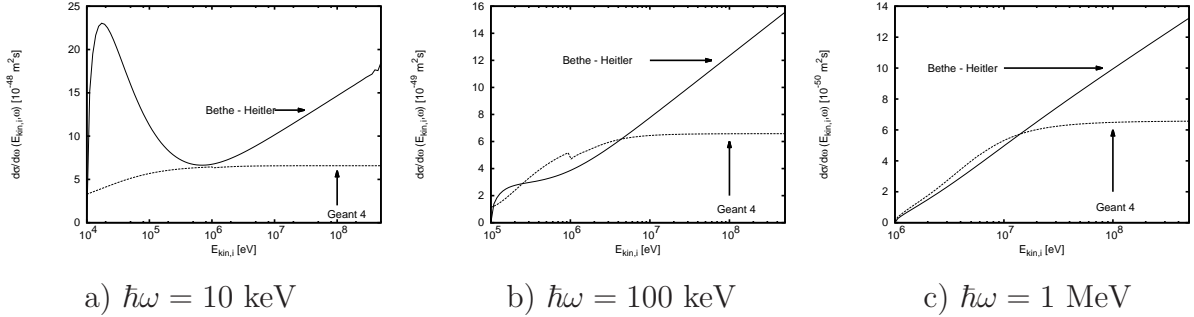


Figure 2.14: The singly differential cross sections (2.160) and (2.167) as a function of the kinetic energy $E_{kin,i}$ of the incident electron for $Z = 7$ (nitrogen) and for fixed photon energy a) $\hbar\omega = 10$ keV, b) $\hbar\omega = 100$ keV and c) $\hbar\omega = 1$ MeV.

of magnitude of (2.160) and (2.167) agree with each other. It shows that (using exactly the values provided in the source code of Geant 4) that there is a good quantitative and qualitative agreement for electron energies of ≈ 1 MeV and ≈ 10 MeV. But above and below that, both cross sections certainly differ.

That is because Geant 4 was developed for high energy physics in particle accelerators and thus for high atomic numbers. Thus the cross sections used in Geant 4 are not appropriate to describe the production of Bremsstrahlung photons in air. The Bethe - Heitler theory for the energy range we consider, is used for small atomic numbers.

Geant 4 also includes dielectric suppression, i.e. the suppression of the emission of lowly energetic photons because of their interaction with the electrons of the background medium [156], and the Landau-Pomeranchuk-Migdal (LPM) effect [96], i.e. the suppression of photon production due to the multiple scattering of electrons.

The influence of the dielectric effect can be estimated by

$$S(\hbar\omega) = \frac{(\hbar\omega)^2}{(\hbar\omega)^2 + \frac{\hbar^2 E_i^2 n_e e^2}{m_e^2 c^2 \epsilon_0}} \quad (2.183)$$

where n_e is the density of free electrons. For densities between 10^{20} m^{-3} and 10^{25} m^{-3} , S is almost 1. Figure 2.15 shows (2.183) for different photon energies, electron energies and densities. Dielectric suppression has a very small effect when $E_{kin,i} \approx 1$ GeV; thus it can be neglected.

The LPM effect is not important, either. The LPM threshold energy is $\approx 10^{19}$ eV [11]; this is much higher than typical energies of electrons in the atmosphere.

The preimplemented cross sections used in Geant 4 are supposed to be used for high electron energies $\gtrsim 1$ MeV and high atomic numbers Z . In the case of TGFs it is necessary to treat electron energies in the keV and MeV range and small atomic numbers where the LPM effect and dielectric suppression are not significant.

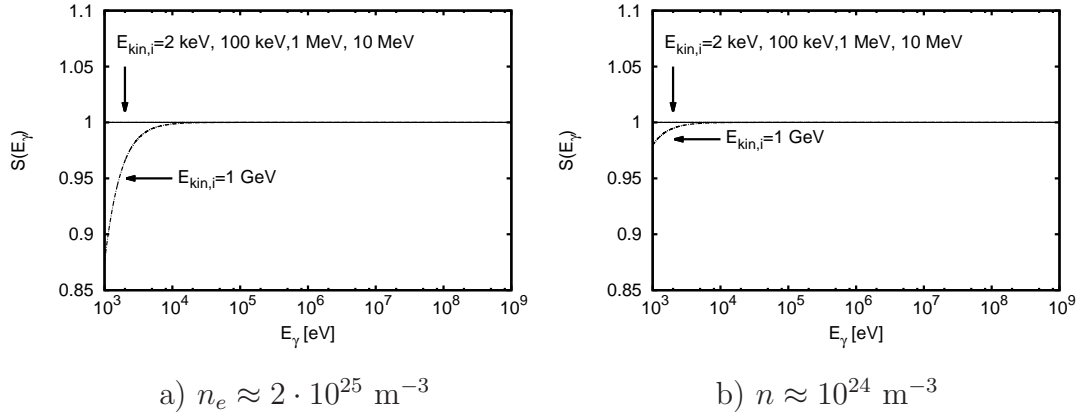


Figure 2.15: The dielectric factor S (2.183) vs. the photon energy for different electron energies for a) $n_e \approx 2 \cdot 10^{25} \text{ m}^{-3}$ and b) $n_e \approx 10^{24} \text{ m}^{-3}$

2.E Comparison with Lehtinen

Figure 2.16 shows the comparison of (2.67) and the doubly differential cross section used by Lehtinen [98]. Lehtinen uses a product ansatz for the angular and the frequency part; here the angular part is a non-quantum mechanical expression taken from [81]. This cross section is only valid if $\hbar\omega \ll E_i$. There is a good agreement for low ratios between photon and electron energy, but a large deviation for larger ratios. Therefore this cross section is not appropriate for high ratios needed to obtain photons with energies up to several tens of MeV to determine the high energy tail of the TGF spectrum where almost all electron energy is converted into photon energy.

2.F Contribution of the atomic form factor

Dwyer [42] uses the triply differential cross section by Bethe and Heitler [12], but with an additional form factor $F(\mathbf{q})$ parameterizing the structure of the nucleus [87]. F is defined as

$$F(\mathbf{q}) := -\frac{1}{Ze} \int d^3\mathbf{r} \varrho(\mathbf{r}) e^{-\frac{i}{\hbar} \mathbf{q} \cdot \mathbf{r}} \quad (2.184)$$

where Z is the atomic number and ϱ the charge density

$$\varrho(\mathbf{r}) = Ze\delta(\mathbf{r}) - \frac{Ze}{4\pi a^2 r} e^{-\frac{r}{a}} \quad (2.185)$$

with $a = 111\lambda Z^{-1/3}$ where $\lambda = \lambda/(2\pi)$ is the reduced Compton wave length of the electron. The delta function describes the nucleus itself and the Debye term describes the

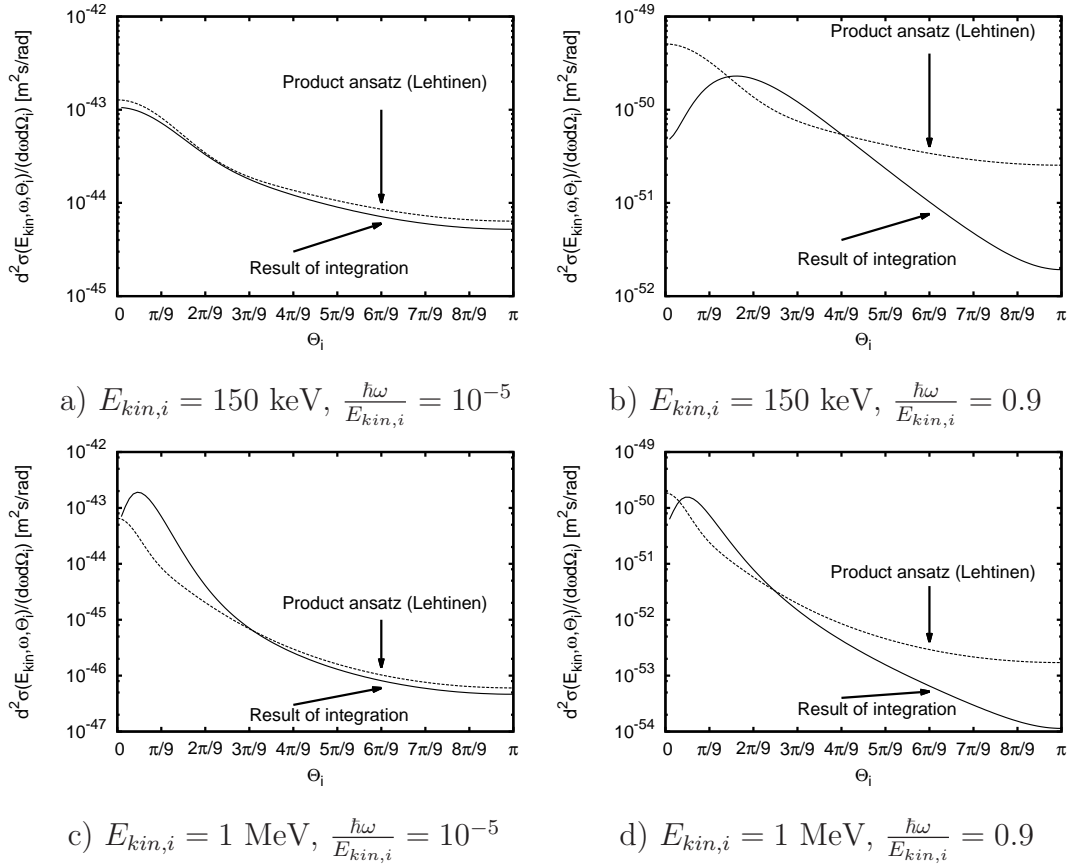


Figure 2.16: Comparison of the product ansatz from Lehtinen [98] with our result (2.67) of the integration of (2.1) for different electron energies ($Z = 7$): doubly differential cross section versus the scattering angle Θ_i between incident electron and emitted photon. The ratio between the photon energy $\hbar\omega$ and the kinetic electron energy $E_{kin,i}$ is fixed to 0.001% and 90%. The Born approximation (2.11) is valid in all cases.

electrons of the shell. Performing the Fourier transformation in (2.184) gives

$$F(\mathbf{q}) = \frac{\mathbf{q}^2}{\mathbf{q}^2 + \frac{\hbar^2}{a^2}} \quad (2.186)$$

with \mathbf{q} as in Eq. (2.9). We calculated the value of $F(\mathbf{q})$ for different angles, electron and photon energies [a) $E_{kin,i} = 100$ keV, $\hbar\omega = 10$ keV, $\Theta_f = 37^\circ$, $\Phi = 87^\circ$; b) $E_{kin,i} = 100$ keV, $\hbar\omega = 80$ keV, $\Theta_f = 62^\circ$, $\Phi = 43^\circ$; c) $E_{kin,i} = 10$ MeV, $\hbar\omega = 1$ MeV, $\Theta_f = 12^\circ$, $\Phi = 31^\circ$ and d) $E_{kin,i} = 50$ MeV, $\hbar\omega = 10$ MeV, $\Theta_f = 52^\circ$, $\Phi = 90^\circ$]. In all these cases the atomic form factor is 1. Hence, it can be neglected. As it makes the integration over Φ and Θ_f more complicated, it is useful not to use $F(\mathbf{q})$.

2.G Contribution of the integrals

As equation (2.67) is rather complicated, it is interesting to see which terms have the most important contribution. Figure 2.17 shows the contribution of all parts to the final result in a logarithmic scale while Fig. 2.18 shows the same in a linear scale. In all cases, i.e. low and high electron energies and low and high ratios between $\hbar\omega$ and $E_{kin,i}$, the main contribution comes from (2.70). It is important to state that not all contributions can be seen in figure 2.17 because some of the terms have negative values which, however, are shown in figure 2.18. So one might think that for $E_{kin,i} = 100$ keV and $\hbar\omega = 1$ keV, equation (2.73) has the largest contribution, but as figure 2.18 shows, (2.72) has nearly the same absolute value, but opposite sign; therefore they cancel. Thus the third integral (2.70) is the most important one. The same holds for other electron energies and ratios between $\hbar\omega$ and $E_{kin,i}$. We conclude that (2.70) is the dominant contribution for all relevant parameter values.

2.H Conservation of energy and momentum

One can also gain information on the scattering angle Θ_i for high electron energies from the conservation of energy and momentum,

$$E_i + E_q = E_f + \hbar\omega, \quad (2.187)$$

$$\mathbf{p}_i + \mathbf{q} = \mathbf{p}_f + \hbar\mathbf{k} \quad (2.188)$$

where $E_{i,f}$ and $p_{i,f}$ are the energy and the momentum of the electron in the initial and final state. $\hbar\mathbf{k}$ is the momentum of the photon which is related to its energy $\hbar\omega$ through

$$\hbar|\mathbf{k}| = \frac{\hbar}{c}\omega, \quad (2.189)$$

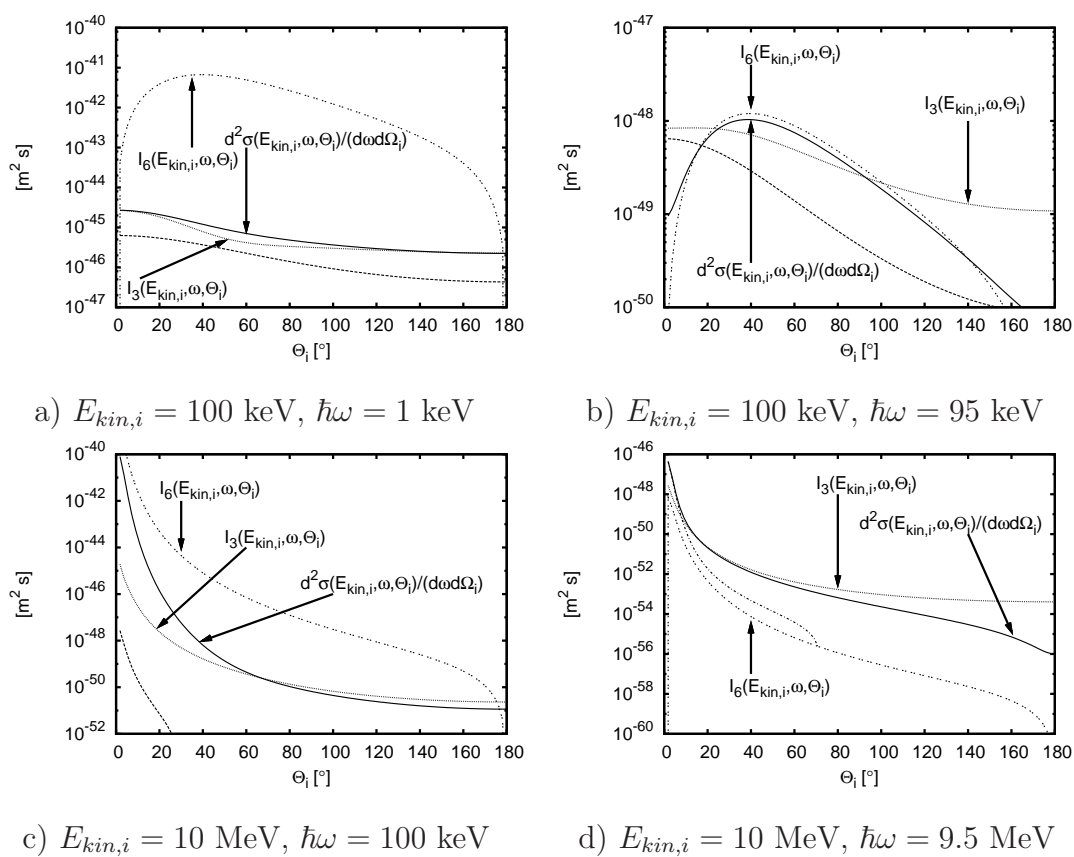
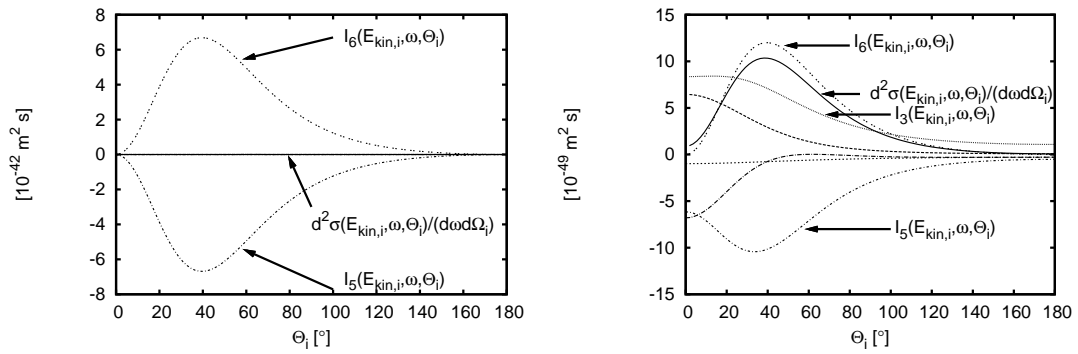
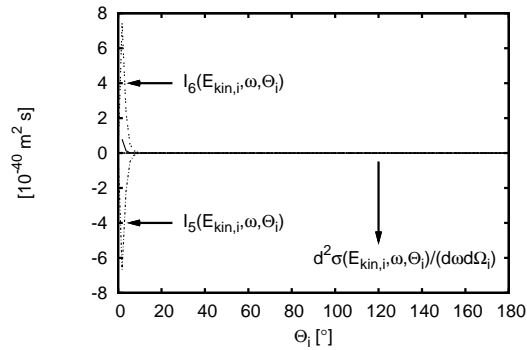


Figure 2.17: Contribution of (2.68) - (2.73) to (2.67) in a semilog plot for different electron and photon energies ($Z = 7$).



a) $E_{kin,i} = 100 \text{ keV}$, $\hbar\omega = 1 \text{ keV}$

b) $E_{kin,i} = 100 \text{ keV}$, $\hbar\omega = 95 \text{ keV}$



c) $E_{kin,i} = 10 \text{ MeV}$, $\hbar\omega = 100 \text{ keV}$

Figure 2.18: Contribution of (2.68) - (2.73) to (2.67) in a linear plot for different electron and photon energies ($Z = 7$).

and E_q and \mathbf{q} are the energy and the momentum of the virtual photon between electron and nucleus. \mathbf{q} changes the momentum of the nucleus. But the contribution to the kinetic energy can be neglected; thus $E_q \equiv 0$ and

$$E_i = E_f + \hbar\omega, \quad (2.190)$$

$$\mathbf{p}_i - \hbar\mathbf{k} = \mathbf{p}_f - \mathbf{q}. \quad (2.191)$$

Squaring (2.191) and using $\mathbf{p}_i \cdot \mathbf{k} = |\mathbf{p}_i||\mathbf{k}| \cos \angle(\mathbf{p}_i, \mathbf{k}) = p_i k \cos \Theta_i$, the angle Θ_i is:

$$\cos \Theta_i = \frac{(\mathbf{p}_f - \mathbf{q})^2 - p_i^2 - \hbar^2 k^2}{-2\hbar p_i k}. \quad (2.192)$$

By using (2.190) and the relativistic energy-momentum relation (2.2) we get an expression for the momentum of the electron in the final state

$$p_f = \sqrt{p_i^2 + \hbar^2 k^2 - 2\hbar k \sqrt{p_i^2 + m_e^2 c^2}} \quad (2.193)$$

which leads to

$$\cos \Theta_i = \frac{2\hbar\omega \frac{E_i}{c} + 2q \sqrt{(E_i - \hbar\omega)^2 - m_e^2 c^4} \cos \angle(\mathbf{p}_f, \mathbf{q}) - cq^2}{2\hbar\omega p_i}. \quad (2.194)$$

Although this is an analytical expression for the scattering angle Θ_i one should take into account that it depends on the vector \mathbf{q} of the virtual photon which is not known in forehand. Thus, depending on \mathbf{q} , only a statistical statement can be made about Θ_i .

It is, however, possible to investigate the limit of (2.194) for high electron energies which yields

$$\lim_{E_i \rightarrow \infty} \cos \Theta_i = 1 + \frac{cq}{\hbar\omega} \cos \angle(\mathbf{p}_f, \mathbf{q}). \quad (2.195)$$

As $\Theta_i \in \mathbb{R} \Leftrightarrow \cos \Theta_i \in [-1, +1]$ and $c, q, \hbar\omega > 0$ we can conclude that

$$\cos \angle(\mathbf{p}_f, \mathbf{q}) \leq 0. \quad (2.196)$$

Especially for $|\frac{cq}{\hbar\omega} \cos \angle(\mathbf{p}_f, \mathbf{q})| \ll 1, \Theta_i \approx 0$, i.e., the photon is mainly emitted in forward direction.

If, additionally, the photon energy $\hbar\omega$ also increases more and more (for high electron energies) it is

$$\lim_{\hbar\omega \rightarrow \infty} \left(1 + \frac{cq}{\hbar\omega} \cos \angle(\mathbf{p}_f, \mathbf{q}) \right) = 1; \quad (2.197)$$

thus

$$\lim_{E_i, \hbar\omega \rightarrow \infty} \Theta_i = 0. \quad (2.198)$$

Hence, we conclude from simple considerations about energy and momentum conservation that the photon is mainly scattered in forward direction if the energies of electron and photon are both very high.

2.1 Approximation for Θ_i

In order to obtain (2.114) we calculate the derivative of (2.88) after Θ_i :

$$\begin{aligned}
\frac{\partial}{\partial \Theta_i} \left(\frac{d^2 \sigma}{d\omega \sin \Theta_i d\Theta_i} \right) &= \frac{Z^2 \alpha_{fine}^3 \hbar^2 |\mathbf{p}_f| |\mathbf{p}_i|}{\pi \omega} \left[\frac{4 \frac{\hbar}{c} \omega |\mathbf{p}_i| \sin \Theta_i}{\delta^3(\Theta_i)} \times \right. \\
&\times \left(\frac{\sin^2 \Theta_i}{(E_i - c|\mathbf{p}_i| \cos \Theta_i)^2} (4E_f^2 + \delta(\Theta_i)c^2) + \frac{2\hbar^2 \omega^2 \sin^2 \Theta_i}{E_f (E_i - c|\mathbf{p}_i| \cos \Theta_i)} \right) \\
&+ \frac{1}{\delta^2(\Theta_i)} \left(\frac{2 \sin \Theta_i \cos \Theta_i (E_i - c|\mathbf{p}_i| \cos \Theta_i) - 2c|\mathbf{p}_i| \sin^3 \Theta_i}{(E_i - c|\mathbf{p}_i| \cos \Theta_i)^3} \right. \\
&\times (4E_f^2 + \delta(\Theta_i)c^2) - \frac{2\hbar c \omega |\mathbf{p}_i| \sin^3 \Theta_i}{(E_i - c|\mathbf{p}_i| \cos \Theta_i)^2} \\
&\left. \left. + \frac{2\hbar^2 \omega^2}{E_f} \frac{2 \sin \Theta_i \cos \Theta_i (E_i - c|\mathbf{p}_i| \cos \Theta_i) - c|\mathbf{p}_i| \sin^3 \Theta_i}{(E_i - c|\mathbf{p}_i| \cos \Theta_i)^2} \right) \right]
\end{aligned} \tag{2.199}$$

with definition (2.84) for δ . In order to calculate the extrema one has to set equation (2.199) equal to zero:

$$\begin{aligned}
0 &= 4 \frac{\hbar}{c} \omega |\mathbf{p}_i| \left[\frac{\sin^2 \Theta_i}{(E_i - c|\mathbf{p}_i| \cos \Theta_i)^2} (4E_f^2 + \delta(\Theta_i)c^2) \right. \\
&+ \left. \frac{2\hbar^2 \omega^2 \sin^2 \Theta_i}{E_f (E_i - c|\mathbf{p}_i| \cos \Theta_i)} \right] (E_i - c|\mathbf{p}_i| \cos \Theta_i)^3 \\
&+ \delta(\Theta_i) [2(E_i \cos \Theta_i - c|\mathbf{p}_i|)(4E_f^2 + \delta(\Theta_i)c^2) \\
&- 2\hbar c \omega |\mathbf{p}_i| \sin^2 \Theta_i (E_i - c|\mathbf{p}_i| \cos \Theta_i) \\
&+ \frac{2\hbar^2 \omega^2}{E_f} (2 \cos \Theta_i (E_i - c|\mathbf{p}_i| \cos \Theta_i)^2 \\
&- c|\mathbf{p}_i| \sin^2 \Theta_i (E_i - c|\mathbf{p}_i| \cos \Theta_i))] .
\end{aligned} \tag{2.200}$$

As $\delta(\Theta_i) \sim \cos \Theta_i$, expression (2.200) is quartic in $\cos \Theta_i$; therefore (2.200) can be solved analytically in principle, but the solution will be long and complicated. Figure 2.3 also shows that the angles for maximal scattering are very small for relativistic electrons, therefore one can approximate $\cos \Theta_i \approx 1$ and $\sin \Theta_i \approx \Theta_i$. This leads to

$$\delta(\Theta_i) \approx -|\mathbf{p}_i|^2 - \left(\frac{\hbar}{c} \omega \right)^2 + 2 \frac{\hbar}{c} \omega |\mathbf{p}_i| = \delta(\Theta_i = 0) =: \delta_0 \tag{2.201}$$

and

$$\begin{aligned}
0 &= 4\frac{\hbar}{c}\omega|\mathbf{p}_i| \left[\Theta_i^2(4E_f^2 + \delta_0c^2) + \frac{2\hbar^2\omega^2}{E_f}\Theta_i^2(E_i - c|\mathbf{p}_i|) \right] \\
&+ \delta_0 \left[2(4E_f^2 + \delta_0c^2) - 2\hbar c\omega|\mathbf{p}_i|\Theta_i^2 + \frac{2\hbar^2\omega^2}{E_f} (2(E_i - c|\mathbf{p}_i|) - c|\mathbf{p}_i|\Theta_i^2) \right]
\end{aligned} \tag{2.202}$$

with solution

$$\Theta_i = \sqrt{\frac{-\frac{\delta_0}{\hbar\omega}(4E_f^2 + \delta_0c^2) - \frac{2\delta_0\hbar\omega}{E_f}(E_i - c|\mathbf{p}_i|)}{2\frac{|\mathbf{p}_i|}{c} \left[4E_f^2 + \delta_0c^2 + \frac{2\hbar^2\omega^2}{E_f}(E_i - c|\mathbf{p}_i|) \right] - |\mathbf{p}_i|\delta_0c - \frac{\hbar\omega}{E_f}c|\mathbf{p}_i|\delta_0}} \tag{2.203}$$

2.J C++ code

In this section we present a C++ code which can be used to create data tables for the doubly differential cross sections (2.67) and (2.101). The code consists of two parts: In the beginning there is a header which defines the functions for Bremsstrahlung and pair production. These lines have to appear in the beginning of a C++ code. Then the functions for Bremsstrahlung and pair production follow which can be placed any where else in the code.

The function to calculate the doubly differential cross section for Bremsstrahlung can be called as

```
brems (E_kin , omega , Theta_i)
```

where E_kin denotes the kinetic energy of the incident electron in Joule, omega is the frequency of the emitted photon in s⁻¹ and Theta_i is the scattering angle. The function to calculate the doubly differential cross section for pair production can be called as

```
pair_pr (E_kin , omega , Theta_p)
```

where E_kin denotes the kinetic energy of the created positron in Joule, omega the frequency of the incident photon in s⁻¹ and Theta_p the angle between both.

The whole code to calculate the doubly differential cross sections for Bremsstrahlung and pair production reads

```
// Doubly differential cross section for
// Bremsstrahlung and pair production
// -----
// (C) Christoph Koehn, Ute Ebert
// Centrum Wiskunde en Informatica
// P.O. Box 94079, NL-1090 GB, Amsterdam

#include <math.h>

using namespace std;

// Define functions for doubly differential
// cross section for Bremsstrahlung and
// pair production, also to be set in the
```

```

// beginning of the code

double brems(double E_kin, double omega, double Theta_i); // Doubly differential cross
// section for Bremsstrahlung
// which depends on
// the kinetic
// energy of the
// incident
// electron,
// frequency of the
// emitted photon
// and angle between
// both
// (in radian)

double pair_pr(double E_kin, double omega, double Theta-p); // Doubly differential
// cross section for
// pair
// production
// which
// depends
// on the
// kinetic
// energy of
// the
// generated
// positron,
// frequency
// of the
// incident
// photon
// and angle
// between
// both
// (in
// radian)

// -----

// functions for calculating doubly differential
// cross sections for Bremsstrahlung and pair
// production

// Bremsstrahlung
double brems(double E_kin, double omega, double Theta_i)
{
// define constants
int i;

//define constants
double hbar=1.054571726e-34; // Planck's constant
double SpeedOfLight=299792458.0; // Speed of light in
// vacuum
double SpeedOfLight2=299792458.0*299792458.0; // Speed of light in
// vacuum, squared
double electronMass=9.10938291e-31; // Mass of an
// electron
double electronCharge=1.602176565e-19; // Charge of an
// electron (without sign)
double rest_energy=electronMass*SpeedOfLight2; // Rest energy of
// the electron
double alpha_fine=7.2973525698e-3; // finestructure
// constant
double PI=3.14159265358979; // PI

// define physical quantities: energies and momenta

double E_i=E_kin+rest_energy; // total energy of incident electron
double E_f=E_i-hbar*omega; // total energy of outgoing electron
// momentum of incident electron
double p_i=sqrt(E_i*E_i*1/SpeedOfLight2-electronMass*electronMass*SpeedOfLight2);
// momentum of outgoing electron
double p_f=sqrt(E_f*E_f*1/SpeedOfLight2-electronMass*electronMass*SpeedOfLight2);

// define help functions
int Z=7; // atomic number, can be changed arbitrarily
// overall prefactor, defined in (11)
double A=Z*Z*pow(alpha_fine,3)/(4*PI*PI)*p_f/p_i*hbar*hbar/omega;
// overall prefactor for Theta_i=0
double B=Z*Z*pow(alpha_fine,3)/(2*PI)*p_f/p_i*hbar*hbar/omega;
// delta functions defined in (40) and (41)

```

```

double tri_1=-p_i*p_i-p_f*p_f-hbar*hbar*1/SpeedOfLight*omega*omega+2*hbar*1/SpeedOfLight*omega*p_i*cos(Theta_i);
double tri_2=-2*hbar*1/SpeedOfLight*omega*p_f+2*p_i*p_f*cos(Theta_i);

double I[8]={0}; // parts of the cross section
double cross=0; // total result of cross section

// all terms which are needed for the cross section
if (Theta_i!=0) // calculate cross section for all angles, except for 0 degree
{
I[0]=2*PI*A/sqrt(tri_2*tri_2+(2*p_i*p_f*sin(Theta_i))*(2*p_i*p_f*sin(Theta_i)))*log(((tri_2*tri_2+(2*p_i*p_f*sin(Theta_i))*(2*p_i*p_f*sin(Theta_i)))-
(tri_1+tri_2)*sqrt(tri_2*tri_2+(2*p_i*p_f*sin(Theta_i))*(2*p_i*p_f*sin(Theta_i)))+tri_1*tri_2)/(-tri_2*tri_2-(2*p_i*p_f*sin(Theta_i))*(2*p_i*p_f*sin(Theta_i)))-
(tri_1-tri_2)*sqrt(tri_2*tri_2+(2*p_i*p_f*sin(Theta_i))*(2*p_i*p_f*sin(Theta_i)))+tri_1*tri_2)/(1+SpeedOfLight*tri_2/(p_f*(E_i-p_i*SpeedOfLight*cos(Theta_i)))-
(p_i*SpeedOfLight*sin(Theta_i))*(p_i*SpeedOfLight*sin(Theta_i)))/((E_i-SpeedOfLight*p_i*cos(Theta_i))*(E_i-SpeedOfLight*p_i*cos(Theta_i)))-
2*hbar*hbar*omega*omega*p_f*tri_2/(SpeedOfLight*(E_i-SpeedOfLight*p_i*cos(Theta_i))*(tri_2*tri_2+(2*p_i*p_f*sin(Theta_i))*(2*p_i*p_f*sin(Theta_i)))));

I[1]=-2*PI*A*SpeedOfLight/(p_f*(E_i-SpeedOfLight*p_i*cos(Theta_i)))*log((E_f+SpeedOfLight*p_f)/(E_f-SpeedOfLight*p_f));

I[2]=2*PI*A/sqrt(((tri_2*E_f+tri_1*p_f*SpeedOfLight)*(tri_2*E_f+tri_1*p_f*SpeedOfLight)+(2*rest_energy*p_i*p_f*sin(Theta_i))*(2*rest_energy*p_i*p_f*sin(Theta_i)))*log(((E_f+p_f*SpeedOfLight)*((2*p_i*p_f*sin(Theta_i))*(2*p_i*p_f*sin(Theta_i)))+(E_f-p_f*SpeedOfLight)+(tri_1+tri_2)*((tri_2*E_f+tri_1*p_f*SpeedOfLight)-sqrt(((tri_2*E_f+tri_1*p_f*SpeedOfLight)*(tri_2*E_f+tri_1*p_f*SpeedOfLight)+(2*rest_energy*p_i*p_f*sin(Theta_i))*(2*rest_energy*p_i*p_f*sin(Theta_i)))))/((E_f-p_f*SpeedOfLight)*((2*p_i*p_f*sin(Theta_i))*(2*p_i*p_f*sin(Theta_i)))-
(E_f-p_f*SpeedOfLight)+(tri_1-tri_2)*((tri_2*E_f+tri_1*p_f*SpeedOfLight)-sqrt(((tri_2*E_f+tri_1*p_f*SpeedOfLight)*(tri_2*E_f+tri_1*p_f*SpeedOfLight)+(2*rest_energy*p_i*p_f*sin(Theta_i))*(2*rest_energy*p_i*p_f*sin(Theta_i)))))-
((tri_2*tri_2+(2*p_i*p_f*sin(Theta_i))*(2*p_i*p_f*sin(Theta_i)))*(pow(E_f,3)+E_f*p_f*p_f*SpeedOfLight)+p_f*SpeedOfLight*(2*(tri_1*tri_1-(2*p_i*p_f*sin(Theta_i))*(2*p_i*p_f*sin(Theta_i)))*E_f*p_f*SpeedOfLight+tri_1*tri_2*(3*E_f*E_f+p_f*p_f*SpeedOfLight2)))/((tri_2*E_f+tri_1*p_f*SpeedOfLight)*(tri_2*E_f+tri_1*p_f*SpeedOfLight)+(2*rest_energy*p_i*p_f*sin(Theta_i))*(2*rest_energy*p_i*p_f*sin(Theta_i)))/((E_i-SpeedOfLight*p_i*cos(Theta_i)))-
(4*E_i*E_i*p_f*p_f*(2*(tri_2*E_f+tri_1*p_f*SpeedOfLight)*(tri_2*E_f+tri_1*p_f*SpeedOfLight)-(2*electronMass*SpeedOfLight2*p_i*p_f*sin(Theta_i))*(2*electronMass*SpeedOfLight2*p_i*p_f*sin(Theta_i)))+(tri_1*E_f+tri_2*p_f*SpeedOfLight))/((tri_2*E_f+tri_1*p_f*SpeedOfLight)*(tri_2*E_f+tri_1*p_f*SpeedOfLight)+(2*rest_energy*p_i*p_f*sin(Theta_i))*(2*rest_energy*p_i*p_f*sin(Theta_i)))+(2*rest_energy*p_i*p_f*SpeedOfLight)+(2*rest_energy*p_i*p_f*sin(Theta_i)))+(8*(p_i*p_f*rest_energy*sin(Theta_i))*(p_i*p_f*rest_energy*sin(Theta_i))*(E_i*E_i+E_f*E_f)-2*(hbar*omega*p_i*sin(Theta_i))*(hbar*omega*p_i*sin(Theta_i))*p_f*SpeedOfLight*(tri_2*E_f+tri_1*p_f*SpeedOfLight)+2*hbar*hbar*omega*omega*p_f*electronMass*electronMass*pow(SpeedOfLight,3)*(tri_2*E_f+tri_1*p_f*SpeedOfLight))/((E_i-SpeedOfLight*p_i*cos(Theta_i)))*((tri_2*E_f+tri_1*p_f*SpeedOfLight)+(tri_2*E_f+tri_1*p_f*SpeedOfLight)+(2*rest_energy*p_i*p_f*sin(Theta_i))*(2*rest_energy*p_i*p_f*sin(Theta_i)))));

I[3]=-4*PI*A*p_f*SpeedOfLight*(tri_2*E_f+tri_1*p_f*SpeedOfLight)/((tri_2*E_f+tri_1*p_f*SpeedOfLight)*(tri_2*E_f+tri_1*p_f*SpeedOfLight)+4*(rest_energy*p_i*p_f*sin(Theta_i))*(rest_energy*p_i*p_f*sin(Theta_i)))-16*PI*E_i*E_i*p_f*p_f*(tri_2*E_f+tri_1*p_f*SpeedOfLight)*(tri_2*E_f+tri_1*p_f*SpeedOfLight)/(((tri_2*E_f+tri_1*p_f*SpeedOfLight)*(tri_2*E_f+tri_1*p_f*SpeedOfLight)+4*(rest_energy*p_i*p_f*sin(Theta_i))*(rest_energy*p_i*p_f*sin(Theta_i)))*((tri_2*E_f+tri_1*p_f*SpeedOfLight)*(tri_2*E_f+tri_1*p_f*SpeedOfLight)+4*(rest_energy*p_i*p_f*sin(Theta_i))*(rest_energy*p_i*p_f*sin(Theta_i)))));

I[4]=4*PI*A/((-tri_2*tri_2+tri_1*tri_1-(2*p_i*p_f*sin(Theta_i))*(2*p_i*p_f*sin(Theta_i)))*((tri_2*E_f+tri_1*p_f*SpeedOfLight)*(tri_2*E_f+tri_1*p_f*SpeedOfLight)+(2*rest_energy*p_i*p_f*sin(Theta_i))*(2*rest_energy*p_i*p_f*sin(Theta_i))))*(hbar*hbar*omega*omega*p_f*p_f/(E_i-SpeedOfLight*p_i*cos(Theta_i)))*(E_f*(2*tri_2*tri_2*(tri_2*tri_2-tri_1*tri_1)+8*(p_i*p_f*sin(Theta_i))*(p_i*p_f*sin(Theta_i)))+(tri_2*tri_2+tri_1*tri_1)+p_f*SpeedOfLight*(2*tri_1*tri_2*(tri_2*tri_2-tri_1*tri_1)+tri_1*tri_2*(4*p_i*p_f*sin(Theta_i))*(4*p_i*p_f*sin(Theta_i)))/((tri_2*tri_2+(2*p_i*p_f*sin(Theta_i))*(2*p_i*p_f*sin(Theta_i)))+2*(hbar*omega*p_i*sin(Theta_i))*(hbar*omega*p_i*sin(Theta_i)))+(2*tri_1*tri_2*p_f*SpeedOfLight+2*tri_2*tri_2*E_f+8*(p_i*p_f*sin(Theta_i))*(p_i*p_f*sin(Theta_i)))*E_f)/(E_i-p_i*SpeedOfLight*cos(Theta_i))+2*E_i*E_i*p_f*p_f*(2*(tri_2*tri_2-tri_1*tri_1)*(tri_2*E_f+tri_1*p_f*SpeedOfLight)*(tri_2*E_f+tri_1*p_f*SpeedOfLight)+8*(p_i*p_f*sin(Theta_i))*(p_i*p_f*sin(Theta_i)))*((tri_1*tri_1+tri_2*tri_2)*(E_f*E_f+p_f*p_f*SpeedOfLight2)+4*tri_1*tri_2*E_f*p_f*SpeedOfLight)/((tri_2*E_f+tri_1*p_f*SpeedOfLight)*(tri_2*E_f+tri_1*p_f*SpeedOfLight)+(2*rest_energy*p_i*p_f*sin(Theta_i))*(2*rest_energy*p_i*p_f*sin(Theta_i)))+8*(p_i*p_f*sin(Theta_i))*(p_i*p_f*sin(Theta_i))*(E_i*E_i+E_f*E_f)*(tri_2*p_f*SpeedOfLight+tri_1*E_f)/(E_i-SpeedOfLight*p_i*cos(Theta_i)));

I[5]=16*PI*E_f*E_f*p_i*p_i*sin(Theta_i)*sin(Theta_i)*A/((E_i-SpeedOfLight*p_i*cos(Theta_i))*(E_i-SpeedOfLight*p_i*cos(Theta_i)))-
(tri_2*tri_2+tri_1*tri_1-4*p_i*p_i*p_f*p_f*sin(Theta_i))*sin(Theta_i));
}
else // calculate cross section for 0 degree
{
I[0]=-2*B*p_f*SpeedOfLight/(tri_2*E_f+tri_1*p_f*SpeedOfLight);

I[1]=B*p_f*p_f*SpeedOfLight2*(-tri_1*tri_1+tri_2*tri_2)/(tri_2*(tri_2*E_f+tri_1*p_f*SpeedOfLight)*(tri_2*E_f+tri_1*p_f*SpeedOfLight))*log(((tri_1+tri_2)/(tri_1-tri_2)));
}

```

```

I[2]=B*(2* tri_1 *E_f*p_f*SpeedOfLight+tri_2*(E_f*E_f+p_f*p_f*SpeedOfLight2))/(( tri_2*E_f+tri_1*p_f*
SpeedOfLight)*( tri_2*E_f+tri_1*p_f*SpeedOfLight))*log((E_f+p_f*SpeedOfLight)/(E_f-p_f*SpeedOfLight
));
I[3]=-B*(4*E_i*p_f)*(4*E_i*p_f)/(( tri_2*E_f+tri_1*p_f*SpeedOfLight)*( tri_2*E_f+tri_1*p_f*SpeedOfLight))
;
I[4]=-8*B*E_i*E_i*p_f*p_f*( tri_1*E_f+tri_2*p_f*SpeedOfLight)/(pow( tri_2*E_f+tri_1*p_f*SpeedOfLight ,3))*
log((( tri_1-tri_2)*(E_f-p_f*SpeedOfLight))/(( tri_1+tri_2)*(E_f+p_f*SpeedOfLight)));
I[5]=-B*4*hbar*hbar*p_f*p_f*omega*omega/(( tri_2*E_f+tri_1*p_f*SpeedOfLight)*(E_i-p_i*SpeedOfLight)*
tri_2);
I[6]=2*B*hbar*hbar*p_f*p_f*omega*omega*(2* tri_1* tri_2*E_f+p_f*SpeedOfLight*( tri_1* tri_1+tri_2* tri_2))
/(( tri_2*E_f+tri_1*p_f*SpeedOfLight)*( tri_2*E_f+tri_1*p_f*SpeedOfLight)*(E_i-p_i*SpeedOfLight)*
tri_2* tri_2)*log(( tri_1+tri_2)/( tri_1-tri_2));
I[7]=2*B*hbar*hbar*omega*omega*p_f*(E_f*E_f-p_f*p_f*SpeedOfLight2)/(( tri_2*E_f+tri_1*p_f*SpeedOfLight)
*( tri_2*E_f+tri_1*p_f*SpeedOfLight)*(E_i-SpeedOfLight*p_i)*SpeedOfLight)*log((E_f-p_f*SpeedOfLight
)/(E_f+p_f*SpeedOfLight));
}
// sum up all terms to get value for cross section
for (i=0;i<=7;i++)
{
    cross=cross+I[i];
}

return cross;
// give back result of cross section calculation
}

// pair production
double pair_pr(double E_kin,double omega,double Theta_p)
{
    int i;

    //define constants
    double hbar=1.054571726e-34; // Planck's constant
    double SpeedOfLight=299792458.0; // Speed of light in
    // vacuum
    double SpeedOfLight2=299792458.0*299792458.0; // Speed of light in
    // vacuum, squared
    double electronMass=9.10938291e-31; // Mass of an
    // electron
    double electronCharge=1.602176565e-19; // Charge of an
    // electron (without sign)
    double rest_energy=electronMass*SpeedOfLight2; // Rest energy of
    // the electron
    double alpha_fine=7.2973525698e-3; // finestructure
    // constant
    double PI=3.14159265358979; // PI

    // define physical quantities: energies and momenta
    double E_p=E_kin+rest_energy; // total energy of created positron
    double E_m=(hbar*omega-rest_energy)-E_kin; // total energy of created electron
    // momentum of created positron
    double p_p=sqrt(E_p*E_p*1/SpeedOfLight2-electronMass*electronMass*SpeedOfLight2);
    // momentum of created electron
    double p_m=sqrt(E_m*E_m*1/SpeedOfLight2-electronMass*electronMass*SpeedOfLight2);

    // define help functions
    int Z=7; // atomic number, can be changed arbitrarily
    // overall prefactor, defined in (96)
    double A=Z*Z*pow(alpha_fine ,3)*SpeedOfLight2*p_p*p_m/(4*PI*PI*hbar*pow(omega ,3));
    // overall prefactor for Theta_p=0 and Theta_p=180 degree
    double B=Z*Z*pow(alpha_fine ,3)*SpeedOfLight2*p_p*p_m/(2*PI*hbar*pow(omega ,3));

    // delta functions defined in (40) and (41)
    double tri_1=-p_p*p_p-p_m*p_m-hbar*hbar*1/SpeedOfLight2*omega*omega+2*hbar*1/SpeedOfLight*omega*p_p*
cos(Theta_p);
    double tri_2=2*hbar*1/SpeedOfLight*omega*p_m-2*p_p*p_m*cos(Theta_p);

    double I[8]={0}; // parts of the cross section
    double cross=0; // total result of cross section

    // all terms which are needed for the cross section
    if (Theta_p!=0 && Theta_p!=PI) // calculate cross section for all angles, except for 0 and 180
        degree
    {

```

```

I[0]=2*PI*A/sqrt((tri_2*tri_2+(2*p-p*p*m*sin(Theta_p))*(2*p-p*p*m*sin(Theta_p))))*log(((tri_2*tri_2+(2*p-p
*p*m*sin(Theta_p))*(2*p-p*p*m*sin(Theta_p))-(tri_1+tri_2)*sqrt((tri_2*tri_2+(2*p-p*p*m*sin(Theta_p))
)*(2*p-p*p*m*sin(Theta_p))))+tri_1*tri_2)/(-tri_2*tri_2-(2*p-p*p*m*sin(Theta_p))*(2*p-p*p*m*sin(
Theta_p))-(tri_1-tri_2)*sqrt((tri_2*tri_2+(2*p-p*p*m*sin(Theta_p))*(2*p-p*p*m*sin(Theta_p))))+tri_1*
tri_2))*(-1-SpeedOfLight*tri_2/(p*m*(E_p-p*p*SpeedOfLight*cos(Theta_p)))+(p*p*SpeedOfLight*sin(
Theta_p))*(p*p*SpeedOfLight*sin(Theta_p))/((E_p-SpeedOfLight*p*p*cos(Theta_p))*(E_p-SpeedOfLight*
p*p*cos(Theta_p))-2*hbar*hbar*omega*omega*p*m*tri_2/(SpeedOfLight*(E_p-SpeedOfLight*p*p*cos(
Theta_p)))*(tri_2*tri_2+(2*p-p*p*m*sin(Theta_p)))*(2*p-p*p*m*sin(Theta_p)))));

I[1]=2*PI*A*SpeedOfLight/(p*m*(E_p-SpeedOfLight*p*p*cos(Theta_p)))*log((E_m+SpeedOfLight*p*m)/(E_m-
SpeedOfLight*p*m));

I[2]=2*PI*A/sqrt(((tri_2*E_m+tri_1*p*m*SpeedOfLight)*(tri_2*E_m+tri_1*p*m*SpeedOfLight)+(2*rest_energy*
p-p*p*m*sin(Theta_p))*(2*rest_energy*p-p*p*m*sin(Theta_p)))*log(((E_m+p*m*SpeedOfLight)*((2*p-p
*p*m*sin(Theta_p))*(2*p-p*p*m*sin(Theta_p)))*(E_m-p*m*SpeedOfLight)+(tri_1+tri_2)*((tri_2*E_m+tri_1*
p*m*SpeedOfLight)-sqrt((tri_2*E_m+tri_1*p*m*SpeedOfLight)*(tri_2*E_m+tri_1*p*m*SpeedOfLight)+(2*
rest_energy*p-p*p*m*sin(Theta_p))*(2*rest_energy*p-p*p*m*sin(Theta_p)))))/((E_m-p*m*SpeedOfLight)
*((2*p-p*p*m*sin(Theta_p))*(2*p-p*p*m*sin(Theta_p))*(-E_m-p*m*SpeedOfLight)+(tri_1-tri_2)*((tri_2*
E_m+tri_1*p*m*SpeedOfLight)-sqrt((tri_2*E_m+tri_1*p*m*SpeedOfLight)*(tri_2*E_m+tri_1*p*m*
SpeedOfLight)+(2*rest_energy*p-p*p*m*sin(Theta_p))*(2*rest_energy*p-p*p*m*sin(Theta_p)))))))*(((
tri_2*tri_2+(2*p-p*p*m*sin(Theta_p))*(2*p-p*p*m*sin(Theta_p)))*(pow(E_m,3)+E_m*p*p*m*
SpeedOfLight2)+p*m*SpeedOfLight*(2*(tri_1*tri_1-(2*p-p*p*m*sin(Theta_p))*(2*p-p*p*m*sin(Theta_p))
)*E_m*p*m*SpeedOfLight+tri_1*tri_2*(3*E_m*E_m+p*m*p*m*SpeedOfLight2)))/((tri_2*E_m+tri_1*p*m*
SpeedOfLight)*(tri_2*E_m+tri_1*p*m*SpeedOfLight)+(2*rest_energy*p-p*p*m*sin(Theta_p)))*(2*
rest_energy*p-p*p*m*sin(Theta_p))+SpeedOfLight*(tri_2*E_m+tri_1*p*m*SpeedOfLight)/(p*m*(E_p-
SpeedOfLight*p*p*cos(Theta_p)))+(4*E_p*E_p*p*p*m*(2*(tri_2*E_m+tri_1*p*m*SpeedOfLight)*(tri_2*
E_m+tri_1*p*m*SpeedOfLight)-(2*electronMass*SpeedOfLight2*p-p*p*m*sin(Theta_p))*(2*electronMass*
SpeedOfLight2*p-p*p*m*sin(Theta_p)))*(tri_1*E_m+tri_2*p*m*SpeedOfLight))/(((tri_2*E_m+tri_1*p*m*
SpeedOfLight)*(tri_2*E_m+tri_1*p*m*SpeedOfLight)+(2*rest_energy*p-p*p*m*sin(Theta_p)))*(2*
rest_energy*p-p*p*m*sin(Theta_p)))*((tri_2*E_m+tri_1*p*m*SpeedOfLight)*(tri_2*E_m+tri_1*p*m*
SpeedOfLight)+(2*rest_energy*p-p*p*m*sin(Theta_p))*(2*rest_energy*p-p*p*m*sin(Theta_p)))+(8*(p-p
*p*m*rest_energy*sin(Theta_p))*(p-p*p*m*rest_energy*sin(Theta_p))*(E_p*E_p+E_m*E_m)-2*(hbar*omega*
p-p*p*sin(Theta_p))*(hbar*omega*p-p*p*sin(Theta_p))*p*m*SpeedOfLight*(tri_2*E_m+tri_1*p*m*SpeedOfLight
)+2*hbar*hbar*omega*omega*p*m*electronMass*electronMass*pow(SpeedOfLight,3)*(tri_2*E_m+tri_1*p*m*
SpeedOfLight))/((E_p-SpeedOfLight*p*p*cos(Theta_p))*((tri_2*E_m+tri_1*p*m*SpeedOfLight)*(tri_2*E_m
+tri_1*p*m*SpeedOfLight)+(2*rest_energy*p-p*p*m*sin(Theta_p))*(2*rest_energy*p-p*p*m*sin(Theta_p)
)))));

I[3]=4*PI*A*p*m*SpeedOfLight*(tri_2*E_m+tri_1*p*m*SpeedOfLight)/(((tri_2*E_m+tri_1*p*m*SpeedOfLight)*(
tri_2*E_m+tri_1*p*m*SpeedOfLight)+4*(rest_energy*p-p*p*m*sin(Theta_p))*(rest_energy*p-p*p*m*sin(
Theta_p))+16*PI*E_p*E_p*p*p*m*A*(tri_2*E_m+tri_1*p*m*SpeedOfLight)*(tri_2*E_m+tri_1*p*m*
SpeedOfLight)/(((tri_2*E_m+tri_1*p*m*SpeedOfLight)*(tri_2*E_m+tri_1*p*m*SpeedOfLight)+(2*
rest_energy*p-p*p*m*sin(Theta_p))*(2*rest_energy*p-p*p*m*sin(Theta_p)))*((tri_2*E_m+tri_1*p*m*
SpeedOfLight)*(tri_2*E_m+tri_1*p*m*SpeedOfLight)+(2*rest_energy*p-p*p*m*sin(Theta_p))*(2*
rest_energy*p-p*p*m*sin(Theta_p)))));

I[4]=4*PI*A/((-tri_2*tri_2+tri_1*tri_1-(2*p-p*p*m*sin(Theta_p))*(2*p-p*p*m*sin(Theta_p)))*((tri_2*E_m+
tri_1*p*m*SpeedOfLight)*(tri_2*E_m+tri_1*p*m*SpeedOfLight)+(2*rest_energy*p-p*p*m*sin(Theta_p))
*(2*rest_energy*p-p*p*m*sin(Theta_p)))*((hbar*omega*p*m)*(hbar*omega*p*m)/(E_p-SpeedOfLight*p*p*
cos(Theta_p)))*(E_m*(2*tri_2*tri_2*(tri_2*tri_2-tri_1*tri_1)+8*(p-p*p*m*sin(Theta_p))*(p-p*p*m*sin(
Theta_p)))*(tri_2*tri_2+tri_1*tri_1))+p*m*SpeedOfLight*(2*tri_1*tri_2*(tri_2*tri_2-tri_1*tri_1)+
tri_1*tri_2*(4*p-p*p*m*sin(Theta_p))*(4*p-p*p*m*sin(Theta_p)))/((tri_2*tri_2+(2*p-p*p*m*sin(
Theta_p))*(2*p-p*p*m*sin(Theta_p)))+2*(hbar*omega*p-p*p*sin(Theta_p))*(hbar*omega*p-p*p*sin(Theta_p))
*(2*tri_1*tri_2*p*m*SpeedOfLight+2*tri_2*tri_2*E_m+8*(p-p*p*m*sin(Theta_p))*(p-p*p*m*sin(Theta_p))
)*E_m)/(E_p-p*p*SpeedOfLight*cos(Theta_p))-2*E_p*E_p*p*p*m*(2*(tri_2*tri_2-tri_1*tri_1)*(tri_2*
E_m+tri_1*p*m*SpeedOfLight)*(tri_2*E_m+tri_1*p*m*SpeedOfLight)+8*(p-p*p*m*sin(Theta_p))*(p-p*p*m*
sin(Theta_p))*((tri_1*tri_1+tri_2*tri_2)*(E_m*E_m+p*m*p*m*SpeedOfLight2)+4*tri_1*tri_2*E_m*p*m*
SpeedOfLight))/((tri_2*E_m+tri_1*p*m*SpeedOfLight)*(tri_2*E_m+tri_1*p*m*SpeedOfLight)+(2*
rest_energy*p-p*p*m*sin(Theta_p))*(2*rest_energy*p-p*p*m*sin(Theta_p)))-8*(p-p*p*m*sin(Theta_p))*(
p-p*p*m*sin(Theta_p))*(E_p*E_p+E_m*E_m)*(tri_2*p*m*SpeedOfLight+tri_1*E_m)/(E_p-SpeedOfLight*p-p*
cos(Theta_p)));

I[5]=-16*PI*E_m*E_m*p-p*p*p*sin(Theta_p)*sin(Theta_p)*A/((E_p-SpeedOfLight*p-p*cos(Theta_p))*(E_p-
SpeedOfLight*p-p*cos(Theta_p))*(-tri_2*tri_2+tri_1*tri_1-4*p-p*p*p-p*p*m*sin(Theta_p))*sin(
Theta_p));
}
else
{
if(Theta_p!=PI) // calculate cross section for 0 degree
{
I[0]=2*B*p*m*SpeedOfLight/(tri_2*E_m+tri_1*p*m*SpeedOfLight);

I[1]=-B*p*m*SpeedOfLight2*(-tri_1*tri_1+tri_2*tri_2)/((tri_2*(tri_2*E_m+tri_1*p*m*SpeedOfLight)*(tri_2*
E_m+tri_1*p*m*SpeedOfLight))*log((tri_1+tri_2)/(tri_1-tri_2));

I[2]=-B*(2*tri_1*E_m*p*m*SpeedOfLight+tri_2*(E_m*E_m+p*m*p*m*SpeedOfLight2))/((tri_2*E_m+tri_1*p*m*
SpeedOfLight)*(tri_2*E_m+tri_1*p*m*SpeedOfLight))*log((E_m+p*m*SpeedOfLight)/(E_m-p*m*SpeedOfLight
));

I[3]=B*(4*E_p*p*m)*(4*E_p*p*m)/((tri_2*E_m+tri_1*p*m*SpeedOfLight)*(tri_2*E_m+tri_1*p*m*SpeedOfLight));

I[4]=8*B*E_p*E_p*p*p*m*(tri_1*E_m+tri_2*p*m*SpeedOfLight)/(pow(tri_2*E_m+tri_1*p*m*SpeedOfLight,3))*
log(((tri_1-tri_2)*(E_m-p*m*SpeedOfLight))/((tri_1+tri_2)*(E_m+p*m*SpeedOfLight)));
}
}

```

```

I[5]=-B*4*hbar*hbar*p_m*p_m*omega*omega/((tri_2*E_m+tri_1*p_m*SpeedOfLight)*(E_p-p_p*SpeedOfLight)*
tri_2);
I[6]=2*B*hbar*hbar*p_m*p_m*omega*omega*(2*tri_1*tri_2*E_m+p_m*SpeedOfLight*(tri_1*tri_1+tri_2*tri_2))
/((tri_2*E_m+tri_1*p_m*SpeedOfLight)*(tri_2*E_m+tri_1*p_m*SpeedOfLight)*(E_p-p_p*SpeedOfLight)*
tri_2*tri_2)*log((tri_1+tri_2)/(tri_1-tri_2));
I[7]=2*B*hbar*hbar*omega*omega*p_m*(E_m*E_m-p_m*p_m*SpeedOfLight^2)/((tri_2*E_m+tri_1*p_m*SpeedOfLight)
*(tri_2*E_m+tri_1*p_m*SpeedOfLight)*(E_p-SpeedOfLight*p_p)*SpeedOfLight)*log((E_m-p_m*SpeedOfLight
)/(E_m+p_m*SpeedOfLight));
}
else // calculate cross section for 180 degree
{
I[0]=2*B*p_m*SpeedOfLight/(tri_2*E_m+tri_1*p_m*SpeedOfLight);
I[1]=-B*p_m*p_m*SpeedOfLight^2*(-tri_1*tri_1+tri_2*tri_2)/(tri_2*(tri_2*E_m+tri_1*p_m*SpeedOfLight)*(
tri_2*E_m+tri_1*p_m*SpeedOfLight))*log((tri_1+tri_2)/(tri_1-tri_2));
I[2]=-B*(2*tri_1*E_m*p_m*SpeedOfLight+tri_2*(E_m*E_m+p_m*p_m*SpeedOfLight^2))/((tri_2*E_m+tri_1*p_m*
SpeedOfLight)*(tri_2*E_m+tri_1*p_m*SpeedOfLight))*log((E_m+p_m*SpeedOfLight)/(E_m-p_m*SpeedOfLight
));
I[3]=B*(4*E_p*p_m)*(4*E_p*p_m)/((tri_2*E_m+tri_1*p_m*SpeedOfLight)*(tri_2*E_m+tri_1*p_m*SpeedOfLight));
I[4]=8*B*E_p*p_m*E_p*p_m*(tri_1*E_m+tri_2*p_m*SpeedOfLight)/(pow(tri_2*E_m+tri_1*p_m*SpeedOfLight,3))*
log(((tri_1-tri_2)*(E_m-p_m*SpeedOfLight))/((tri_1+tri_2)*(E_m+p_m*SpeedOfLight)));
I[5]=-B*4*hbar*hbar*p_m*p_m*omega*omega/((tri_2*E_m+tri_1*p_m*SpeedOfLight)*(E_p+p_p*SpeedOfLight)*
tri_2);
I[6]=2*B*hbar*hbar*p_m*p_m*omega*omega*(2*tri_1*tri_2*E_m+p_m*SpeedOfLight*(tri_1*tri_1+tri_2*tri_2))
/((tri_2*E_m+tri_1*p_m*SpeedOfLight)*(tri_2*E_m+tri_1*p_m*SpeedOfLight)*(E_p+p_p*SpeedOfLight)*
tri_2*tri_2)*log((tri_1+tri_2)/(tri_1-tri_2));
I[7]=2*B*hbar*hbar*omega*omega*p_m*(E_m*E_m-p_m*p_m*SpeedOfLight^2)/((tri_2*E_m+tri_1*p_m*SpeedOfLight)
*(tri_2*E_m+tri_1*p_m*SpeedOfLight)*(E_p+SpeedOfLight*p_p)*SpeedOfLight)*log((E_m-p_m*SpeedOfLight
)/(E_m+p_m*SpeedOfLight));
}
}

// sum up all terms to get value for cross section
for (i=0;i<=7;i++)
{
cross=cross+I[i];
}

return cross; // give back result of cross section calculation
}

```


The importance of electron-electron Bremsstrahlung for terrestrial gamma-ray flashes, electron beams and electron-positron beams

Thunderstorms emit terrestrial gamma-ray flashes with photon energies of up to tens of MeV and electron-positron beams that are created by photons with energies above 1.022 MeV. These photons are produced through the Bremsstrahlung process when energetic electrons collide with air molecules. However, presently used cross sections for Bremsstrahlung treat only the interaction of the electrons with the nuclei of molecules while we here include their interaction with shell electrons. We simulate the production of energetic photons by a negative stepped lightning leader, and we find that electron-electron Bremsstrahlung contributes significantly, although the direct photon emission is less than from electron-nucleus Bremsstrahlung. However, electron-electron Bremsstrahlung also ejects shell electrons and therefore feeds the electron population above 1 MeV significantly. We find that it hence dominates the photon spectrum of the stepped lightning leader at 10 MeV.

This chapter has been published as [C. Köhn, U. Ebert and A. Mangiarotti, 2014. J. Phys. D: Appl. Phys. as Fast Track Communication, **47**, 252001]

3.1 Introduction

3.1.1 Energetic radiation from thunderstorms and laboratory discharges

Terrestrial gamma-ray flashes during thunderstorms were first observed by Fishman et al. [54]. Meanwhile TGFs were also measured by the Reuven Ramaty High Energy Solar Spectroscopic Imager (RHESSI) [35, 149, 150], by the Fermi Gamma-ray Space Telescope [17] and by the Gamma-Ray Observation of Winter Thunderclouds (GROWTH) [162]. The Astrorivelatore Gamma a Immagini Leggero (AGILE) has measured quantum energies of up to 100 MeV [112, 155]. Hard radiation was also observed from lightning leaders approaching the ground [115, 40] and in many discharge experiments performed in the laboratory under controlled conditions [44, 121, 134, 111, 143, 88] where high-energy photons were created in the streamer-leader stage. It was soon understood that these flashes of energetic photons are Bremsstrahlung photons emitted when fast electrons are scattered at air molecules [54, 158].

Next to gamma-rays, also flashes of electrons were found to be emitted by thunderstorms [44]; they are distinguished from photons by their dispersion relation, i.e. how they move in given media, and by their location since electrons as charged particles follow the geomagnetic field lines sufficiently far outside the atmosphere.

Briggs et al. detected beams of positrons and electrons with the FERMI satellite over Egypt during a thunderstorm over Zambia [18]. Photons with an energy above 1 MeV can produce pairs of electrons and positrons when scattering on the air molecules. Since positrons are charged, they will follow the geomagnetic field lines in the same manner as electrons and were thus guided from Zambia to the satellite over Egypt.

3.1.2 Energetic electrons from discharges and the previously used Bremsstrahlung cross sections

The energetic photons are created through the Bremsstrahlung process of energetic electrons. For the generation of energetic electrons, there are two mechanisms under debate: the older model of relativistic run-away electron avalanche in a rather homogeneous electric field inside the cloud [165, 67, 37, 42, 114], and the acceleration of electrons in the highly enhanced field at the tip of a streamer or leader [117, 101, 24, 26].

For both types of models, appropriate Bremsstrahlung cross sections are required to derive the photon spectrum from the electron energies. So far, geophysical researchers have used cross sections for the scattering of electrons at the nuclei of molecules. It is known [90] that the Bethe-Heitler theory for Bremsstrahlung [12, 75] covers the energy range between 1 keV and 1 GeV for the small atomic numbers of air and for $Z < 29$ the Bethe-Heitler theory agrees well with experimental data for the relevant energies for air molecules ($Z = 7$ for nitrogen and $Z = 8$ for oxygen) [140]. Koch and Motz [87] as

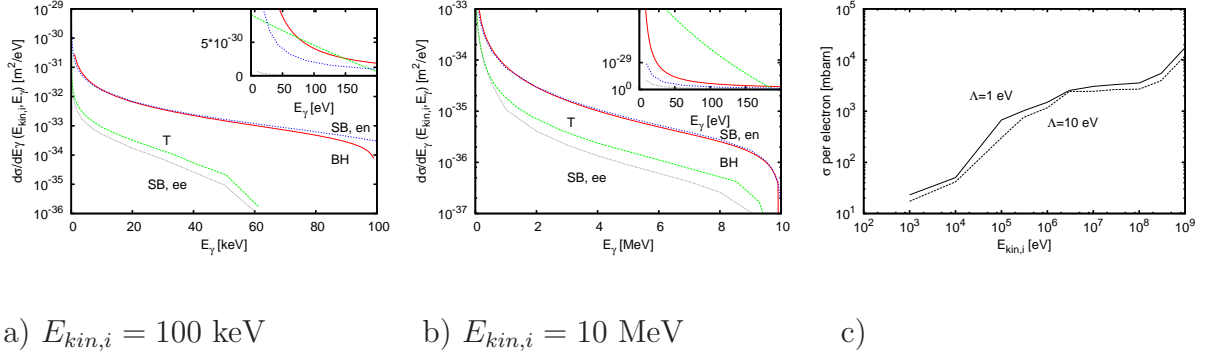
well as Seltzer and Berger [138] give very detailed overviews over different cross sections. They confirm that the Bethe Heitler cross section is valid for the electron scattering at light nuclei and energies between 1 keV and 1 GeV. The tabulations by Seltzer and Berger [138, 139] are considered a standard reference in the field. They cover electron energies from 1 keV to 10 GeV and they include both electron-nucleus and electron-electron Bremsstrahlung; however, only the cross section singly differential in the photon energy is reported. In turn, the tabulations by Seltzer and Berger are based, for energies below or equal to 2 MeV and for the electron-nucleus Bremsstrahlung, on fully numerical calculations by Pratt and Tseng [132, 133]. The latter are commonly considered the best available theoretical values because they employ a partial wave expansion with a self consistent procedure to describe the wavefunctions of the atomic electrons [161]. The number of partial waves necessary to accurately determine the cross section increases with energy and for this reason their tabulations stop at 2 MeV, moreover they cover only the cross section singly differential in photon energy. A detailed overview over the history of Bremsstrahlung cross sections is given in chapter 2. We conclude that for the parameter range considered here, Bethe-Heitler is the most accurate theory available.

Up to now researchers have been using different sets of cross sections for the production of TGFs by electron-nucleus Bremsstrahlung. Carlson et al. [24] used the Geant 4 package with intrinsic cross sections for high atomic numbers like $Z = 82$ (lead) [2]; however, we have shown in chapter 2, that the cross sections in Geant 4 are not appropriate for energies below 1 MeV and for the small atomic numbers of air molecules. Xu et al. [169] used a doubly differential cross section resolving the photon energy and the scattering angle of the emitted photon. They use the product ansatz introduced by Lehtinen [98] where the photon energy part is based on the Bethe-Heitler theory and the angular part is a non-quantum-mechanical relativistic expression by Jackson [81]. However, this ansatz is only valid for small ratios between the energy of the emitted photon and the incident electron [90]. Dwyer [42] uses the triply differential cross section by Bethe and Heitler which resolves the full geometry of the Bremsstrahlung process together with the dependence on the photon energy, including an atomic form factor. In chapter 2 we derived a doubly differential cross section based on the Bethe-Heitler theory which relates the angle between incident electron and emitted photon to the energy of the photon.

3.2 Electron-nucleus versus electron-electron Bremsstrahlung

3.2.1 Overview of mechanisms

All the cross sections discussed above are for electron-nucleus Bremsstrahlung, i.e., they parameterize the emission of photons when electrons scatter on the nuclei of atoms or molecules. However, electrons can also scatter on the shell electrons of an atom or



a) $E_{kin,i} = 100 \text{ keV}$ b) $E_{kin,i} = 10 \text{ MeV}$ c)

Figure 3.1: The differential cross section $d\sigma/dE_\gamma$ for photon emission as a function of the photon energy E_γ for nitrogen ($Z = 7$). The kinetic energy $E_{kin,i}$ of the incident electron is a) 100 keV and b) 10 MeV. The insets zoom into the energy region with $0 \leq E_\gamma \leq 200 \text{ eV}$; the y axis of the insets is linear. The grey [138, 139] and green [157] line show cross sections for electron-electron Bremsstrahlung. The red [12] and blue [138, 139] line show cross sections for electron-nucleus Bremsstrahlung. SB denotes values by Seltzer and Berger [138, 139] for electron-nucleus (en) and electron-electron (ee) Bremsstrahlung; BH denotes results by Bethe and Heitler [12, 75] and T by Tessier and Kawrakow [157]. c) The total electron-electron Bremsstrahlung cross section σ per electron as a function of the energy $E_{kin,i}$ of the incident electron for the cutoffs of the photon energy at $\Lambda = 1 \text{ eV}$ and $\Lambda = 10 \text{ eV}$.

molecule. Since electron-nucleus Bremsstrahlung is proportional to Z^2 where Z is the atomic number, and electron-electron Bremsstrahlung is proportional to the number of shell electrons and hence to Z , electron-nucleus Bremsstrahlung is more dominant for heavy elements than for light elements.

Electron-electron Bremsstrahlung was first investigated thoroughly by Haug [72] and has been reviewed by Haug and Nakel [74]. These works treat electron-electron Bremsstrahlung only between free electrons. For Bremsstrahlung from shell electrons, the electron binding to the nucleus has to be included. Seltzer and Berger [138] and the ICRU [79] developed approximate expressions for Bremsstrahlung from bound electrons: the ICRU [79] only for incident electrons with kinetic energy larger than 50 MeV, Seltzer and Berger [138] for energies between 1 keV and 10 GeV and $Z = 1$ to 100. Tessier and Kawrakow [157] extending the work by Haug and Nakel [74] calculated electron-electron Bremsstrahlung cross sections for elements with $Z = 1$ to 100 for incident electron energies between 1 keV and 1 GeV, taking into account that the shell electron is initially bound and ejected during the scattering process. Thus the electron-electron Bremsstrahlung process is a source of photons as well as of free electrons.

3.2.2 Comparison of processes

In this paper we use the cross sections by Bethe and Heitler [12] for electron-nucleus Bremsstrahlung and the cross sections by Haug and Nakel [74] and by Tessier and Kawrakow [157] which are based on previous work by Haug, for electron-electron Bremsstrahlung to investigate their role in the production of terrestrial gamma-ray flashes in air.

In Figure 3.1, we compare these two processes in terms of the differential cross section $d\sigma(E_{kin,i}, E_\gamma)/dE_\gamma$ which is proportional to the probability that an electron with energy $E_{kin,i}$ produces a photon with an energy in the interval $[E_\gamma, E_\gamma + dE_\gamma]$ when colliding with a nitrogen nucleus or its seven electrons. Panel a) shows the cross sections for an incident electron energy of 100 keV, panel b) for 10 MeV. For electron-nucleus Bremsstrahlung we plot the results by Bethe and Heitler (BH) [12] and Seltzer and Berger (SB,en) [138, 139]. They agree well. For electron-electron Bremsstrahlung we plot calculations by Seltzer and Berger (SB,ee) [138, 139] and Tessier and Kawrakow (T) [157]. Note that the differential cross section for both types of Bremsstrahlung decrease rapidly as a function of the photon energy. The figures show that the cross sections for electron-electron Bremsstrahlung are much smaller than for electron-nucleus Bremsstrahlung for photon energies above 200 eV. For electron-electron Bremsstrahlung, both models have the same order of magnitude. Moreover the calculations by Tessier and Kawrakow [157] show a different behaviour for small photon energies. Especially for $E_{kin,i} = 10$ MeV the differential cross section for electron-electron Bremsstrahlung according to Tessier and Kawrakow [157] becomes more important than the one for electron-nucleus Bremsstrahlung for $0 \leq E_\gamma \leq 200$ eV; this is the energy region where the differential cross section contributes most to the total cross section.

The total cross section σ given by the integral of the differential cross section $d\sigma/dE_\gamma$ over the photon energy E_γ depends on the lower limit, the cutoff Λ . In quantum electrodynamics there is an infra-red divergence in the cross section of a certain process radiating a photon whenever the same final state without that photon can be produced by another process. In the case of electron-nucleus and electron-electron Bremsstrahlung, the same final state without the generation of the photon is the result of elastic electron-nucleus or elastic electron-electron (Møller) scattering, respectively. The Bremsstrahlung cross section will diverge if the lowest allowed energy Λ of the emitted photon goes to zero; therefore the cross sections are not valid for very small Λ . In our simulations we have chosen $\Lambda = 1$ eV. Figure 3.1 c) shows the total cross section for cutoffs $\Lambda = 1$ eV and $\Lambda = 10$ eV for electron-electron Bremsstrahlung. It demonstrates that the total cross section does not change significantly if a higher cutoff is chosen; thus our results do not depend on the choice of Λ severely.

An important fact is that the electron-electron Bremsstrahlung process does not only emit Bremsstrahlung photons, but also ejects shell electrons. The electron-electron Bremsstrahlung cross sections by Tessier and Kawrakow [157] and subsequently by Haug [73] show that during the emission of low-energy photons the residual energy is distributed

more evenly between scattered and ejected electron than for the electron impact ionization cross sections by Kim et al. [84] commonly used in discharge physics [25].

3.3 Electron and photon spectra for a stepped lightning leader

3.3.1 Set-up of model and its validation

To test the influence of electron-electron Bremsstrahlung we simulate the acceleration of electrons in air consisting of 78.12% N₂, 20.95% O₂ and 0.93% Ar. We use the Monte Carlo code in three spatial dimensions that was originally designed and thoroughly tested for streamer modeling [104] and extend it to energies above 1 keV, also tracing photons, as described in chapter 6. Between two collisions we calculate the new position and velocity of an electron or photon using three dimensional relativistic equations of motion. For electrons, we include Bremsstrahlung, elastic scattering [82, 129, 130], excitations [97], ionization [84] and attachment [97, 125] as used by [101, 25, 26]. For electron-nucleus Bremsstrahlung the energy of the emitted photon is related to its scattering angle Θ_i by the doubly differential cross section calculated from the Bethe-Heitler theory [12, 90]. For electron-electron Bremsstrahlung the energy of the emitted photon is given by the spectrum as calculated by Tessier and Kawrakow [157]. The geometry of the scattered electron, the ejected electron and the emitted photon is determined by the triply differential cross section by Haug and Nakel [74]. For photons, we include Compton scattering [128], pair production [90], Rayleigh scattering [144] and photoionization [131] where a Bremsstrahlung photon ionizes a background molecule and emits an electron. Because the equations describing the cross sections for all these processes are sometimes rather involved, extensive checks have been performed to ensure that all the interactions really occur with the appropriate probabilities. We have also checked that the final state, possibly involving the emission of another species, is correctly generated both in terms of kinematics and of probability distributions.

We investigate the production of photons in the field of a stepped lightning leader. We start with 50 electrons with initial energy 0.1 eV and perform two simulations with electron-nucleus Bremsstrahlung only and one including electron-electron Bremsstrahlung. Hence we are able to compare the significance of both types of Bremsstrahlung.

We adopt the model by Xu et al. [169] of a stepped lightning leader. We approximate the leader as a stationary ideally conducting ellipsoid with a length of 4 km and a curvature radius at the tip of 1 cm in an ambient field of 0.5 kV/cm; its upper tip is at 16 km altitude in the terrestrial atmosphere, and the electrons are inserted at 30 cm ahead of the tip. The long half axis is orientated along the z axis and the leader tip at (0,0,0) of our computational domain; thus the enhancement of the electric field is highest on this axis and the motion of electrons is symmetric in x and y . Like Xu et al., we neglect the electric

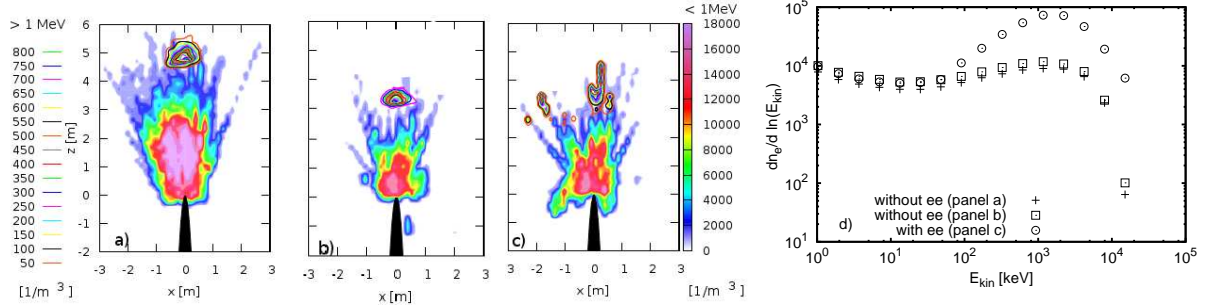


Figure 3.2: The electron density for different electron energies without (a,b) and with (c) electron-electron Bremsstrahlung projected into the xz plane. The lightning leader is indicated by the black region. The electrons were initially set 30 cm ahead from the tip. Colorlines and colormaps represent the densities of electrons with kinetic energies above and below 1 MeV, respectively. Panel a) and b) refer to two different stochastic Monte Carlo processes with the same distribution. d) The electron number as a function of energy for the cases shown in panels a), b) and c).

field due to space charge effects between electrons and ions for simplicity. Therefore the low-energy spectrum is not quite physical and we only plot photon energies above 1 keV.

3.3.2 Results and discussion

Figure 3.2 shows the electron distributions in space without (panel a and b) and with (panel c) electron-electron Bremsstrahlung. The corresponding distributions in energy space after 24 ns are also displayed (panel d). Panel a) and b) are derived with different realisations of the random numbers in the Monte Carlo process while their distribution is the same. In the plots we distinguish the electrons with energies above or below 1 MeV. The fewer high-energy electrons are far ahead of the large number of low-energy electrons that would screen the electric field if space charge effects were included. But due to the spatial separation, the high-energy electrons would hardly be affected, thus justifying our approximation. Fig. 3.2 d) shows the electron number as a function of energy above 1 keV from panels a,b and c: the distributions look similar for the two cases without electron-electron Bremsstrahlung even though the spatial plots are quite different, and the electron numbers are almost the same for energies below 100 keV in all three cases. However, there are substantially more electrons with energies above 100 keV when electron-electron Bremsstrahlung is included as this process contributes not only to the emission of photons, but also to the ejection of shell electrons. Figures 1, 2, 5 and 6 in Ref. [73] demonstrate that the residual energy $E_{kin,i} - E_\gamma$ is shared more evenly between scattered and ejected electron than for impact ionization. Since the electron-electron Bremsstrahlung process produces mostly low-energy photons, we get an enrichment of

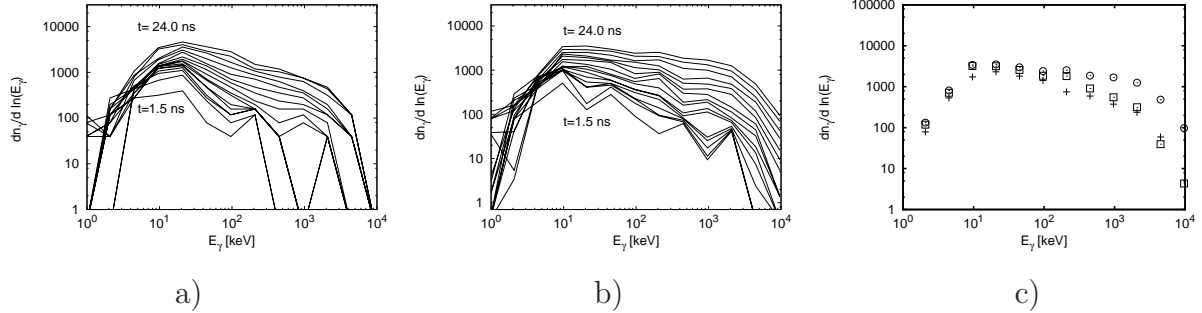


Figure 3.3: The time evolution of the energy resolved photon numbers produced in the field of a negative stepped leader a) without and b) with electron-electron Bremsstrahlung. Every line belongs to a different time: time progresses from 1.5 ns for the lowest line to 24 ns for the highest line, in time steps of 1.5 ns. Panel c) compares the energy dependent photon numbers with (circles) or without (crosses, boxes) electron-electron Bremsstrahlung for the cases shown in Fig. 3.2. There is a substantial contribution from electron-electron Bremsstrahlung at 10 MeV, with photon numbers 25 times higher than without.

high-energy electrons which contribute to the production of high-energy Bremsstrahlung photons.

Figure 3.3 shows the time evolution of the photon energy spectrum between 1 keV and 10 MeV without (panel a) and with (panel b) electron-electron Bremsstrahlung. Figure 3.3 c) compares the photon spectra after 24 ns. Including electron-electron Bremsstrahlung, the number of photons with energies above 1 MeV is a factor 4 higher than without this process. For photons with energies above 10 MeV this factor is 25. The comparison also shows that the spectrum with electron-electron Bremsstrahlung is slightly flatter and decreases more slowly.

3.4 Conclusion

While the past theory of terrestrial gamma-ray flashes only used the electron-nucleus Bremsstrahlung process to calculate the photon spectrum, we here show that electron-electron Bremsstrahlung should be included. This might be surprising at first sight since electron-electron Bremsstrahlung generates less photons in the MeV range than the electron-nucleus process. But electron-electron Bremsstrahlung contributes to the enrichment of electrons in the high-energy regime through the ejection of shell electrons. Thus there are more high-energy electrons which can produce high-energy Bremsstrahlung photons. We have studied the electron acceleration in the field of a stepped lightning leader. In this case there are 4 times as many photons with energies above 1 MeV. There are

even 25 times as many photons in the energy range between 4.8 MeV and 10 MeV.

We conclude that electron-electron Bremsstrahlung dominates the high energy spectrum of TGFs through electron ejection and hence must not be neglected. Photons with energies above 1.022 MeV also create electron-positron pairs, therefore electron-electron Bremsstrahlung is also vital for the explanation of electron-positron beams. Since electron-electron Bremsstrahlung is a source of high-energy electrons, this mechanism is also important for high-energy electron beams ejected from thunderstorms.

Calculation of beams of positrons, neutrons and protons associated with terrestrial gamma-ray flashes

Positron beams have been observed by the Fermi satellite to be correlated with lightning leaders, and neutron emissions have been attributed to lightning and to laboratory sparks as well. Here we discuss the cross sections to be used for modeling these emissions, and we calculate the emissions of positrons, neutrons and also protons from lightning leaders. Neutrons were first erroneously attributed to fusion reactions, but the photonuclear reaction responsible for neutrons should create protons as well. We predict them here; they have not been observed yet.

In this chapter, we first revisit the model for stepped lightning leaders of Xu, Celestin and Pasko with updated cross sections, we analyze the spatial and energetic structure of the electron beam and provide the spectrum of the generated gamma-ray beam at 16 km altitude. Then we launch a gamma-ray beam with this spectrum from 16 km upward and calculate the the production and energy of positrons, neutrons and protons as well as the propagation of positrons. For photons with energies above 5 MeV we present the energy distribution of Compton scattered photons and show that there are large energy losses through Compton scattering. Finally, we provide tools and concepts to easily estimate the spatial and energetic distribution of positrons, neutrons and protons for gamma-ray beams of arbitrary spectra launched at arbitrary altitudes into arbitrary directions.

This chapter has been revised for J. Geophys. Res.

4.1 Introduction

4.1.1 High-energy emissions from thunderstorms

High energy emissions from thunderstorms were first observed from satellites. It started in 1994 with the discovery of terrestrial gamma ray flashes (TGFs) by the BATSE satellite [54]. The RHESSI satellite [149] and the Fermi Gamma-Ray Space Telescope [17] have confirmed the production of high-energy bursts in thunderclouds, extended the measurements and found quantum energies up to 40 MeV. The team of the AGILE satellite measured energies up to 100 MeV [112, 155].

Hard radiation was also measured from lightning leaders approaching ground [115, 40] and from laboratory discharges [121, 134, 111, 143, 88, 89] where high-energy electrons are created in the streamer-leader stage. It was soon understood that these energetic photons were generated by the Bremsstrahlung process when energetic electrons collide with air molecules [54, 158].

In December 2009 NASA's Fermi satellite detected beams of positrons and electrons [18] following the geomagnetic field lines sufficiently high above the atmosphere. They are distinguished from gamma-ray flashes by their dispersion and their location relative to the cloud as electrons as charged particles follow the geomagnetic field lines.

It is generally assumed that positrons in air are produced by the interaction of gamma-rays with air molecules through pair production [12, 75, 90].

In 1974 Fleischer et al. [55] were the first to measure neutron fluxes from man-made discharges. They extrapolated their measurements and estimated that there are $4 \cdot 10^8$ thermal neutrons and $7 \cdot 10^{10}$ neutrons with energies of approximately 2.45 MeV per lightning flash.

Recently the production of neutrons with energies between 0.01 eV and 10 MeV has been reported in laboratory discharges [1]. However, these experiments are performed in laboratory discharges with 1 MV applied to a 1 meter gap and it is not clear how neutrons in these experiments can have energies of up to 10 MeV. There are two possible explanations for neutron production in a discharge [5]: either fusion processes involving deuterium [171] or photoproduction where a photon is absorbed by an air molecule which subsequently releases a neutron. Babich [5] compared both processes using the relevant cross sections and rate coefficients. He concluded that the first process cannot play a significant role and hence that the photonuclear process must be dominant.

To produce the initial set of energetic electrons within a thundercloud which then create high-energy gamma rays which in turn produce positrons and hadrons, it needs electric fields which by far exceed the average electric field in a thundercloud. Average fields in a thundercloud are in the order of several tens of kV/m [113]; over lengths of several m, electrons could only gain several tens of keV if they were not hindered by friction. Thus, for electrons to gain energies of several MeV, high fields are needed as they can occur locally during the initial leader stage of the electric breakdown. In

laboratory experiments [99, 57] as well as in thunderstorms, leaders have been observed to move stepwise [166, 48]. Dwyer et al [40] showed that there is a correlation between the stepping process and the production of X-rays; Moss et al [117] proposed that the production of photons above 1 MeV be correlated to leader stepping. Carlson et al. [23, 24] have calculated the correlation between lightning leaders and the production of terrestrial gamma-ray flashes. Thus here we concentrate on the field enhancement of a negative leader. For a given photon spectrum Celestin and Pasko [27] calculated the influence of Compton scattering on the time resolution of a TGF signal at satellite altitudes. Xu et al. [169] were the first to model the production of TGFs from a negative stepped lightning leader. They assume an upwards directed stationary leader channel during the stepping process in a given ambient field at altitudes between 12 and 16 km. They calculate the electric field of the leader in the ambient field using the method of moments [9]; the curvature at the leader tip enhances the electric field such that electrons can be accelerated from sub-eV into the run-away regime. They use a three dimensional Monte Carlo code to trace electrons and simulate the production and motion of Bremsstrahlung photons in air. So far there has not been a Monte Carlo simulation which models the production of positrons, neutrons and protons for a photon spectrum of a negative stepped lightning leader. The present work is devoted to this task. Especially we investigate the energy loss of photons with energies above 5 MeV and take the positron motion into account.

4.1.2 Organization of the chapter

This chapter is divided into two parts. In section 4.2 we describe how we model the production of Bremsstrahlung photons from a negative stepped lightning leader. Since we use fully quantum field theoretical cross sections, our results differ from those of previous authors [169, 98]. In section 4.3 we present the cross sections to produce positrons and hadrons by photons scattered at air molecules for arbitrary energies above 10 MeV. As a test case we consider the production of positrons and hadrons by a photon beam with the in section 4.2 determined initial energy spectrum.

In section 4.2.1 we briefly describe how we model a stationary leader and the electron motion in its electric field. We also list the collisions implemented into our code.

In sections 4.2.2 and 4.2.2 we present our results. We present the spatial distribution of electrons and focus on the energy and direction of photons. The result suggests a simple representation of the distribution of high-energy photons which then is used as a starting point for further simulations.

In section 4.2.2 we compare the influence of the Bethe-Heitler cross section and the Lehtinen cross section for electron-nucleus Bremsstrahlung on the production of photons from a stepped lightning leader.

In section 4.3.1 we briefly describe how we model the propagation of photons and the production of positrons and hadrons from a given photon distribution. We also give details about modeling the positron motion through air. We list all cross sections we use

for the motion of photons and positrons and estimate the influence of the geomagnetic field for the motion of relativistic electrons or positrons. We show that most photons with energies between 5 MeV and 50 MeV at 16 km altitude lost most of their energy through Compton scattering within few μs . Hence only a small fraction of these high-energy photons will reach satellite altitudes [123, 59]. This is different than for photons with energies below 500 keV that lose a smaller fraction of their energy through Compton scattering [27].

In section 4.3.2 we present the positron and hadron distribution as produced by the photon distribution. Finally we show the positron distributions evolve in time and how the beam widens.

We briefly summarize our results in section 4.4.

Details of our calculations can be found in section 4.A. There we calculate the electric field of a negative stepped lightning leader modelled as a conductive ellipsoid.

4.2 Gamma-ray production by a negative stepped lightning leader

A simplified model for a negative lightning leader during stepping was introduced by Xu et al. [169, 170]. We here revisit this model, suggest a different manner to calculate the electric field of the leader, and discuss the cross-sections we use. In particular, we emphasize the choice of the cross-sections for electron nucleus Bremsstrahlung [90] and the necessity to include electron electron Bremsstrahlung [92]. We note here that electron electron Bremsstrahlung is included also in CORSIKA [33], EGS5 [49] and EGSnrc [50]. The model to correctly predict the photon number and spectrum created by the run-away electrons at the leader tip was already used in chapter 3 where we concentrated on the importance of electron electron Bremsstrahlung. Details, images of the evolution of the distribution of electrons in space and energy, and a comparison with spectra derived with different cross-sections by other authors are presented in this section. It forms the starting step for the calculation of positron and hadron generation in the next section.

4.2.1 Set-up of the model

Stepped lightning leader

For the stepped lightning leader, we use precisely the model of [169] with the same parameters. The leader is vertical, 4 km long and has a tip radius of 1 cm. It is assumed to be equipotential and embedded in an external electric field of 0.5 kV/cm far from the leader. This model approximates the leader at the moment of stepping: the space stem has connected to the leader, and the full electric potential is now on the new leader tip. At this moment the leader tip “explodes” with ionization, similarly as described by Sun

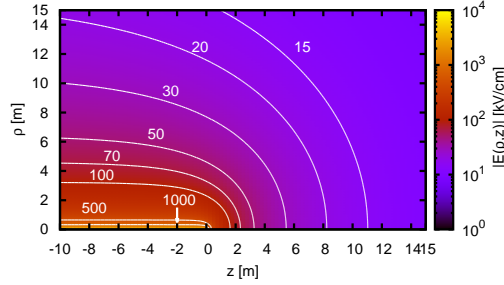


Figure 4.1: Electric field strength (color coded) in the vicinity of the tip for a leader of 4 km length in an ambient field of 0.5 kV/cm. Cylindrical coordinates ($\rho = \sqrt{x^2 + y^2}, z$) are used, and the upper leader tip lies at the origin of the coordinate system. The white level lines indicate fixed values of the electric field strength from 15 to 1000 kV/cm as indicated.

et al. [153], creating an inception cloud [16] and a later streamer corona. The field of the leader is tested by inserting 50 electrons with 0.1 eV energy on the symmetry axis 30 cm ahead of the leader tip. We also follow the approach of Xu et al. [169] by not taking the space charge effects of the developing corona discharge into account, but only that of the stationary leader; this approximation will be justified in Fig. 4.3 for the electrons with the highest energy. Therefore the approximation of taking only the electrostatic leader field into account is reasonable, even if the inception cloud develops into a relativistic impact ionization front [109].

Rather than approximating the leader as a cylinder with semispherical caps as Xu et al. [169], we approximate it as an ellipsoid with a length of 4 km and a curvature radius of 1 cm at the tip. This has the advantage that we can calculate the electric field $\mathbf{E}(\mathbf{r})$ analytically, as summarized in section 4.A. Figure 4.1 shows the electric field strength in the vicinity of the leader tip. It shows that the ellipsoid is a reasonable approximation when comparing with Figure 1 a) of [169], and it illustrates the strong field enhancement close to the leader and its tip. The field is approximately 500 kV/cm at 30 cm ahead of the leader tip, thus certainly large enough to accelerate the electrons into the run-away regime.

Air composition and Monte Carlo approach

We model the air as consisting of 78.12% N_2 , 20.95 % O_2 and 0.93 % Ar. To control the air density as a function of altitude, we use the barometric formula with a scale height of 8.33 km. We assume the upper leader tip where the electrons are accelerated to lie at 16 km altitude which corresponds to an air density of 1/10 of the density at sea level if the

temperature change with altitude is taken into account.

We trace the positions of electrons and photons in three dimensions with a Monte Carlo code where the neutral air molecules are treated as a random background with appropriate statistical weight. Between collisions the electrons follow classical or relativistic trajectories within the given electric field, depending on their energy, while the photons move with the speed of light into the direction of emission. The collisions are treated with a Monte Carlo scheme.

We now list the collision types included.

Cross-sections for electrons

We start with the cross sections where electrons are liberated or lost, or where they gain or lose energy and momentum. Electron-nucleus and electron-electron Bremsstrahlung will be treated in two separate subsections, before treating the photon motion.

Details about our Monte Carlo code and its validation can be found in chapters 3 and 6. There we also describe which collisions we take into account and how we have implemented them into our code. We remark here that the choice of cross sections is essential for correct results as shown in section 6.C and that there is current research of which cross sections are appropriate for the propagation and production of high-energy particles in the atmosphere.

We have estimated the influence of the geomagnetic field. In section 4.3 we show that the geomagnetic field has basically no effect on the electron motion during the time interval considered here.

Electron nucleus Bremsstrahlung

Electron nucleus Bremsstrahlung is the process when a free electron scatters at a nucleus and emits a photon, electron electron Bremsstrahlung is the same process where the electron scatters at another electron and emits a photon. As electron electron Bremsstrahlung is frequently considered as negligible compared to electron nucleus Bremsstrahlung, the general term Bremsstrahlung refers typically to electron nucleus Bremsstrahlung.

Different cross-sections for electron nucleus Bremsstrahlung are used in different databases and by different researchers. In the field of terrestrial gamma-ray flashes, Carlson et al. [24] use the Geant 4 simulation tool kit with its intrinsic cross sections [2]. Dwyer [42] uses the Bethe Heitler cross section [12, 75] resolving the full geometry of the process; he includes an atomic form factor to take the structure of the atomic shell into account. Xu et al. [169] use the simple product ansatz of Lehtinen [98] to relate energy and direction of the emitted photons.

Now Geant 4 [2] uses cross sections appropriate for the large atomic numbers Z of heavy nuclei while nitrogen and oxygen have $Z = 7$ and 8. According to Shaffer et al. [140], the old Bethe-Heitler theory keeps being the appropriate theory for $Z < 29$ for electron energies between 1 keV and 1 GeV, as we have already discussed in chapter 2. In

section 2.F we have also shown that the atomic form factor used by Dwyer [42] is close to unity in the relevant cases and thus negligible. The product ansatz of Lehtinen [98] that is used by Xu et al. [169] is not compatible with a full quantum field theoretical model of collisions where the photon obtains almost all the electron energy, as we have discussed in section 2.E; in section 4.2.2 we will compare results of TGF calculations under the same conditions using either the cross sections of Lehtinen [98] or of the ones derived in chapter 2.

We use the doubly differential cross section derived in chapter 2 for the relation between the photon energy $E_\gamma = \hbar\omega$ and the angle Θ_i between the incident electron and the emitted photon. This cross section has been obtained by integrating the direction of the emitted electron out in the Bethe Heitler cross sections; and it is implemented using rejection sampling as described in [86]. The scattered electron keeps its initial direction.

Electron electron Bremsstrahlung

As databases like Geant 4 concentrate on the Bremsstrahlung for metals like iron ($Z = 26$) or lead ($Z = 82$), electron-electron Bremsstrahlung is considered as irrelevant, because it scales with Z rather than with Z^2 . Furthermore, the photons emitted in electron electron Bremsstrahlung by nitrogen or oxygen ($Z = 7, 8$) are negligible as well compared to electron nucleus Bremsstrahlung. However, we have shown recently [92] that electron electron Bremsstrahlung also ejects the shell electron on which the free electron is scattered, and that these electrons have higher energies than those created by normal impact ionization [84]. Using the cross sections of Tessier and Kawrakow [157] the effect is important in air for electron energies of several MeV. Electron electron Bremsstrahlung hence largely increases the number of electrons with energies above 1 MeV, and it subsequently contributes substantially to the number of high-energy photons from a negative stepped lightning leader. We remark here that electron electron Bremsstrahlung also has been included recently in simulation packets like CORSIKA [33] and EGS5 [49] simulating extensive air showers, as well as in EGSnrc [50] for medical applications.

Cross-sections for photons

Figure 4.2 shows cross-sections of photon processes as a function of the photon energy. For the photons, we use the cross sections for photoionization [131], Compton scattering [66, 128], hadron production [56] and pair production [90]. Fig. 4.2 shows that photoionization is dominant for photon energies below 1 keV. Thus new electrons are created not only by electron impact ionization and the electron-electron Bremsstrahlung process, but also by photoionization.

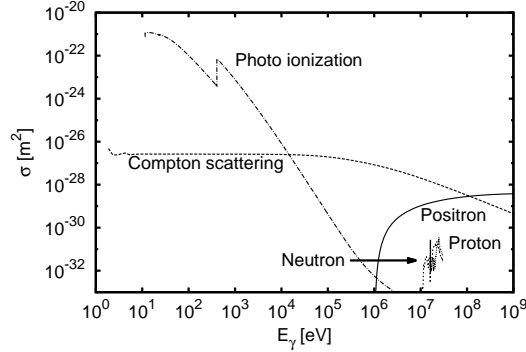


Figure 4.2: Total cross sections of photons for photoionization, Compton scattering, hadron production and pair production as a function of incident photon energy E_γ for nitrogen.

4.2.2 Simulation results

Distribution of electrons in energy and space

In chapter 3 we have already presented the electron energy distribution ahead of the stepped lightning leader after 24 ns of evolution when either including or neglecting the electron electron Bremsstrahlung. There we have shown the energy distribution of electrons for different runs with different realisations of random numbers, and we have seen that the energy distribution is stable against different sets of random numbers already for 50 initial particles; hence 50 initial electrons is already enough for good statistics. Due to the limited space of a fast track communication, we could not present the build-up of the spatial distribution. Therefore, we present here in Figure 4.3 this evolution including electron electron Bremsstrahlung, when 50 test electrons are inserted 30 cm ahead of the leader tip. The leader is indicated in black. The spatial distributions of the electrons after 5 ns, 10 ns, 15 ns and 20 ns are plotted; the continuous colors indicate the electron densities with energies below 1 MeV, the color lines the electron densities with energies above 1 MeV in the xz plane where a slice was evaluated in the y direction from -3 cm to 3 cm.

The figure shows that at all instances the high energy electrons are ahead of the lower energy electrons and more on axis. The reason is obviously that the high energy electrons are accelerated continuously while the lower energy electrons have lost energy in collisions, and these collisions also lead to a widening of the electron beam. The figure shows as well that new ionization patches are created at the sides of the leader, probably due to photo-ionization created by Bremsstrahlung photons. It should be noted though that the motion of the low energy electrons is not quite physical as we neglect the space charge effects of the newly created ionization, just like Xu et al. [169, 170]. However, as there is

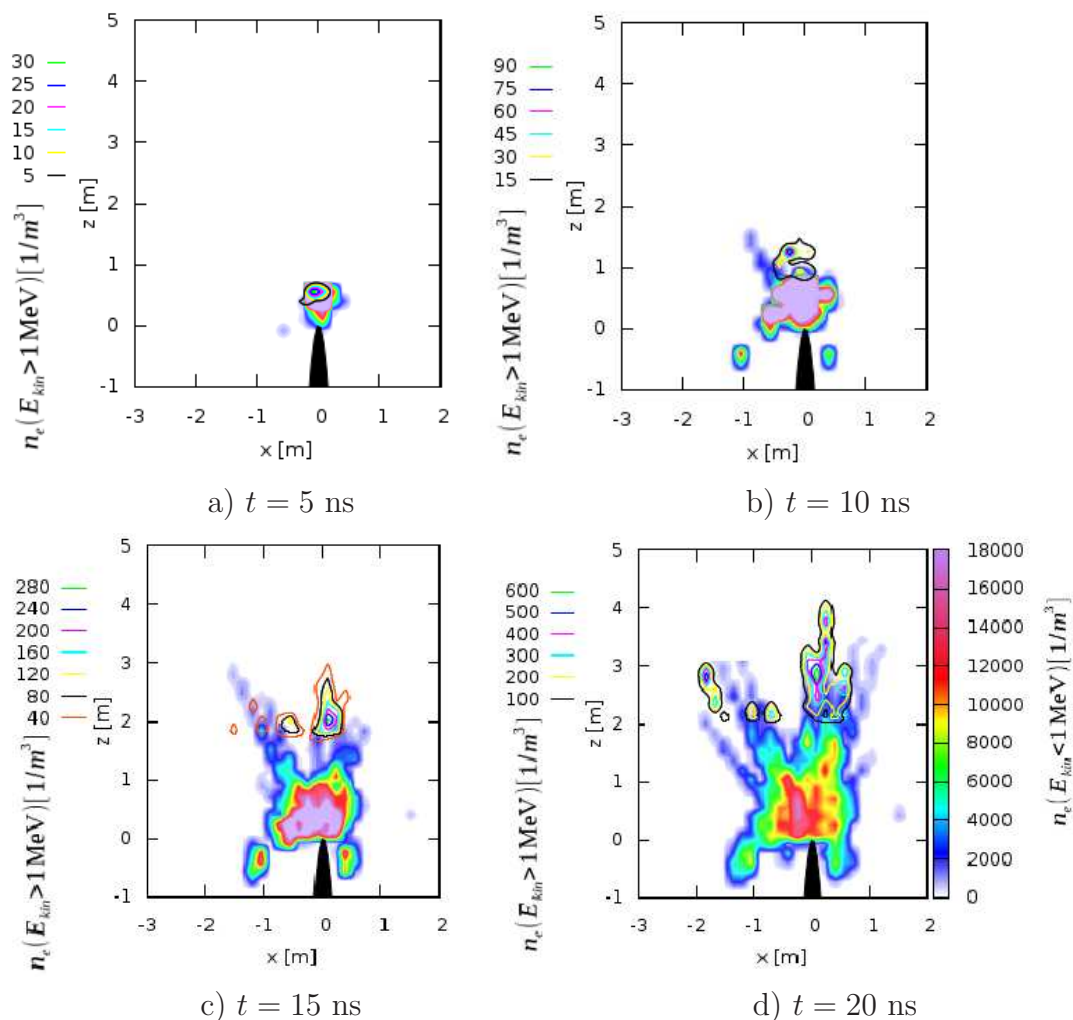


Figure 4.3: Evolution of the electron density distribution in the xz plane in a y range from -3 cm to 3 cm after a) 5 ns, b) 10 ns, c) 15 ns and d) 20 ns. The bin size is $\Delta x = \Delta z = 16$ cm and $\Delta y = 6$ cm. The final moment $t = 24$ ns has already been displayed in Fig. 3.2 with the same color scheme. The black ellipsoid indicates the position of the leader. Electrons with energies below or above 1 MeV are marked with different symbols. The density of electrons with energy below 1 MeV is indicated with continuous coloring, and the color map is the same in all panels. The density of electrons with energies above 1 MeV is indicated with color lines, and the values attributed to the color lines change for each panel.

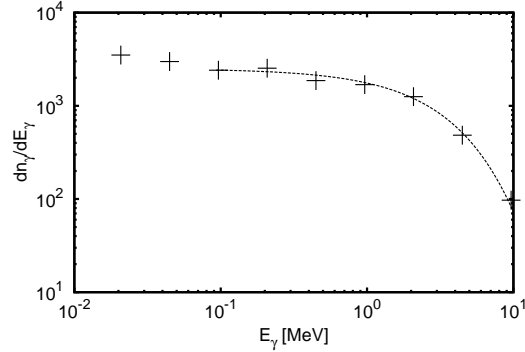


Figure 4.4: Photon energy distribution after 24 ns as calculated in chapter 3. The line shows the fit $\sim e^{-E_\gamma/3 \text{ MeV}}$.

a clear spatial separation between the electron populations at different energies, we argue that the calculation approximates the high energy spectrum of the electrons well. We remark that electrons with energies of 10 keV, 100 keV, 1 MeV and 10 MeV move with 19.5, 54.8, 94.1, and 99.9% of the speed of light, and that light travels 6 m within 20 ns. The electrons with energies above 1 MeV are concentrated in one region on axis after 5 and 10 ns; after 15 ns new patches with high energy electrons have formed in new beam directions slightly off axis. We emphasize that the channel-like structures forming from 10 ns on are not streamers, as space charge effects are not included, but they are probably rather ionization traces of the created high energy electrons, similarly as in cosmic particle showers [91], but enhanced by the electric field.

We remark that the geomagnetic field has no influence on the electrons at these altitudes, and we will discuss the role of the geomagnetic field in more detail in section 4.3.

Distribution of photons in energy and space

Figure 4.4 shows the photon energy distribution after 24 ns. As we have found in chapter 3, the spectrum of Bremsstrahlung photons, and in particular, the high energy tail, does not change significantly after about 15 ns. For reasons of computer memory we anyhow have inserted only 50 test electrons into the leader field and we follow the motion of the electrons until 24 ns. The total number of photons with energies between 0.01 eV and 10 MeV in our simulation is approximately 5000, thus there are 100 photons per initial electron. As we have neglected the space charge effects of the developing corona discharge, the low-energy part of the distribution is not quite physical and we concentrate here on photon energies above 10 keV. The maximal photon energy after 24 ns is approximately 10 MeV. Figure 4.4 also shows that for energies above 1 MeV the distribution can be fitted well by the exponential $e^{-E_\gamma/3 \text{ MeV}}$.

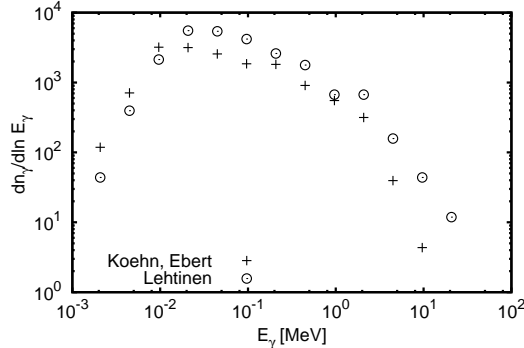


Figure 4.5: The photon energy distribution after 24 ns with the following cross sections: electron nucleus Bremsstrahlung only according to Eq. (2.67) (crosses) or according to Lehtinen [98] (circles).

From our analysis in chapter 2 we know that photons with energies above 1 MeV are emitted predominantly in forward direction relative to the direction of the incident electron. Since the electrons which can create such photons, mainly move upwards (see Fig. 4.3), this suggests the simple representation of the beam of initial photons described in section 4.3.1 as a test case to simulate the production of positrons and hadrons.

Results for different Bremsstrahlung cross sections

We tested the dependence of the simulation results on different Bremsstrahlung cross sections. Figure 4.5 shows the photon energy distribution after 24 ns for energies above 1 keV. The two curves are both without electron electron Bremsstrahlung, and either the product ansatz of Lehtinen [98] or the integrated Bethe-Heitler cross section (2.67) for the electron nucleus Bremsstrahlung is used. The plot shows that the product ansatz of Lehtinen [98] that is used by Xu et al. [169, 170], substantially overestimates the number of photons with energies above 1 MeV.

4.3 Production and motion of positrons, neutrons and protons in a TGF

4.3.1 Modeling

Photon processes in air

Photons with energies above 10 MeV will lose most or all their energy in pair production, hadron production and Compton scattering. Therefore Figure 4.6 a) shows the cumulative

total cross sections for these processes for photons with energies between 10 MeV and 100 MeV. $N_{int}(a, b) := \int_a^b dz n(z)$ is the column density from a to b where $n(z) = 2.6885 \cdot 10^{25} \text{ 1/m}^3 e^{-z/8.33 \text{ km}}$ is the air density in the atmosphere. A collision with cross section σ is likely if a photon has travelled through a column density larger than $1/\sigma$, i.e. if $\sigma \cdot N_{int} \gg 1$. Hence, Fig. 4.6 a) shows that photons with energies between 10 MeV and 50 MeV are very likely to either create an electron-positron pair or a hadron or to Compton scatter between 16 km and 20 km, losing most of their energy.

For Compton scattering Figure 4.7 shows the cross section $d\sigma/dE'_\gamma$ differential in the energy E'_γ of the scattered photons. It shows that there is a large energy loss through Compton scattering where most energy is transferred onto electrons which we do not trace further. Thus the energy of photons is not shifted down slowly, but very rapidly and they are removed from our pool since we are not interested in photons with energies below 5 MeV. Hence only a small fraction of these high-energy photons will reach satellite altitudes [123, 59]. This is different for photons with energies below 1 MeV where the energy loss is not so significant [27]. The number of new electrons produced through Compton scattering is small compared to the number of ambient electrons, thus negligible.

We also calculate the photo-production of neutrons and protons [56] where a photon γ is absorbed by the nucleus of a molecule emitting a neutron n or a proton p :



Here Z is the atomic number and M is the rest mass of atom or molecule A . In our model we only use molecules of ${}^{14}_7 \text{N}$ and ${}^{16}_8 \text{O}$ as the percentage of other nitrogen or oxygen isotopes in air is negligible. Since the binding energy E_{bind} of a nucleon is approximately 7.4 MeV for nitrogen and 8.0 MeV for oxygen (calculated with the Bethe Weizsäcker equation [164]), photons need tens of MeV to produce hadrons. The kinetic energy E_{kin} of the emitted hadron is simply

$$E_{kin} = E_\gamma - E_{bind}. \quad (4.3)$$

Hadrons are emitted isotropically; we neglect the motion of the residual nuclei as their rest mass is much higher than the rest mass of a neutron or a proton.

Figure 4.6 b) shows the ratio of the number of produced protons and neutrons to the number of produced positrons. It shows that the photo-production of hadrons is most efficient for photon energies between 20 MeV and 25 MeV and that in this energy range the production of hadrons is one to two orders of magnitude less than the production of positrons. Since the production of positrons and hadrons is very inefficient, we need a high number of initial photons.

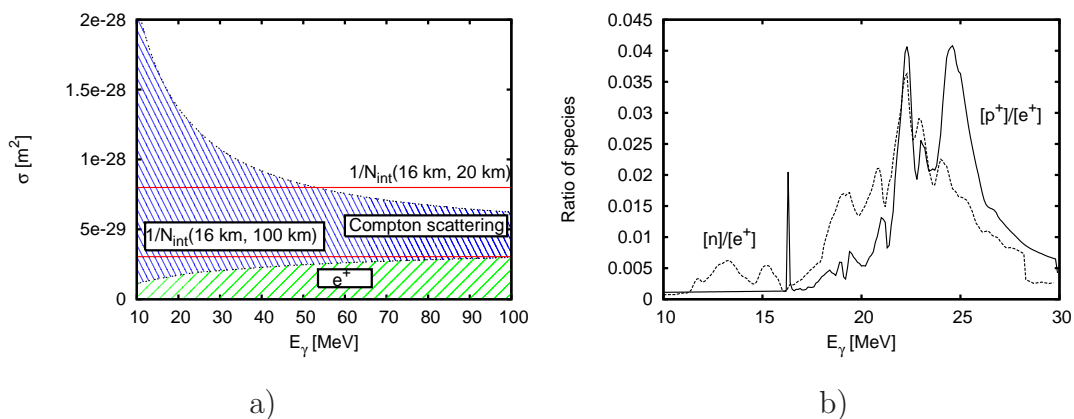


Figure 4.6: a) The cumulative cross sections as a function of the incident photon energy for positron production (green, wide hatches) and Compton scattering (blue, narrow hatches) in air. The red lines denote the inverse of the integrated air density from 16 km up to 20 km or up to 100 km, $N_{int}(a, b) = \int_a^b n(z) dz$. b) The ratio of neutron or proton production over positron production as a function of the incident photon energy.

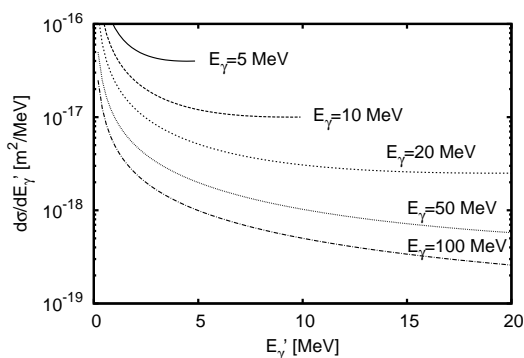


Figure 4.7: The differential cross section $d\sigma/dE'_\gamma$ of energies E'_γ of Compton scattered photons for different initial energies E_γ .

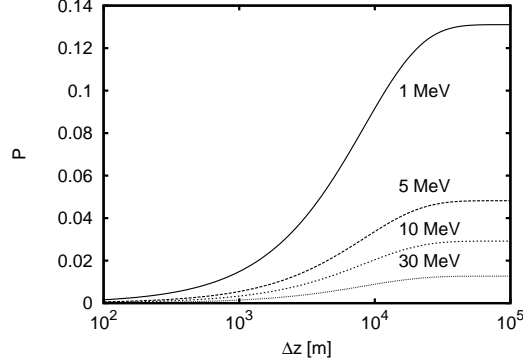


Figure 4.8: The probability of annihilation of positrons at shell electrons as a function of path length for different positron energies. Δz is the distance of a positron moving straight upwards from 16 km altitude.

The initial photon spectrum

As an input for our model for the production of leptons and hadrons we use the photon distribution at 16 km altitude as in Fig. 4.4. The solid line in Fig. 4.4 shows

$$n_\gamma(E_\gamma) \sim e^{-\frac{E_\gamma}{3 \text{ MeV}}} \quad (4.4)$$

as a fit for photon energies above 1 MeV where n_γ is the number of photons with energy E_γ . We note here that the considerations in section 4.3.1 are independent of spectrum (4.4).

As Figure 4.2 shows, pair production and hadron production become relevant for energies above approximately 10 MeV. Since measurements [17, 112, 155] have shown that TGFs can have energies up to 40 MeV, we use the distribution (4.4) from 5 MeV up to that energy for the production of positrons and hadrons. As the photons in our simulation are produced within 24 ns, thus within some meters and without much spatial separation, we initiate the photon beam at one single point at 16 km altitude corresponding to $t_0 = 0$. We use a monodirectional beam because photons with energies above several MeV are emitted in forward direction and most high-energy photon producing electrons move in forward direction. We trace the photon beam and its particle production for 1 ms which corresponds to a distance of about 300 km.

The production and motion of positrons

We sample the total positron energy E_+ and positron direction Θ_+ relative to the direction of the incident photon, using the differential cross section (2.101) and we follow them through air where we use the barometric formula to describe the density change

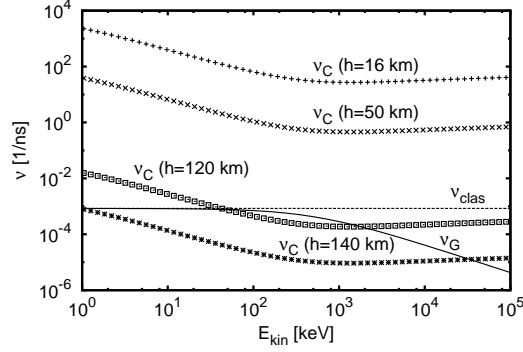


Figure 4.9: The gyration frequency ν_G (4.5) and the classical expression $\nu_{clas} = e_0 B / (2\pi \cdot m_0)$ for $B = 3 \cdot 10^{-5}$ T as well as the collision frequencies ν_C (4.6) at 16 km, 50 km, 120 km and 140 km altitude as a function of the electron energy.

as a function of altitude. We include elastic scattering, ionization and Bremsstrahlung cross sections derived for electrons. This is feasible since cross sections for electrons and positrons are similar for kinetic energies above 1 MeV [2, 94]. We have also included the annihilation of positrons at shell electrons using analytic equations from [66]. Figure 4.8 shows the probability for annihilation of positrons at shell electrons of air molecules as a function of altitude for different positron energies. It shows that the probability is smaller than 15 % for 1 MeV and decreases rapidly with increasing positron energy.

Influence of the geomagnetic field

In order to estimate the influence of the geomagnetic field for relativistic electrons or positrons we have to compare the gyration frequency in a magnetic field B with the collision frequency of electrons. For energies below 1 keV both frequencies were compared in [47]. The gyration frequency ν_G is

$$\nu_G(E_{kin}) = \frac{1}{2\pi} \omega_G(E_{kin}) = \frac{1}{2\pi} \frac{e_0 B}{m(E_{kin})} = \frac{1}{2\pi} \frac{e_0 B c^2}{E_{kin} + m_0 c^2} \quad (4.5)$$

where we used $m(E_{kin}) = (E_{kin} + m_0 c^2) / c^2$ for an electron with kinetic energy E_{kin} . e_0 and m_0 are the charge and the rest mass of an electron. The geomagnetic field is approximately $3 \cdot 10^{-5}$ T at the equator up to altitudes of approximately 300 km. Note that ν_G is not constant, but decreases with increasing electron energy because of the energy dependence of m . Figure 4.9 compares (4.5) with $\nu_{clas} = e_0 B / (2\pi \cdot m_0)$ where the electron mass is constant. It shows that the gyration frequency (4.5) starts to deviate from the classical value for energies above 10 keV; for 1 MeV the gyration frequency is only one quarter of

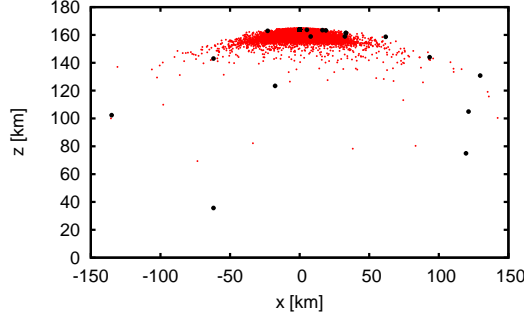


Figure 4.10: The positions of positrons (red dots) and photons with energies above 5 MeV (black dots) after 0.5 ms. As remarked in section 4.3.1, we have neglected the geomagnetic field.

the classical value. The collision frequency ν_C is

$$\nu_C = \sigma_{tot}(E_{kin})n_B(z)v(E_{kin}) = \sigma_{tot}(E_{kin})n_B(z)c\sqrt{1 - \frac{m_0^2c^4}{(E_{kin} + m_0c^2)^2}} \quad (4.6)$$

where $\sigma_{tot}(E_{kin})$ is the total cross section as a function of E_{kin} and $n_B(z)$ the gas density as a function of altitude.

Figure 4.9 shows also the comparison of (4.5) with (4.6) for different altitudes for energies above 1 keV. It shows that for 16 km or 50 km and energies between 1 keV and 100 MeV the collision frequency is higher than the gyration frequency. Thus the geomagnetic field is negligible. For approximately 140 km altitude the collision frequency is smaller than (4.5) for energies below 40 MeV. Hence, from 140 km on, electrons and positrons with energies above 40 MeV will follow the geomagnetic field lines. In our simulations we do not take the geomagnetic field into account. For altitudes below 140 km altitude we have just shown that the geomagnetic field is negligible; for altitudes above 140 km the spatial distributions of the positron beams we have calculated, simply should be tilted around the field lines to be more realistic.

4.3.2 The energy and the temporal evolution of positrons and the energy of hadrons

Figure 4.10 shows the position of photons (black) with energies above 5 MeV and of positrons (red) after 0.5 ms. As Figure 4.6 a) shows, a collision of a photon with an air molecule is very likely between 16 km and 20 km altitude. Thus almost all photons have disappeared due to two effects, either the production of positrons or hadrons or due to

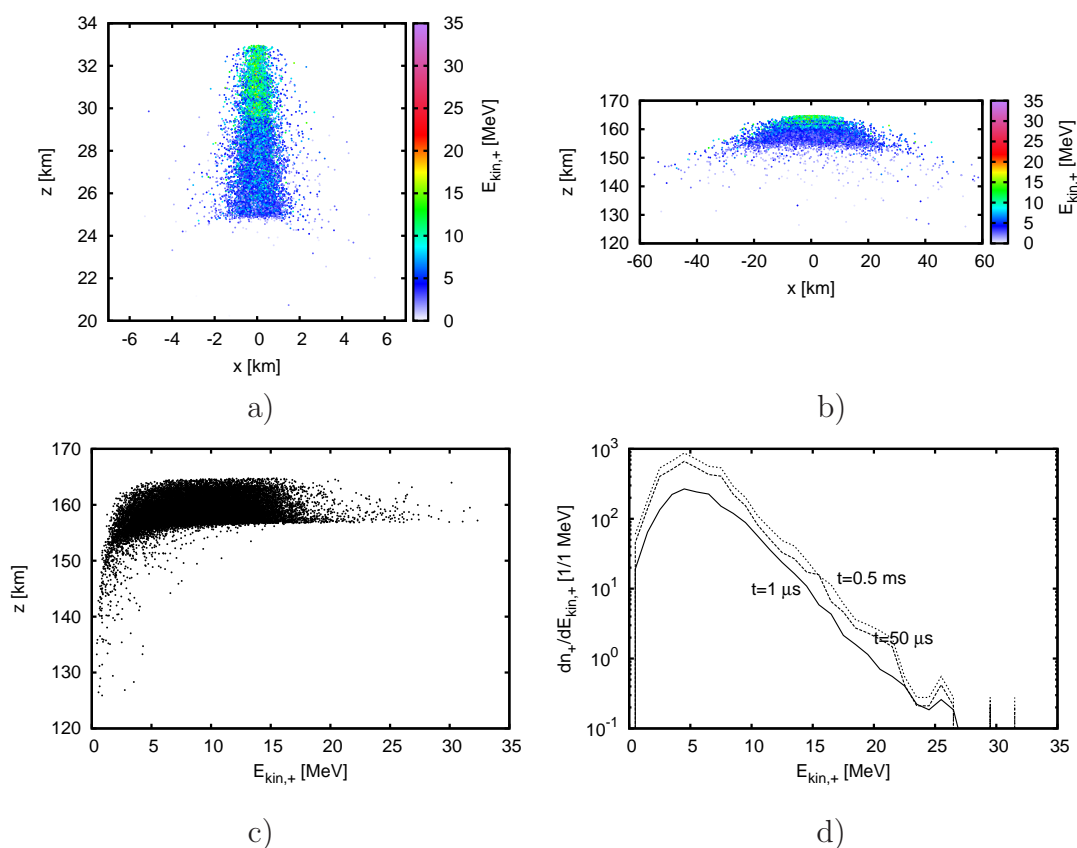


Figure 4.11: The spatial distribution of positrons after a) $50 \mu\text{s}$ and b) 0.5 ms . The color code resolves the kinetic energy. c) The altitude as a function of the kinetic energy after 0.5 ms . d) The energy distributions of positrons after $1 \mu\text{s}$, $50 \mu\text{s}$ and 0.5 ms . The original photon beam was ejected at 16 km altitude on the axis. As remarked in section 4.3.1 and in Fig. 4.10 the geomagnetic field has been neglected.

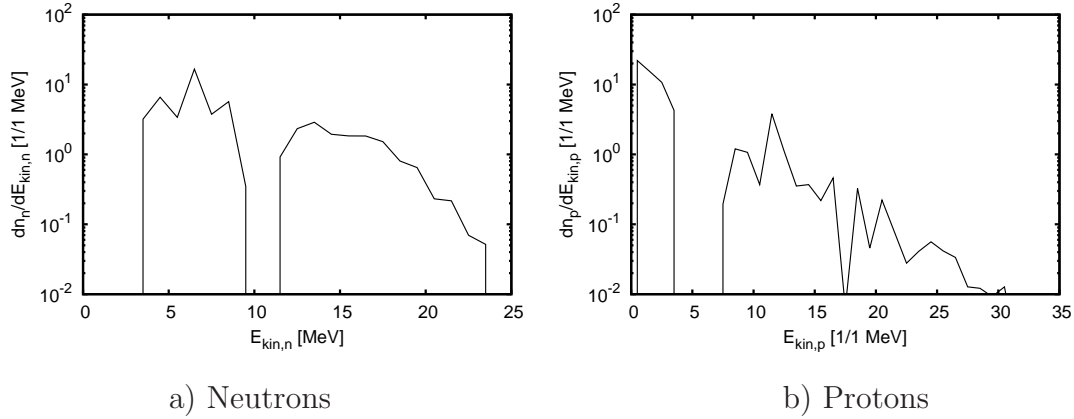


Figure 4.12: The energy distribution of a) neutrons and b) protons after $14 \mu\text{s}$ which corresponds to a photon travel distance of approximately 4 km.

Compton scattering as explained in section 4.3.1. In contrast, Celestin and Pasko [27] investigated photons with energies below 1 MeV where the energy loss through Compton scattering is not so effective. Furthermore Fig. 4.10 shows that there is positron beam which is limited by positrons moving with almost the speed of light.

Figure 4.11 shows the position and energies of all positrons. Panel a) shows their position after $50 \mu\text{s}$ where the color denotes their kinetic energy. Then the positrons already show a beamed behaviour which is more pronounced after 0.5 ms (panel b). Panel c) explicitly shows that positrons with energies above 20 MeV are in front of the positron beam whilst positrons with energies below 5 MeV are located rather at the end of the beam. Panel d) shows the energy distribution of positrons after $1 \mu\text{s}$, $50 \mu\text{s}$ and 0.5 ms. It has a clear maximum at approximately 5 MeV. The shape of the distribution does not change significantly in time, but only the total positron number.

Figure 4.12 shows the energy distributions of neutrons (panel a) and protons (panel b) after $10 \mu\text{s}$. It shows the energies of hadrons as they are produced since we do not trace them through air. In both cases there are distinct maxima and minima due to the discrete structure of the photonuclear cross sections. For neutrons the energies range from 4 MeV to 24 MeV; protons even have energies up to 33 MeV. Babich [6] calculates photon and neutron fluxes from an upwards atmospheric discharge with the help of cross sections and rate coefficients. He calculates the mean energies of neutrons to be approximately 10 MeV which is consistent with the energy distribution of neutrons in Fig. 4.12.

4.4 Conclusion and outlook

We have adopted the model of Xu et al. [169, 170] and have simulated the acceleration of electrons and the production of Bremsstrahlung photons from a negative stepped lightning leader at 16 km altitude starting with 50 initial electrons. We have calculated the electric field of a stationary leader in an ambient field. Using the electron-nucleus Bremsstrahlung cross section (2.67) based on the Bethe Heitler theory we have calculated the energy distribution of Bremsstrahlung photons and compared this distribution with the one calculated by [169] using different cross sections [98]. We have seen that these cross sections lead to unphysically high photon energies. Adding electron-electron Bremsstrahlung [92] we have calculated the spatial distribution of electrons; some electrons reach the run-away regime and produce Bremsstrahlung photons with energies of up to 10 MeV. Photons with energies above 1 MeV are emitted forward relative to the direction of the incident electrons. In our simulations we obtain approximately 5000 photons with energies from 0.01 eV up to 10 MeV, hence 100 photons per initial electron.

Using the photon distribution we have calculated the motion of photons and the generation of positrons and hadrons. We have seen that photons with energies below 50 MeV will most likely scatter within 4 km distance after being emitted upwards at 16 km altitude. Photons either will disappear through the production of leptons or hadrons or will lose most of their energy through Compton scattering. Thus most photons with energies between 1 MeV and 50 MeV produced at 16 km altitude cannot reach satellite altitudes leading to the Compton tail in the photon energy distribution as described by Østgaard et al. [123] and Gjesteland et al. [59]. Thus the simple model by Xu et al. [169, 170] is not appropriate to explain terrestrial gamma-ray flashes as measured by satellites and calculations have to be extended to explain the photon production at higher altitudes. The positron distribution shows a maximum at 5 MeV and energies up to approximately 35 MeV. Most of the positrons are emitted in forward direction; a relativistic beam is formed and limited by positrons moving with nearly the speed of light. Positrons with energies below 5 MeV can be found rather in the back of the beam. We have calculated the energy dissipation of positrons in air, and we have seen that the positron distribution does not change significantly in time.

We have shown that photons from a negative stepped lightning leader are also able to produce neutrons and protons. The energies of neutrons and protons range from 5 MeV up 33 MeV; in literature [5] mean energies of 10 MeV for neutrons are predicted by calculating neutron fluxes with rate coefficients and cross sections starting from a relativistic run-away electron avalanche. In contrast we have taken into account a more realistic photon spectrum and more photon processes and thus obtained a more accurate energy spectrum of neutrons and even protons that have not been reported before.

In future work a sophisticated model for the motion of hadrons should be developed which contains appropriate cross sections for the interaction of neutrons or protons with air molecules. Consequently it will be possible to estimate the flux of hadrons upwards

and downwards. This will be of interest to estimate how many hadrons will reach the earth's surface and hence can be measured.

4.A The electric field of a negative leader

4.A.1 Calculation of the electric field of a negative leader

Adopting the model of [169], we need to calculate the electric field of a stationary negative leader. We here calculate $\mathbf{E}(\mathbf{r})$ analytically assuming the leader be spheroidal; this is reasonable as long as we keep the same curvature radius at the tip.

The spheroidal coordinates are defined by the solutions of [96]

$$\frac{x^2 + y^2}{b^2 + u} + \frac{z^2}{a^2 + u} = 1, \quad a > b \quad (4.7)$$

where $(0, 0, 0)$ is the center of the ellipsoid and the small half axis b is the same in x and y direction. The electric potential of a conducting ellipsoid in an ambient electric field E_0 is [96]

$$\Phi(\mathbf{r}) = -E_0 z \left[1 - \frac{\xi}{\int_0^\infty \frac{ds}{(s+a^2)R_s}} \right] \quad (4.8)$$

with $R_s = \sqrt{(s+a^2)(s+b^2)}$ and

$$\begin{aligned} \xi(\mathbf{r}) &= \frac{1}{2} \left[-a^2 - b^2 + z^2 + \varrho^2 \right. \\ &\quad \left. + \sqrt{(-a^2 - b^2 + z^2 + \varrho^2)^2 + 4(-a^2 b^2 + b^2 z^2 + a^2 \varrho^2)} \right] \end{aligned} \quad (4.9)$$

as a solution of (4.7) with $\varrho^2(x, y) := x^2 + y^2$, $\xi(\mathbf{r}) \geq -a^2$ and $\xi(\mathbf{r}) \equiv 0$ on the leader surface. The components of the electric field are

$$E_\varrho = -\frac{\partial \Phi}{\partial \varrho} = \frac{E_0 z}{\int_0^\infty \frac{ds}{(s+a^2)R_s}} \frac{1}{(\xi + a^2)R_\xi} \frac{\partial \xi}{\partial \varrho}, \quad (4.10)$$

$$E_z = -\frac{\partial \Phi}{\partial z} = E_0 \left[1 - \frac{\xi}{\int_0^\infty \frac{ds}{(s+a^2)R_s}} \right] + \frac{E_0 z}{\int_0^\infty \frac{ds}{(s+a^2)R_s}} \frac{1}{(\xi + a^2)R_\xi} \frac{\partial \xi}{\partial z}. \quad (4.11)$$

Furthermore

$$\nabla\xi(\mathbf{r}) = \mathbf{r} + \frac{\begin{pmatrix} x(a^2 - b^2 + z^2 + \varrho^2) \\ y(a^2 - b^2 + z^2 + \varrho^2) \\ z(-a^2 + b^2 + z^2 + \varrho^2) \end{pmatrix}}{\sqrt{(-a^2 - b^2 + z^2 + \varrho^2)^2 + 4(-a^2b^2 + b^2z^2 + a^2\varrho^2)}} \quad (4.12)$$

and

$$\int \frac{ds}{(s+a^2)R_s} = \frac{2}{(a^2-b^2)\sqrt{s+a^2}} + \frac{1}{\sqrt{a^2-b^2}^3} \ln \left(\frac{\sqrt{s+a^2} - \sqrt{a^2-b^2}}{\sqrt{s+a^2} + \sqrt{a^2-b^2}} \right) + C \quad (4.13)$$

where C is an integration constant. By inserting (4.12) and (4.13) into (4.10) and (4.11), we obtain the electric field of a negative leader in the ambient field E_0 :

$$\begin{aligned} \mathbf{E}(\mathbf{r}) = & E_0 \left[1 - \frac{\frac{2\sqrt{a^2-b^2}}{\sqrt{\xi+a^2}} + \ln \left(\frac{\sqrt{\xi+a^2} - \sqrt{a^2-b^2}}{\sqrt{\xi+a^2} + \sqrt{a^2-b^2}} \right)}{\frac{2\sqrt{a^2-b^2}}{a} + \ln \left(\frac{a-\sqrt{a^2-b^2}}{a+\sqrt{a^2-b^2}} \right)} \right] \mathbf{e}_z \\ & - \frac{E_0 z}{\sqrt{\xi+a^2}^3 (\xi+b^2)} \frac{1}{\frac{2}{(a^2-b^2)a} + \frac{1}{\sqrt{a^2-b^2}^3} \ln \left(\frac{a-\sqrt{a^2-b^2}}{a+\sqrt{a^2-b^2}} \right)} \\ & \times \left[\mathbf{r} + \frac{\begin{pmatrix} x(a^2 - b^2 + z^2 + \varrho^2) \\ y(a^2 - b^2 + z^2 + \varrho^2) \\ z(-a^2 + b^2 + z^2 + \varrho^2) \end{pmatrix}}{\sqrt{(-a^2 - b^2 + z^2 + \varrho^2)^2 + 4(-a^2b^2 + b^2z^2 + a^2\varrho^2)}} \right] \quad (4.14) \end{aligned}$$

4.A.2 Field enhancement close to the tip

To estimate the field close to the tip, we evaluate (4.14) on the symmetry axis $x = y \equiv 0$ for $z = a + a_0$ where a_0 is the distance from the tip. Obviously $E_x = E_y \equiv 0$ and

$$\begin{aligned} \frac{E_z}{E_0} = & 1 - \frac{\frac{2\sqrt{a^2-b^2}}{a+a_0} + \ln \left(\frac{a+a_0-\sqrt{a^2-b^2}}{a+a_0+\sqrt{a^2-b^2}} \right)}{\frac{2\sqrt{a^2-b^2}}{a} + \ln \left(\frac{a-\sqrt{a^2-b^2}}{a+\sqrt{a^2-b^2}} \right)} \\ & - \frac{2}{(a+a_0) \left((a+a_0)^2 - a^2 + b^2 \right)} \frac{1}{\frac{2}{(a^2-b^2)a} + \frac{1}{\sqrt{a^2-b^2}^3} \ln \left(\frac{a-\sqrt{a^2-b^2}}{a+\sqrt{a^2-b^2}} \right)}. \quad (4.15) \end{aligned}$$

The production of X-rays in air by monoenergetic electron beams with energies of 1 MeV or less

Experiments have shown that laboratory discharges in air with voltage pulses of 1 MV can produce X-rays at 1 to 2 m distance with a maximum in the energy distribution at approximately 200 keV. Triggered lightning generates a considerable number of photons with energies between 30 keV and 250 keV. We model the motion and energy dissipation of monoenergetic beams of electrons with energies of up to 1 MeV in air at 1 bar using a three dimensional relativistic Monte Carlo code. We simulate the production of photons through Bremsstrahlung on air molecules. Detectors used by Kochkin et al. do not detect photons with energies below 30 keV. Thus we remove electrons with energies below 30 keV. We present the spatial and energy distribution of photons after all electron energies have dropped below 30 keV which happens after less than 1 ns. Most photons with energies above 30 keV are emitted in an angle of approximately 30° relative to the initial electron beam whereas photons with lower energies are emitted more isotropically. Photons are observed below 20 eV, then there is an energy gap due to photoionization up to approximately 500 eV. The upper part of the photon spectrum is concentrated between 10 keV and 250 keV.

5.1 Introduction

Very energetic photons were measured not only in thunderstorms, but also in laboratory discharges [152, 41, 93, 43, 121, 134, 136, 122, 111, 143, 88, 89]. Kochkin et al. [88, 89] have imaged the temporal evolution of a discharge identifying the moment when X-rays are produced. They have shown that X-rays are generated when positive and negative streamers approach each other, enhance the electric field between them beyond the generic streamer effect and accelerate electrons into the relativistic regime. For an applied voltage of 1 MV these electrons create Bremsstrahlung photons whose energy distribution shows a maximum at approximately 200 keV. In triggered lightning [38] X-rays with energies between 30 keV and 250 keV have been measured. In the following chapter we investigate the production of Bremsstrahlung photons by monoenergetic electron beams with energies between 100 keV and 1 MeV in air at 300 K at 1 bar; we see that a considerable number of photons with energies between 10 keV and approximately 250 keV is produced and also maintained.

5.1.1 Organization of the chapter

In section 5.2 we briefly describe the model to trace electrons and photons through air and list all collision processes of these species with air molecules that we have implemented.

In section 5.3 we present and discuss our results. We present the number and mean energy of electrons as a function of time. We also give the photon number as well as the energy and spatial distribution of photons. We show that the photon energy distribution can be fitted with analytical equations; these can help to predict the photon energy distribution for different initial electron energies.

We summarize our results in section 5.4.

5.2 Set-up of the model

We use a three dimensional relativistic Monte Carlo code where we trace electrons and photons through air at 1 bar and 300 K. The experiments for the investigation of X-ray production from discharges by Kochkin et al. [88, 89], have voltages of approximately 1 MV. Here we start with preaccelerated electron beams with initial energies of $E_0 = 100 \text{ keV}, 200 \text{ keV}, \dots, 1000 \text{ keV}$ and do not take any electric field into account. Hence there is no additional energy source. Since detectors in these experiments have detection thresholds of approximately $E_{th} = 30 \text{ keV}$, we are interested in the production of photons above this energy and we remove electrons with energies below 30 keV from our simulations. We start with 500.000 initial electrons.

In our Monte Carlo code we use relativistic equations of motion to update the position of single electrons between two collisions with air molecules. Since we do not take any electric or magnetic field into account, the velocity is constant between two collisions.

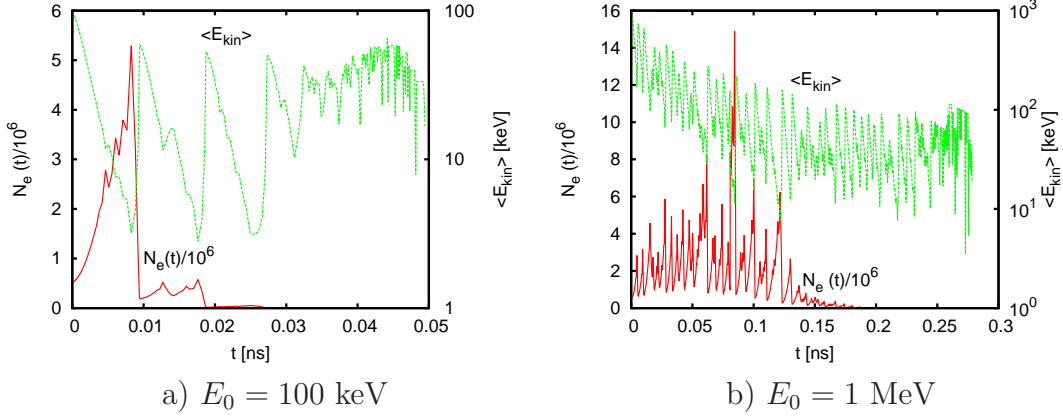


Figure 5.1: The electron number $N_e(t)$ (red) and the mean electron energy $\langle E_{kin} \rangle$ (green) as a function of time for a shower with 500.000 initial electrons with energies a) $E_0 = 100 \text{ keV}$ and b) $E_0 = 1 \text{ MeV}$.

As scattering processes we include elastic electron-nucleus scattering [110, 82, 129, 130, 52, 163], molecular excitations [110, 97], electron impact ionization [84], electron-nucleus Bremsstrahlung [12, 75, 90] and attachment [108, 125, 97] of electrons to oxygen, as previously used in [29, 101, 104, 25, 26, 92, 91]. Details on the implementation of the angle of elastic scattering and the energy splitting for an ionization event as well as the validation of our code can be found in chapter 6 and Appendix A. We note here that electron-electron Bremsstrahlung will not contribute to the photon spectrum since this process is only important for electron energies above 1 MeV [92]. Hence photons are produced by electron-nucleus Bremsstrahlung. We treat these photons as particles moving with the speed of light and we include photoionization [131], Compton scattering [66, 128], pair production [90] and Rayleigh scattering [144]. The simulation ends when the number of electrons with energy larger than 30 keV vanishes.

5.3 Results

5.3.1 Number and energy of electrons

Figure 5.1 shows the number $N_e(t)$ of electrons with energy above 30 keV and the mean energy $\langle E_{kin} \rangle(t)$ of these electrons as a function of time for electron showers of a) 100 keV and b) 1 MeV. Fig. 5.1 shows that the electron number increases due to ionization. After a time there are electrons with energies below 30 keV which are removed from the simulation; thus the electron number of decreases. Subsequently ionization leads to an increase of the electron number again. Hence there is an oscillating behaviour until all electrons have energies below 30 keV and are removed. Since the mean energy increases,

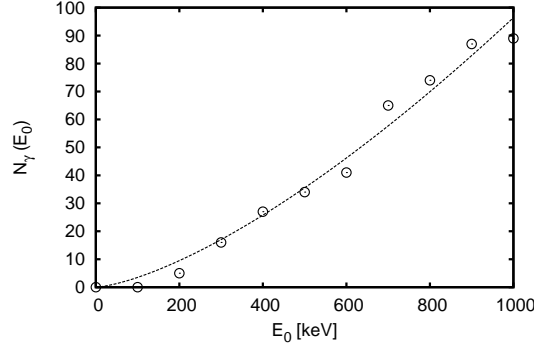


Figure 5.2: The number N_γ of photons with energy above 30 keV as a function of the initial energy E_0 for 500.000 initial electrons with energies $E_0 = 100, \dots, 1000$ keV. The line shows fit (5.1).

whenever an electron drops below 30 keV and is removed from the statistics, the mean energy oscillates as well.

Figure 5.1 also shows that there is a sudden decrease of the electron number after 0.01 ns for a beam of $E_0 = 100$ keV whereas the loss of electrons for $E_0 = 1$ MeV is rather continuous. As we will explore further in chapter 6, for electron showers with higher initial energies, different subshowers develop at slightly different times and hence, here the electron number evolves more smoothly in time. The life time of the electron showers depends on the initial energy E_0 ; it reaches from ≈ 0.05 ns for 100 keV up to ≈ 0.27 ns for 1 MeV.

5.3.2 The number, energy and spatial distribution of photons

Figure 5.2 shows the final photon number $N_\gamma(E_0)$ as a function of the initial electron energy E_0 of a shower with 500.000 initial electrons. The line in Fig. 5.2 shows fit

$$N_\gamma(E_0) = \left(\frac{E_0}{(40 \pm 2) \text{ keV}} \right)^{1.44 \pm 0.11} \quad (5.1)$$

which was determined by gnuplot's [63] intrinsic least square fit algorithm. On average one photon with energy above 30 keV is produced by 100.000 electrons with $E_0 = 200$ keV or 5600 electrons with $E_0 = 1$ MeV.

The crosses in Figure 5.3 show the logarithmic energy distributions of photons for electron showers of 500.000 initial electrons with energies of a) 400 keV after 0.17 ns, b) 600 keV after 0.22 ns and c) 1 MeV after 0.27 ns when all electron energies have dropped below 30 keV and thus no new photons with energies above 30 keV can be produced. The

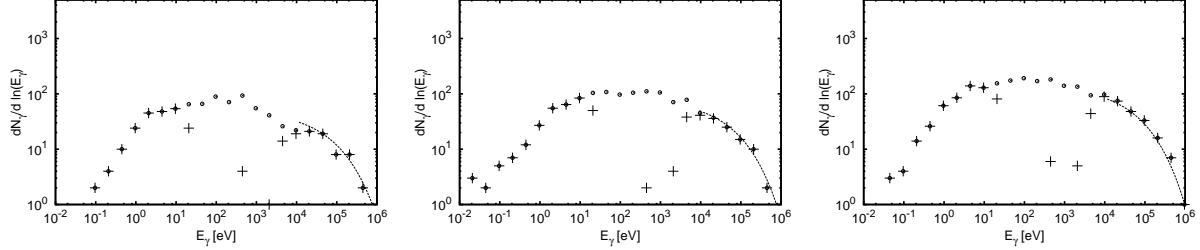


Figure 5.3: The logarithmic energy distribution $dN_\gamma/d \ln E_\gamma$ for an electron beam with a) $E_0 = 400$ keV, b) $E_0 = 600$ keV and c) $E_0 = 1$ MeV as a function of the photon energy E_γ . The crosses show the distribution at the end of the simulation when all electron energies have dropped below 30 keV. The circles show the distribution of all photons as they are produced, thus without their energy losses. The solid lines show fit (5.2).

lines show that the photon energy distribution can be fitted well with

$$n_\gamma(E_\gamma) \sim e^{-\sqrt{\frac{E_\gamma}{29 \text{ MeV}}}} \quad (5.2)$$

for photon energies above 10 keV. Figure 5.3 shows that for all three cases there are many photons with energies below 20 eV. Then there is a gap due to photoionization between 20 eV and ≈ 500 eV where photons are absorbed by air molecules liberating an electron. The circles in Fig. 5.3 show the energy distribution of photons as they are produced, integrated over time. It shows that the low-energy part below 20 eV and the high-energy part above approximately 1 keV have hardly changed in time. However, photons generated in the energy range between 20 eV and 500 eV are absorbed by air molecules. The photon energy distribution above 1 keV can be clearly distinguished from the low-energy part. There is a clear maximum at approximately 10 keV. Taking the energy threshold of 30 keV of the detectors in the experiments by Kochkin et al. [88, 89] into account, there is still a considerable number of photons between 30 keV and 250 keV.

Figure 5.4 shows the spatial distribution of all photons (panels a and b) and of all photons with energies above 30 keV (panels c-f) after 0.17 ns (when all electron energies have dropped below 30 keV) for $E_0 = 400$ keV and after 0.27 ns for $E_0 = 1$ MeV. The projections onto the xz plane show that photons with energies above 30 keV are beamed into the z direction which is the initial direction of the electrons as indicated by the arrow. It also shows that electron beams with an initial energy of 400 keV produce less photons above 30 keV than a shower of 1 MeV electrons. In both cases there is a symmetry between the x and y coordinate since there is no ambient electric field and the beam was emitted in the z direction. From a detailed analysis [90], we know that relativistic electrons emit photons predominantly in forward direction; thus the emission angle of most high-energy photons has to be close to 0° . Photons with energies below 30 keV are

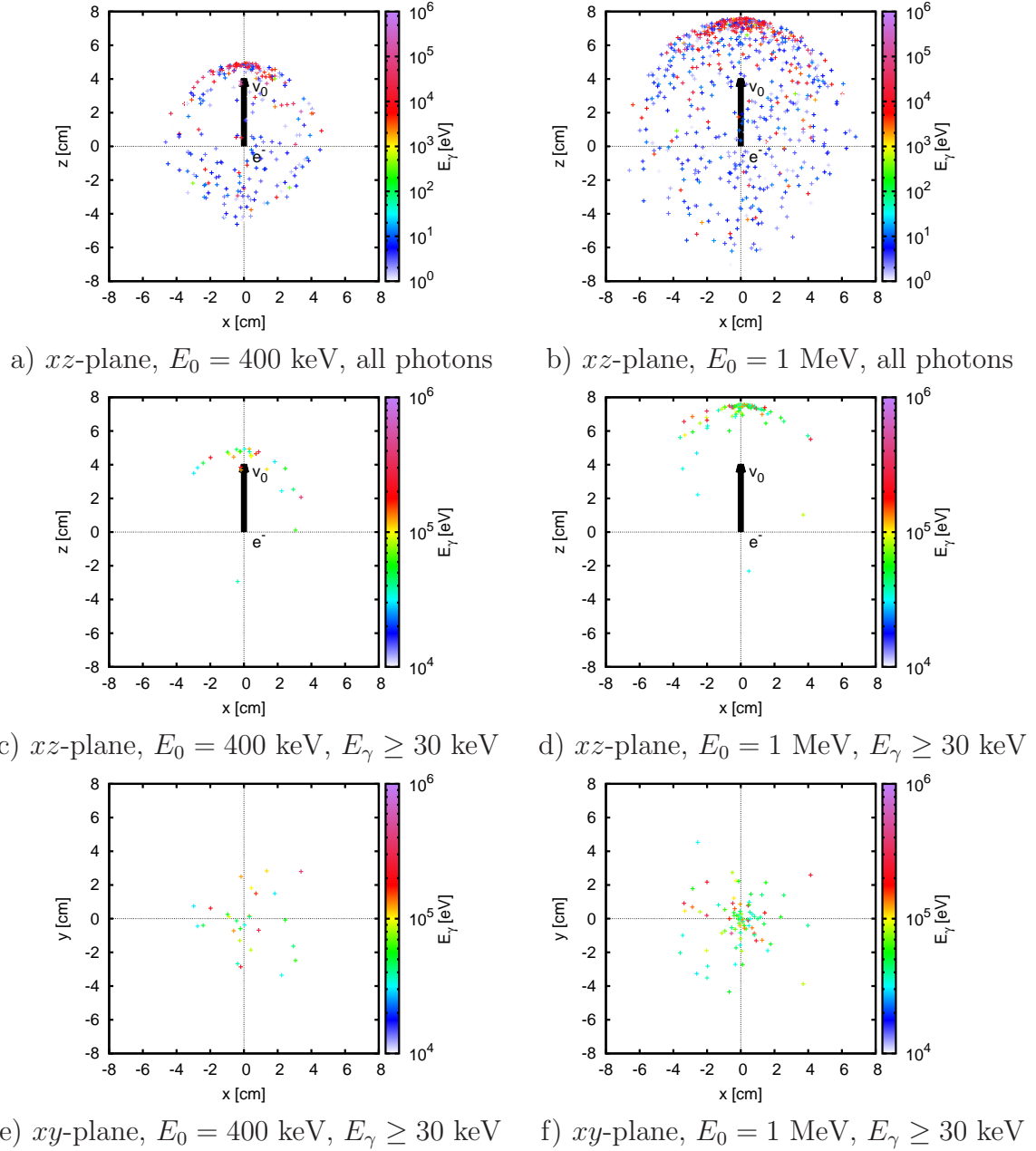


Figure 5.4: Position and energy of all photons (panels a and b) and of all photons with energy above 30 keV (panels c - f) generated by a beam of 500.000 electrons moving in z direction, all with initial energy of 400 keV after 0.17 ns (panels a, c and e) and for an electron beam with initial energy of 1 MeV after 0.27 ns (panels b, d and f). Panels a) - d) show the projection onto the xz plane, panels e) and f) onto the xy plane. The arrow indicates the direction of the initial electron beam, and the color the photon energy.

not emitted in forward direction; additionally Compton scattering changing the photon direction, is more important for photons with lower energies. For $E_0 = 400$ keV and $E_0 = 1$ MeV most photons with energies above 30 keV are emitted within an angle of $\approx 32^\circ$ relative to the direction of the initial electron beam whereas photons with energies below 30 keV show a more isotropic behaviour.

5.4 Conclusion

We have calculated the motion of preaccelerated, monodirected and monoenergetic electron beams with energies from 100 keV to 1 MeV in air at standard temperature and pressure without electric field, and we have removed electrons with energies below 30 keV. Electron beams with initial energy of 1 MeV produce 18 times as many photons with energy above 30 keV than electron beams with an initial energy of 200 keV; all of these photons are produced within 1 ns.

We have presented the spatial and energy distribution of the photons. Whilst photons with energies above 30 keV are emitted in an angle of $\approx 30^\circ$ relative to the direction of the original electron beam, photons with lower energies are emitted more isotropically. Additionally Compton scattering changes the direction of low-energy photons and leads to a widening of the photon beam. We have seen that the energy distribution of photons consists of a low-energy and a high-energy part. Inbetween there is a gap for energies between ≈ 10 eV and ≈ 500 eV due to photoionization where a photon is absorbed by an air molecule and an electron is emitted. For electron beams with initial energies from 400 keV up to 1 MeV, the high-energy tail of the photon distribution can be fitted quite well by the same exponential after different times. For beams of electrons with initial energies above 400 keV, we have obtained a considerable number of photons with energies between 30 keV and ≈ 250 keV. We remark that this is also the energy range where a considerable number of photons was detected by triggered lightning [38].

The structure of ionization showers in air generated by electrons with 1 MeV energy or less

Ionization showers are created in the earth's atmosphere by cosmic particles or by runaway electrons from pulsed discharges or by the decay of radioactive elements like radon and krypton. These showers provide pre-ionization that can play a role for discharge inception or evolution; radioactive admixtures in plasma technology use the same effect. While the CORSIKA program provides cross sections and models for cosmic particle showers down to the MeV level, we here analyze the shower structure below 1 MeV by using a three dimensional relativistic Monte Carlo discharge code for the electron dynamics. We provide a few analytical results to speed up the numerical implementation of the scattering processes. We derive and analyse the spatio-temporal structure of ionization and electron energies in the shower for incident electrons with energies of 1 keV to 1 MeV, at air pressures of 10, 100 and 1000 mbar at room temperature in great detail. We calculate the final density of O_2^- and O^- ions and the average input energy per ion. We show that the average input energy per ion increases from 20 eV for initial energies of 1 keV to 33 eV for 250 MeV and above. We also derive the electric fields generated by the electrons and residual ions of the particle showers. Finally, we study how the shower evolution and the electron energy at 1 bar is influenced by ambient electric fields of 5 or 8 kV/cm and see that for 1 keV the electron number decreases, but more slowly than without field, whereas the electron number continuously grows for 1 MeV.

This chapter has been published as [C. Köhn and U. Ebert, 2014. Plasma Sour. Sci. Technol., **23**, 045001]

6.1 Introduction

6.1.1 Energetic particles and discharges

Energetic radiation in the atmosphere can contribute to discharge inception or it can influence discharge evolution. The primary motivation of our study are high energy cosmic particle showers, but the results apply as well to ionization showers generated by radioactive decay [120] or by run-away electrons from powerful negative discharges like lightning leaders [71, 26, 95, 169] or megavolt sparks [88, 89].

Cosmic particles with energies up to 10^{20} eV [105] bombard our earth and create extensive air showers. The detection and identification of the cosmic particles is of high current interest for astroparticle physics [28, 36, 13], but their air showers also might play a role in lightning inception [148, 7, 19] or in triggering terrestrial gamma-ray flashes [70, 22, 8]. The high energy part of these particle showers is well characterized by CORSIKA (COsmic Ray SIMulations for KAscade) which is a tool to simulate extensive air showers initiated by high energy cosmic ray particles [33]. The initial incident particles can be protons, light nuclei up to iron ($Z = 26$), photons and electrons. CORSIKA simulates the particle showers they create in earth's atmosphere, taking hadronic and electromagnetic interactions with air molecules into account [21, 85]. CORSIKA can also be used to calculate the production of neutrinos and Cherenkov radiation [32], i.e. radiation of electrons in dense media when they travel faster than the local speed of light. However, these models do not resolve particle dynamics below 1 MeV which is the limiting energy for electron-positron pair production. On the other hand, common plasma discharge models and cross section data bases [110] extend only up to electron energies of 1 keV. Therefore there is a need to fill the gap and to derive the spatio-temporal distribution of electrons in the eV and the thermal range created by particles in the keV and GeV regime, in particular, when we want to study the sensitivity of these particle showers to ambient electric fields.

The same question arises when discharge inception is facilitated by radioactive admixtures. The streamer discharge experiments performed with an admixture of ^{85}Kr in [120] clearly show that the traces of the emitted β electrons with a maximal energy of 687 keV and an average energy of 251 keV have a different influence on discharge morphology than a more uniform background ionization.

6.1.2 Simulating showers created by electrons with energies ≤ 1 MeV

For particle energies of 1 MeV or below, the showers consist predominantly of electrons and positrons. Therefore we here simulate and characterize ionization showers created by electrons with initial energies between 1 keV and 1 MeV in air at room temperature for pressures of 10, 100 and 1000 mbar which correspond to altitudes in the atmosphere of

32, 16 and 0 km.

We use the Monte Carlo code in three spatial dimensions that was originally designed for streamer modeling and described in [103]; in simulations with this code run-away electrons with energies up to 3.5 keV were found [101]. We extended this code with relativistic equations of motion for the electrons and with cross sections for electron-nucleus Bremsstrahlung, elastic scattering and ionization for electrons up to 1 MeV. We concentrate on electrons with initial energies of 1 MeV or lower as the high-energy models stop at this energy.

6.1.3 Content and organization of the chapter

In section 6.2 we introduce the model. We discuss the collisions included, especially how we have implemented ionization, elastic, inelastic and reaction mechanisms. We also describe briefly how we include thermal effects. The results are presented in section 6.3. We plot and discuss the temporal evolution of the electron number and the spatio-temporal distribution of the electrons as well as the energy of the electrons and of the negative oxygen ions. We also calculate the electric field generated by the space charge separation within the particle shower. In section 6.4 we will show how an ambient field influences the shower. Section 6.5 summarizes our results and gives a brief outlook to future research. Details of our calculations regarding the ionization cross section which help to speed up calculations, can be found in section 6.A and regarding the speed of oxygen ions in section 6.B. In section 6.C we briefly show how results change if we use different cross sections.

6.2 Cross sections and air temperature model

As the mass of air molecules is much higher than that of an electron, we consider them to be immobile and do not trace them. We implicitly place air molecules at random positions, thus as a constant background and draw random numbers to determine whether there is a collision of an electron with an air molecule and, if so, which collision takes place.

We model the motion of electrons in air which consists of 78.12% N₂, 20.946% O₂ and 0.934% Ar. In most cases we do not consider any electric or magnetic field; hence there is no external energy source. Especially we do not take space charge effects into account; thus the physics of such showers do not depend on the initial electron number. For an initial electron energy of 1 keV and 1 MeV we will also include an ambient electric field. We include ionization [84], elastic scattering [110, 82, 129, 130, 52, 163], electron-nucleus Bremsstrahlung [12, 90], excitations [110, 97] and attachment [97, 108]. We note here that we ran also simulations where we trace Bremsstrahlung photons and included photoionization. However, we have not seen any significant changes to the results presented here.

6.2.1 Elastic scattering

Our particle code was originally developed to study streamer dynamics [103] where electrons reached energies up to 3.5 keV in the simulations of [101]. For electron energies below 10 keV, we use cross sections by [129, 130, 52, 163]. For energies above 10 keV, we extended the energy range of the total cross section for elastic scattering with a screened Rutherford expression [82, 118]

$$\sigma(E_{kin}) = \frac{2\pi Z^2 e^4}{v^2 p^2 \eta(\eta + 1)}, \quad (6.1)$$

where v , p and η depend on E_{kin} as
 $v = \sqrt{c^2 - m_e^2 c^6 / (E_{kin} + m_e c^2)^2}$,
 $p = \sqrt{(E_{kin} + m_e c^2) / c^2 - m_e^2 c^2}$ and

$$\eta(E_{kin}) = \frac{\chi_0^2}{2} \left[1 + 4\alpha Z \chi_0 \left(\frac{1 - \beta^2}{\beta} \ln \chi_0 + \frac{0.231}{\beta} + 1.448\beta \right) \right] \quad (6.2)$$

with $m_e \approx 9.1 \cdot 10^{-31}$ kg, $\beta(E_{kin}) = v/c$, $\alpha \approx 1/137$, $\chi_0(E_{kin}) = \hbar \mu Z^{1/3} / (0.885 p a_0)$, $e \approx 4.80 \cdot 10^{-10}$ esu and $a_0 \approx 2.82 \cdot 10^{-13}$ cm where E_{kin} is the kinetic energy of the electron and Z is the atomic number. $\hbar \approx 1.05$ Js is the reduced Planck constant, and $\mu = 0.635$ is a fitting parameter ensuring a continuous transition from Eq. (6.1) to experimental data of energies below 10 keV.

For the azimuthal angle we use [118, 146]

$$\frac{d\sigma}{d\Omega}(E_{kin}, \theta) = \frac{\sigma(E_{kin})}{4\pi} \cdot \frac{4\eta_1(1 + \eta_1)}{(1 - \cos\theta + 2\eta_1)^2} \quad (6.3)$$

with $\eta_1 = 5.77 \cdot E_{kin}^{-1.377}$. The polar angle φ is equally distributed over $[0, 2\pi)$.

6.2.2 Ionization cross section

To model ionization we use the relativistic binary-encounter Bethe (RBEB) total cross section $\sigma(E_{kin})$ and the differential cross section $d\sigma/dW(E_{kin}, W)$ [84] where E_{kin} and W are the energies of the incident and the ejected electron, respectively. W can be obtained by solving [25]

$$R = \frac{\int_{E_{min}}^W \frac{d\sigma}{dW}(E_{kin}, \bar{W}) d\bar{W}}{\int_{E_{min}}^{\frac{E_{kin}}{2}} \frac{d\sigma}{dW}(E_{kin}, \bar{W}) d\bar{W}} \quad (6.4)$$

where $R \in [0, 1)$ is a uniformly distributed random number, and $E_{min} = 0.01$ eV is the lower threshold for the energy of secondary electrons. We have derived an explicit

expression (6.24) for the integrals in (6.4) that can be found in section 6.A. We solve (6.24) by using the regula falsi method [20]. The scattering direction of the electron is parameterized by the angles $\Theta_{sca} = \angle(\mathbf{p}_i, \mathbf{p}_{sca})$ and φ_{sca} , and the direction of the emitted electron relative to the incident electron is $\Theta_e = \angle(\mathbf{p}_i, \mathbf{p}_e)$ and φ_e . Here \mathbf{p}_i is the momentum of the incident electron before scattering, \mathbf{p}_{sca} its momentum after scattering and \mathbf{p}_e the momentum of the emitted electron. $\Theta_{sca,e}$ are given by [25]

$$\cos \Theta_{sca} = \sqrt{\frac{(E_{kin} - W)(E_{kin} + 2m_e c^2)}{E_{kin}(E_{kin} - W + 2m_e c^2)}} \quad (6.5)$$

$$\cos \Theta_e = \sqrt{\frac{W(E_{kin} + 2m_e c^2)}{E_{kin}(W + 2m_e c^2)}}. \quad (6.6)$$

The polar angles $\varphi_{sca,e}$ are uniformly distributed on $[0, 2\pi)$.

6.2.3 Electron attachment

After having lost energy by collisions, electrons can attach to oxygen through two processes [97, 108, 64]: An electron can split an oxygen molecule (two-body or dissociative attachment)



where the binding energy is $E_{bind} = 5.2$ eV. The speed of O^- and O is

$$v_{\text{O}} = v_{\text{O}^-} = \sqrt{\frac{m_e |\mathbf{v}|^2}{2m_{\text{O}}} - \frac{E_{bind}}{m_{\text{O}}}}, \quad (6.8)$$

where \mathbf{v} is the velocity of the incident electron and $m_{\text{O}} \approx 2.6568 \cdot 10^{-26}$ kg is the mass of an oxygen atom or ion. Details of the derivation of (6.8) can be found in section 6.B.

An electron can also attach to an oxygen molecule directly, but only in the presence of a further molecule to conserve energy and momentum (three-body attachment)



where M is N_2 or O_2 [97, 108]. Since three-body attachment needs the presence of two molecules, the rate of this process depends on air density non linearly, but quadratically.

6.2.4 Air temperature

Our first simulations have shown that the energy of electrons continues to decrease to below 0.025 eV. The lower threshold energies for two- and three-body attachment are 4.4

eV and 0.07 eV, respectively. Therefore at vanishing air temperature, there are always very low energy electrons that stay free. Therefore we have included the thermal energy of the neutral air molecules at 300 K (corresponding to 0.025 eV) for collisions with electrons with kinetic energies below 1 keV with the method described in [127]. Here the energy E_n of the neutral is sampled from the Maxwell - Boltzmann distribution

$$f(\epsilon) = \sqrt{2\epsilon} e^{-\epsilon + \frac{1}{2}} \quad (6.10)$$

with $\epsilon = E_n/(k_B T)$ and $k_B \approx 1.38 \cdot 10^{-23}$ J/K.

6.3 Results

6.3.1 Evolution of electron and ion number in the shower

We performed simulations for incident electrons with energies of 1, 10, and 100 keV and 1 MeV. In the first three cases we averaged our results over 100 initial electrons, while for 1 MeV there was already sufficient self-averaging with a single electron starting the shower. We studied the showers in air at 10, 100 and 1000 mbar at room temperature.

Figure 6.1 shows the electron number in the shower as a function of time. Within our simulations the electrons move only by some 100 μm to 30 cm (cf. section 6.3.3 for the shower length). Thus pressure variations within the simulation volume are negligible.

In all cases, first the electron number increases while the shower develops, then it reaches a plateau (except for 1 MeV where the plateau is less pronounced), and finally the electron number decreases due to attachment to oxygen. Starting with an electron with 1 keV at 1 bar, the maximal electron number within the shower is 37.4 ± 2.6 electrons; for 1 MeV, it is approximately 34 000. We determined the error in the electron number for 1 keV by running 20 simulations with one initial electron and different realisations of random numbers. For higher initial energies the statistics becomes better and thus the error becomes smaller. Table 6.1 shows the initial electron energy E_0 and the maximal electron number $N_{max}(E_0) = \max_t N_e(E_0, t)$; the average input energy $E_0/N_{max}(E_0)$ per electron ranges from 27.03 eV for $E_0 = 1$ keV up to 29.52 eV for $E_0 = 1$ MeV independently of pressure p . For comparison, the ionization energy of N_2 is 15.6 eV, and of O_2 12.06 eV.

As expected, the electron density essentially decreases due to electron attachment to oxygen though recombination is included. Figure 6.3 a) shows the production of O_2^- and O^- ions as a function of time for an incident electron with 1 keV energy. Note that the maximal number of oxygen ions is larger than the maximal electron number as some electrons continue to ionize more molecules while other electrons already attach. For all electron energies and for 1 bar as well as for 100 mbar the production of O_2^- ions is the dominant process, while the number of O^- increases for smaller pressure until two-body attachment and the subsequent formation of O^- is the dominant process at 10 mbar. Fig. 6.3 b) shows the electron number and the added number of electrons and O_2^- ions and of

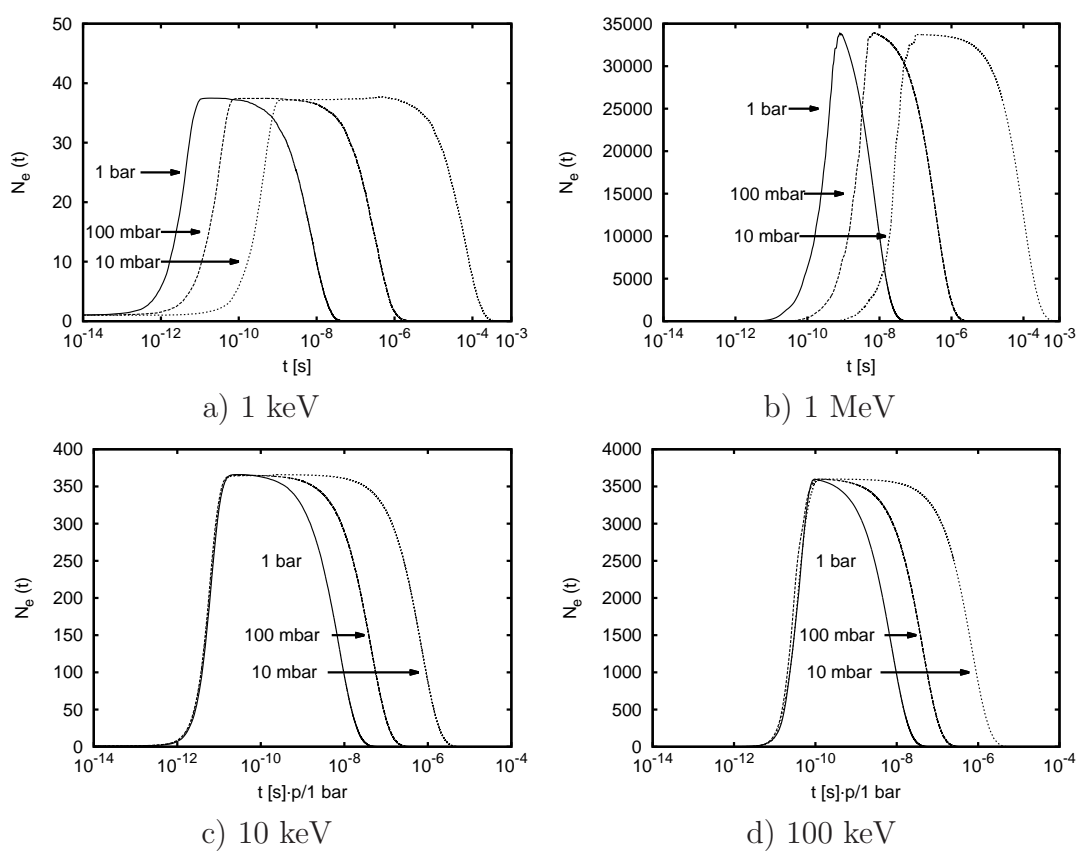


Figure 6.1: The electron number in a shower as a function of time generated by one initial electron with an energy E_0 of a) 1 keV, b) 1 MeV, c) 10 keV and d) 100 keV for 10, 100 and 1000 mbar. For 1, 10, and 100 keV we averaged over 100 runs. In panels c) and d) the plots for 100 mbar (10 mbar) were shifted by a factor 10 (100) on the time axis.

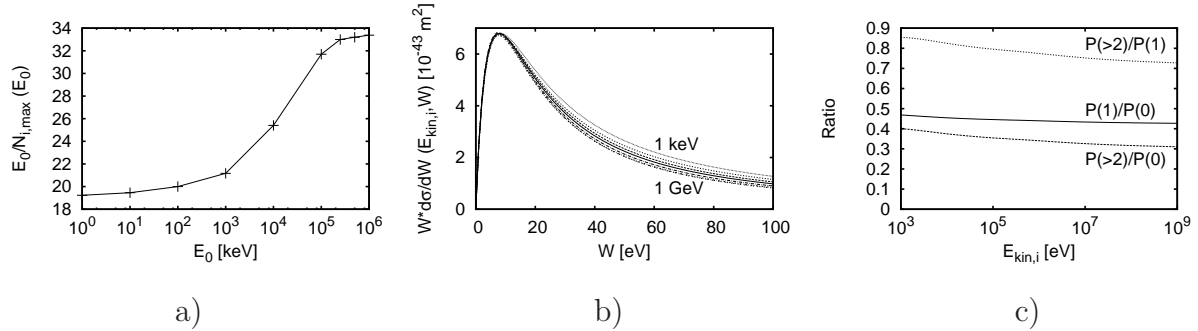


Figure 6.2: a) The average input energy per ion as a function of the initial electron energy E_0 . b) The energy distribution $W \cdot d\sigma/dW$ for ionization as a function of the secondary electron energy W . $d\sigma/dW$ is given by (6.19). All distributions are normalized to the same maximum. The different lines represent different incident energies $E_{kin,i}$ of the primary electron between 1 keV and 1 GeV and increasing by factors of 10. c) The ratio of the probabilities of subsequent ionizations by secondary electrons as function of incident electron energy $E_{kin,i}$. $P(0)$ and $P(1)$ denote the probabilities of no more or only one more subsequent ionization; $P(> 2)$ denotes the probability of two or more subsequent ionizations.

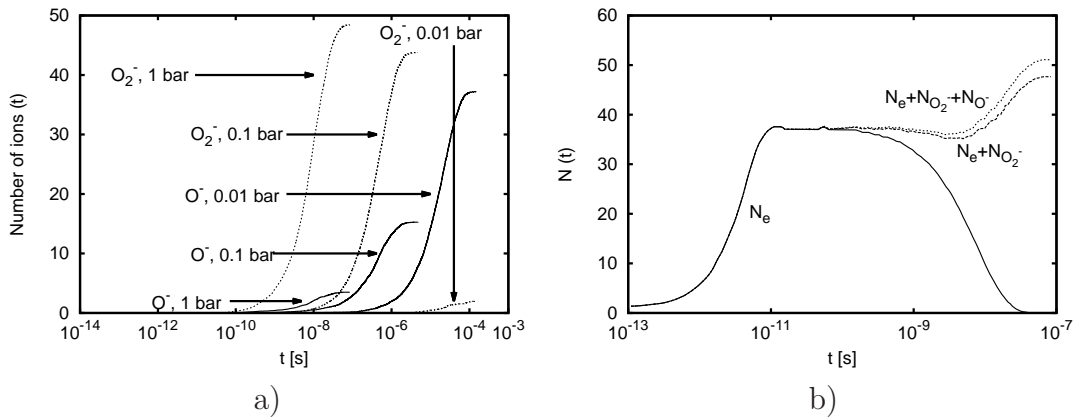


Figure 6.3: a) The number of O_2^- (dotted line) and O^- (solid line) ions as a function of time for an air shower at 1000, 100 and 10 mbar generated by an electron of 1 keV energy. b) The number of electrons (solid line), of electrons and O_2^- ions (dashed line) and of electron, O_2^- and O^- ions (dotted line) as a function of time for 1 keV and 1 bar. The dip at approximately 10 ns is due to recombination with positive ions.

electrons, O_2^- and O^- ions for 1 keV and 1 bar. It shows that when the electron number starts to decrease, first the number of O_2^- ions starts to increase; after approximately 10 ns there is also an effect of O^- ions. Tab. 6.1 shows that the ratio of the initial energy E_0 and the maximal number $N_{i,max}(E_0) = \max_t N_i(t, E_0)$ of positive ions varies from 19.23 eV for 1 keV up to 21.17 eV for 1 MeV. Figure 6.2 a) shows the average input energy per ion as a function of the initial energy E_0 . It shows that the average input energy per ion increases with increasing E_0 . For $E_0 = 250$ MeV, $E_0/N_{i,max}$ is approximately 33 eV which agrees well with 33.38 eV as given in [154]. Above that energy the average input energy saturates. Figure 6.2 b) shows the energy distribution of secondary electrons from impact ionization as a function of the energy W of the secondary electron. It shows that for all shown incident electron energies $E_{kin,i}$ the maximum of the distribution lies at approximately 7 eV. For a given probability which is proportional to the differential cross section, electrons with small incident energies eject electrons with higher secondary energies than electrons with high incident energies. Thus, if secondary electrons have more energy, they can perform more ionizations and thus the average input energy per ion decreases. The plot in panel b) also shows that the energy distributions for 100 MeV and 1 GeV are alike; thus the average input energy per ion saturates for energies above 100 MeV.

The probability $P(n)$ of exactly n subsequent ionizations by secondary electrons is proportional to $\int_{E_{n-1}}^{E_n} \frac{d\sigma}{dW}(E_{kin,i}, W)dW / \int_{E_{n-1}}^{E_{kin,i}/2} \frac{d\sigma}{dW}(E_{kin,i}, W)dW$ where $[E_{n-1}, E_n]$ is the energy interval of a secondary electron to produce exactly n subsequent ions. We can estimate the energy of one more impact ionization: The ionization energy of N_2 which contributes 80% to air, is approximately 15.6 eV. The average excitation energy before ionization is approximately 4.2 eV [4]; thus if the energy of a secondary electrons is below 19.8 eV, there is no expected further ionization. If the energy is above 19.8 eV there is at least one more ionization. The most expected value of the tertiary electron is 9.1 eV [84]; if this electron has also 19.8 eV, hence in total 48.7 eV, it could produce 2 subsequent ions. Hence, if the energy of the secondary electron is between 19.8 eV and 48.7 eV, it will do exactly one more ionization. If it is above 48.7 eV it will do more than two subsequent ionizations. Figure 6.2 c) shows the ratios of probabilities of subsequent ionizations by secondary electrons as a function of the incident electron energy. It shows that more than one subsequent ionization is expected rather for small incident electron energies than for high incident energies. Thus more ions are expected for small initial energies and the ratio of $E_0/N_{i,max}$ decreases.

6.3.2 Growth and decay rates

Figure 6.1 also shows the lifetime of the electron swarm. For 1 bar it takes 65 ns until all electrons have attached. For 100 mbar it takes approximately $2 \mu s$ and for 10 mbar it takes

E_0	$N_{e,max}(E_0)$	$E_0/N_{e,max}(E_0)$	$N_{i,max}(E_0)$	$E_0/N_{i,max}(E_0)$
1 keV	37	27.03 eV	52	19.23 eV
10 keV	363	27.55 eV	514	19.46 eV
100 keV	3595	27.82 eV	5000	20.00 eV
1 MeV	33875	29.52 eV	47235	21.17 eV

Table 6.1: The maximal electron number $N_{e,max}$, the ratio $E_0/N_{e,max}$, the maximal number $N_{i,max}$ of positive ions and the ratio $E_0/N_{i,max}$ as a function of the initial energy E_0 .

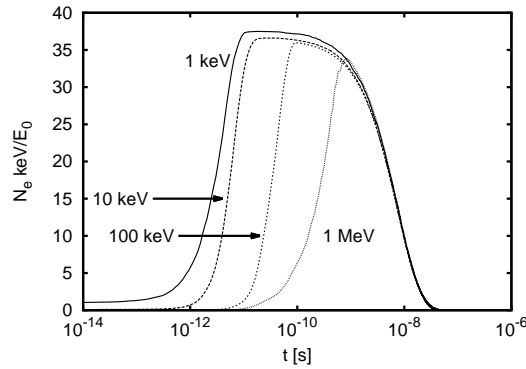


Figure 6.4: The electron number per initial energy N_e keV/ E_0 as a function of time for initial electron energies $E_0 = 1$ keV, 10 keV, 100 keV and 1 MeV for 1 bar.

0.5 ms. That is because electrons need time to lose enough energy through ionization, inelastic scattering and the production of Bremsstrahlung photons to reach the energy range where attachment can occur.

Figure 6.4 explicitly shows how the electron number depends on the initial energy E_0 of the incident electron. The relative electron number per E_0 decreases a bit with increasing initial energy, but is equal for all electron energies after 10 ns. This is because for high initial electron energies, different subshowers develop at slightly different times and their maxima will not occur simultaneously. Hence the maximal electron number in a shower of a 1 keV electron is larger than 1/1000 times the maximal electron number in a shower of a 1 MeV electron.

Growth rate

Furthermore Figure 6.1 shows that the temporal evolution of the electron number depends on pressure. Panels c) and d) in the figure are explicitly constructed to show that the growth rate of the electron number depends on air density (and pressure) according to

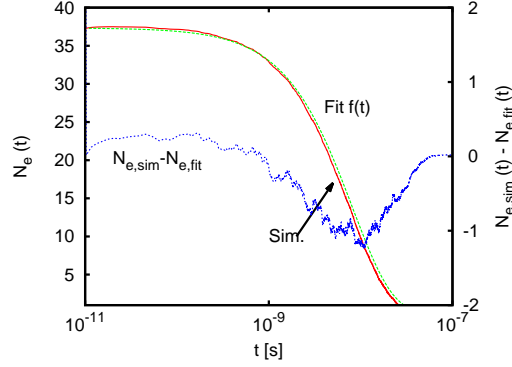


Figure 6.5: The electron number as a function of time for $E_0 = 1$ keV and 1 bar. “Sim.” (red line) denotes the number calculated in our simulation and “Fit” (green line) denotes Eq. (6.12). The blue line denotes the difference of the simulation results and (6.12).

Townsend scaling

$$N_e(p/\delta, t \cdot \delta) = N_e(p, t), \quad (6.11)$$

where δ is an arbitrary number. Here $N_e(p, t)$ is the electron number as a function of pressure and time. This Townsend scaling is due to the fact that the shower growth is dominated by impact ionization which is a two-body process, whose rate scales with the gas density. Hence the intrinsic shower growth times (for a given electron energy) are inversely proportional to the gas density.

Decay rate

However, the electron shower does not decay due to a fixed scaling law. This is related to the fact that for higher pressures the three-body attachment dominates whose rate depends quadratically on the air density; while for lower pressures (below 100 mbar) the two-body process of dissociative attachment takes over, as discussed above.

Figure 6.5 shows an example of an exponential fit to the decay of the electron number for $E_0 = 1$ keV and 1 bar where

$$N_e(t) = N_{max}(E_0) e^{-t/\tau(E_0,p)}. \quad (6.12)$$

The blue lines shows the difference of the electron number of the simulation and of the fit; the difference is at most 1 electron. This exponential fit is very good, mainly because the electrons approach a rather stationary energy distribution at this stage as we will show below, hence the energy dependent attachment rates do not vary in time. (This is also the reason why an exponential curve does not fit the shower growth well.)

E_0	p	$N_{max}(E_0)$	$\tau(E_0, p)$
1 keV	1 bar	37.34	8.19 ns
1 keV	10 mbar	37.34	61.02 μ s
1 MeV	1 bar	33 875	8.19 ns
1 MeV	10 mbar	33 875	61.02 μ s

Table 6.2: Parameters $N_{max}(E_0)$ and τ to fit Eq. (6.12) to the electron number as a function of time as in Figure 6.5.

Table 6.2 shows the values of $\tau(E_0, p)$ for the smallest and highest energies and pressures that we have investigated. Both the table and Figure 6.4 show that the decay of the electron shower does not depend on the energy E_0 of the incident electron.

We finally remark that [120, 116, 124] state that an electron shower initiated by a 1 keV electron in air at standard temperature and pressure has an attachment time of approximately 10 ns, which agrees well with our simulation result of 8.19 ns.

6.3.3 Spatial structure of the shower

Shower at 1 keV and 1 bar

Figure 6.6 shows the structure and evolution of the electron shower created by an electron with initial energy $E_0 = 1$ keV moving in z direction from the origin of the coordinate system. Note that this is the behaviour for one particular cascade. For a different shower, thus for a different realisation of random numbers in our Monte Carlo code, the position of the electrons will be different. Until all electrons have attached, the furthest electron moved about 0.5 mm. The extension of the electron cloud at 1 ns is

$$(\Delta x, \Delta y, \Delta z) \approx (90 \mu\text{m}, 80 \mu\text{m}, 100 \mu\text{m}), \quad (6.13)$$

where Δx is defined as

$$\Delta x := |\max(x) - \min(x)|, \quad (6.14)$$

and $\max(x)$ ($\min(x)$) is the maximum (minimum) of all x coordinates of all electrons at a given time. Δy and Δz are defined in the same manner.

Shower at 1 MeV and 1 bar

For an incident electron energy of 1 MeV Figure 6.7 shows the electron swarm at approximately 0.8 ns when the electron number is maximal. We here started with one (panel a and b for different realisations of random numbers) and 20 (panel c) electrons beamed in z direction. Panel a) shows that the initial electron moves forward and leaves a trace of

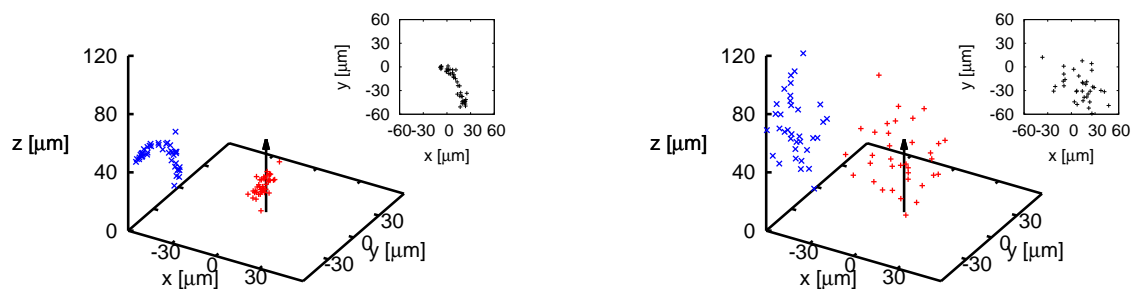
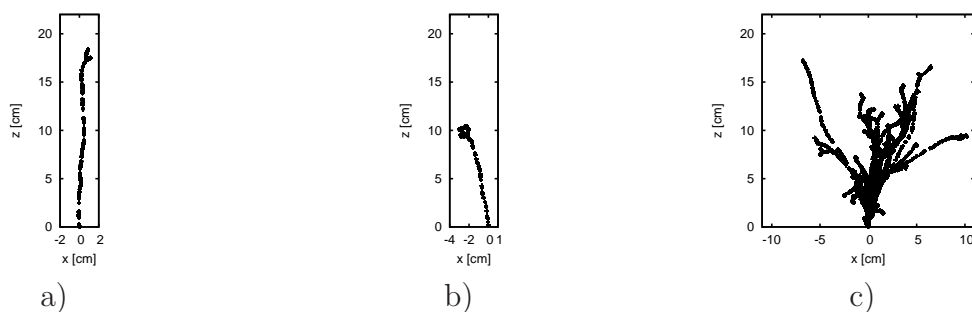
a) $t = 0.02$ nsb) $t = 1$ ns

Figure 6.6: The evolution of an electron shower in air at 1 bar and 300 K with a particular realization of random numbers. The incident electron has an energy of 1 keV; its initial direction of motion is indicated by the arrow; this initial electron attaches at 0.5 ns. The electron number is maximal at 0.02 ns. The electron number reaches zero after approximately 20 ns. The electron positions are indicated by red crosses in three dimensional space at times a) 0.02 ns and b) 1 ns. The blue points indicate the projection of the electrons onto the yz plane. The insets show the position of the electrons projected onto the xy ground plane.



a)

b)

c)

Figure 6.7: The spatial structure of an electron swarm for initial energy 1 MeV at 1 bar after approximately 0.8 ns (when the maximal electron number is reached): The position of electrons projected onto the xz plane for a swarm generated by a) one initial electron, b) one initial electron with a different realisation of random numbers and c) 20 initial electrons each with initial energy 1 MeV. All calculations are done without electrostatic interactions, i.e. panel c) shows the superposition of 20 shower realisations as plotted in panels a) and b).

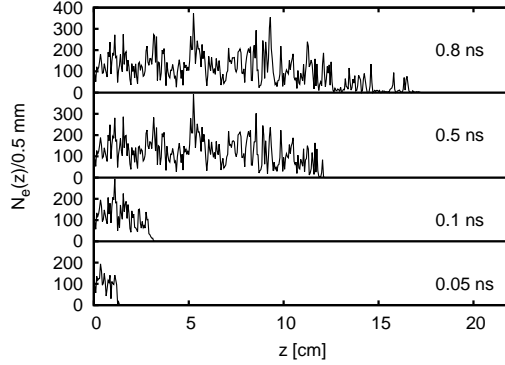


Figure 6.8: The electron number N_e as a function of z for bins of length $\Delta z = 0.5$ mm for $E_0 = 1$ MeV and 1 bar at $t = 0.05$ ns, $t = 0.1$ ns, $t = 0.5$ ns, $t = 0.8$ ns. We started the simulation with and averaged the electron number over 20 electrons.

secondary electrons behind. Panel b) shows the behaviour of one single initial electron for different random numbers. It shows that the strictly forward motion in panel a) is just one example; in panel b) the initial electron moves a bit to the side leaving residual electrons behind. Panel c) shows the position of all electrons projected onto the xz plane for 20 initial electrons. It shows the different trajectories of the high-energy initial electrons.

Figure 6.8 shows the time evolution of the electron number projected on the z axis for 20 initial electrons. It shows that the electron number per bin Δz increases in time and that the swarm moves in forward direction. It also shows that for 0.8 ns most electrons are located at $z < 12$ cm and only a few electrons lie beyond 12 cm.

6.3.4 Swarm induced electric field

Since the electrons move, leaving the positive ions behind, an electric field will be induced by the space charges. This field can be calculated from the positions \mathbf{r}_j of electrons and ions at different time steps as

$$\mathbf{E}(\mathbf{r}, t) = \frac{e}{4\pi\epsilon_0} \left(- \sum_{j=1}^{N_e(t)} \frac{\mathbf{r} - \mathbf{r}_j}{|\mathbf{r} - \mathbf{r}_j|^3} + \sum_{j=1}^{N_{i+}(t)} \frac{\mathbf{r} - \mathbf{r}_j}{|\mathbf{r} - \mathbf{r}_j|^3} - \sum_{j=1}^{N_{i-}(t)} \frac{\mathbf{r} - \mathbf{r}_j}{|\mathbf{r} - \mathbf{r}_j|^3} \right), \mathbf{r} \neq \mathbf{r}_j, \quad (6.15)$$

where $\epsilon_0 \approx 8.85 \cdot 10^{-12}$ As/Vm and $N_e(t)$, $N_{i+}(t)$ and $N_{i-}(t)$ are the numbers of electrons, positive and negative ions at time t . The field strength ranges from approximately 10^{-5} V/m at 0.1 ns when the shower just starts to develop to approximately 10 V/m at 35 ns. Figure 6.9 explicitly shows the absolute value $|\mathbf{E}|(\mathbf{r}, t)$ in the xz plane after 35 ns when most electrons have already attached.

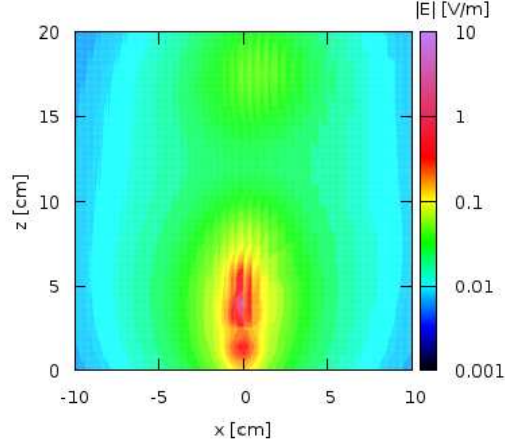


Figure 6.9: The electric field $|\mathbf{E}|$ [V/m] induced by space charge effects at $t = 35$ ns in a swarm of one initial electron with $E_0 = 1$ MeV and 1 bar in the xz plane. This is a late stage of the shower plotted in Fig. 6.7 a).

6.3.5 Energy of electrons and O^- ions

Figure 6.10 shows the electron energy spectrum after 1 ns for a shower in 1 bar air started by 100 electrons with an initial energy of $E_0 = 1$ keV. There is a gap in the energy spectrum at approximately 0.1 eV; this is the energy range where three-body attachment dominates over other processes.

Figure 6.11 shows how the mean electron energy decreases in time in a 1 MeV shower and that the most energetic electrons are in the front part of the shower. The energy of the electrons in the tail tends to approximately 1.0 eV. Thus most of them cannot ionize the background gas and the electron number does not increase further at these positions. After 0.8 ns the mean energy is almost independent of z and amounts to approximately 1.0 eV; this is the energy regime when attachment dominates over impact ionization.

Figure 6.12 shows this evolution on a logarithmic time scale, with the electron number and the mean energy of the complete electron shower as a function of time. It also shows explicitly that the electron number starts to decay when the average electron energy $\langle E_{kin} \rangle$ approaches 1 eV. As Figure 6.10 shows, there is a gap in the energy regime of three-body attachment at 0.1 eV which is more significant at higher pressures. This is probably the reason why the mean energy saturates to a value of 1.0 eV for 1 bar and only to 0.9 eV for 100 mbar. Figure 6.13 shows that O^- ions are produced by electrons with kinetic energy of approximately 10 eV, actually independently of their initial energy E_0 . The kinetic energy of most O^- ions is below 1 eV. Thus detachment from O^- ions cannot play a significant role. Detachment from O^- would play a role in increasing the number of electrons at pressures below 10 mbar [108] where the number of O_2^- is negligible. Even so

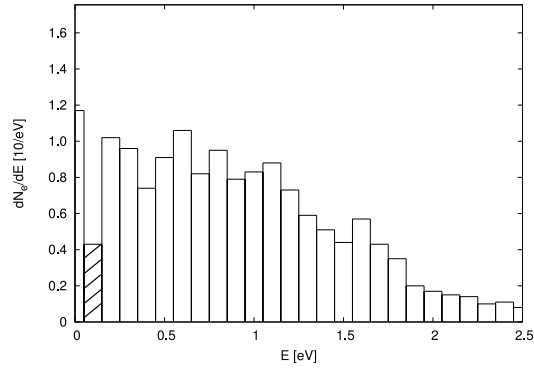


Figure 6.10: The electron energy spectrum at 1 ns in the low energy range from 0 to 2.5 eV. The shower was generated by and averaged over 100 electrons in 1 bar air if $E_0 = 1$ keV. The hatched area indicates the gap where three-body attachment is dominant. The bin size is 0.1 eV.

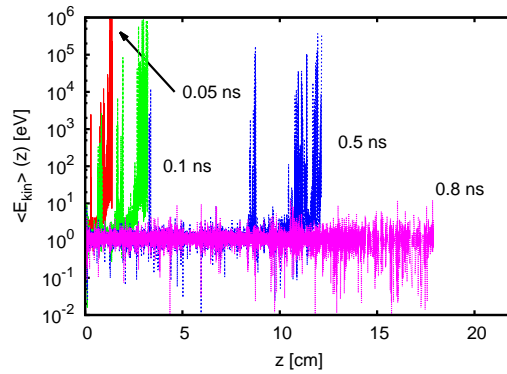


Figure 6.11: The average energy $\langle E_{kin} \rangle$ per bin $\Delta z = 0.01$ mm as a function of z for $E_0 = 1$ MeV and 1 bar at $t = 0.05$ ns (red), $t = 0.1$ ns (green), $t = 0.5$ ns (blue) and $t = 0.8$ ns (purple). We started the simulation with 20 electrons.

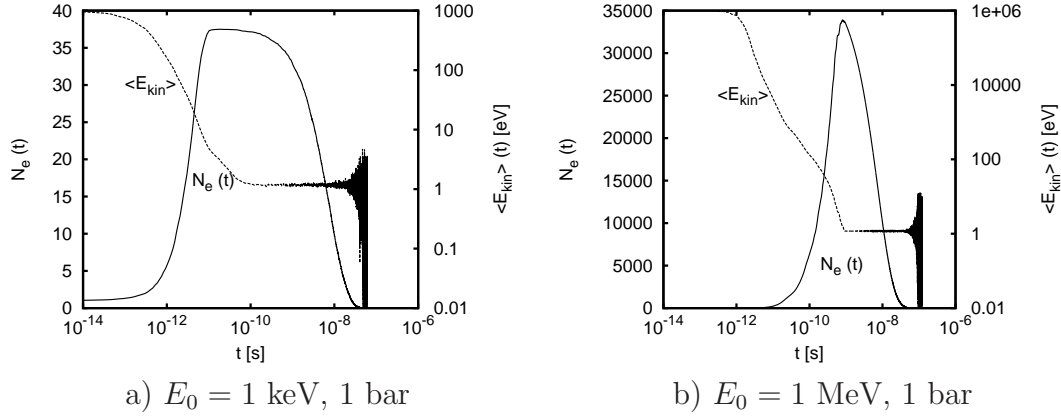


Figure 6.12: The electron number and the mean electron energy as a function of time if the energy of the initial electron was a) $E_0 = 1 \text{ keV}$ (100 initial electrons) and b) $E_0 = 1 \text{ MeV}$ (20 initial electrons); the pressure is 1 bar in both cases. The mean energy fluctuations at the end appear because the electron number becomes small.

an ambient electric field [108] would be needed.

6.4 Influence of an ambient electric field

Figure 6.14 shows the electron number and the mean energy of electrons in an external field at 1 bar. The initial energies of the incident electrons are $E_0 = 1 \text{ keV}$ and $E_0 = 1 \text{ MeV}$. For 1 keV electrons and for electric fields of 5 or 8 kV/cm the friction force through inelastic collisions with molecules is larger than the electric acceleration force [67]; thus all electrons eventually attach to oxygen. But for 1 MeV and 5 kV/cm as well as 8 kV/cm the electric force on average is larger than the friction force, and the shower grows and becomes a relativistic run-away electron avalanche (RREA). We note here that the breakdown field of classical breakdown is approximately 3 MV/m [114] while the breakdown field for run-away breakdown is 0.3 MV/m [68].

But even if no RREA is formed finally, the electrons gain more energy in a shower aligned with the electric field, and the number density and duration of the shower is higher than without electric field. A 1 keV electron creates 39 electrons in a field of 5 kV/cm and 41 in a field of 8 kV/cm, rather than 37 without field. For 0 or 5 kV/cm, it takes approximately 1 ns till the electron number decreases. But for 8 kV/cm the plateau lasts for approximately 14 ns; thus it takes a factor of 14 longer. Since electrons gain energy from the external field, the mean electron energy $\langle E_{kin} \rangle$ in the shower is higher as well. It relaxes to approximately 1.6 eV for 5 kV/cm or to 2.0 eV for 8 kV/cm. This is considerably higher than the 1.0 eV in vanishing field (see Figure 6.12).

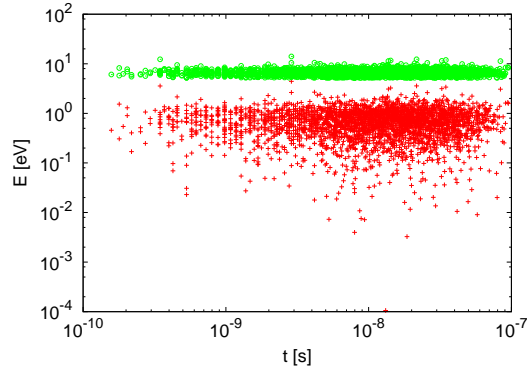


Figure 6.13: The energy of the electrons (green) attaching to oxygen and the energy of O^- (red) as a function of time for 1 bar and $E_0 = 1$ MeV. Every single point represents one electron attaching to oxygen or a O^- ion created by an electron, respectively.

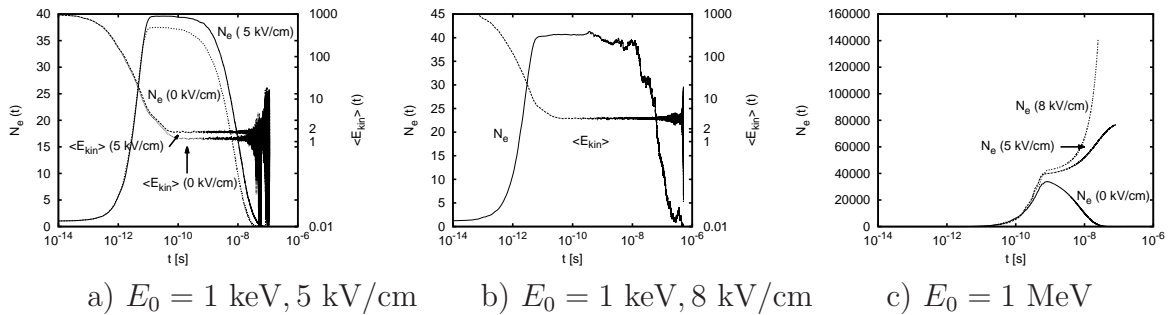


Figure 6.14: The electron number and the mean electron energy as a function of time for different external electric fields. The electric field amounts to a) 5.0 kV/cm, b) 8.0 kV/cm. The initial energy is $E_0 = 1$ keV; the pressure is 1 bar. Panel a) also shows the electron number and mean energy without electric field. c) The electron number for $E_0 = 1$ MeV at 1 bar as function of time without electric field and for 5 kV/cm as well as for 8 kV/cm.

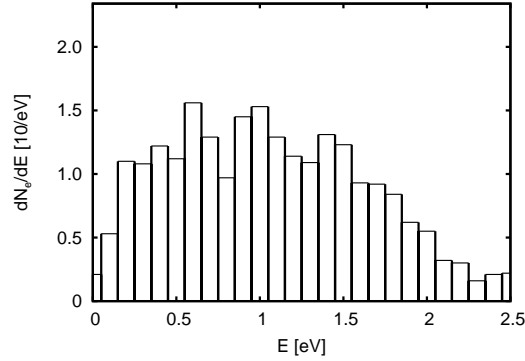


Figure 6.15: The energy spectrum in the low energy range where attachment is dominant after 1 ns. The energy of the initial electron was $E_0 = 1$ keV, and the ambient field 8 kV/cm, as in Fig. 6.14 b). The bin size is 0.1 eV.

Figure 6.15 explicitly shows the low energy spectrum of the electrons for 8 kV/cm and for a 1 keV electron (the case of Fig. 6.14 b). In contrast to Fig. 6.10 the electron number below 0.05 eV is negligible. Thus the gap of Fig. 6.10 is not visible in Fig. 6.15 although the electron number at 0.1 eV is similar. Without electric field the maximum of the spectrum lies at approximately 0.5 eV. At 8 kV/cm it lies at approximately 1 eV because of the energy gain by the ambient field. The average energy of 2 eV, however, is larger than 1 eV since there are still electrons in the energy tail up to 100 eV.

Since the number and energy of electrons is higher than in the case without ambient field, it takes longer till all electrons attach. Instead of 65 ns, it takes approximately 100 ns (for 5 kV/cm) and 500 ns (for 8 kV/cm) for all electrons to disappear. As stated in section 6.3.1, the exponential decay time without field is 8.19 ns. For 8 kV/cm it is approximately 80 ns which agrees well with data of [116] where they have simulated the motion of streamers in air in an ambient field of 10 kV/cm with a fluid model.

6.5 Conclusion and outlook

We have simulated the motion of electrons with initial energies $E_0 = 1$ keV, 10 keV, 100 keV and 1 MeV at 10 mbar, 100 mbar and 1000 mbar with and without an ambient electric field and analysed the spatial and energy distribution of the shower electrons as well as the swarm induced electric field in great detail.

We have seen that the electron number first increases due to ionization and then decreases because of the two-body and three-body attachment of electrons at oxygen. We have seen that the growth rate of the electron number is inversely proportional to the pressure, but that the decay is not. The average input energy per ion ranges from

approximately 20 eV for 1 keV till 33 eV for 1 GeV; for 250 MeV we obtain an energy of approximately 33 eV/ion as given in [154]. We have shown that more subsequent ionizations of a secondary electron are more probable for small incident electron energies and thus the energy per ion pair decreases for decreasing initial electron energy.

The exponential decay time depends on the pressure and is about 10 ns for 1 bar as mentioned in [120, 116, 124] and $\approx 61 \mu\text{s}$ for 0.01 bar. The mean electron energy tends to 1 eV. The energy spectrum of electrons shows that there is a gap at ≈ 0.1 eV where three-body attachment is dominant. For 100 mbar and 1000 mbar the production of O_2^- ions through three-body attachment is dominant; for 10 mbar it is the production of O^- ions.

We have shown that the energy dissipates as a function of time and space. While the shower propagates, the mean energy saturates to 1 eV when the maximal electron number is reached. We have calculated the electric field created by electrons and residual ions. For 1 MeV we have shown that the field is at most 10 V/m in the vicinity of the origin of the shower. Thus space charge effects can be neglected for those energies.

We have also investigated the influence of two different ambient fields on the maximal electron number and the exponential decay time for initial electron energies of 1 keV and 1 MeV. For 1 keV and fields of 5 kV/cm and 8 kV/cm the friction force on average is larger than the electric force [67]. Thus there is no continuous growth of the electron number; however, the electron number and the exponential decay time are larger than without ambient field; for 8 kV/cm the decay time is about 80 ns. For 1 MeV the friction force is smaller and thus an electron avalanche forms and the electron number continues increasing.

In the future high-energy particle models, i.e. for particles between 10^{20} eV and 1 MeV, and low-energy particle models (for energies ≤ 1 MeV) should be coupled. Beyond that, electric fields should be included. Thus the whole physics of a particle shower starting with particle energies of up to 10^{20} eV and propagating through an electric field can be captured. By coupling these two models, it will be possible to investigate the correlation between cosmic particle showers and the inception of lightning and vice versa the influence of thunderstorm fields on the detection of particle showers.

6.A The relativistic binary-encounter Bethe (RBEB) approach

In this appendix we will derive an explicit expression for Eq. (6.4). The total cross section for ionization in the relativistic binary-encounter-Bethe (RBEB) model is [84]

$$\begin{aligned} \sigma_{RBEB}(E_{kin}) &= \frac{4\pi a_0^2 \alpha^4 N}{(\beta_t^2 + \beta_u^2 + \beta_b^2) 2b'} \left\{ \frac{1}{2} \left[\ln \left(\frac{\beta_t^2}{1 - \beta_t^2} \right) - \beta_t^2 - \ln(2b') \right] \right. \\ &\times \left. \left(1 - \frac{1}{t^2} \right) + 1 - \frac{1}{t} - \frac{\ln t}{t+1} \frac{1+2t'}{(1+t'/2)^2} + \frac{b'^2}{(1+t'/2)^2} \frac{t-1}{2} \right\} \end{aligned} \quad (6.16)$$

where E_{kin} is the kinetic energy of the incident electron, $a_0 \approx 0.0529 \cdot 10^{-10}$ m the Bohr radius, $\alpha \approx 1/137$ the fine structure constant and N the orbital electron occupation number, e.g. $N_{N_2} = 10$ and $N_{O_2} = 12$. The β_i are defined as

$$\beta_i^2 := 1 - \frac{1}{(1+i')^2}, \quad i \in \{t, b, u\} \quad (6.17)$$

with $t := E_{kin}/B$ and

$$i' := \frac{I}{m_e c^2}, \quad I \in \{T = E_{kin}, B, U\} \quad (6.18)$$

where B is the ionization energy and U the kinetic energy of the bound electron on the shell, $m_e \approx 9.1 \cdot 10^{-31}$ kg the electron mass and $c \approx 3 \cdot 10^8$ m/s the speed of light. The singly differential cross section is

$$\begin{aligned} \frac{d\sigma}{dW} &= \frac{4\pi a_0^2 \alpha^4 N}{(\beta_t^2 + \beta_u^2 + \beta_b^2) 2b'} \left\{ \frac{\frac{N_i}{N} - 2}{t+1} \left(\frac{1}{w+1} + \frac{1}{t-w} \right) \frac{1+2t'}{\left(1 + \frac{t'}{2}\right)^2} \right. \\ &+ \left(2 - \frac{N_i}{N} \right) \left[\frac{1}{(w+1)^2} + \frac{1}{(t-w)^2} + \frac{b'^2}{\left(1 + \frac{t'}{2}\right)^2} \right] \\ &+ \left. \frac{1}{N(w+1)} \frac{df}{dw} \left[\ln \left(\frac{\beta_t^2}{1 - \beta_t^2} \right) - \beta_t^2 - \ln(2b') \right] \right\} \end{aligned} \quad (6.19)$$

where W is the kinetic energy of the emitted electron and $w := W/B$. df/dw is the differential dipole oscillator strength which determines N_i through

$$N_i := \int_0^\infty \frac{df}{dw} dw. \quad (6.20)$$

The integrals in Eq. (6.4) can be calculated analytically:

$$\begin{aligned}
& \int_{E_{min}}^A \frac{d\sigma}{d\bar{W}}(E_{kin}, \bar{W}) d\bar{W} \\
&= \frac{4\pi a_0^2 \alpha^4 N}{(\beta_t^2 + \beta_u^2 + \beta_b^2) 2b'} \left\{ -\frac{1}{t+1} \frac{1+2t'}{\left(1+\frac{t'}{2}\right)^2} B \ln \frac{\left(\frac{A}{B}+1\right) \left(t-\frac{E_{min}}{B}\right)}{\left(\frac{E_{min}}{B}+1\right) \left(t-\frac{A}{B}\right)} \right. \\
&+ (A-E_{min}) \left(\frac{1}{\left(t-\frac{A}{B}\right) \left(t-\frac{E_{min}}{B}\right)} + \frac{1}{\left(\frac{A}{B}+1\right) \left(\frac{E_{min}}{B}+1\right)} + \frac{b'^2}{\left(1+\frac{t'}{2}\right)^2} \right) \\
&\left. - \frac{1}{2} B \left[\ln \left(\frac{\beta_t^2}{1-\beta_t^2} \right) - \beta_t^2 - \ln(2b') \right] \left[\frac{1}{\left(\frac{A}{B}+1\right)^2} - \frac{1}{\left(\frac{E_{min}}{B}+1\right)^2} \right] \right\} \quad (6.21)
\end{aligned}$$

with [84, 83]

$$\frac{df}{dw} := \frac{N_i}{(w+1)^2}. \quad (6.22)$$

and

$$\frac{N_i}{N} \equiv 1. \quad (6.23)$$

for the binary-encounter-Bethe (BEB) model.

Inserting $E_{kin}/2$ or W for A , Eq. (6.4) becomes

$$\begin{aligned}
R &= \left[-\frac{1}{t+1} B \ln \left(\frac{\left(\frac{W}{B}+1\right) \left(t-\frac{E_{min}}{B}\right)}{\left(\frac{E_{min}}{B}+1\right) \left(t-\frac{W}{B}\right)} \right) \frac{1+2t'}{\left(1+\frac{t'}{2}\right)^2} + (W-E_{min}) \left(\frac{1}{\left(t-\frac{W}{B}\right) \left(t-\frac{E_{min}}{B}\right)} \right. \right. \\
&+ \left. \frac{1}{\left(\frac{W}{B}+1\right) \left(\frac{E_{min}}{B}+1\right)} + \frac{b'^2}{\left(1+\frac{t'}{2}\right)^2} \right) - \frac{1}{2} B \left[\ln \left(\frac{\beta_t^2}{1-\beta_t^2} \right) - \beta_t^2 - \ln(2b') \right] \left[\frac{1}{\left(\frac{W}{B}+1\right)^2} - \frac{1}{\left(\frac{E_{min}}{B}+1\right)^2} \right] \right] \\
&\times \left[-\frac{1}{t+1} B \ln \left(\frac{\left(\frac{E_{kin}}{2B}+1\right) \left(t-\frac{E_{min}}{B}\right)}{\left(\frac{E_{min}}{B}+1\right) \left(t-\frac{E_{kin}}{2B}\right)} \right) \frac{1+2t'}{\left(1+\frac{t'}{2}\right)^2} + \left(\frac{E_{kin}}{2} - E_{min} \right) \left(\frac{1}{\left(t-\frac{E_{kin}}{2B}\right) \left(t-\frac{E_{min}}{B}\right)} \right. \right. \\
&+ \left. \left. \frac{1}{\left(\frac{E_{kin}}{2B}+1\right) \left(\frac{E_{min}}{B}+1\right)} + \frac{b'^2}{\left(1+\frac{t'}{2}\right)^2} \right) - \frac{1}{2} B \left[\ln \left(\frac{\beta_t^2}{1-\beta_t^2} \right) - \beta_t^2 - \ln(2b') \right] \left[\frac{1}{\left(\frac{E_{kin}}{2B}+1\right)^2} - \frac{1}{\left(\frac{E_{min}}{B}+1\right)^2} \right] \right]^{-1}. \quad (6.24)
\end{aligned}$$

6.B Speed of oxygen ions

We will derive an expression in two steps for the speed of O and O^- produced through dissociative attachment. First we will show that $v_O = v_{O^-}$ and then we give expressions for v_O . To show that $v_O = v_{O^-}$, we start with the conservation of energy and momentum in the rest frame of oxygen, thus $v_{O_2} \equiv 0$:

$$\frac{m_e v^2}{2} = m_O \frac{v_O^2}{2} + m_O \frac{v_{O^-}^2}{2} + E_{bind} \quad (6.25)$$

$$m_e \mathbf{v} = m_O \mathbf{v}_O + m_O \mathbf{v}_{O^-} \quad (6.26)$$

where we used non-relativistic expressions for energy and momentum because of the small velocity of all particles. Since the electron mass is much smaller than the mass of O and O^- and we are in the non-relativistic regime, we can approximate $m_e \mathbf{v} \approx 0$, thus

$$0 = m_O \mathbf{v}_O + m_O \mathbf{v}_{O^-} \Rightarrow \mathbf{v}_O = -\mathbf{v}_{O^-}. \quad (6.27)$$

Using Eq. (6.27), (6.25) leads to

$$v_O = v_{O^-} = \sqrt{\frac{m_e |\mathbf{v}|^2}{2m_O} - \frac{E_{bind}}{m_O}} \quad (6.28)$$

where \mathbf{v} is the velocity of the electron.

6.C Dependence on the cross sections

The results depend sensitively on the cross sections as input data. Figure 6.16 a) shows the cross sections for three-body attachment by Phelps [97] and Biagi [15] normalized to gas density. It shows that these two cross sections have different lower and upper threshold energies. Figure 6.16 b) shows the cross sections for electronic excitation $O_2 \rightarrow O_2(a1)$ from [147] and [110, 97]. Figure 6.17 compares the time evolution of the electron number at 1 bar if $E_0 = 1$ keV. Using data for excitation of Siglo [147] and attachment of Biagi [15], the maximal electron number is 32 and the attachment time is approximately 1 ns. However, using data for excitation of LXcat [110] and attachment of Phelps [97] yields to a maximum of 37 electrons, the exponential decay time is approximately 8 ns. Thus we can conclude that the time evolution is different for different kind of cross sections and that the data of [147] and [15] lead to an unphysically short attachment time.

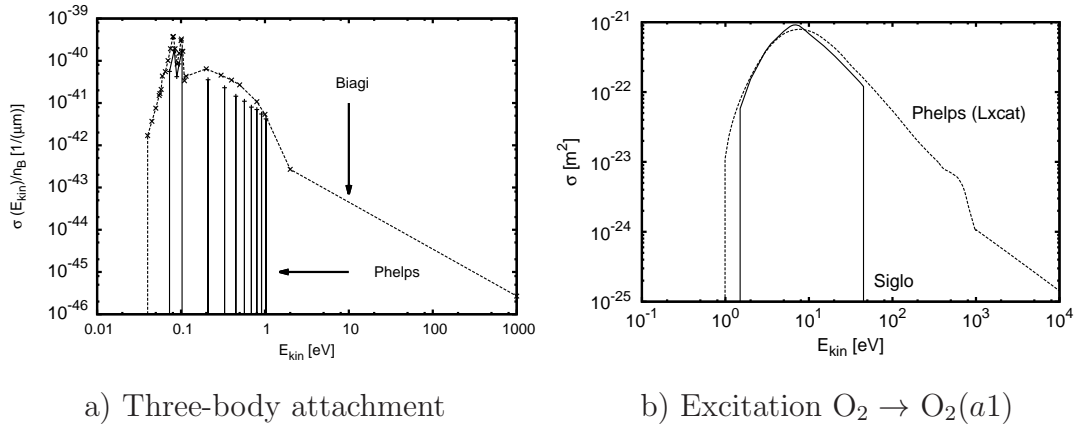


Figure 6.16: a) The total cross section for three-body attachment normalized to the gas density $2.6884 \cdot 10^{19} / \text{cm}^3$ as a function of the energy E_{kin} of the incident electron by Phelps [97] and Biagi [15]. b) Cross sections [110, 97, 147] for the electronic excitation $O_2 \rightarrow O_2(a_1)$ as a function of incident electron energy E_{kin} .

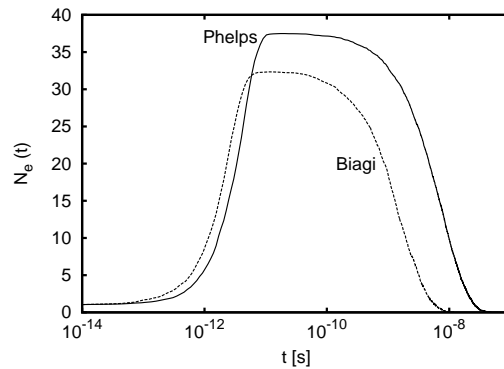


Figure 6.17: The electron number at 1 bar as a function of time in the case of $E_0 = 1$ keV using the cross sections of Phelps and Biagi for electronic excitations and attachment [97, 15].

7.1 Bremsstrahlung cross sections for free electrons in air

In chapter 2 we have derived cross-sections to calculate the generation of photons through electron-nucleus Bremsstrahlung in air. We have integrated the Bethe Heitler cross section [12, 75] to link the emission angle of a Bremsstrahlung photon explicitly to the photon energy. We have seen that electrons with incident energy above their rest energy emit photons dominantly in forward direction; our calculations have also shown that the emission of photons with energies small compared to the incident electron energy is more probable than the emission of photons which obtain almost all the electron energy. The comparison of our analytical results with cross sections used by other authors [42, 2, 24, 98, 169] has shown that we provide appropriate cross sections to calculate the production of Bremsstrahlung photons through free electrons in air whereas previously used cross sections are not always suitable.

As electron-positron pairs are created in thunderstorms as well, we have used a quantum field theoretical symmetry to calculate the cross section for pair production where an incident photon interacts with a nucleus and emits an electron-positron pair. We have related the energy and emission angle of the positron; we have seen that positrons with kinetic energies above 500 keV are emitted in forward direction.

In section 2.J we have provided a C++ code for Bremsstrahlung and pair production cross sections doubly differential in the energy and the emission angle of the produced photon/positron. This code either can be implemented directly into a Monte Carlo code or can be used to calculate tables of cross sections.

In chapter 3 we have tested the influence of electron-electron Bremsstrahlung on the production of TGFs. We have seen that this process plays a significant role in air for incident electron energies above 1 MeV. When electron-electron Bremsstrahlung occurs, not only a photon, but also a shell electron is emitted. Since the energy between the

incident and secondary electron is shared more evenly than for electron impact ionization, there is an enrichment of electrons with energies above 100 keV. Consequently these high-energy electrons can produce photons through the electron-nucleus Bremsstrahlung process. Thus the electron-electron Bremsstrahlung process contributes indirectly, but significantly to the production of photons with energies above 1 MeV.

We remark here that both the calculation and the measurements of cross sections, also for scattering of leptons and hadrons at air molecules, is still a vivid research area. In the future it will be necessary to sift new data for cross sections, identify their usefulness for, e.g., the motion of high-energy electrons in air and apply them to these models.

7.2 Generation of photons, positrons and hadrons above a thundercloud

In chapter 3 and in the first part of chapter 4 we adopted the model of Xu et al. [169, 170] when simulating the motion of electrons in the electric field of a stationary, negative stepped lightning leader as presented in section 4.A and calculated the energy distribution of Bremsstrahlung photons at 16 km altitude. For this purpose we implemented the cross sections for electron-nucleus Bremsstrahlung and electron-electron Bremsstrahlung as presented in chapters 2 and 3. We have seen that the electric field in the vicinity of the leader tip is sufficiently high to accelerate a few electrons into the run-away regime. We have seen that after 24 ns electrons are in the run-away regime with energies of up to approximately 50 MeV and that there are photons with energies of up to 10 MeV. The spatial distribution shows that low-energy electrons with energies below 1 MeV show a more diffuse behaviour whereas the high-energy electrons with energies above 1 MeV run ahead of the many low-energy electrons. This justifies the approximation to neglect the self-consistent field for the high-energy electrons. To test the influence of the choice of electron-nucleus Bremsstrahlung cross sections, we have also run simulations without electron-electron Bremsstrahlung, and with cross sections for electron-nucleus Bremsstrahlung from other authors; these calculations yield different energy distributions of photons. As we have shown in chapter 2, our cross sections are appropriate; thus the implementation of some previously used cross sections lead to unphysical photon distributions.

We ejected a photon beam with energies sampled from the previously calculated photon distribution from 16 km altitude upwards and simulated their motion through the atmosphere. We have seen that most photons with energies above 5 MeV and below 50 MeV will collide with air molecules and lose most of their energy through Compton scattering or create electron-positron pairs as well as hadrons. Thus most photons with energies above 5 MeV will not reach satellite altitude. Rather we have calculated that positrons and hadrons are produced with energies of up to several tens of MeV; especially, we have seen that the positron beam is emitted upwards and reaches altitudes of 150 km.

Above 150 km the air density is so thin that the positron beam will follow the geomagnetic field lines and can be detected by satellites in the orbit.

In the future the motion of the leader and its stepping mechanism should be modelled as well. This will give a more detailed view on how photon beams are produced by a lightning leader and what the photon energy distribution looks like. For this purpose it will be essential to include space charge effects of free electrons and residual ions. Beyond that, proper cross sections to simulate the motion of hadrons through air are desired. The identification of these mechanisms is current research; it will allow to predict how far hadrons can travel through air, what their energy losses are and what fluxes can be expected at different altitudes.

7.3 Generation of photons from monoenergetic electron beams

In chapter 5 we have simulated the motion of monoenergetic electron beams with energies from 100 keV to 1 MeV at standard temperature and pressure and the subsequent generation of Bremsstrahlung photons. The direction of most photons with energies above 30 keV encloses an angle of 30° with the direction of the initial electron beam, partly because photons produced by relativistic electrons are emitted in a small angle relative to the initial electron direction, partly because Compton scattering is less likely for photons with higher energies; vice versa, low-energy photons show a more isotropic distribution. The photon energy spectrum shows a gap between 20 eV and 500 eV because of photoionization where the photon is absorbed by an air molecule and a shell electron ejected. Above 10 keV the photon energy distribution can be fitted well by an exponential, when all electron energies have dropped below 30 keV, for all electron beams with initial energies between 400 keV and 1 MeV. The photon energy distribution shows that there is a significant number of photons between 10 keV and 250 keV as they were observed in laboratory discharges [88, 89] or from triggered lightning [38].

In the future the acceleration of electrons in a discharge should be taken into account. Therefore it will be important to include space charge effects originating from free electrons and residual ions. This will allow determining the actual energy distribution of electrons more accurately yielding a more realistic spatial and energy distribution of Bremsstrahlung photons.

7.4 Electron showers for energies below 1 MeV

In chapter 6 we have analysed the structure of electron showers for energies below 1 MeV. The electron number as a function of time first increases due to ionization and, after a period of saturation, decreases as electrons attach to oxygen. We have seen that incident

electrons with higher energies produce secondary electrons which can do less subsequent ionizations per energy than low-energy electrons. Thus the average particle energy per produced electron ranges from 20 eV for initial energies of 1 keV to 33 eV for initial energies above 250 MeV.

There are two different attachment mechanisms: two body (dissociative) attachment producing O^- ions and three body attachment yielding O_2^- ; the first one is important for pressures of 10 mbar, the latter one for pressures of 100 and 1000 mbar leading to a gap at 0.1 eV in the electron energy spectrum as three body attachment becomes dominant for electron energies below 1 eV; above that energy three body attachment is negligible and thus there are no gaps in the electron energy distribution above 1 eV.

For initial energies of 1 MeV the electron motion is rather beamed while for initial energies of 1 keV the electron motion shows a more isotropic distribution. On basis of the position of electrons and ions we have calculated the swarm induced field; we have seen that this field does not exceed 10 V/m for initial energies of 1 MeV.

Finally we have calculated the electron motion within ambient fields of 5 kV/cm and 8 kV/cm in air at 1000 mbar. Since the electric force is larger than the friction force for initial energies of 1 MeV [67], electrons will continuously gain energy and the electron number will continuously grow. For energies of 1 keV, however, the friction is larger than the electric force and thus all electrons will finally attach to oxygen. However, the mean energy and the exponential decay time are larger than for vanishing electric field: For 1 bar and 8 kV/cm the exponential decay time is approximately 80 ns where it is approximately 10 ns without electric field.

The investigation of electron showers for energies below 1 MeV is the first step to understand how cosmic particles contribute to lightning inception. For the understanding of this phenomenon, it is essential to couple low-energy models for energies below 1 MeV with high-energy models whose range of validity stops at 1 MeV.

The relativistic leap-frog scheme

Between two collisions with air molecules, a particle in our Monte Carlo code can only be influenced by the local electric field $\mathbf{E}(\mathbf{r}, t)$ or magnetic field $\mathbf{B}(\mathbf{r}, t)$. In this appendix we present the leap frog scheme for relativistic equations of motion and check its implementation by comparing our simulation results to analytical test cases.

For non-relativistic equations of motion the leap frog scheme in a given electromagnetic field reads [103]

$$\mathbf{r}_{n+1} = \mathbf{r}_n + \Delta t \mathbf{v}_{n+\frac{1}{2}} \quad (\text{A.1})$$

$$\mathbf{v}_{n+\frac{1}{2}} = \mathbf{v}_{n-\frac{1}{2}} + \Delta t \frac{q}{m} \left(\mathbf{E}(\mathbf{r}_n, t_n) + \mathbf{v}_{n-\frac{1}{2}} \times \mathbf{B}(\mathbf{r}_n, t_n) \right) \quad (\text{A.2})$$

where \mathbf{r}_n is the particle position at time t_n , $\mathbf{v}_{n+\frac{1}{2}}$ the velocity at time $t_{n+\frac{1}{2}}$ and Δt the current time step. m is the particle mass and q the particle charge. For the relativistic case we update momentum and energy as

$$\mathbf{p}_{n+\frac{1}{2}} = \mathbf{p}_{n-\frac{1}{2}} + q\Delta t \left(\mathbf{E}(\mathbf{r}_n, t_n) + \mathbf{v}_{n-\frac{1}{2}} \times \mathbf{B}(\mathbf{r}_n, t_n) \right) \quad (\text{A.3})$$

$$\mathcal{E}_{n+\frac{1}{2}} = \sqrt{c^2 |\mathbf{p}_{n+\frac{1}{2}}|^2 + m^2 c^4} \quad (\text{A.4})$$

and use the relativistic relation

$$\mathbf{v}_{n+\frac{1}{2}} = \frac{c^2}{\mathcal{E}_{n+\frac{1}{2}}} \cdot \mathbf{p}_{n+\frac{1}{2}} \quad (\text{A.5})$$

to update the particle velocity; the position is then updated as in (A.1).

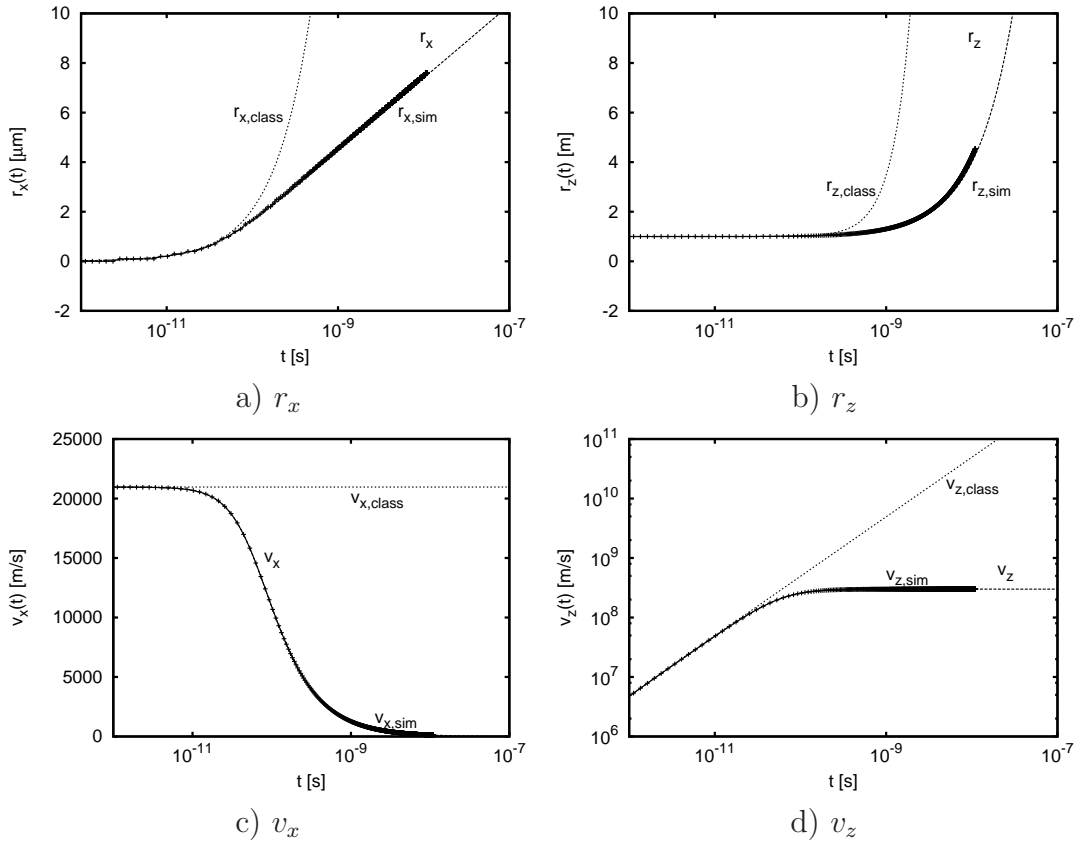


Figure A.1: a) r_x , b) r_z , c) v_x and d) v_z as a function of time for an electron with $\mathbf{r}_0 = (0, 0, 1)$ m and $\mathbf{v}_0 = (20961.3, 9711.84, -161502.0)$ m/s in a field of $\mathbf{E}_0 = -280$ V/m \mathbf{e}_z comparing numerical results (crosses, with subscript "sim") with the analytical equations of motion (lines, without subscript for relativistic equations of motion and "class" for classical equations of motion).

A.1 Test in a uniform, constant electric field

First we test the implementation of (A.1) and (A.5) in a uniform, constant electric field $\mathbf{E}(\mathbf{r}, t) \equiv \mathbf{E}_0$. The equation of motion reads

$$\frac{d\mathbf{p}}{dt} = q\mathbf{E}_0 \quad (\text{A.6})$$

$$\Leftrightarrow d\mathbf{p} = q\mathbf{E}_0 dt. \quad (\text{A.7})$$

Integrating from \mathbf{p}_0 to $\mathbf{p}(t)$ on the left-hand side and from t_0 to t on the right-hand side yields

$$\mathbf{p}(t) = \mathbf{p}_0 + q\mathbf{E}_0(t - t_0) \quad (\text{A.8})$$

$$\frac{m\mathbf{v}(t)}{\sqrt{1 - \frac{|\mathbf{v}(t)|^2}{c^2}}} = \mathbf{p}_0 + q\mathbf{E}_0(t - t_0). \quad (\text{A.9})$$

where we used the relativistic relation between the momentum \mathbf{p} and velocity \mathbf{v} . In order to solve (A.9) for \mathbf{v} we decompose the velocity into $\mathbf{v} = \nu(t) \cdot \mathbf{n}(t)$ where ν is the absolute value and \mathbf{n} the direction of \mathbf{v} with $|\mathbf{n}(t)| \equiv 1$. Inserting this into (A.9) and squaring leads to

$$\frac{m^2\nu^2}{1 - \frac{\nu^2}{c^2}} = (\mathbf{p}_0 + q\mathbf{E}_0(t - t_0))^2 \quad (\text{A.10})$$

with solution

$$\nu(t) = \sqrt{\frac{(\mathbf{p}_0 + q\mathbf{E}_0(t - t_0))^2}{m^2 + \frac{1}{c^2}(\mathbf{p}_0 + q\mathbf{E}_0(t - t_0))^2}}. \quad (\text{A.11})$$

Inserting $\mathbf{v} = \nu \cdot \mathbf{n}$ into (A.9) leads to

$$\frac{m\nu\mathbf{n}}{\sqrt{1 - \frac{\nu^2}{c^2}}} = \mathbf{p}_0 + q\mathbf{E}_0(t - t_0) \quad (\text{A.12})$$

with

$$\mathbf{n}(t) = \frac{1}{m\nu} \sqrt{1 - \frac{\nu^2}{c^2}} [\mathbf{p}_0 + q\mathbf{E}_0(t - t_0)] \quad (\text{A.13})$$

and thus totally

$$\mathbf{v}(t) = \sqrt{1 - \frac{\nu^2}{c^2}} \left[\mathbf{v}_0 + \frac{q}{m} \mathbf{E}_0(t - t_0) \right]. \quad (\text{A.14})$$

Finally we can integrate (A.14) and obtain

$$\begin{aligned}
\mathbf{r}(t) &= \mathbf{r}_0 + \frac{c}{E_0^3 q} \left[\mathbf{E}_0 \left(\sqrt{m^2 c^2 + p_0^2 - 2q\mathbf{p}_0 \cdot \mathbf{E}_0(t-t_0) + q^2 E_0^2 (t-t_0)^2} \right. \right. \\
&\quad \left. \left. - \sqrt{m^2 c^2 + p_0^2} \right) + (E_0^2 \mathbf{p}_0 - \mathbf{E}_0 (\mathbf{p}_0 \cdot \mathbf{E}_0)) \right. \\
&\quad \left. \times \ln \left(\frac{E^2 q(t-t_0) + \mathbf{p}_0 \cdot \mathbf{E}_0 + E_0 \sqrt{m^2 c^2 + p_0^2 - 2q\mathbf{p}_0 \cdot \mathbf{E}_0(t-t_0) + q^2 E_0^2 (t-t_0)^2}}{\mathbf{p}_0 \cdot \mathbf{E}_0 + E_0 \sqrt{m^2 c^2 + p_0^2}} \right) \right]
\end{aligned} \tag{A.15}$$

which gives the position of a particle as a function of time. We note here that (A.14) and (A.15) still apply if the electric field is not uniform, but depends on the position \mathbf{r} since (A.7) and (A.14) were integrated only over t .

Figure A.1 shows the position and velocity of an electron with $\mathbf{r}_0 = (0, 0, 1)$ m and $\mathbf{v}_0 = (20961.3, 9711.84, -161502.0)$ m/s in a field of $\mathbf{E}_0 = -280$ V/m \mathbf{e}_z as a function of time; we have turned off all collisions, hence equations (A.14) and (A.15) apply. Fig. A.1 compares the numerical results obtained with the leap-frog scheme (A.1) and (A.5) with the analytical results (A.14) and (A.15) and the classical equations of motion. It shows that we have implemented the leap-frog scheme correctly and also illustrates that from a certain point of time the classical equations of motion deviate severely from the relativistic equations of motion.

A.2 Test in a constant, uniform magnetic field

In a given constant magnetic field \mathbf{B}_0 , the equation of motion reads

$$\frac{d\mathbf{p}}{dt} = q\mathbf{v} \times \mathbf{B}_0. \tag{A.16}$$

Since \mathbf{v} appears on the right-hand side, we use $\mathbf{v} = c^2/\mathcal{E}\mathbf{p}$ and $\mathcal{E} = \sqrt{p^2 c^2 + m^2 c^4}$ to rewrite (A.16) into

$$\frac{d\mathbf{p}}{dt} = \frac{qc^2}{\sqrt{p^2 c^2 + m^2 c^4}} \mathbf{p} \times \mathbf{B}_0. \tag{A.17}$$

As done for \mathbf{v} in section A.1, we decompose the momentum \mathbf{p} into its absolute value $\rho(t)$ and its direction $\mathbf{n}(t)$ with $|\mathbf{n}(t)| \equiv 1$ through $\mathbf{p}(t) = \rho(t) \cdot \mathbf{n}(t)$:

$$\frac{d(\rho\mathbf{n})}{dt} = \frac{qc^2\rho}{\sqrt{\rho^2 c^2 + m^2 c^4}} \mathbf{n} \times \mathbf{B}_0 \tag{A.18}$$

$$\frac{d\rho}{dt} \mathbf{n} + \rho \frac{d\mathbf{n}}{dt} = \frac{qc^2\rho}{\sqrt{\rho^2 c^2 + m^2 c^4}} \mathbf{n} \times \mathbf{B}_0. \tag{A.19}$$

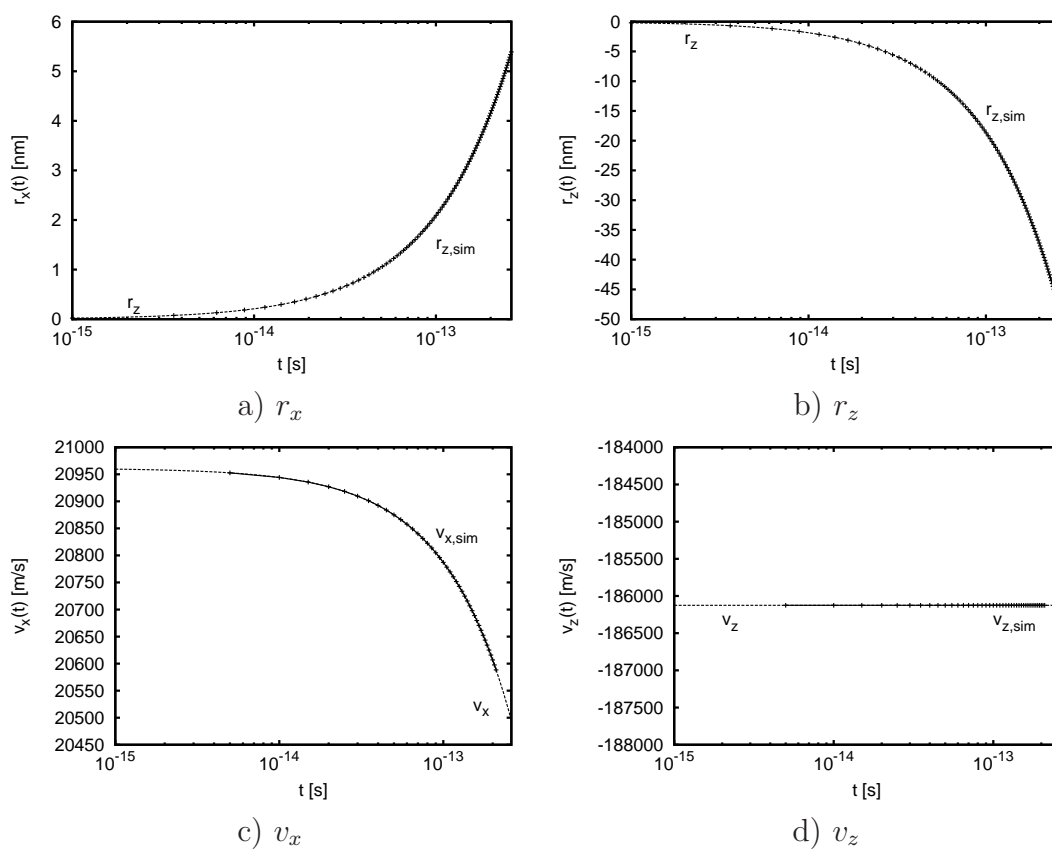


Figure A.2: a) r_x , b) r_z , c) v_x and d) v_z as a function of time for an electron with $\mathbf{r}_0 = (0, 0, 0)$ m and $\mathbf{v}_0 = (20952.7, 9730.26, -186125.0)$ m/s in a field of $\mathbf{B}_0 = 1$ T \mathbf{e}_z comparing numerical results (crosses, with subscript "sim") with the analytical equations of motion (line, without subscript).

If we multiply (A.19) with \mathbf{n} and use $\mathbf{n} \cdot \dot{\mathbf{n}} = 0$, we obtain

$$\frac{d\rho}{dt} = 0, \quad (\text{A.20})$$

thus $\rho(t) \equiv \rho_0$ is constant in time. Hence (A.19) can be written as

$$\frac{d\mathbf{n}}{dt} = \gamma \mathbf{n} \times \mathbf{B}_0 \quad (\text{A.21})$$

with $\gamma = qc^2 / \sqrt{\rho_0^2 c^2 + m^2 c^4}$. The solution of (A.21) is

$$\mathbf{n}(t) = \frac{1}{B_0^2} [\mathbf{B}_0 \cdot (\mathbf{B}_0 \cdot \mathbf{C}) - \mathbf{B}_0 \times (\mathbf{B}_0 \times \mathbf{C}) \cos(B_0 \gamma t) - B_0 (\mathbf{B}_0 \times \mathbf{C}) \sin(B_0 \gamma t)] \quad (\text{A.22})$$

where \mathbf{C} is such that $\mathbf{n}(0) = \mathbf{n}_0$ for the initial direction \mathbf{n}_0 is fulfilled. Thus it is

$$\begin{aligned} \mathbf{v}(t) &= \frac{c^2 \rho_0}{B_0^2 \sqrt{\rho_0^2 c^2 + m^2 c^4}} \\ &\times [\mathbf{B}_0 \cdot (\mathbf{B}_0 \cdot \mathbf{C}) - \mathbf{B}_0 \times (\mathbf{B}_0 \times \mathbf{C}) \cos(B_0 \gamma t) - B_0 (\mathbf{B}_0 \times \mathbf{C}) \sin(B_0 \gamma t)] \end{aligned} \quad (\text{A.23})$$

and through integration

$$\begin{aligned} \mathbf{r}(t) &= \mathbf{r}_0 + \frac{c^2 \rho_0}{B_0^2 \sqrt{\rho_0^2 c^2 + m^2 c^4}} \\ &\times \left[\mathbf{B}_0 \cdot (\mathbf{B}_0 \cdot \mathbf{C}) t - \frac{1}{B_0 \gamma} \mathbf{B}_0 \times (\mathbf{B}_0 \times \mathbf{C}) \sin(B_0 \gamma t) + \frac{1}{\gamma} (\mathbf{B}_0 \times \mathbf{C}) \cos(B_0 \gamma t) \right] \end{aligned} \quad (\text{A.24})$$

Figure A.2 shows the position and velocity of an electron with $r_0 = (0, 0, 0)$ and $v_0 = (20952.7, 9730.26, -186125.0)$ m/s in a magnetic field of 1 T comparing (A.23) and (A.24) with our simulation results. It shows that there is a perfect agreement between the simulation and analytical results and, hence, that we have implemented (A.1) and (A.5) correctly.

Bibliography

- [1] A.V. Agafonov et al., 2013. Observation of neutron bursts produced by laboratory high-voltage atmospheric discharge. *Phys. Rev. Lett.*, vol. 111, 115003
- [2] S. Agostinelli et al., 2003. G4-a simulation toolkit. *Nucl. Instrum. Methods Phys. Res., Sect. A*, vol. 506, pp. 250-303
- [3] H. Aiginger, 1966. Elektron-Bremsstrahlungswirkungsquerschnitte von 180 und 380 keV-Elektronen. *Zeitschrift fuer Physik* , vol. 197, pp. 8-25
- [4] F. Arqueros et al., 2009. Analysis of the fluorescence emission from atmospheric nitrogen by electron excitation, and its application to fluorescence telescopes. *New J. Phys.*, vol. 11, 065011
- [5] L.P. Babich, 2003. High-energy phenomena in electric discharges in dense gases. Theory, experiment and natural phenomena. *ISTC Science and technology series*, vol. 2 Futurepast
- [6] L.P. Babich, 2007. Neutron generation mechanism correlated with lightning discharges. *Geomag. and Aero.*, vol 47, pp. 664-670
- [7] L.P. Babich et al., 2011. Lightning initiation mechanism based on the development of relativistic runaway electron avalanches triggered by background cosmic radiation: Numerical simulation. *Jour. Exp. Theo. Phys.*, vol. 112, pp. 902-909
- [8] L.P. Babich et al., 2012. Numerical simulations of local thundercloud field enhancement caused by runaway avalanches seeded by cosmic rays and their role in lightning initiation. *J. Geophys. Res.-Space Phys.*, vol. 117, A09316

-
- [9] C.A. Balanis C.A., 2009. Advanced engineering electromagnetics, John Wiley, New York
- [10] E.M. Bazelyan and Y. P. Raizer, 2000. Lightning physics and lightning protection. Inst. of Phys. Pub., Bristol and Philadelphia
- [11] X. Bertou et al., 2000. LPM effect and pair production in the geomagnetic field: a signature of ultra-high energy photons in the Pierre Auger Observatory, *Astro. Phys.*, vol. 14, pp. 121-130
- [12] H.A. Bethe and W. Heitler, 1934. On the stopping of fast particles and on the creation of positive electrons. *Proc. Phys. Soc. London*, vol. 146, pp. 83-112
- [13] P. Bhattacharjee and G. Sigl, 2000. Origin and propagation of extremely high-energy cosmic rays. *Phys. Rep.*, vol. 327, pp. 109-247
- [14] C.J. Biagi et al., 2010. Observations of stepping mechanisms in a rocket-and-wire triggered lightning flash. *J. Geophys. Res.*, vol. 115, D23215
- [15] Transcribed from S.F. Biagi's FORTRAN code Magboltz, version 8.97, Oct. 2012. <http://consult.cern.ch/writeup/magboltz/>
- [16] T.M.P. Briels et al., 2008. Time resolved measurements of streamer inception in air. *IEEE Trans. Plasma Sci.*, vol. 36, 908
- [17] M.S. Briggs et al., 2010. First results on terrestrial gamma ray flashes from the Fermi Gamma-ray Burst Monitor. *J. Geophys. Res.*, vol. 115, A07323
- [18] M.S. Briggs et al., 2011. Electron-positron beams from terrestrial lightning observed with Fermi GBM. *Geophys. Res. Lett.*, vol. 38, L02808
- [19] W.C. Brown et al., 2012. A beginning investigation into the possible role of cosmic rays in the initiation of lightning discharges at the Pierre Auger Observatory. *Europ. Phys. Jour. Plus*, vol. 127, 95
- [20] R.L. Burden and J.D. Faires, 2000. Numerical Analysis, Brookes/Cole, Scarborough, Canada ISBN 0-534-38216-9
- [21] J.N. Capdevielle et al., 2000. Simulation of extensive air showers at ultra-high energy using the CORSIKA Monte Carlo code. *Astropart. Phys.*, vol. 13, pp. 259-275
- [22] B.E. Carlson et al., 2008. Runaway relativistic electron avalanche seeding in the Earth's atmosphere. *J. Geophys. Res.*, vol. 113, A10307

-
- [23] B.E. Carlson et al., 2009. Terrestrial gamma ray flashes production by lightning current pulses. *J. Geophys. Res.*, vol. 114, A00E08
- [24] B.E. Carlson et al., 2010. Terrestrial gamma ray flash production by active lightning leader channels. *J. Geophys. Res.*, vol. 115, A10324
- [25] S. Celestin and V.P. Pasko, 2010. Soft collisions in relativistic runaway electron avalanches. *J. Phys. D: Appl. Phys.*, vol. 43, 315206.
- [26] S. Celestin and V.P. Pasko, 2011. Energy and fluxes of thermal runaway electrons produced by exponential growth of streamers during the stepping of lightning leaders and in transient luminous events. *J. Geophys. Res.*, vol. 116, A03315
- [27] S. Celestin and V.P. Pasko, 2012. Compton scattering effects on the duration of terrestrial gamma-ray flashes. *Geophys. Res. Lett.*, vol. 39, L02802
- [28] S. Chakraborti et al., 2011. Ultra-high-energy cosmic ray acceleration in engine-driven relativistic supernovae. *Nature Comm.*, vol. 2, 175
- [29] O. Chanrion and T. Neubert, 2008. A PIC-MCC code for simulation of streamer propagation in air. *J. Comput. Phys.*, vol. 227, pp. 7222-7245
- [30] O. Chanrion and T. Neubert, 2010. Production of runaway electrons by negative streamer discharges. *J. Geophys. Res.*, vol. 115, A00E32
- [31] S. Chapman and T.G. Cowling, 1974. *The mathematical theory of non-uniform gases*. Cambridge University Press
- [32] P.A. Cherenkov, 1934. Visible emissions of clean liquids by action of γ radiation. *Doklady Akademii Nauk SSSR*, vol. 2, 451
- [33] CORSIKA, 2013. <http://www-ik.fzk.de/~corsika/>
- [34] D.E. Cullen et al., 1991. *Tables and Graphs of Electron Interaction Cross 10 eV to 100 GeV Derived from the LLNL Evaluated Electron Data Library (EEDL), Z = 1 - 100*. Lawrence Livermore National Laboratory, UCRL-50400, vol. 31
- [35] S.A. Cummer et al., 2005. Measurements and implications of the relationship between lightning and terrestrial gamma ray flashes. *Geophys. Res. Lett.*, vol. 32, L08811
- [36] C.D. Dermer et al., 2009. Ultra-high-energy cosmic rays from black hole jets of radio galaxies. *New J. Phys.*, vol. 11, 065016
- [37] J.R. Dwyer, 2003. A fundamental limit on electric fields in air. *Geophys. Res. Lett.*, vol. 30, 2055

- [38] J.R. Dwyer et al., 2004. Measurements of x-ray emission from rocket-triggered lightning. *Geophys. Res. Lett.*, vol. 31, L05118
- [39] J.R. Dwyer and D.M. Smith, 2005a. A comparison between Monte Carlo simulations of runaway breakdown and terrestrial gamma-ray flashes. *Geophys. Res. Lett.*, vol. 32, L22804
- [40] J.R. Dwyer et al., 2005b. X-ray bursts associated with leader steps in cloud-to-ground lightning. *Geophys. Res. Lett.*, vol. 32, L01803
- [41] J.R. Dwyer et al., 2005c. X-ray bursts produced by laboratory sparks in air. *Geophys. Res. Lett.*, vol. 32, L20809
- [42] J.R. Dwyer, 2007. Relativistic breakdown in planetary atmospheres, *Physics of plasmas*. vol. 14, 042901
- [43] J.R. Dwyer et al., 2008a. A study of X-ray emission from laboratory sparks in air at atmospheric pressure. *J. Geophys. Res.*, vol. 113, D23207
- [44] J.R. Dwyer et al., 2008b. High-energy electron beams launched into space by thunderstorms. *Geophys. Res. Lett.*, vol. 35, L02815
- [45] J.R. Dwyer, 2012. The relativistic feedback discharge model of terrestrial gamma ray flashes. *Journal of Geophys. Res. - Space Phys.*, vol. 117, A02308
- [46] U. Ebert et al., 1997. Propagation and structure of planar streamer fronts. *Phys. Rev. E*, vol. 55, pp. 1530-1549
- [47] U. Ebert et al., 2010. Review of recent results on streamer discharges and discussion of their relevance for sprites and lightning. *J. Geophys. Res.*, vol. 115, A00E43
- [48] H.E. Edens et al., 2014. Photographic observations of streamers and steps in a cloud-to-air negative leader. DOI: 10.1002/2013GL059180
- [49] EGS5, 2005. <http://rcwww.kek.jp/research/egs/egs5.html>
- [50] EGSnrs, 2014. http://www.nrc-cnrc.gc.ca/eng/solutions/advisory/egsnrc_index.html
- [51] G. Elwert and E. Haug, 1969. Calculation of Bremsstrahlung cross sections with Sommerfeld-Maue eigenfunctions. *Phys. Rev.*, vol. 183, pp. 90-105
- [52] A. Fiala et al., 1994. 2-dimensional, hybrid model of low-pressure glow-discharges. *Phys. Rev. E*, vol. 49, pp. 5607-5622

- [53] J.K. Fink and R.H. Pratt, 1973. Use of Furry-Sommerfeld-Maue wave functions in pair production and Bremsstrahlung. *Phys. Rev. A*, vol. 7, pp. 392-403
- [54] G.J. Fishman et al., 1994. Discovery of intense gamma-ray flashes of atmospheric origin. *Science*, vol. 264, pp. 1313-1316
- [55] R.L. Fleischer et al., 1974. Are neutrons generated by lightning?, *J. Geophys. Res.*, vol. 79, pp. 5013-5017
- [56] E.G. Fuller, 1985. Photonuclear reaction cross sections for ^{12}C , ^{14}N and ^{16}O . *Phys. Rep.*, vol.127, pp. 185-231
- [57] I. Gallimberti et al., 2002. Fundamental processes in long air gap discharges. *C. R. Physique*, vol. 3, pp. 1335-1359
- [58] Geant4 (2014), <http://geant4.cern.ch/>
- [59] T. Gjesteland et al., 2010. Effects of dead time losses on terrestrial gamma ray flash measurements with the Burst and Transient Source Experiment. *J. Geophys. Res.*, vol. 115, A00E21
- [60] T. Gjesteland et al., 2011. Confining the angular distribution of terrestrial-gamma ray flash emission. *J. Geophys. Res.*, vol. 116, A11313
- [61] E. Gogolides and H.H. Sawin, 1992. Continuum modelling of radio-frequency glow discharges. I. Theory and results for electropositive and electronegative gases. *J. Appl. Phys.*, vol. 72, pp. 3971-3987
- [62] P.W. Gorham, 2001. On the possibility of radar echo detection of ultra-high energy cosmic ray- and neutrino-induced extensive air showers. *Astropart. Phys.*, vol. 15, pp. 177-202
- [63] Gnuplot: <http://www.gnuplot.info/>
- [64] F.J. Gordillo-Vázquez, 2008. Air plasma kinetics under the influence of sprites. *J. Phys. D: Appl. Phys.*, vol. 41, 234016
- [65] B.W. Grefenstette et al., 2009. First RHESSI terrestrial gamma ray flash catalog. *J. Geophys. Res.*, vol. 114, A02314
- [66] W. Greiner and J. Reinhardt, 1995. *Quantenelektrodynamik*, Verlag Harri Deutsch
- [67] A.V. Gurevich, 1961. On the theory of runaway electrons. *Soviet Physics JETP-USSR*, vol. 12, pp. 904-912

-
- [68] A.V. Gurevich et al., 1992. Runaway electron mechanism of air breakdown and preconditioning during a thunderstorm. *Phys. Lett. A*, vol. 165, pp. 463-468
- [69] A.V. Gurevich and K. P. Zybin, 2001. Runaway breakdown and electric discharges in thunderstorms. *Physics-USpekhi*, vol. 44, pp. 1119-1140
- [70] A.V. Gurevich et al., 2004. New type discharge generated in thunderclouds by joint action of runaway breakdown and extensive atmospheric shower. *Phys. Lett. A*, vol. 329, pp. 348-361
- [71] A.V. Gurevich et al., 2007. Runaway breakdown in strong electric field as a source of terrestrial gamma flashes and gamma bursts in lightning leader steps. *Phys. Lett. A*, vol. 361, pp. 119-125
- [72] E. Haug, 1975. Bremsstrahlung and pair production in field of free electrons. *Z. Naturforschung*, vol. 30, pp. 1099-1113
- [73] E. Haug, 2008. Electron-electron bremsstrahlung for bound target electrons, *Eur. Phys. J. D*, vol. 49, pp. 193-199
- [74] E. Haug and W. Nakel, 2004. *The elementary process of Bremsstrahlung*, World Scientific, Singapore
- [75] W. Heitler, 1944. *The quantum theory of radiation*. Oxford University Press
- [76] J.D. Hill et al., 2011. High-speed video observations of a lightning stepped leader. *J. Geophys. Res.*, vol. 116, D16117
- [77] J.O. Hirschfelder et al., 1964. *Molecular theory of gases and liquids*. Wiley & Sons, New York
- [78] P.V.C. Hough, 1948. The angular distribution of pair-produced electrons and Bremsstrahlung. *Phys. Rev.*, vol. 74, pp. 80-86
- [79] ICRU, 1984. Stopping powers for electrons and positrons. ICRU Report no. 37
- [80] U.S. Inan and N.G. Lehtinen, 2005. Production of terrestrial gamma-ray flashes by an electromagnetic pulse from a lightning return stroke. *Geophys. Res. Lett.*, vol. 32, L19818
- [81] J.D. Jackson, 1975. *Classical electrodynamics*. John Wiley & Sons, New York
- [82] J.H. Jacob, 1973. Multiple electron-scattering through a slab. *Phys. Rev. A*, vol. 8, pp. 226-235

- [83] Y.K. Kim and M.E. Rudd, 1994. Binary-encounter-dipole model for electron-impact ionization. *Phys. Rev. A*, vol. 50, pp. 3954-3967
- [84] Y.K. Kim et al., 2000. Extension of the binary-encounter-dipole model to relativistic incident electrons, *Phys. Rev. A*, vol. 62, 052710
- [85] J. Knapp et al., 2003. Extensive air shower simulations at the highest energies. *Astroparticle Phys.*, vol. 19, pp. 77-99
- [86] D. E. Knuth, 1997. *The Art of Computer Programming. Vol. 2: Seminumerical algorithms.* Addison-Wesley, Massachusetts
- [87] H.W. Koch and J.W. Motz, 1959. Bremsstrahlung Cross-Section Formulas and Related Data. *Rev. Mod. Phys.*, vol. 31, pp. 920-956
- [88] P.O. Kochkin et al., 2012. Experimental study of hard x-rays emitted from metre-scale positive discharges in air. *J. Phys. D: Appl. Phys.*, vol. 45, 425202
- [89] P.O. Kochkin et al., 2014. Experimental study of the spatio-temporal development of meter-scale negative discharge in air. *J. Phys. D: Appl. Phys.*, vol. 47, 145203
- [90] C. Köhn and U. Ebert, 2014a. Angular distribution of Bremsstrahlung photons and of positrons for calculations of terrestrial gamma-ray flashes and positron beams. *Atmos Res.*, vol. 135-136, pp. 432-465
- [91] C. Köhn and U. Ebert, 2014b. The structure of ionization showers in air generated by electrons with 1 MeV energy or less. *Plasma Sour. Sci. Techn.*, vol. 23, 045001
- [92] C. Köhn et al., 2014. The importance of electron-electron Bremsstrahlung for terrestrial gamma-ray flashes, electron beams and electron-positron beams. *J. Phys. D:Appl. Phys as Fast Track Communication*, vol. 47, 252001
- [93] I.D. Kostyrya et al., 2006. X-ray radiation due to nanosecond volume discharges in air under atmospheric pressure. *Techn. Phys.*, vol. 51, pp. 356-361
- [94] H.N. Kothari and K.N. Joshipura, 2011. Total and ionization cross-sections of N₂ and CO by positron impact: Theoretical investigations. *Pramana - J. of Phys.*, vol. 76, pp. 477-488
- [95] I.M. Kutsyk et al., 2011. Self-sustained relativistic runaway electron avalanches in the transverse field of lightning leader as sources of terrestrial gamma-ray flashes. *JETP Lett.*, vol. 94, pp. 606-609

- [96] L. Landau and I. Pomeranchuk, 1953. Dokl. Akad. Nauk SSSR, vol. 92, pp. 535-536
- [97] S.A. Lawton and A.V. Phelps, 1978. Excitation of $b^1\Sigma_g^+$ state of O_2 by low-energy electrons. J. Chem. Phys., vol. 69, pp. 1055-1068
- [98] N.G. Lehtinen, 2000. Relativistic runaway electrons above thunderstorms. Ph.D. thesis, Stanford University, Stanford, CA
- [99] Les Renardières Group, 1978. Negative discharges in long air gaps at les Renardières. Paper presented at the request of the Chairman of Study Committee No. 33
- [100] C. Li et al., 2007. Deviations from the local field approximation in negative streamer heads. J. Appl. Phys., vol. 101, 123305
- [101] C. Li et al., 2009. 3D hybrid computations for streamer discharges and production of runaway electrons. J. Phys. D: Appl. Phys., vol. 42, 202003
- [102] C. Li et al., 2010. Spatially hybrid computations for streamer discharges with generic features of pulled fronts: I. Planar fronts. J. Comput. Phys., vol. 229, pp. 200-220
- [103] C. Li et al., 2012a. Spatially hybrid computations for streamer discharges: II. Fully 3D simulations. J. Comp. Phys., vol. 231, pp. 1020-1050
- [104] C. Li et al., 2012b. A comparison of 3D fluid, particle and hybrid model for negative streamers. Plasma Sour. Sci. Technol., vol. 21, 055019
- [105] J. Linsley, 1963. Evidence for a primary cosmic-ray particle with energy 10^{20} eV. Phys. Rev. Lett, vol. 10, pp. 146-148
- [106] G. Lu et al., 2011. Characteristics of broadband magnetic lightning emissions associated with terrestrial gamma-ray flashes. J. Geophys. Res., vol. 116, A03316
- [107] A. Luque et al., 2008. Positive and negative streamers in ambient air: modeling evolution and velocities. J. Phys. D: Appl. Phys., vol. 41, 234005
- [108] A. Luque and F.J. Gordillo-Vázquez, 2012. Mesospheric electric breakdown and delayed sprite ignition caused by electron detachment. Nature Geophys., vol. 5, pp. 22-25
- [109] A. Luque, 2014. Relativistic runaway ionization fronts. Phys. Rev. Lett., vol. 112, 045003
- [110] Electron scattering database LXCat, <http://www.lxcat.laplace.univ-tlse.fr>

- [111] V. March and J. Montanyà, 2010. Influence of the voltage-time derivative in X-ray emission from laboratory sparks. *Geophys. Res. Lett.*, vol. 37, L19801
- [112] M. Marisaldi et al., 2010. Detection of terrestrial gamma ray flashes up to 40 MeV by the AGILE satellite. *J. Geophys. Res.*, vol. 115, A00E13
- [113] T.C. Marshall et al., 2001. Positive charge in the stratiform cloud of a mesoscale convective system. *J. Geophys. Res.*, 106, pp. 1157-1164
- [114] G. Milikh and R. Roussel-Dupré, 2010. Runaway breakdown and electrical discharges in thunderstorms. *J. Geophys. Res.*, vol. 115, A00E60
- [115] C.B. Moore et al., 2001. Energetic radiation associated with lightning stepped-leaders. *Geophys. Res. Lett.*, vol. 28, pp. 2141-2144
- [116] R. Morrow and J.J. Lowke, 1997. Streamer propagation in air. *J. Phys. D: Appl. Phys.*, vol. 30, pp. 614-627
- [117] G.D. Moss et al., 2006. Monte Carlo model for analysis of thermal runaway electrons in streamer tips in transient luminous events and streamer zones of lightning leaders. *J. Geophys. Res.*, vol. 111, A02307
- [118] T. Murphy, 1988. Total and differential electron collision cross sections for O₂ and N₂. Los Alamos National Laboratory, 1988.
- [119] W. Nackel, 1994. The elementary process of Bremsstrahlung. *Phys. Rep.*, vol. 243, pp. 317-353
- [120] S. Nijdam et al., 2011. Probing background ionization: positive streamers with varying pulse repetition rate and with a radioactive admixture. *J. Phys. D: Appl. Phys.*, vol. 44, 455201
- [121] C.V. Nguyen et al., 2008. Multiple x-ray bursts from long discharges in air. *J. Phys. D-Appl. Phys.*, vol. 41, 234012
- [122] C.V. Nguyen et al., 2010. X-ray emission in streamer-corona plasma. *J. Phys. D-Appl. Phys.*, vol. 43, 025202
- [123] N. Østgaard et al., 2008. Production altitude and time delays of the terrestrial gamma flashes: Revisiting the Burst and Transient Source Experiment spectra. *J. Geophys. Res.*, vo. 113, A02307
- [124] S. Pancheshnyi, 2005. Role of electronegative gas admixture in streamer start, propagation and branching phenomena. *Plasma Sources Sci. Technol.*, vol. 14, pp. 645-653

- [125] S. Pancheshnyi et al., 2008. Computer code ZDPlasKin, <http://www.zdplaskin.laplace.univ-tlse.fr> (University of Toulouse, LAPLACE, CNRS-UPS-INP, Toulouse, France)
- [126] P.E. Penczynski and H.L. Wehner, 1970. Measurement of the energetic and angular dependence of the external Bremsstrahlung asymmetry. *Z. Physik*, vol. 237, pp. 75-85
- [127] L. Peralta, 2002. Monte Carlo simulation of neutron thermalization in matter. *Eur. J. Phys.*, vol. 23, pp. 307-314
- [128] M.E. Peskin and D.V. Schroeder, 1995. An introduction to quantum field theory, Westview Press
- [129] A.V. Phelps and L.C. Pitchford, 1985. Anisotropic scattering of electrons by N_2 and its effect on electron transport. *Phys. Rev. A*, vol. 31, pp. 2932-2949
- [130] A.V. Phelps, 1985. JILA Information Center Report No. 28, University of Colorado
- [131] Photon and electron interaction data, 1997. <http://www-nds.iaea.org/epdl97/>
- [132] R.H. Pratt et al., 1977. Bremsstrahlung energy spectra from electrons of kinetic energy $1 \text{ keV} < T_1 < 2000 \text{ keV}$ incident on neutral atoms $2 < Z < 29$. *Atom. Data Nucl. Data*, vol. 20, pp. 175-209
- [133] R.H. Pratt et al., 1981. Errata of Bremsstrahlung energy spectra from electrons of kinetic energy $1 \text{ keV} < T_1 < 2000 \text{ keV}$ incident on neutral atoms $2 < Z < 29$. *Atom. Data Nucl. Data*, vol. 26, pp. 477-481
- [134] M. Rahman et al., 2008. X-rays from 80 cm long sparks in air. *Geophys. Res. Lett.*, vol. 35, L06805
- [135] A.V. Rakov and M.A. Uman, 2003. Lightning: Physics and effects. Cambridge University Press
- [136] A.G. Rep'ev and P.B. Repin, 2008. Spatiotemporal parameters of the X-ray radiation from a diffuse atmospheric-pressure discharge. *Techn. Phys.*, vol. 53, pp. 73-80
- [137] E. Segrè, 1977. *Nuclei and Particles*, 2nd ed., W. A. Benjamin Inc., Massachusetts
- [138] S.M.Seltzer and M.J.Berger, 1985. Bremsstrahlung spectra from electron interactions with screened atomic nuclei and orbital electrons. *Nucl. Inst. Meth. B12*, pp. 95-134

- [139] S.M. Seltzer and M.J. Berger, 1986. Bremsstrahlung energy-spectra from electrons with kinetic energy 1 keV-10 GeV incident on screened nuclei and orbital electrons of neutral atoms with $Z = 1 - 100$. *Atom. Data Nucl. Data.*, vol. 35, pp. 345-418
- [140] C.D. Shaffer et al., 1996. Triply differential cross section and polarization correlations in electron Bremsstrahlung emission. *Phys. Rev. A*, vol. 53, pp. 4158-4163
- [141] C. D. Shaffer and R.H. Pratt, 1997. Comparison of relativistic partial-wave calculations of triply differential electron-atom bremsstrahlung with simpler theories. *Phys. Rev. A*, vol. 56, pp. 3653-3658
- [142] X.M. Shao et al., 2010. A closer examination of terrestrial gamma-ray flash-related lightning processes. *J. Geophys. Res.*, vol. 115, A00E30
- [143] T. Shao et al., 2011. Diffuse discharge, runaway electron, and x-ray in atmospheric pressure air in an inhomogeneous electrical field in repetitive pulsed modes. *Appl. Phys. Lett.*, vol. 98, 021506
- [144] Shardanand and A.D. Prasad Rao, 1977. Absolute Rayleigh scattering cross sections of gases and freons of stratospheric interest in the visible and ultraviolet regions. NASA Technical Note
- [145] I.P. Shkarofsky et al., 1966. *The particle kinetics of plasmas*. Addison-Wesley
- [146] T.W. Shyn et al., 1972. Angular distribution of electrons elastically scattered from N₂. *Phys. Rev. A*, vol. 6, pp. 1002-1012
- [147] The Siglo Data base, CPAT and Kinema Software, <http://www.siglo-kinema.com>
- [148] D. Siingh and R.P. Singh, 2010. The role of cosmic rays in the earth's atmospheric processes. *Pramana Jour. Phys.*, vol. 71, pp. 153-168
- [149] D.M. Smith et al., 2005. Terrestrial gamma-ray flashes observed up to 20 Mev. *Science*, vol. 307, pp. 1085-1088
- [150] D.M. Smith et al., 2010. Terrestrial gamma ray flashes correlated to storm phase and tropopause height. *J. Geophys. Res.*, vol. 115, A00E49
- [151] D.M. Smith et al., 2011. The rarity of terrestrial gamma-ray flashes. *Geophys. Res. Lett.*, vol. 38, L08807

-
- [152] Y.L. Stankevich and V.G. Kalinin, 1967. Fast electrons and X-ray radiation during the initial stage of growth of a pulsed spark discharge in air. *Sov. Phys. Dokl.*, vol. 12, pp. 1042-1043
- [153] A.B. Sun et al., 2013. Why isolated streamer discharges hardly exist above the breakdown field in atmospheric air. *Geophys. Res. Lett.*, vol. 40, 2417
- [154] T. Suwada et al., 2000. Absolute beam-charge measurements for single-bunch electron beams. *Jpn. J. Appl. Phys.*, vol. 39, pp. 628-634
- [155] M. Tavani et al., 2011. Terrestrial gamma-ray flashes as powerful particle accelerators. *Phys. Rev. Lett.*, vol. 106, 018501
- [156] M.L. Ter-Mikaelian, 1954. *Dokl. Akad. Nauk SSSR*, vol. 94, p 1033
- [157] F. Tessier and I. Kawrakow, 2007. Calculation of the electron-electron bremsstrahlung cross-section in the field of atomic electrons. *NIM. Phys. Res. B*, vol. 266, pp. 625-634
- [158] T. Torii et al., 2004. Downward emission of runaway electrons and bremsstrahlung photons in thunderstorm electric fields. *Geophys. Res. Lett.*, vol. 31, L05113
- [159] Y-S. Tsai, 1974. *Rev. Mod. Phys.*, vol. 46, p. 815
- [160] Y-S. Tsai, 1977. *Rev. Mod. Phys.*, vol. 49, p. 421
- [161] H.K. Tseng and R.H. Pratt, 1971. Exact screened calculations of atomic-field Bremsstrahlung. *Phys. Rev. A*, vol. 3, pp. 100-115
- [162] H. Tsuchiya et al., 2011. Long-duration gamma ray emissions from 2007 and 2008 winter thunderstorms. *J. Geophys. Res.*, vol. 116, D09113
- [163] V. Vahedi and M. Surendra, 1995. A Monte Carlo collision model for the particle-in-cell method applications to argon and oxygen discharges. *Comp. Phys. Comm.*, vol. 87, pp. 179-198
- [164] C.F. Weizsäcker, 1935. Zur Theorie der Kernmassen, *Zeitschrift für Physik*. vol. 96, pp. 431-458
- [165] C. Wilson, 1925. The electric field of a thundercloud and some of its effects. *Proc. Phys. Soc. London*, vol. 37A, pp. 32D-37D
- [166] W.P. Winn et al., 2011. Lightning leader stepping, K changes, and other observations near an intracloud flash. *J. Geophys. Res.*, vol. 116, D23115

-
- [167] G. Wormeester et al., 2010. Probing photo-ionization: Simulations of positive streamers in varying N₂:O₂-mixtures. *J. Phys. D: Appl. Phys.*, vol. 43, 505201
- [168] G.A. Wurden and D.O. Whiteson, 1996. High-speed plasma imaging: A lightning bolt. *IEEE Trans. On Plasma Science*, vol. 24, pp. 83-84
- [169] W. Xu et al., 2012a. Source altitudes of Terrestrial Gamma-ray Flashes produced by lightning leaders, *Geophys. Res. Lett.*, vol. 39, L08801
- [170] W. Xu et al., 2012b. Terrestrial gamma ray flashes with energies up to 100 MeV produced by nonequilibrium acceleration of electrons in lightning. *J. Geophys. Res. Space Phys.*, vol. 117, A05315
- [171] F.C. Young et al., 1973. Neutron production by hot dense plasmas generated with high power pulses. *IEEE Trans. Nucl. Sci.*, vol. 20, 439

Acknowledgements

Als Erstes möchte ich meinen Eltern Gisela Maria Monica Köhn und Joachim Köhn danken, die mich immer bei allem unterstützt haben. Ohne ihre Hilfe wäre ich erst gar nicht so weit gekommen, überhaupt ein Diplom in Physik machen zu können und dadurch die Möglichkeit bekommen zu haben, nach Amsterdam zu ziehen und hier meine Dissertation zu schreiben. Genauso scheint es heutzutage anscheinend auch nicht mehr selbstverständlich zu sein, dass Eltern ihre Kinder aufnehmen, so sie einmal ausgezogen sind. Deshalb auch ein Danke dafür! Genauso möchte ich auch meiner weiteren Familie danken (Waltraud, Hella, Sigggi, Anne, Rainer, Christina, Manni, Ernst-Georg, Jennifer, Eckhard, Mechthild, Sven, Maria und Sven-Thomas), die immer zu mir gehalten und mich immer, so gut es nur ging, unterstützt hat. Vielen lieben Dank!

Furthermore I would like to thank my supervisor Prof. Dr. Ute Ebert who helped me in finishing this project into a thesis. She gave me the right guidance and still freedom to develop into an independent thinker. Whenever I needed her advise, I got it. Whenever I had an idea, she listened. Whenever I told her I wanted to investigate a particular subject, she gave me enough time to work on it. Overall, I do not think that this project would have been successful without so much of her effort. Beyond that, she is a joyous person who manages to lighten up even very severe discussions. Thank you for that, Ute.

Moreover I would like to thank my group fellows Jannis Teunissen, Casper Rutjes, Anna Dubinova, Ashutosh Agnihotri, Enrico Camporeale, Willem Hundsdorfer and Margreet Nool to whom I could always come whenever I had the urge to talk about personal or scientific issues.

Besides there are my appreciated colleagues from the Technical University of Eindhoven, Pavlo Kochkin and Dr. Lex van Deursen. Pavlo, it was always a pleasure to work with you. I will never forget the so many times when we shared an apartment or hotel room in San Francisco or Vienna. It was really nice exploring these cities together with you. Lex, thank you for the many discussions with you and for letting me bend your ear.

You always had good suggestions both for work-related and also private issues.

Then there are my former group fellows: Anna Mozartova with whom I shared an office for several months and Anbang Sun who supported our CWI soccer team. Jens Rademacher who got to know his wife in Heiligenhafen, my home town, and whose family I got to know in Bremen. Then there is Chao Li who developed and explained the Monte Carlo code to me which was the basis for me to extend this code and ran simulations on my own. Aram Markosyan and Gideon Wormeester, the last two PhD students to finish. Aram, thank you for the various night hours. I was glad that I could discuss every personal and work-related topics with you. Although we had a tough start, it was finally a great time with you. Don't forget that we will have to skype once and drink Armenian brandy together ;) Then there is Gideon, one of the few collaegues to speak Dutch to me as often as possible. Thank you for supporting me in learning Dutch. He has also helped me in organizing the printing of my thesis and all PhD stuff related to Eindhoven. Although I could never convince him to join our soccer team, we played a lot of ping pong against each other. Even if you are convinced that your record might be positive, don't forget that I won the last time we played against each other. Finally there is my "Serbian friend" Saša Dujko without whom, I think, I would not have been able to finish my PhD studies in such a successful manner. He gave me scientific and mental support. I will never forget various discussions about politics and life in Serbia as well as about electrons and photons. I remember the parties we went to (Korsakov, R.I.P.) and my stays in Belgrade. It was very nice there and I thank you to have taught me very important Serbian words ("Jelen pivo"). Take care and say greetings to your family.

Daarnaast wil ik bijzonders de Nederlanders danken met wie ik altijd over alles kon praten en die mij hielpen, mijn Nederlanders te verbeteren. Iraes Rabbers, Bram van Es en Linda Plantagie. Ik ben heel blij dat ik jullie mocht leren kennen en ook dat jullie mij hielpen, de Nederlandse cultuur te begrijpen. Hetzelfde geldt voor de mensen die ik in de rookkamer ontmoette (toen ik nog rookte): Johan Schlepers, Coby van Vonderen, Henk Roose.

Besides the Dutch speaking people, I got to know so many fellow PhD students and postdocs with whom I spent so many smoking sessions, night-outs in Amsterdam or simply so many interesting conversations. Thank you Yunnus Hassen, Jānis Bajars, Wagner Fortes, Rodrigo Laioloa and Marwin Schmitt.

Furthermore I would like to thank the (former) members (who have not been mentioned before) of the PhD activity committee which I was allowed to chair from 2012 till 2014: Floor Sietsma chairing from 2011 till 2012, Emma Beauxis-Aussalet (still making posters for us, merci beaucoup ;)), Behnaz Changizi, Sara Ramezani, Rodrigo Guimaraes, Eleni Petraki, Yagiz Kargin, Sonja Boas, Mona Rahn, Simon Gunkel and Lisanne Rens. It was always fun to have meetings with you guys. I really enjoyed the environment. It was not always about organizing activities for our fellow PhD students (as well as for postdocs and master students ^), but all these meetings were both funny and productive. Thank you for the various hours together ;) Besides I would like to especially thank Léon

Ouwerkerk from the Personal Department who not only established the PhD activity committee in 2011, but also had an open ear for what topics ever.

One main part of my time at CWI was definitely the CWI soccer team: I thank Pham Duc, Willem Haverkort, Gunnar Klau, Alvaro Leitao, Tobias Marschall, Diego Mirandola, Keith Myerscough, Teresa Piovesan, Benjamin Sanderse, Tom Sterkenburg, Nick Verheul, Remi Verhoeven for the many football sessions and tournaments we had.

There are so many other people, I would like to thank at CWI for making this time so interesting, memorable, successful and joyable, especially Irma van Lunenburg and Karin van Gemert as well as Nada Mitrovic and Minnie Middelburg.

One big part of my life, even during my PhD studies, are my friends from Germany who always gave me mental support when I was down. I will never forget the parties I could still celebrate when I was back home. Many thanks to (and there is no particular order to be found.... probably a random number generator was involved in this) Michael Wende, Marijana Wende, Marco Wende (of course, also to your parents) Björn Engler, Sören Engler (and your parents, too), Leif Engler, Sven Engler, Jacky Weidemann, Yasmin Bösherz, Ulrich Smola, Sergej Renner, Thorge-Fynn Stein, Julia Struwe, Patrick Haller, Dennis Hauschild, Marek Wilsch, Eike-Sebastian Schlupp, Torben Reichstein, Jolande Heidenreich, Aileen König, Miriam Wichelmann, Dirk Perner, Janin Reimers, Björn Krups, Nico Fernow, Wiebke Schmütz, Janna Heinrich, Jannes Heinrich (and your parents), Sascha Lauer and Leif Bünning. Since I do not want to blow these acknowledgements up, I have relinquished commenting you all, but I guess and hope very much that you all know why you were taken over in this list!

Last, but not least there are those two people who supported me till the very end of my PhD time: Shashi Jain and Ramona Uthmann, my Paranimfs. Shashi, I actually do not recall how and where we first met, but I am very happy that I got to know you and that we had such a great time in Amsterdam. Finally, Mona, friend, girlfriend, paranimf. I am very happy that I got to know you so many years ago. You were always there for me when I was upset and tried to cheer me up and encourage me to continue with whatever path I had chosen. I am so happy that you could have taken part in this very important episode of my life.

Christoph Köhn

Curriculum vitae

Personal information

Date of birth: 31 Aug. 1984
Place of birth: Oldenburg in Holstein, Germany
Nationality: German

Education and employment

2010 - 2014 PhD Studies at the Centrum voor Wiskunde & Informatica (CWI),
Amsterdam, The Netherlands
Dissertation: “High-energy phenomena in laboratory
and thunderstorm discharges”

2008 - 2010 Study of physics at the University of Hamburg and DESY
in collaboration with CAU

2005 - 2010 Study of physics at the “Christian-Albrechts-Universität (CAU) zu Kiel”,
Germany
Intermediate diploma with mark “Very good”
Diploma thesis “ $N = 4$ Supergravitation einer T^2 - kompaktifizierten
sechsdimensionalen Theorie ”
Diploma with mark “Very good”

2004 “Abitur” (A levels) at the “Freiherr-vom-Stein-Gymnasium”
in Oldenburg in Holstein, Germany

Assistant teacher

- 2009/10 Analysis I, 1 group
- 2008/09 Theoretical Physics I (Mechanics), 2 groups

- 2008 Theoretical Physics II (Electrodynamics and special relativity), 1 group
- 2008 Elementary mathematical methods of physics II, 3 groups
- 2007/08 Theoretical Physics I (Mechanics), 1 group
- 2007/08 Elementary mathematical methods of physics I, 3 groups
- 2007 Theoretical Physics II (Electrodynamics and special relativity), 1 group
- 2006/07 Theoretical Physics I (Mechanics), 1 group

Journal papers

- Christoph Köhn and Ute Ebert, 2014. Angular distribution of Bremsstrahlung photons and of positrons for calculations of terrestrial gamma-ray flashes and positron beams. *Atmos. Res.*, **135-136**, 432-465 [Chapter 2]
- Christoph Köhn, Ute Ebert and Alessio Mangiarotti, 2014. The importance of electron-electron Bremsstrahlung for terrestrial gamma-ray flashes, electron beams and electron-positron beams. *J. Phys. D: Appl. Phys. as Fast Track Communication*, **47**, 252001 [Chapter 3]
- Christoph Köhn and Ute Ebert, 2014. Calculation of beams of positrons, neutrons and protons associated with terrestrial gamma-ray flashes. Revised for *J. Geophys. Res.* [Chapter 4]
- Christoph Köhn and Ute Ebert, 2014. The structure of ionization showers in air generated by electrons with 1 MeV energy or less. *Plasma Sources Sci. Technol.*, **23**, 045001 [Chapter 6]

Conference proceedings

- Christoph Köhn and Ute Ebert, 2014. Energy resolved positron and hadron spectrum produced by a negative stepped lightning leader. 2nd TEA-IS summer school, Collioure, France [2 pages]
- Gia Trinh, Olaf Scholten, Ad van den Berg, Stijn Buitink, Ute Ebert, Casper Rutjes and Christoph Köhn, 2014. Effects of atmospheric electric fields on radio emission from air showers. 2nd TEA-IS summer school, Collioure, France [2 pages]

- Christoph Köhn and Ute Ebert, 2013. Cross sections and modelling results for high-energy radiation and positron beams produced within a thundercloud. Int. Conf. Phenomena in ionized gases (ICPIG), Granada, Spain [2 pages]
- Christoph Köhn and Ute Ebert, 2012. Energy resolved TGF- and positron spectrum produced by a negative stepped lightning leader. TEA-IS summer school, Torremolinos, Spain [2 pages]
- Chao Li, Christoph Köhn and Ute Ebert, 2011. Modeling hard radiation from streamers and leaders and terrestrial gamma-ray flashes. Int. Conf. Phenomena in ionized gases (ICPIG), Belfast, Ireland [3 pages]
- Chao Li, Christoph Köhn, Ute Ebert and Willem Hundsdorfer, 2011. Understanding electron run-away and hard radiation from streamers and lightning. Int. Conf. Atmos. Elec. (ICAE), Rio de Janeiro, Brazil [4 pages]

Others

- Christoph Köhn, Margreet Nool and Ute Ebert, 2013. Onweer: een bron van broeikasgassen en antimaterie. Nieuw archief voor wiskunde, deel 14, nummer 3, pp. 212-216

Presentations

2014

- *Energy resolved positron and hadron spectrum produced by a negative stepped lightning leader.* 2nd TEA-IS summer school, 23. - 27. June 2014, Collioure, France [Poster presentation + conference proceedings]
- *Energy resolved positron and hadron spectrum produced by a negative stepped lightning leader.* EGU General Assembly, 2. May 2014, Vienna, Austria [Oral presentation]
- *Energy resolved positron and hadron spectrum produced by a negative stepped lightning leader.* 26th Symposium Plasma Physics & Radiation Technology, 11./12. March 2014, Lunteren, The Netherlands [Oral presentation]
- *Energy resolved positron and neutron spectrum produced by a negative stepped lightning leader.* Physics@FOM Veldhoven, 17./18. Jan. 2014, Veldhoven, The Netherlands [Poster presentation]

2013

- *The importance of electron-electron Bremsstrahlung for terrestrial gamma-ray flashes and electron-positron beams.* AGU Fall Meeting, 9. - 13. Dec. 2013, San Francisco, United States of America [Poster presentation]
- *Energy resolved positron and hadron spectrum produced by a negative stepped lightning leader.* 16th Workshop on the exploration of low temperature plasma physics (WELTPP), 21./22. Nov. 2013, Kerkrade, The Netherlands [Oral presentation]

- *Cross sections and modelling results for high-energy photons and for positron beams produced in a thundercloud.* 3rd National Conference on electron, atomic, molecular and photonic Physics (CEAMPP), 25. Aug. 2013, Belgrade, Serbia [Invited oral presentation]
- *Modelling terrestrial gamma-ray flashes from a negative stepped lightning leader.* 23th International Conference on Phenomena in Ionized Gases (ICPIG), 15. - 19. July 2013, Granada, Spain [Poster presentation + conference proceedings]
- *Energy and density of low-energy electrons produced by high-energy cosmic particles in the troposphere.* EGU General Assembly, 9. -11. April 2013, Vienna, Austria [Poster presentation]
- *Modelling terrestrial gamma-ray flashes from a negative stepped lightning leader.* 25th Symposium Plasma Physics & Radiation Technology, 5./6. March 2013, Lunteren, The Netherlands [Poster presentation]
- *A model for terrestrial gamma-ray flashes from thunderstorms.* Physics@FOM Veldhoven, 22./23. Jan. 2013, Veldhoven, The Netherlands [Oral presentation]

2012

- *Low-energy electrons produced by high-energy cosmic particles in the upper atmosphere.* AGU Fall Meeting, 3. - 7. Dec. 2012, San Francisco, United States of America [Poster presentation]
- *Modelling a negative stepped lightning leader and Bremsstrahlung photons.* 1st TEA-IS summer school, 17. - 22. June 2012, Torremolinos, Spain [Oral presentation + conference proceedings]
- *Towards understanding terrestrial gamma-ray flashes (TGFs), hard X-rays and positron production in thunderclouds.* 24th Symposium Plasma Physics & Radiation Technology, 6./7. March 2012, Lunteren, The Netherlands [Poster presentation]
- *Towards understanding terrestrial gamma-ray flashes (TGFs), hard X-rays and positron production in thunderclouds.* Physics@FOM Veldhoven, 17./18. Jan. 2012, Veldhoven, The Netherlands [Poster presentation]

2011

- *Angular distribution of Bremsstrahlung photons for calculations of terrestrial gamma-ray flashes (TGFs).* 14th Workshop on the exploration of low temperature plasma

physics (WELTPP), 1./2. Dec. 2011, Kerkrade, The Netherlands [Poster presentation]

- *Angular distribution of Bremsstrahlung photons for calculations of terrestrial gamma-ray flashes (TGFs)*. TEA-IS kick-off meeting, Oct. 2011, Leiden, The Netherlands [Poster presentation]
- *Modelling Bremsstrahlung and calculating energies and angles of hard photons ahead of lightning leaders*. TGF Workshop, 13./14. July 2011, Huntsville, United States of America [Poster presentation]
- *Differential Bremsstrahlung cross sections for predicting terrestrial gamma-ray flashes*. 2nd National Conference on electron, atomic, molecular and photonic Physics (CEAMPP), 21. June 2011, Belgrade, Serbia [Poster presentation]